Final Report

3-D Enzymatic Nanomaterial Architectures
For Energy Harvesting
FA9550-12-1-0112

Principal Investigator:

Scott Banta
Department of Chemical Engineering
Columbia University (CU)
820 Mudd, MC4721, 500 W 120th St, New York, NY 10027
Tel: (212) 854-7531 Fax: (212) 854-3054
E-mail: sbanta@columbia.edu

Co-Principal Investigators:

Plamen Atanassov
Department of Chemical and Biological Engineering, University of New Mexico (UNM), Albuquerque, NM

David Baker
Department of Biochemistry, University of Washington (UW), Seattle, WA

Shelley D. Minteer
Department of Chemistry, University of Utah (UU), Salt Lake City, UT

Table of Contents

Introduction……………………………………………………………………………………3

Research Thrust I: Rationally Designed Heterogenous Biomolecular Complexes for Biomaterial Interfaces

Designed Protein Aggregates Entrapping Carbon Nanotubes for Bioelectrochemical Oxygen Reduction……………………………………………………………………...8

Functional Interfaces for Biomimetic Energy Harvesting: CNTs-DNA Matrix for Enzyme Assembly……………………………………………………………………………………24

A Hybrid DNA-Templated Gold Nanocluster for Enhanced Enzymatic Reduction of Oxygen………………………………………………………………………………...…42

Electrochemical Enhancement of Small Laccase DNA Complex with DNA-Templated Gold Nanoclusters……………………………………………………………………………..65

Malate Dehydrogenase and Citrate Synthase on Modified Multi-Walled Carbon Nanotubes for Mediated L-Malate Oxidation…………………………………………………82

Research Thrust II: Computationally Designed Biomolecular Interactions for Structured, Crystalline Self-Assembly

Computational design for protein self-assembly………………………………………....95

Doubling the cross-linking interface of a rationally-designed beta roll peptide for calcium-dependent proteinaceous hydrogel formation………………………………....105

Research Thrust III: Protein Engineering for Enzyme Active Site Organization: Artificial Metabolons

The TCA Cycle Metabolon…………………………………………………………….….119

The ETC Metabolon……………………………………………………………………….127

DNA as a Scaffold for Forming Artificial Metabolons…………………………………150

Metabolon formation and substrate channeling in recombinant TCA cycle enzymes…157

Recombinant TCA Cycle Enzymes Arranged on DNA scaffolds by Fused Zinc Finger Domains…………………………………………………………………………………...181

Introduction

In this innovative and highly collaborative 4 year proposal, we had two overriding objectives: 1) to design, develop, and demonstrate new techniques for engineering biological components that are optimized for integration with nanoscale materials and 2) to create and characterize multi-functional heterogeneous biomacromolecular assemblies that will facilitate energy harvesting applications. To accomplish these goals, a holistic approach was taken both experimentally and computationally that helped build a foundation for a new paradigm in biotechnology. Specifically, we designed, developed and created these systems at the molecular level while using a systems level process view to guide the designs.

In order to create these new materials, three complimentary research approaches were pursued:

Research Thrust I: Rationally Designed Heterogenous Biomolecular Complexes for Biomaterial Interfaces

This part of the program focused on the assembly of different component parts to create new multi-functional complexes. Nature has evolved many different domains that can be assembled together to make various chimeric protein and biomacromolecular systems. Although these different interactions have been studied to understand their biological function, they are rarely exploited for technological advancement. In addition, there is a growing interest in the interface between biological molecules and non-natural, nano-scaled inorganic and organic materials. The overall goal of this Research Thrust was to rationally engineer heterogenous macromolecular assemblies and nanoscale components that are designed for use in energy harvesting applications.

Research Thrust II: Computationally Designed Biomolecular Interactions for Structured, Crystalline Self-Assembly

In this thrust, we proposed to make advances in the computational and experimental science with respect to understanding enzyme-nano-materials interaction that allow engineering bio/nano-interfaces with practical applications in enzymatic biofuel cells and other energy harvesting devices. As this goal is achieved, a practical direction towards the replacement of metal catalysts with composite materials made from biological enzymes and single walled carbon nanotubes (SWCNTs) can be charted. Such a biomimetic approach was timely as we are witnessing increased accumulation of the empirical knowledge pertinent to enzyme integration with electrodes. Further, current advances in bioengineering and computational protein design brought an opportunity to incorporate these approaches into a concerted effort for bio-electrocatalytic materials design.

The leading computational component of this research has provided the unique ability to chart approaches towards the creation of full inorganic enzyme mimics. The revolutionary charter of this concept is that for the first time such a biomimetic approach in electrocatalysis is being conceived as a materials design concept, as opposed to molecular mimic of the active site. Years of fruitless attempts to mimic the enzyme activity, particularly in charge transfer reactions, with organo-metallic complexes is being surpassed by rational design based on materials integration at the nano-scale. This allowed for the demonstration of current densities of merit for practical electrocatalysis.

Research Thrust III: Protein Engineering for Enzyme Active Site Organization: Artificial Metabolons

The existence of organizational, intermolecular interactions between sequential enzymes of metabolic pathways has been explored extensively throughout the field of biochemistry. These closely coupled pathways, termed *metabolons*, have been demonstrated to induce substrate channeling that results in increased efficiency by enhancing local substrate concentrations, protecting liable intermediates, and limiting distance between enzyme active sites. This phenomenon may have direct implication in the advancement of enzyme cascade-based bioanodes for enzymatic biofuel cells through the use of supercomplex formations of metabolic pathways as bioanode catalysts. This results in an efficient means of a more complete oxidation of a fuel, while optimizing the flux of the system through the recreation of a phenomenon that is conserved throughout biology. This research thrust explored two different experimental approaches for formation of metabolons. (1) Chemical conjugation techniques for forming in-vivo metabolons and creating artificial metabolons was employed to better understand the important structure and intermolecular interactions that are necessary for metabolon formation and substrate channeling. (2) The second approach was to employ protein engineering techniques for producing artificial metabolons. Molecular engineering can be used to add new linking and assembly domains and that will allow "Lego-like" construction of optimized supercomplexes.

The result of this project led to the submission or publication of 33 peer reviewed manuscripts as follows:

1. F. Wu and **S.D. Minteer**, "Fluorescent Characterization of Co-Immobilization Induced Multi-Enzyme Aggregation in a Polymer Matrix Using Förster Resonance Energy Transfer (FRET): Towards the Metabolon Biomimic," Biomacromolecules, 2013, 14(8), 2739-2749.

2. D. Hickey, F. Giroud, D. Schmidke, D. Glatzhofer, and **S.D. Minteer**, "Enzyme Cascade for Catalyzing Sucrose Oxidation," ACS Catalysis, 2013, 3(12), 2729-2737.

3. R. Milton, F. Giroud, A. Thumser, **S.D. Minteer**, and R. Slade, "Hydrogen peroxide produced by glucose oxidase affects the performance of laccase cathodes in glucose/oxygen fuel cells: FAD-dependent glucose dehydrogenase as a replacement," Physical Chemistry Chemical Physics, 2013, 15(44), 19371-19379.

4. King NP, Bale JB, Sheffler W, McNamara DE, Gonen S, Gonen T, Yeates TO, **Baker D.** Accurate design of co-assembling multi-component protein nanomaterials. *Nature*. 2014 Jun 5;510(7503):103-8.

5. R. Milton, F. Giroud, A. Thumser, **S.D. Minteer**, and R. Slade, "Bilirubin oxidase bioelectrocatalytic cathodes: the impact of hydrogen peroxide," ChemComm, 2014, 50(1), 94-96.

6. Dooley, K., Bulutoglu, B. and **Banta, S.** (2014) “Doubling the cross-linking interface of a rationally-designed beta roll peptide for calcium-dependent proteinaceous hydrogel formation” *Biomacromolecules* **15**(10) 3617-3624.
7. K. Nguyen, F. Giroud, and **S.D. Minteer**, “Improved bioelectrocatalytic oxidation of sucrose in a biofuel cell with an enzyme cascade assembled on a DNA scaffold,” Journal of the Electrochemical Society, 2014, 161(14), H930-H933.
8. N. Hausman, **S.D. Minteer**, and D. Baum, “Controlled Placement of Enzymes on Carbon Nanotubes using Comb-Branched DNA,” Journal of the Electrochemical Society, 2014, 161(13), H3001-H3004.
9. C.W. Narváez Villarrubia, C. Lau, G.P.M.K. Ciniciato, S.O. Garcia, S.S. Sibbett, D.N. Petsev, S. Babanova, G. Gupta and **P. Atanassov**, Practical Electricity Generation from a Paper Based Biofuel Cell Powered by Glucose in a Commercial Beverage, *Electrochem. Comm*., 45 (2014) 44-47
10. Brunette TJ, Parmeggiani F, Huang PS, Bhabha G, Ekiert DC, Tsutakawa SE, Hura GL, Tainer JA, **Baker D.** Exploring the repeat protein universe through computational protein design. *Nature*. 2015 Dec 24;528(7583):580-4.
11. Bale JB, Park RU, Liu Y, Gonen S, Gonen T, Cascio D, King NP, Yeates TO, **Baker D.** Structure of a designed tetrahedral protein assembly variant engineered to have improved soluble expression. *Protein Sci*. 2015 Oct;24(10):1695-701.
12. Gonen S, DiMaio F, Gonen T, **Baker D.** Design of ordered two-dimensional arrays mediated by noncovalent protein-protein interfaces. *Science*. 2015 Jun 19;348(6241):1365-8.
13. Lau, C., Moehlenbrock, M.J., Arechederra, R.L., Falase, A., Garcia, K., Rincon, R., **Minteer, S.D**., **Banta, S.,** Gupta, G., Babanova, S. and **Atanassov, P.** (2015) “Paper based biofuel cells: Incorporating enzymatic cascades for ethanol and methanol oxidation” *International Journal of Hydrogen Energy* **40**(42) 14661-14666.
14. K. Van Nguyen and **S.D. Minteer**, “Investigating DNA hydrogels as a new biomaterial for enzyme immobilization in biobatteries ,” Chemical Communications, 2015, 51, 13071-13073.
15. K. Nguyen and **S.D. Minteer**, “DNA-Functionalized Pt nanoparticles as catalyst for chemically powered micromotor: Toward signal-on motion-based DNA biosensor,”Chemical Communications, 2015, 51, 4792-4784.
16. F. Wu and **S.D. Minteer**, “Krebs Cycle Metabolon: Structural Evidence of Substrate Channeling,” Angewandte Chemie, 2015, 54(6), 1851-1854.

17. F. Wu, L. Pelster, and **S.D. Minteer**, "Krebs Cycle Metabolon Formation: Metabolite Concentration Gradient Enhanced Compartmentation of Sequential Enzymes," Chemical Communications, 2015, 51, 1244-1247.

18. B. Tan, D. Hickey, R. Milton, and **S.D. Minteer**, "Regeneration of the NADH Cofactor by a Rhodium Complex Immobilized on Multi-Walled Carbon Nanotubes," Journal of the Electrochemical Society, 2015, 162(3), H102-H107

19. S. Chakraborty, S. Babanova, R.C. Rocha, A. Desireddy, K. Artyushkova, A.E. Boncella, **P. Atanassov**, J.S. Martinez, A Hybrid DNA-Templated Gold Nanocluster for Enhanced Enzymatic Reduction of Oxygen, *Journal of the American Chemical Society*, 137 (2015) 11678–11687

20. Hjelm, R., Garcia, E., Babanova, S., Artyushkova, K., **Banta, S.** and **Atanassov, P.** (2016) "Functional Interfaces for Biomimetic Energy Harvesting: CNTs-DNA Matrix for Enzyme Assembly" *Biophysica et Biochimica Acta (Bioenergetics)* (Special Issue: Biodesign for Bioenergetics) **1857**(5) 612-620.

21. **S.D. Minteer**, "Oxidative Bioelectrocatalysis: From Natural Metabolic Pathways to Synthetic Metabolons and Minimal Enzyme Cascades," Biochimica et Biophysica Acta – Bioenergetics, 2016, 1857, 621-624. (Special Issue: Biodesign for Bioenergetics)

22. R.D. Milton, T. Wang, K. Knoche, and **S.D. Minteer**, "Tailoring Biointerfaces for Electrocatalysis," Langmuir, 2016, 32, 2291-2301.

23. K. Van Nguygen, Y. Holade, and **S.D. Minteer**, "DNA redox hydrogels: Improving mediated enzymatic bioelectrocatalysis," ACS Catalysis, 2016, 6, 2603-2607.

24. Bale JB, Gonen S, Liu Y, Sheffler W, Ellis D, Thomas C, Cascio D, Yeates TO, Gonen T, King NP, **Baker D.** Accurate design of megadalton-scale multi-component icosahedral protein complexes. *Science* (Accepted)

25. Garcia, K., Babanova, S., Sheffler, W., Hans, M., Baker, D., **Atanassov, P.**, and **Banta, S.** (2016) "Designed Protein Aggregates Entrapping Carbon Nanotubes for Bioelectrochemical Oxygen Reduction" *Biotechnology and Bioengineering* (In Press).

26. L. Pelster and S.D. Minteer, "Mitochondrial Inner Membrane Biomimic for the Investigation of Electron Transport Chain Supercomplex Bioelectrocatalysis**," ACS Catalysis,** (In press).

27. Fallas JA, Ueda G, Sheffler W, McNamara DE, Sankaran B, Pereira JH, Parmeggiani F, Brunette TJ, Cascio D, Yeates TR, Zwart P, **Baker D.** Computational design of self-assembling cyclic protein homooligomers. *Nature Chemistry* (In review).

28. Bulutoglu, B., Garcia, K.E., Wu, F., **Minteer, S.D**., and **Banta, S.** “Direct evidence for metabolon formation and substrate channeling in recombinant TCA cycle enzymes” *ACS Chemical Biology* (Submitted).

29. M. Rasmussen, A. Serov, T. C. Rose, **P. Atanassov**, J. M. Harris, and **S. D. Minteer**, Enhancement of Electrocatalytic Oxidation of Glycerol by Plasmonics, *Journal of Power Sources,* (2016) (Re-submitted after revision)

30. R. Hjelm, R., S. Babanova, **S. Minteer** and **P. Atanassov**, Malate Dehydrogenase and Citrate Synthase on Modified Multi-Walled Carbon Nanotubes for Mediated L-Malate Oxidation (In preparation)

31. R. Hjelm, S. Chakroborty, S. Babanova, S. Martinez and **P. Atanassov**, Electrochemical Activity Enhancement of Small laccase zinc finger DNA complex with gold nano clusters (In preparation)

32. K. Garcia, R. Hjelm, S. Babanova, K. Artyushkova, **P. Atanassov** Decoration of Single-walled Carbon Nanotubes with an Oxygen Reducing Laccase Enzyme Enabled by Genetic Fusion to a Self-assembling Peptide Coating, (In preparation)

33. Garcia, K., Bulutoglu, B., and **Banta, S.** “Recombinant TCA Cycle Enzymes Arranged on DNA scaffolds by Fused Zinc Finger Domains” (In Preparation)

Designed Protein Aggregates Entrapping Carbon Nanotubes for Bioelectrochemical Oxygen Reduction

Introduction

A grand challenge in the development of efficient bioelectrocatalytic systems is the optimization of transport and reaction kinetics within robust electrode surface modifications. The incorporation of enzymes into these systems presents unique challenges including operational stability, poor compatibility with entrapping polymer matrices, and optimizing spatial arrangements with mediating or relay systems (Kim et al., 2006; Minteer et al., 2007). A variety of materials engineering approaches have been developed to better enable the incorporation of native enzymes into electrode systems (Addo et al., 2010; Lau et al., 2012; Lim et al., 2007), and a few protein engineering approaches have been used to improve the protein/nanomaterial interface (Holland et al., 2011; Szilvay et al., 2011; Wong and Schwaneberg, 2003).

Computational protein design has been successfully used to engineer almost every feature of proteins, including binding, stability and catalysis (Jiang et al., 2008; King et al., 2012; King et al., 2014; Korkegian et al., 2005; Padilla et al., 2001; Usui et al., 2009). A recent trend is the use of protein design principles to create non-natural assemblies of protein structures to generate long-range order in self-assembling systems (Padilla et al., 2001; Usui et al., 2009). These unique protein structures show great promise for the development and improvement of bio/nano interfacial systems as these arrangements can lead to improved stability and optimized spatial orientations.

Multi-copper oxidase enzymes directly reduce oxygen and have been extensively explored for use in enzymatic bio-cathodes to be used in biological fuel cells (BFCs), bio-batteries and self-powered bio-sensors (Babanova et al., 2014; Lau et al., 2012; Tsujimura et al., 2007). BFCs are devices that utilize biocatalysts for energy transformation (Barton et al., 2004; Cooney et al., 2008; Davila et al., 2008; Logan et al., 2006; Luckarift et al., 2014). Since the chemical energy stored in ubiquitous fuels available in the environment is transformed into electricity in BFCs, the practical application of these systems is often associated with energy harvesting. BFCs using enzymes as catalytic units are predominantly associated with the design of small devices, generating relatively high power (Luckarift et al., 2014). The critical drawback of enzymatic BFCs is their operational lifetime, which can be limited by the environmental stability of immobilized enzymes.

The fungal laccases have been well-studied for the development of bio-cathodes due to their high activity and redox potential, but the engineering of these proteins is more challenging as they generally do not express well in prokaryotic hosts (Glykys et al., 2011). Bacterial laccases, such as the small laccase (SLAC) from *Streptomyces coelicolor* can have lower redox potentials but are more active at neutral pH and are more amenable to protein engineering strategies (Machczynski et al., 2004). Previously, the trimeric SLAC enzyme has been combined with single-walled carbon nanotubes (SWNTs) and also engineered to form self-assembling protein hydrogels with osmium redox centers, demonstrating its utility as a biocathode modification (Gallaway et al., 2008; Szilvay et al., 2011; Wheeldon and Gallaway, 2008). Here we use computational design to identify mutations for the introduction of new inter-protein disulfide bonds that would enable the SLAC enzyme to self-assemble into stable, functional crystalline-like assemblies.

Materials and Methods

Materials

Oligonucleotides were purchased from Integrated DNA Technologies (Coralville, IA). All cloning enzymes and *E. coli* BL21 (DE3) competent cells were from New England Biolabs (Ipswich, MA). Isopropyl β-D-1-thiogalactopyranoside (IPTG) was from Gold Biotechnology (St. Louis, MO). HALT protease inhibitor, Pierce Coomassie (Bradford) Protein Assay Kit, precast NuPAGE SDS-PAGE gels, NuPAGE SDS MES running buffer and Novex Sharp Pre-stained Protein Standard were from Thermo Fisher Scientific (Waltham, MA). HisTrap FF columns and the ÄKTA FPLC system were purchased from GE Healthcare (Piscataway, NJ). Uranyl acetate was purchased from Polysciences Inc. (Warrington, PA). Carbon black Vulcan X72 was purchased from Cabot Corporation (Boston, MA), Carbon coated 400 mush Cu/Rh grids were purchased from Ted Pella Inc (Redding, CA). All other chemicals were purchased from Sigma-Aldrich (St. Louis, MO) at the highest purity unless otherwise specified.

Construction, expression and purification of enzymes

The pSLAC-His vector encodes for the SLAC enzyme from *Streptomyces coelicolor* with a C-terminal His$_6$-tag (Szilvay et al., 2011). The Gly70 and Ala189 amino acids were mutated to cysteine by site-directed mutagenesis generating pSLAC-DC-His. The vector pSLAC-DC-His was transformed into *E. coli* BL21(DE3) cells for SLAC-DC-His protein expression.

Cells were grown in 2xYT media at 37°C. At OD_{600} ~1.5, protein expression was induced by the addition of 0.4 mM IPTG, and the cells were grown an additional 20 hours at 25°C. Cells were collected by centrifugation and stored at -20°C. Frozen cell pellets corresponding to 1 L of culture were thawed on ice for 30 minutes and the suspended in 50 mL of Buffer A (20 mM sodium phosphate buffer, 40 mM imidazole, 50 mM NaCl at 7.3 mM) with HALT EDTA-free protease inhibitor. Cells were sonicated for 6 minutes using a microtip probe, and lysates were centrifuged for 30 minutes at 15,000 x *g*. Lysates were applied to a HisTrap FF column equilibrated with Buffer A, and bound proteins were eluted with a linear gradient of 0 to 100% Buffer B (20 mM sodium phosphate buffer, 500 mM Imidazole, 500 mM NaCl at 7.3 mM) using an ÄKTA FPLC system. Fractions containing SLAC-His or SLAC-DC-His shown by SDS PAGE with bands at 38 kDa were pooled, dialyzed four times against 10 mM sodium phosphate buffer at pH 7.3 and concentrated by ultrafiltration.

Purified SLAC-DC-His and SLAC-His solutions were incubated with $CuSO_4$ corresponding to five times the concentration of the enzyme at 4°C for several hours. SLAC-DC-His aggregates were collected by centrifugation. SLAC-His was dialyzed against 50 mM ammonium bicarbonate buffer and lyophilized for long-term storage. Protein concentrations were determined by Bradford assay with bovine serum albumin standards for both SLAC-His and SLAC-DC-His and by absorbance at 590 nm with the extinction coefficient 4400 M^{-1} cm^{-1} for SLAC-His after the addition of $CuSO_4$ (Machczynski et al., 2004).

Kinetic characterization

The activity of SLAC-DC-His aggregates for 2,6-Dimethylphenol (DMP) was verified visually after the addition of 10 mM DMP, and SLAC-DC-His aggregates formed in the presence of single-walled carbon nanotubes were also active. 20 µL samples containing 1.8 mg of SLAC-His and pre-formed SLAC-DC-His aggregates were incubated with an equal volume of SWNT ink for 1 hour at room temperature. Samples were also prepared in which SLAC-DC-His aggregates were formed after incubating SLAC-DC-His with the SWNT ink. Samples were then diluted 100x and assayed in 10 mM DMP. Measurements were performed in triplicate on a Spectramax M2 plate reader (Molecular Devices, Sunnyvale, CA), and reactions were monitored at 468 nm for the formation of the dimeric product 3,3',5,5'-tetramethoxydiphenylquinone with the extinction coefficient 14,800 M^{-1} cm^{-1}. Activities were normalized by their activity without SWNTs.

Dilute protein solutions were prepared to determine kinetic activities by adding $CuSO_4$ to 200 nM SLAC-DC-His. Protein solutions were incubated for several hours at 4°C with $CuSO_4$ corresponding to 5 times the concentration of enzyme. SLAC-DC-His activity was determined using concentrations ranging from 0 – 100 mM DMP in air-saturated 10 mM sodium phosphate buffer pH 7.3 with a final enzyme concentration of 20 nM. Measurements were performed in triplicate, and reactions were monitored at 468 nm. All data were fit to the Michaelis-Menten equation using SigmaPlot nonlinear regression software.

Transmission Electron Microscopy (TEM)

SLAC-DC-His aggregates with a final concentration of 0.7 mg/mL following a 10x dilution were negatively stained with 1% uranyl acetate in water on a carbon coated 400 mesh Cu/Rh grids that had been glow discharged for 1 minute before use. Samples were imaged on a Philips CM12 Tungsten Emission TEM (FEI, Eindhoven, Netherlands) at 120 kV with a Gatan 4 k x 2.67 k digital camera (Gatan Inc., Pleasanton, CA).

Aggregate Size Analysis

Samples of SLAC-DC-His with a concentration of 7 mg/mL were incubated for 20 minutes on ice, room temperature, and 50°C. $CuSO_4$ was then added and samples were incubated for 1 hour under the same conditions. Samples were diluted 100x then imaged using an Olympus CKX41 microscope with a Canon EOS 60D camera. At least 6 images per sample were analyzed with ImageJ to determine the area of 800 aggregates.

Thermostability measurements

Samples containing 200 nM of SLAC-DC-His aggregates or SLAC-His in 10 mM sodium phosphate buffer, pH 7.3, were incubated at 25°C, 70°C, and 98°C for 30 minutes Samples were then cooled on ice for 10 minutes. Three samples at each temperature were assayed for residual activity in 10 mM DMP as described above. Average residual activities were normalized with respect to the residual activities at 25°C.

Rotating Disk Electrode (RDE) measurements

Three different configurations for SLAC-DC-His immobilization and incorporation into the SWNTs matrix were utilized: i) SLAC-DC-His aggregates were adsorbed on a surface modified with SWNTs; ii) pre-formed SLAC-DC-His aggregates were combined with SWNTs; iii) SWNTs were incorporated with SLAC-DC-His during aggregation. For the first configuration, 30 μL of the SWNT ink was deposited on the surface of RDE and dried under nitrogen. Then 20 μL (0.9 mg) of SLAC-DC-His aggregates in 0.1 M phosphate buffer (pH 7.5) was dropped on the SWNTs surface and dried at ambient conditions. For the second configuration, 20 μL of the SWNT ink was deposited on the surface of RDE and dried under nitrogen. 1.8 mg of SLAC-DC-His after their aggregation were dissolved in 20 μL of 0.1 M phosphate buffer (pH 7.5), mixed with 20 μL of the SWNT ink and left at ambient temperature for 1 hour. Then 20 μL of this enzyme-nanotubes assembly was dropped on the surface of the already placed SWNTs and dried under ambient conditions. For the final configuration in which the SWNTs were incorporated with SLAC-DC-His prior to their aggregation, 20 μL of the SWNT ink was deposited on the surface of the RDE and dried under nitrogen. 1.8 mg of SLAC-DC-His before aggregate formation was initiated in 20 μL of 0.1 M phosphate buffer (pH 7.5) was mixed with 20 μL of the SWNT ink and left at ambient temperature for 1 hour. $CuSO_4$ was added to the mixture and incubated so SLAC-DC-His aggregates can form in the presence of the SWNTs. Then 20 μL of this enzyme-nanotubes assembly was dropped on the surface of the already placed SWNTs and dried under ambient conditions.

An enzyme-free control electrode was prepared by depositing 20 μL of the SWNT ink on the surface of the RDE and then dried under nitrogen. A second control electrode with the control enzyme SLAC-His was also prepared. 20 μL of the SWNT ink was deposited on the surface of RDE and dried under nitrogen. 1.8 mg of SLAC-His were dissolved in 20 μL of 0.1 M phosphate buffer (pH 7.5), mixed with 20 μL of the SWNT ink and left at ambient temperature for 1 hour. Then 20 μL of this enzyme-nanotubes assembly was dropped on the surface of the already placed SWNTs and dried under ambient conditions. A third control electrode with denatured SLAC-His was also prepared. SLAC-His was incubated at 98°C for 1 hour in the presence of 8 M urea, dialyzed three times against 0.1 M phosphate buffer (pH 7.5) and checked for loss of activity for DMP. 20 μL containing 1.8 mg of denatured SLAC-His was mixed with 20 μL of the SWNT ink and left at ambient temperature for 1 hour. Then 20 μL of this enzyme-nanotubes assembly was dropped on the surface of the already placed SWNTs and dried under ambient conditions. Each of the studied electrodes had 0.9 mg of enzyme per electrode.

All electrochemical measurements were performed in a three-electrode configuration with the cathode connected as working electrode, saturated Ag/AgCl and Pt-wire as reference and counter electrodes, respectively. 0.1 M phosphate buffer (pH 7.5) was used as electrolyte. For the RDE measurements, Pine Research Instrumentation rotator (Grove City, PA) coupled with a VersaSTAT 3 potentiostat (Princeton Applied Research, Oak Ridge, TN). Linear sweep voltammetry from 0.8 to -0.60 V vs. Ag/AgCl with 10 mV/s and different rotating rates was carried out in oxygen depleted, oxygen saturated and an electrolyte with dissolved oxygen. Reverse scans were initially performed, but it was found that they did not provide any additional information and were excluded from subsequent measurements for simplicity. RDE measurements of SWNT-modified electrodes without enzyme were performed as a control. The oxygen concentration during the RDE measurements was monitored using DO probe. Three independent identical electrodes for each cathode type were prepared and tested for reproducibility.

Temperature-controlled RDE measurements

The modified RDE electrodes were introduced into electrochemical cell, and the temperature of the electrolyte was kept for 30 minutes at 25, 50 and 70°C, respectively, using a water jacket.

Linear sweep voltammetry from 0.8 to -0.60 V vs. Ag/AgCl with 10 mV/s and 1600 rpm was carried out in oxygen saturated electrolyte. Current densities at -50 mV with the SWNT control current density subtracted were used as comparison. Three independent identical cathodes were tested at each temperature for reproducibility.

Gas-diffusion cathodes

SLAC-DC-His was incorporated in the design of gas-diffusion cathodes. The cathodes were composed of plastic case, carbon black Vulcan X72, modified with 35% of polytetrafluoroethylene referred in this study as XC35 for the development of the gas-diffusion layer (GDL) and 100 mg of XC35 covered by a mixture of 50 mg XC35, 50 mg SWNTs and SLAC-DC-His aggregates formed in presence of SWNTs as it was described before, or SLAC-His explored as a catalytic layer (CL). The CL was pressed at 500 psi for 5 min and circular discs with 0.15 cm diameter were cut for the cathode assembly. The final loading of SLAC-DC-His or SLAC-His per electrode was 9.2 μg of enzyme. Ni wire going from the catalytic layer through the GDL was placed for electrical contact. This cathode design allows manufacturing of multiple electrodes from a single XC35-carbon black-SLAC pressed tablet and thus increases the reproducibility of the preparation procedure. Pure oxygen was blown from the outer side of the GDL while potentiostatic polarization curves were obtained using a Gamry 600 potentiostat (Warminster, PA). Three independent identical electrodes for each cathode type were prepared and tested for reproducibility.

Results and Discussion

The guiding principle in the assembly design process is to introduce a single new dimeric interface between SLAC protein molecules, which, in combination with the threefold symmetry of SLAC, will drive self-assembly of a material. Following the geometric constraints presented by Padilla et al. (Padilla et al., 2001), the SLAC enzyme can be assembled into a P 41 3 2 crystal architecture via a dimer interface between two trimers by constraining the angle between the respective dimer and trimer symmetry axes to 35.3 degrees. The design principle is illustrated in Fig. 1a. Beginning with two SLAC molecules in a two-fold symmetric arrangement, additional copies of SLAC bound with identical binding modes to the first pair, gradually build a coherent symmetric assembly.

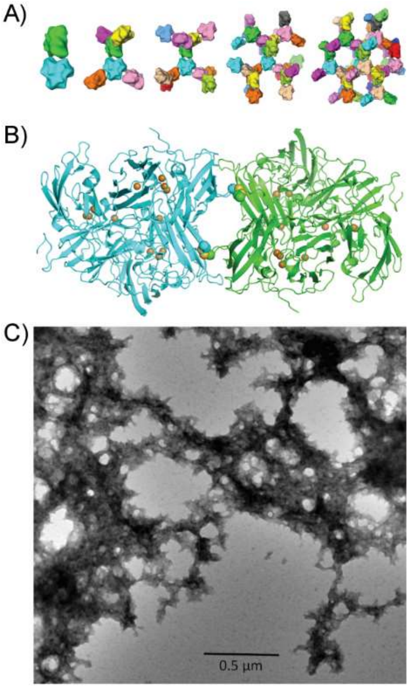

Figure 1. Design of the SLAC-DC-His assembly: A) Illustration of one-interface design principle, wherein a single new interface gives rise to self-assembly. Shown is the stepwise application of the dimer interface to terminal SLAC-DC-His trimers, adding new trimers to the assembly until a fully connected crystalline architecture is attained. B) Detail of the designed dimer interface between SLAC-DC-His trimers, showing the two disulfide linkages which form the interface as green, blue and yellow spheres. The active site copper atoms are also shown as gold spheres. C)TEM image of SLAC-DC-His aggregates.

Disulfide bonds were chosen to drive interface formation. This both simplifies the interface design problem and yields a very stable connection between subunits in an oxidizing environment. The symmetric angular constraint described above, along with the requirement that the trimers must be in contact with one another in order to form an interface, drastically limits the number of possible interfaces that can form the desired structure (King et al., 2012). This limited set of compatible binding modes was searched exhaustively with Rosetta for shape complementarity and cross-interface positions capable of accommodating a disulfide bond (King et al., 2014). One such disulfide-compatible geometry was found to be very similar to a crystal contact in the SLAC crystal structure (PDB id 3CG8), making it likely to be physically reasonable, and was selected as the design of choice. The chosen disulfide-mediated interface is shown in Fig. 1b. The new mutations (Gly70 and Ala189 mutated to Cys) were made to SLAC-His using site-directed mutagenesis and the resultant protein with a C-terminal polyhistidine tag was named SLAC-DC-His.

Kinetic parameters for SLAC-DC-His and SLAC-His were determined in dilute solution with the substrate 2,6-dimethoxyphenol (DMP) (Table 1). We have previously observed that the addition of an N-terminal polypeptide fusion can dramatically decrease the turnover number (kcat) compared to the wild-type while fusions to the C-terminus had a far less impact (Szilvay et al., 2011; Wheeldon and Gallaway, 2008). The double cysteine mutations in SLAC-DC-His did not significantly affect the turnover number compared to SLAC-His. However, the Michaelis constant K_M is larger for SLAC-DC-His, resulting in a decreased catalytic efficiency (k_{cat}/K_M).

Table 1. Kinetic parameters of SLAC-DC-His and SLAC-His for DMP oxidation. Measurements were performed in triplicate, and represented with their mean and standard deviation from the mean.

	K_M [mM]	k_{cat} [min^{-1}]	k_{cat}/K_M [mM^{-1}min^{-1}]
SLAC-DC-His	13 ± 2[a]	110 ± 10	8.2 ± 1.6[a]
SLAC-His	4.7 ± 0.4	120 ± 10	25 ± 2

[a] $p < 0.01$, where statistical significance of SLAC-DC-His parameters compared to the control SLAC-His were calculated by unpaired two-sample t-test

Purified SLAC-DC-His was studied for aggregate formation. Blue aggregates were seen to form in an oxidative environment when $CuSO_4$ was incubated with samples containing SLAC-DC-His. TEM images of the aggregates showed assemblies with regions of 3-fold symmetry consistent with the computational design (Fig. 1c). Protein aggregates were not seen to form when SLAC-His was exposed to the same conditions. SLAC-DC-His aggregates also formed in the presence of SWNTs after the addition of $CuSO_4$. Aggregates formed with and without SWNTs were found to be active with DMP, and SWNTs were not found to significantly affect enzyme activity for DMP. SLAC-DC-His aggregates were dissolved upon addition of the reducing agent dithiothreitol (DTT). Aggregates exhibited a large variation of sizes. The aggregates did not appear to dissolve after storing them in buffer over a period of months.

In order to explore electrochemical function of the SLAC aggregates, rotating disk electrode (RDE) measurements were used to study the rate of oxygen reduction, which eliminates diffusional limitations and allows the study of oxygen reduction reaction activity in kinetically limited conditions. Three main electrochemical parameters were used for comparison: generated current density, onset and half-wave potentials (Bard and Faulkner, 2001). The onset potential provides information for the thermodynamic aspect of the reaction, and a higher onset potential is an indication for decreased overpotential of the reaction or decreased activation energy. The generated current is descriptive for the kinetics of the oxygen reduction reaction, and higher current densities are indicative of improved reaction kinetics. The half-wave potential gives information for both the thermodynamics and kinetics of the process. It is the potential of a voltammetric curve at the point where the difference between the faradaic current and the non-faradaic current is equal to one-half of the limiting current.

To provide increased surface area and a better contact between the electrode and the enzyme aggregates, SWNTs were explored. This technique was applied to study the electrochemical activity of SLAC-DC-His aggregates when combined with SWNTs in three configurations: i) SLAC-DC-His aggregates were adsorbed on a surface modified with SWNTs; ii) pre-formed SLAC-DC-His aggregates were combined with SWNTs; iii) SWNTs were incorporated with SLAC-DC-His during aggregation. For each configuration, current production from the oxygen reduction reaction was observed, and the current was linearly dependent on the oxygen concentration (Fig. 2). Redox peaks observed with oxygen-depleted electrolyte were also observed without the enzyme catalyst and are likely due to impurities in the SWNTs. The enzymatic aggregates were stably absorbed on the rotating disk electrodes, and we did not visually observe loss of the deposited ink even at rotation rates of 1600 rpm.

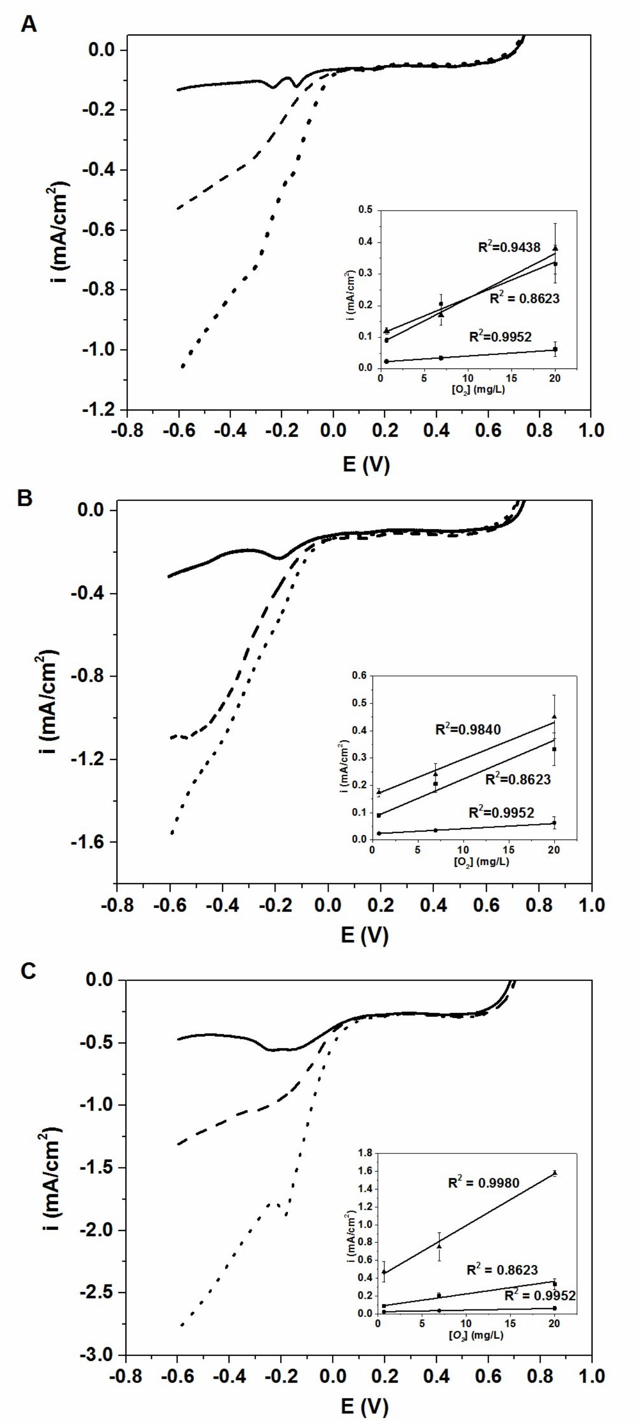

Figure 2. RDE measurements of A) SLAC-DC-His aggregates adsorbed on SWNTs B) pre-formed SLAC-DC-His aggregates mixed with SWNT inks, and C) SWNTs incorporated into SLAC-DC-His aggregates. Experiments were performed in an oxygen depleted electrolyte (solid lines), oxygen saturated electrolyte (dash dotted lines) and an electrolyte exposed to air (dashed lines) (10 mV/s, 1600 rpm). Insets show the dependence of the current density at -0.15 V vs. Ag/AgCl on the oxygen concentration in the electrolyte with SLAC-DC-His aggregates (triangles), SLAC-His (squares) and SWNTs only (diamonds). Three independent identical

electrodes for each cathode type were prepared and tested for reproducibility. The results are represented with the mean from the three measurements and the standard deviation from the mean.

Comparing the electrochemical response of the SLAC-DC-His/SWNT composites, a sequential increase in the oxygen reduction reaction current densities can be seen, demonstrating the importance of enzyme-nanomaterial interfacial interactions (Fig. 3). The increase in current density observed when SLAC-DC-His aggregates are combined with SWNTs before being deposited onto the electrode is likely due to increased contacts between the enzymes and the SWNTs. Contact between the SWNTs and enzyme active sites is further increased in the case where SWNTs were introduced into a solution of purified SLAC-DC-His before aggregation was initiated. This enabled self-assembly to entrap SWNTs within the aggregates. This approach dramatically increased current densities during oxygen reduction. The generated current at -0.15 V and 19.8 ± 4.2 mg/mL oxygen content was 3.5 times higher than the preformed SLAC-DC-His aggregates mixed with SWNTs and 4.2 times higher than the physically adsorbed aggregates.

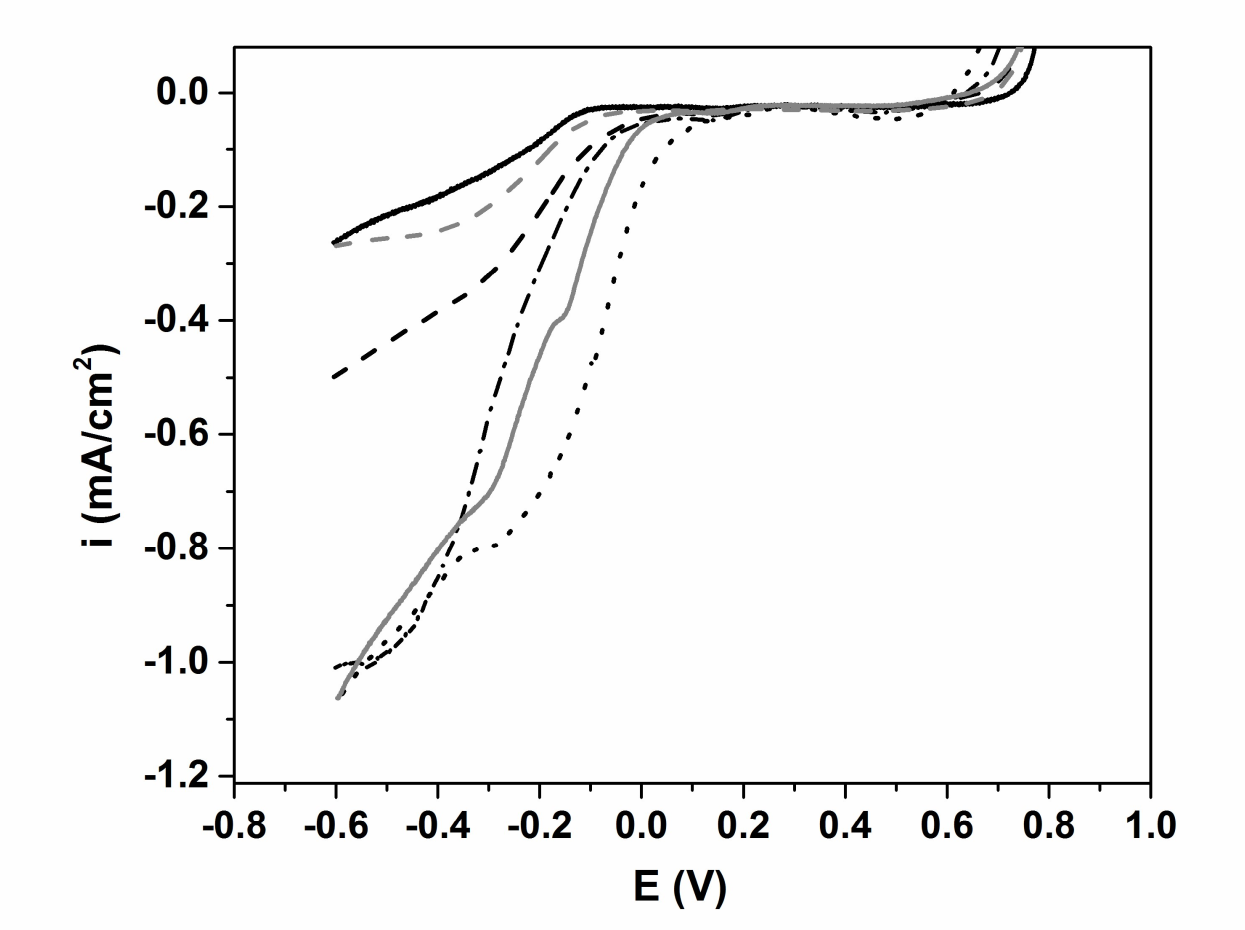

Figure 3. RDE measurements of SWNTs only (solid black line), SLAC-His mixed with SWNTs (gray line), denatured SLAC-His mixed with SWNTs (gray dashed line), SLAC-DC-His

aggregates adsorbed on SWNTs (dashed line) pre-formed SLAC-DC-His aggregates mixed with SWNT ink (dash dotted line) and SLAC-DC-His with incorporated SWNTs before aggregation (dotted line) in electrolyte exposed to ambient air (10 mV/s and 1600 rpm).

The nonspecific incorporation of the SWNTs into SLAC-DC-His assemblies not only leads to enhanced current generation but also a significant positive shift in the onset potential, from 0.075 V vs. Ag/AgCl for SLAC-His to 0.220 V vs. Ag/AgCl for SLAC-DC-His, and half-wave potential of approximately 100 mV, from - 0.168 V vs. Ag/AgCl for SLAC-His to -0.070 V vs. Ag/AgCl for SLAC-DC-His (Fig. 3). These indicate a decrease of the reaction overpotential and improvement in kinetics are most likely due to the decreased tunneling distance and the orientation of the enzyme active site (Ramírez et al., 2008). Based on the Butler-Volmer equation, a decrease in reaction overpotential by 100 mV leads to a 90 times increase in reaction kinetics and generated current.

SLAC-His and SLAC-DC-His aggregates were incubated at elevated temperatures and assayed in solution for DMP oxidation activity at room temperature in order to compare the resistance to irreversible thermal denaturation (Table 2). After incubation at 70°C, the residual activities of both samples decreased, with SLAC-His exhibiting a larger decrease in activity. This difference was more pronounced for the samples incubated at 98°C. The activity of the SLAC-His samples was reduced by 99% while the SLAC-DC-His samples retained 43% of the original activity.

Table 2. Residual specific activities of SLAC-His and SLAC-DC-His for DMP oxidation measured at 25°C after 30 minute incubation at elevated temperatures. Measurements were performed in triplicate, normalized by the activity at 25°C and represented with their mean and standard deviation from the mean.

	25°C	70°C	98°C
SLAC-DC-His	1.0 ± 0.1	0.50 ± 0.08[a]	0.43 ± 0.08[a]
SLAC-His	1.0 ± 0.1	0.31 ± 0.05[a]	0.011 ± 0.004[a]

[a] $p < 0.01$, where statistical significance compared to measurements at 25°C calculated by unpaired two-sample t-test

Electrochemical activities were also measured at elevated temperatures for RDE electrodes (Table 3). At 50°C, there is no statistically significant difference in the retained activities of the SLAC-His/SWNTs and SLAC-DC-His/SWNTs composites. At 70°C, the SLAC-DC-His/SWNTs composite demonstrated higher electrochemical activity than the SLAC-His/SWNTs composite, retaining 47% activity. These results indicate that SLAC-DC-His aggregates are more resistant to thermal denaturation than SLAC-His. Although it is unlikely that these electrodes would be operated at these higher temperatures, the increased resistance to thermal denaturation is likely due to the prevention of irreversible unfolding or the facilitated refolding enabled by the engineered disulfide bonds, and this would likely lead to increased operational lifetimes at ambient temperatures.

Table 3. Retained electrochemical activity of SLAC-His/SWNTs and SLAC-DC-His/SWNTs composites where SWNTs were incorporated prior to aggregation. Measurements were performed in triplicate, normalized by the activity at 25°C and represented with their mean and standard deviation from the mean.

	25°C	50°C	70°C
SLAC-DC-His	1.0 ± 0.1	0.77 ± 0.10[b]	0.47 ± 0.03[a]
SLAC-His	1.0 ± 0.1	0.81 ± 0.02[b]	0.05 ± 0.04[a]

[a] $p < 0.01$, where statistical significance compared to measurements at 25°C calculated by unpaired two-sample t-test

[b] $p < 0.05$, where statistical significance compared to measurements at 25°C calculated by unpaired two-sample t-test

Gas diffusion cathodes are advantageous due to the higher oxygen concentration available for reduction at the cathode compared to in solution. Therefore, the SLAC-DC-His assembly with incorporated SWNTs was integrated into the design of an air-breathing cathode and compared to a SLAC-His air- breathing cathode via steady state polarization curves (Fig. 4). The current density at 0.0 V vs. Ag/AgCl recorded with the gas-diffusion SLAC-DC-His cathode was 1.1 mA/cm^2, which was significantly higher than the SLAC-His cathode. The SLAC-DC gas-diffusion cathode outperformed the SLAC-His cathode design throughout the potential region tested.

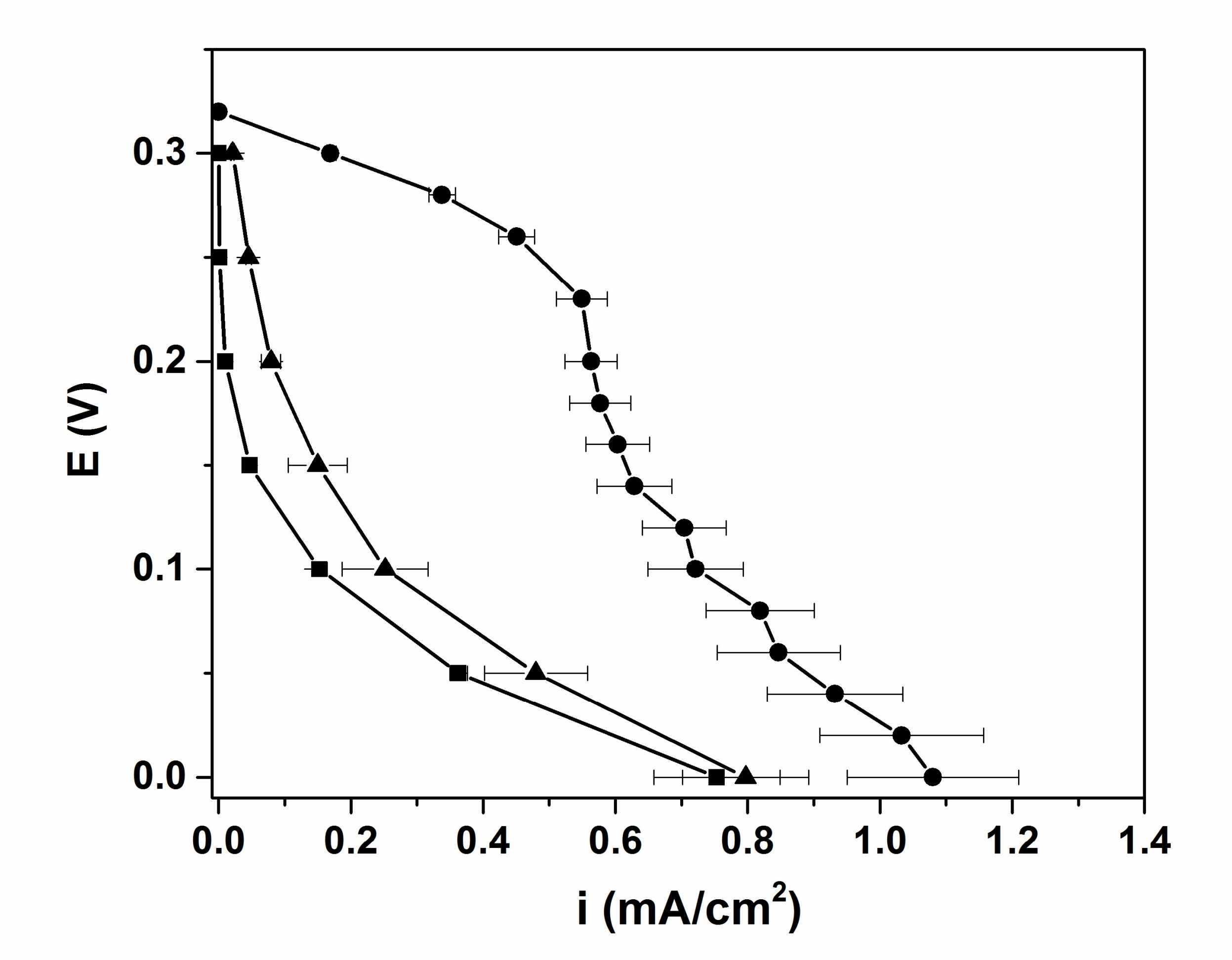

Figure 4. Potentiostatic polarization curves for SLAC-DC-His aggregates (circles), SLAC-His (triangles) and neat SWNTs (squares) when incorporated into the design of a gas-diffusion cathode with 9.2 μg of enzyme deposited on each cathode. Three independent identical electrodes for each cathode type were prepared and tested for reproducibility. The results in the figure are represented with the mean and the standard deviation from the mean.

This result can be compared to previous reports in the literature. A laccase-based gas-diffusion cathode with an identical design to the one used in this study generated 0.70 mA/cm^2 using air as the source of oxygen (Gupta et al., 2011a). The interactions between the enzyme and the carbon black material relied on physical adsorption of the enzyme and direct electron transfer from the electrode to SLAC. To improve the direct electron transfer rate in the current design, we incorporated SWNTs along with the protein engineering approach and thus achieved 1.5 times higher current densities in comparison to the same miniature GDE exploring laccase as catalyst. Bilirubin oxidase (BOx) gas-diffusion cathode where BOx was physically adsorbed on the electrode surface demonstrated 0.35-0.50 mA/cm^2 (Gupta et al., 2011b). When an orienting agent (syringaldazine) and a tethering agent (1-pyrenebutanoic acid, succinimidyl ester) were used for more efficient enzyme orientation, improved electron transfer and stability, the current densities of a BOx-GDE reached 0.70 mA/cm^2 (Ulyanova et al., 2014). Using more complex tethering agent 4,4′-[(8,16-dihydro-8,16-dioxodibenzo[a,j]perylene-2,10-diyl)dioxy] dibutyric acid di(N-succinimidyl ester (DDPSE) and no orienting agent in the construction of laccase cathode demonstrated ~0.44 mA/cm^2 (Lau et al., 2012).

Conclusion

In conclusion, we have used computational protein design to create a SLAC double mutant that can self-assemble into active enzymatic crystalline-like assemblies. The enzyme aggregates were easily immobilized by physical adsorption, enabling high enzyme loadings. Additionally, the nonspecific incorporation of SWNTs into the aggregates led to improved kinetics from increased enzyme-SWNT contacts. The self-assembly increased resistance to thermal denaturation. A current density of 1.1 mA/cm^2 at 0 V vs. Ag/AgCl was achieved in an air-breathing cathode system. This designed self-assembly approach could be employed to create new biomaterials from other enzymes for use in biofuel cells as well as many other biocatalysis applications.

References

Addo PK, Arechederra RL, Minteer SD. 2010. Evaluating Enzyme Cascades for Methanol/Air Biofuel Cells Based on NAD+-Dependent Enzymes. Ed. Evgeny Katz, Plamen Atanassov. *Electroanalysis* **22**:807–812.

Babanova S, Artyushkova K, Ulyanova Y, Singhal S, Atanassov P. 2014. Design of experiments and principal component analysis as approaches for enhancing performance of gas-diffusional air-breathing bilirubin oxidase cathode. *Journal of Power Sources* **245**:389–397.

Bard AJ, Faulkner LR. 2001. Electrochemical Methods: Fundamentals and Applications 2nd ed. New York: John Wiley and Sons.

Barton SC, Gallaway J, Atanassov P. 2004. Enzymatic biofuel cells for implantable and microscale devices. *Chem. Rev.* **104**: 4867-4886.

Cooney MJ, Svoboda V, Lau C, Martin G. 2008. Enzyme catalysed biofuel cells. *Energy & Environmental Science* **1**:320–337.

Davila D, Esquivel JP, Vigues N, Sanchez O, Garrido L, Tomas N, Sabate N, del Campo FJ, Munoz FJ, Mas J. 2008. Development and optimization of microbial fuel cells. *Journal of New Materials for Electrochemical Systems* **11**:99–103.

Gallaway J, Wheeldon I, Rincon R, Atanassov P, Banta S, Barton SC. 2008. Oxygen-reducing enzyme cathodes produced from SLAC, a small laccase from Streptomyces coelicolor. *Biosensors and Bioelectronics* **23**:1229–1235.

Glykys DJ, Szilvay GR, Tortosa P, Suárez Diez M, Jaramillo A, Banta S. 2011. Pushing the limits of automatic computational protein design: design, expression, and characterization of a large synthetic protein based on a fungal laccase scaffold. *Syst Synth Biol* **5**:45–58.

Gupta G, Lau C, Branch B, Rajendran V, Ivnitski D, Atanassov P. 2011a. Direct bio-electrocatalysis by multi-copper oxidases: Gas-diffusion laccase-catalyzed cathodes for biofuel cells. *Electrochimica Acta* **56**:10767–10771.

Gupta G, Lau C, Rajendran V, Colon F, Branch B, Ivnitski D, Atanassov P. 2011b. Direct electron transfer catalyzed by bilirubin oxidase for air breathing gas-diffusion electrodes. *Electrochemistry Communications* **13**:247–249.

Holland JT, Lau C, Brozik S, Atanassov P, Banta S. 2011. Engineering of Glucose Oxidase for Direct Electron Transfer via Site-Specific Gold Nanoparticle Conjugation. *J. Am. Chem. Soc.* **133**:19262–19265.

Jiang L, Althoff EA, Clemente FR, Doyle L, Rothlisberger D, Zanghellini A, Gallaher JL, Betker JL, Tanaka F, Barbas CF, Hilvert D, Houk KN, Stoddard BL, Baker D. 2008. De Novo Computational Design of Retro-Aldol Enzymes. *Science* **319**:1387–1391.

Kim J, Jia H, Wang P. 2006. Challenges in biocatalysis for enzyme-based biofuel cells. *Biotechnology Advances* **24**:296–308.

King NP, Sheffler W, Sawaya MR, Vollmar BS, Sumida JP, Andre I, Gonen T, Yeates TO, Baker D. 2012. Computational Design of Self-Assembling Protein Nanomaterials with Atomic Level Accuracy. *Science* **336**:1171–1174.

King NP, Bale JB, Sheffler W, McNamara DE, Gonen S, Gonen T, Yeates TO, Baker D. 2014. Accurate design of co-assembling multi-component protein nanomaterials. *Nature* **510**:103–108.

Korkegian A, Black ME, Baker D, Stoddard BL. 2005. Computational Thermostabilization of an Enzyme. *Science* **308**:857–860.

Lau C, Adkins ER, Ramasamy RP, Luckarift HR, Johnson GR, Atanassov P. 2012. Design of Carbon Nanotube-Based Gas-Diffusion Cathode for O2 Reduction by Multicopper Oxidases. *Advanced Energy Materials* **2**:162–168.

Lim J, Cirigliano N, Wang J, Dunn B. 2007. Direct electron transfer in nanostructured sol-gel electrodes containing bilirubin oxidase. *Phys. Chem. Chem. Phys.* **9**:1809–1814.

Logan BE, Hamelers B, Rozendal R, Schröder U, Keller J, Freguia S, Aelterman P, Verstraete W, Rabaey K. 2006. Microbial fuel cells: methodology and technology. *Environ. Sci. Technol.* **40**:5181–5192.

Luckarift HR, Atanassov PB, Johnson GR. 2014. Enzymatic fuel cells: From fundamentals to applications. New York: John Wiley and Sons.

Machczynski MC, Vijgenboom E, Samyn B, Canters GW. 2004. Characterization of SLAC: A small laccase from Streptomyces coelicolorwith unprecedented activity. *Protein Sci.* **13**:2388–2397.

Minteer SD, Liaw BY, Cooney MJ. 2007. Enzyme-based biofuel cells. *Current Opinion in Biotechnology* **18**:228–234.

Padilla JE, Colovos C, Yeates TO. 2001. Nanohedra: Using symmetry to design self assembling protein cages, layers, crystals, and filaments. *Proceedings of the National Academy of Sciences* **98**:2217–2221.

Ramírez P, Mano N, Andreu R, Ruzgas T, Heller A, Gorton L, Shleev S. 2008. Direct electron transfer from graphite and functionalized gold electrodes to T1 and T2/T3 copper centers of bilirubin oxidase. *Biochimica et Biophysica Acta (BBA) - Bioenergetics* **1777**:1364–1369.

Szilvay GR, Brocato S, Ivnitski D, Li C, Iglesia PDL, Lau C, Chi E, Werner-Washburne M, Banta S, Atanassov P. 2011. Engineering of a redox protein for DNA-directed assembly. *Chem. Commun.* **47**:7464–7466.

Tsujimura S, Kamitaka Y, Kano K. 2007. Diffusion-Controlled Oxygen Reduction on Multi-Copper Oxidase-Adsorbed Carbon Aerogel Electrodes without Mediator. *Fuel Cells* **7**:463–469.

Ulyanova Y, Babanova S, Pinchon E, Matanovic I, Singhal S, Atanassov P. 2014. Effect of enzymatic orientation through the use of syringaldazine molecules on multiple multi-copper oxidase enzymes. *Phys. Chem. Chem. Phys.* **16**:13367–13375.

Usui K, Maki T, Ito F, Suenaga A, Kidoaki S, Itoh M, Taiji M, Matsuda T, Hayashizaki Y, Suzuki H. 2009. Nanoscale elongating control of the self-assembled protein filament with the cysteine-introduced building blocks. *Protein Sci.* **18**:960–969.

Wheeldon IR, Gallaway JW, Barton SC, Banta S. 2008. Bioelectrocatalytic hydrogels from electron-conducting metallopolypeptides coassembled with bifunctional enzymatic building blocks. *Proc. Natl. Sci.* **105**: 15275-15280.

Wong TS, Schwaneberg U. 2003. Protein engineering in bioelectrocatalysis. *Current Opinion in Biotechnology* **14**:590–596.

Functional Interfaces for Biomimetic Energy Harvesting: CNTs-DNA Matrix for Enzyme Assembly

1. Introduction:

Biomimetics or bio-inspired design is a term that can be seen very often currently in almost any field of scientific research. Facing the rapid technological development and the increasing engineering demands, scientists have looked for new technologies inspired by biological solutions at both the macro- and especially at the nanoscale [1-4].

A key component in the design of enzyme-based technologies, such as enzymatic fuel cells, photo-bio energy harvesting devices, nano-biosensors, bio-actuators and other bio-nano-interfacial architectures is the effectiveness, specificity and stability of the enzyme immobilization [5, 6]. Over the years researchers have developed methods for integration of enzymes and nanomaterials. Some of these methods include direct protein adsorption [7, 8], enzyme tethering [9-11], entrapment in polymers [12], cross-linking [13], chemical bonding [14], protein engineering to form hydrogels [15-17] or fusion of proteins to create novel bioactive materials [18]. Proteins have high affinity for direct absorption onto carbon materials, such as carbon nanotubes (CNTs), however, the hydrophobic nature of the CNTs surface has resulted in lowered catalytic activity and shortened lifetimes likely due to altered tertiary structure and protein denaturing. The use of surfactants, ssDNA and polymers are approaches that have been developed to overcome this problem. These methods are non-covalent and thereby do not directly interfere with the intrinsic properties and structure of either proteins or CNTs [19]. Polymer entrapment of enzymes is one of the most common methods for constraining enzymes on support materials [6, 20-25]. Unfortunately, enzyme distribution throughout the polymer matrix can be heterogeneous [6]. On the other hand, protein engineering strategies has enabled proteins to self-assemble while either retaining or enhancing their catalytic performance [15].

An example of an advanced bio-nano-interfacial architecture has been demonstrated by Rawson et al., who vertically aligned single-walled carbon nanotubes (VASWCNTs) on an indium tin oxide (ITO) surface and explored them for intracellular electrochemical sensing in eukaryotic cells [26]. To achieve uptake of the CNTs into the cells, the VASWCNTs were wrapped with ssDNA. The resulting DNA-VASWCTNs assemblies were taken up naturally by a mouse macrophage cells and used to electrochemically investigate the intracellular environment and activity.

This architecture was further developed in this study and combined with a protein engineering approach for controlled attachment of enzymes. The specificity of zinc finger-DNA interactions was explored for controlled enzyme immobilization. As proof of concept, a zinc finger (ZNF268) was genetically fused to the small laccase (SLAC) from *Streptomyces coelicolor* and attached to a three-dimensional carbon nanotube-DNA assembly. In our previous studies we demonstrated that a multifunctional SLAC-3ZNF fusion protein could be engineered, expressed and successfully immobilized on dsDNA [27]. Here this finding was expanded towards the incorporation of the SLAC-3ZNF protein into a more sophisticated design of the supporting assembly. For the creation of the supporting scaffold, carbon nanotubes aligned in a brush-type formation were wrapped with DNA engineered to be recognized by the zinc finger, acting as a docking place for its attachment.

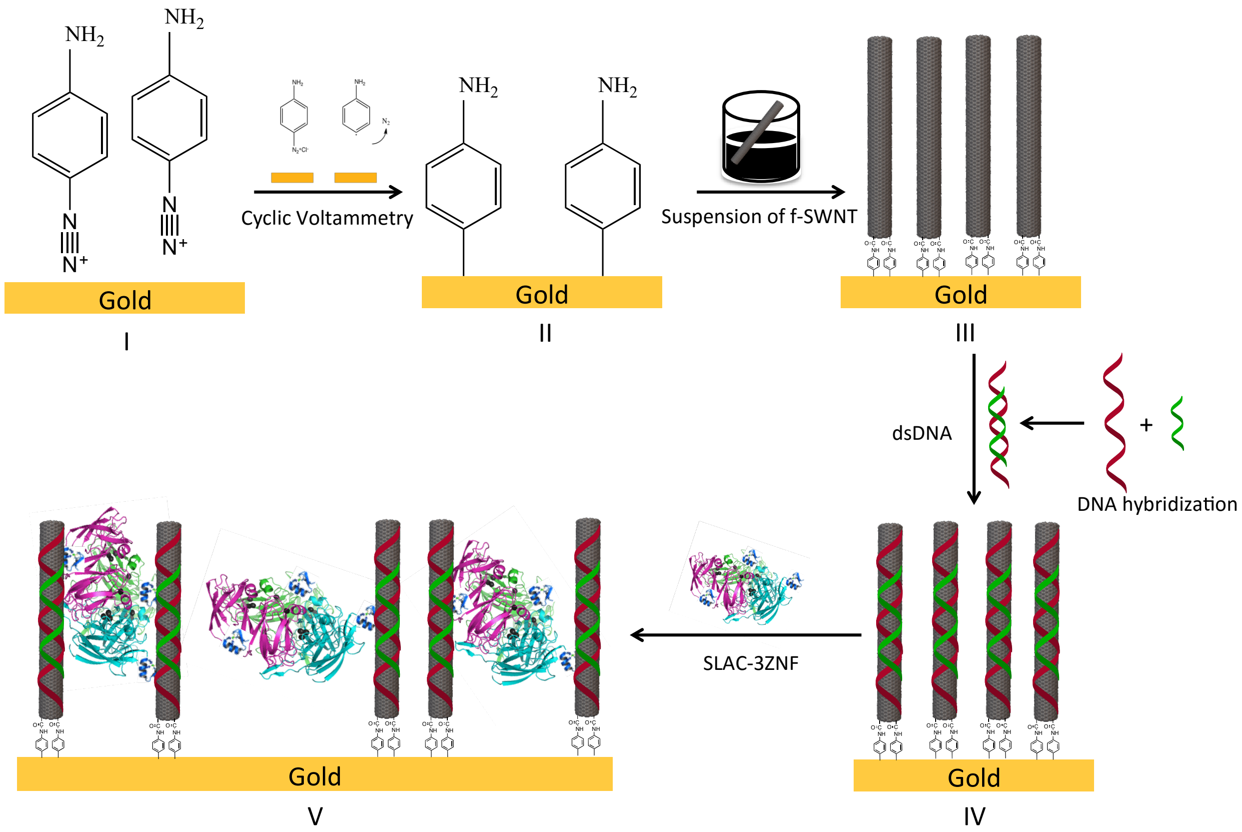

Scheme 1: Schematic representation of the approach and architecture developed in this study where I) modification of the gold surface, II) arylamine modified gold surface, III) attached SWNTs to the support, IV) dsDNA wrapped around the aligned SWNTs, V) SLAC-3ZNF attached to the DNA scaffold on the SWNTs "forest"

2. Materials and Methods:

2.1 Reagents and Stock Solutions

Dibasic potassium phosphate (K_2HPO_4, Lot # 2014091787), monobasic potassium phosphate (KH_2PO_4, Lot #2012022368), dimethyl sulfoxide (DMSO, Lot # SHBC2756V), 1N hydrochloric acid (HCl, Lot # 49279) and HPLC Omnisolv water (Lot #57184) were purchased from EMD Millipore (Billerica, MA). Single walled carbon nanotubes 99 were purchased from cheaptubes.com. Carboxylic acid functionalized single walled carbon nanotubes (f-SWNT, Lot # 03619LD), 2,6-dimethoxyphenol (DMP, Prod. No. D135550-25G), p-phenylenediamine (PPD, Low # MKBJ5024V), N,N-dicyclohexylcarbodiimide (DCC, Lot # SHBC2756V) and sodium nitrite 97+% ($NaNO_2$, Lot # 08316DJ) were purchased from Sigma Aldrich. Acetone (Lot # 050713E) was provided by BHD chemicals. Isopropyl β-D-1-thiogalactopyranoside (IPTG) was from Gold Biotechnology (St. Louis, MO). HALT protease inhibitor, precast NuPAGE SDS-PAGE gels, NuPAGE SDS MES running buffer and Novex Sharp Pre-stained Protein Standard were from Thermo Fisher Scientific (Waltham, MA). HisTrap HP columns and the ÄKTA FPLC system were purchased from GE Healthcare (Piscataway, NJ). All other chemicals were purchased from Sigma-Aldrich (St. Louis, MO) at the highest purity unless otherwise specified.

2.2 Gold modification

Gold deposition on glass support was carried out through spray evaporation. Glass covered slides were cleaned using ozone prior to deposition. A 3 nm layer of chromium and 100 nm layer of gold were deposited subsequently. The gold surface was further modified through electrochemical grafting. Three-electrode set-up with a gold covered slide used as working electrode; Ag/AgCl as reference and Pt-wire as counter electrodes, respectively was used for the electrochemical grafting. 10 ml solution of 7 mM p-phenyleneamine diazonium salt was used as electrolyte and modifying solution. The arylamine diazonium salt was synthesized when 7 mM p-phenylenediamine (PPD) interacted with 1 mM $NaNO_2$ in 0.5 M HCl for 5 min under ice [28]. Cyclic voltammetry (CV) was utilized as electrochemical technique for the grafting procedure. CVs at 100 mV/s in three potential windows starting from 0.4 V to -0.6, -0.4 and -0.2V vs. Ag/AgCl, respectively was carried out to form an arylamine layer on the gold surface [28, 29].

2.3 Nanotube attachment

The next step was covalent attachment of carbon nanotubes onto the modified gold slides. Carboxyl-functionalized single walled carbon nanotubes (f-SWNT, 3 to 5 μm) were explored due to the presence of carboxyl functional groups at the mouth of the nanotubes necessary for the chemical bonding with the amine groups of the arylamine layer deposited onto the support surface. 0.4 mg/mL f-SWNTs were suspended in dimethyl sulfoxide (DMSO), sonicated for 15 minutes and then combined with a solution of 0.4 mg/mL N,N'-dicyclohexylcarbodiimide (DCC) in DMSO. The modified gold samples were submerged in the solution and sonicated for 15 minutes. The submerged samples were then transferred into an oven and heated in a closed cell for 24 hours at 55°C. Samples were then washed with a series of polar solvents starting with 2 minute sonication in acetone followed by 10 seconds sonication in isopropyl alcohol and rinsed with HPLC grade water.

2.4 DNA scaffold

The ssDNA sequence 5’-TTTTTTTTTTTTTTTTTTTTCGCCCACGCTTTTTTTTTTTTTTTTTTT-3’ and ssDNA of complimentary ZNF specific binding base sequence 5’-GCGTGGGCG-3’ were ordered as custom oligomers from Sigma Aldrich. The complementary DNA (5’-GCGTGGGCG-3’) was marked with Thiol-SS-C3, a disulfide-containing oligo modifier, at the 5’ terminus and with Thiol-SS-C6 at the 3’ terminus. DNA hybridization took place in solution. dsDNA was allowed to hybridize through 15-minute sonication prior to submerging Au-Aryl-SWNT samples or f-SWNTs (1:1 molar ratio), depending on the experiment. Samples underwent sonication for 15 minutes and were left in solution for 24 hours before being removed, rinsed with HPLC water and dried with N_2.

2.5 SLAC-3ZNF complex expression and purification

Expression and purification of SLAC-3ZNF with the plasmid pSLAC-3ZF was performed as described in Szilvay et al. 2011 (Supplementary Methods) [27] with minor modifications. Cells were grown in 2xYT media at 37°C until the OD_{600} reached approximately 1.5. Protein expression was induced with 0.4 mM IPTG, and protein expression continued for 20 hours at 25°C before cells were collected by centrifugation and stored at -20°C. Pellets corresponding to 1 L of culture were thawed and suspended in 50 mL of binding buffer (20 mM Na Pi pH 7.3, 50 mM NaCl, 40 mM imidazole) supplemented with HALT EDTA-free protease inhibitor. Cells were sonicated on ice for 6 minutes with a microtip probe, and lysates were clarified by centrifugation. Lysates were then purified using a HisTrap HP column equilibrated with binding buffer. A gradient of elution buffer (20 mM NaPi pH 7.3, 500 mM NaCl, 500 mM imidazole) was applied, and fractions were collected and analyzed with SDS-PAGE. Fractions containing SLAC-3ZF-His shown at 50 kDa were pooled together. The protein was then dialyzed against binding buffer containing 1 mM $CuSO_4$ and 1 mM $ZnSO_4$ at 4°C overnight. The sample was then dialyzed against ammonium bicarbonate buffer and concentrated by ultrafiltration. They were then frozen overnight in micro-centrifuge tubes at -80°C, followed by a minimum of 24 hours of lyophilization.

2.6 Enzyme immobilization

A solution of 1 mg/ml SLAC-3ZNF in HPLC water was prepared. SWNT-dsDNA complexes aligned on the gold support were submerged in the enzyme solution and left for 24 hours at 4°C for enzyme immobilization. The sample was removed from the SLAC-3ZNF solution, washed three times and dried under N_2.

2.7 Atomic Force Microscopy

Surface imaging was done using an Asylum MFP-3D-BIOTM Atomic Force Microscope and NanoWorld Innovative Technologies SuperSharpSilicon^{TM}-Silicon SPM-Sensor non-contact mode (SSS-NCH-10, #76807F4L969). 10x10μm and 5x5μm images were taken of gold deposited on glass substrate, arylamine modified gold layers for the arylamine modifications and the aligned SWNT-arylamine-gold sample. 5x5μm scans were taken at a scan rate of 2.5 μm/s and 10x10μm scans were taken at a scan rate of 5 μm/s.

2.8 X-ray photoelectron spectroscopy:

XPS spectra were acquired using a Kratos AXIS Ultra DLD photoelectron spectrometer with a monochromatic Al Kα source operating at 150W. Charge compensation was accomplished using low energy electrons. Standard operating conditions for good charge compensation were –3.1 V bias voltage, -1.0 V filament voltage and filament current of 2.1 A. The following take-off angles (TOA) are selected for angle resolved studies: 90^{o}, 30^{o} and 15^{o}. All spectra processing was done in CasaXPS. A linear background was used for all high-resolution spectra. Atomic % were calculated from areas under the peak in electron count per second using sensitivity factors provided by the manufacturer. All the spectra were charge referenced to the aliphatic carbon at 284.8 eV or Au 4f at 84 eV for samples where Au was used as substrate. A 70% Gaussian / 30% Lorentzian (GL (30)) line shape was used for the curve-fits. Full width at half maximums (FWHMs) used for curve fits of C 1s spectra were constrained to 1.0 +/- 0.2 eV for all spectra acquired by monochromatic Al Kα source.

The thickness of each individual layer was calculated by using substrate/overlayer model in Arctick. Areas under the peaks in counts of electrons were used for Arctick calculations.

2.9 Activity assay

Two samples containing SLAC-3ZNF were prepared in 500 μl of 0.01 M phosphate buffer (pH 7.5):

1) 1 mg/ml SLAC-3ZNF adsorbed on 1 mg/ml f-SWNT in suspension. Solution containing f-SWNT was prepared first by sonication of a 250 µl suspension of 2 mg/ml f-SWNT and then diluting to final volume of 500 µl with a suspension of 2 mg/ml SLAC-3ZNF. This gave a final weight concentration of 1 mg/ml for f-SWNT and SLAC-3ZNF. The sample was left to incubate at 4°C for 24 hours. After incubation, it was centrifuged for 30 min to remove supernatant and then washed twice with 0.01 M phosphate buffer to remove any unattached enzyme. Sample was suspended to 500 µl with phosphate buffer for final testing.
2) 1 mg/ml SLAC-3ZNF attached to 2 mg/ml dsDNA, wrapped onto 1mg/ml SWNTs in suspension. SLAC-3ZNF sample with dsDNA was prepared by 5-minute sonication of a 250 µl suspension of 2mg/ml f-SWNT with 4 mg/ml dsDNA followed by addition of 250 µl 2mg/ml SLAC-3ZNF. The sample was left to incubate at 4°C for 24 hours. After incubation, it was centrifuged for 30 min to remove supernatant and then washed twice with 0.01 M phosphate buffer to remove any unattached enzyme. Sample was suspended to 500 µl with phosphate buffer for final testing.

   A 1-mg/ml suspension of f-SWNT and a 2-mg/ml SWNTs-dsDNA assembly were prepared as controls for UV-Vis spectroscopic background subtraction.

The samples were prepared and an activity assay was carried out. Then the samples were stored at 4ºC for 24 hours when activity assay was carried out again. Prior to acquiring the activity assay the samples were centrifuged for 30 min to remove supernatant and then washed twice with 0.01 M phosphate buffer to discard the unattached enzyme and the enzyme that has been detached during storage. Samples were then suspended to 500 µl with phosphate buffer and 4 µl of the suspension were transferred in a 96 well plate. Aliquots of 196 µl of DMP were then added to the samples (to a final DMP concentration of 100 mM). The reaction rate of DMP oxidation from the enzyme was examined through UV-Vis spectroscopy at 468 nm for 5 minutes. The amount of enzyme active units was calculated based on the change in DMP absorbance over 5 min and extintion coefficient of DMP equal to 14,800 M^{-1} cm^{-1}. All measurements were taken using SoftMax® Pro5 software and the SpectraMax® M5 Multimode Microplate Reader from Molecular Devices, LLC at 23°C and 0.8 atm.

3. Results and Discussion:

3. 1 Development of CNTs "forest"

The utilization of diazonium salts for surface modification of metal and carbon materials has been heavily explored in the resent years. As a result their surface can be populated with different chemical groups ($-NH_2$, -COOH, -OH, etc.). The aryl diazonium salts are very unstable at temperatures above 0°C and usually are produced right before their use. The process of forming diazonium compounds is called "diazotation" and is a chemical reaction of aromatic amines with nitrous acid, generated *in situ* from sodium nitrite and hydrochloric acid at 0°C. Subsequently, the aryl group (Ar = $-C_6H_5$-R, where R could be $–NH_2$, -COOH, -OH, etc.) is covalently attached to the electrode surface by electrochemical reduction, releasing N_2. During the electrochemical grafting, the diazonium salt reacts with the surface where the diazonium group is lost (Eq. 1) and the formed aryl radical reacts with the surface (Eq. 2) [30]. The electrochemical grafting is carried out by cyclic voltammetry (CV), where the layer coverage depends on the potential range of the CV and the number of cycles.

$ArN_2^+ + 1e^- \rightarrow Ar\bullet + N_2$ Eq. 1

$Surface + Ar\bullet \rightarrow Surface\text{-}Ar$ Eq. 2

$Ar\bullet + 1e^- \rightarrow Ar^-$ Eq. 3

In this study an electrochemical modification with p-phenyleneamine diazonium salt (NH_2-C_6H_5-N_2) was carried out to create an arylamine layer on the gold surface used as a support material (Scheme 1(I and II)). The phenyleneamine diazonium salt was produced *in situ* by chemical interaction of p-phenylenediamine ($C_6H_4(NH_2)_2$, PPD) with sodium nitrite in presence of 0.5 M HCl at 0°C. Factors that affect the surface modification are the reduction potential, deposition time and concentration of the diazonium salt. It is known that expanding the potential toward more negative values and increasing the number of cycles leads to the formation of multilayers with increasing thickness [28]. Therefore to determine the optimal procedure for the arylamine monolayer deposition we prepared three samples. CVs with different potential ranges were used: 1) from 0.4 to -0.6 V vs. Ag/AgCl; 2) from 0.4 to -0.4 V vs. Ag/AgCl ; 3) from 0.4 to -0.2 V vs. Ag/AgCl. Only one cycle of CV was carried out for each sample (Figure 1a). Two reduction peaks at 0.245 V and 0.020 V vs. Ag/AgCl were observed when the potential window was expanded toward more negative potentials and only one peak at 0.245 V vs. Ag/AgCl was recorded swiping the potential between 0.4 and -0.2V vs. Ag/AgCl. The first peak at 0.245 V vs. Ag/AgCl is associated with the formation of aryl radical and the second peak at 0.020 V vs. Ag/AgCl most likely is referred to the reduction of this radical to aryl anion (Eq. 3) and subsequent development of multilayers, which inhibit further the electron transfer [31, 32]. The formation of arylamine layer can be easily detected (

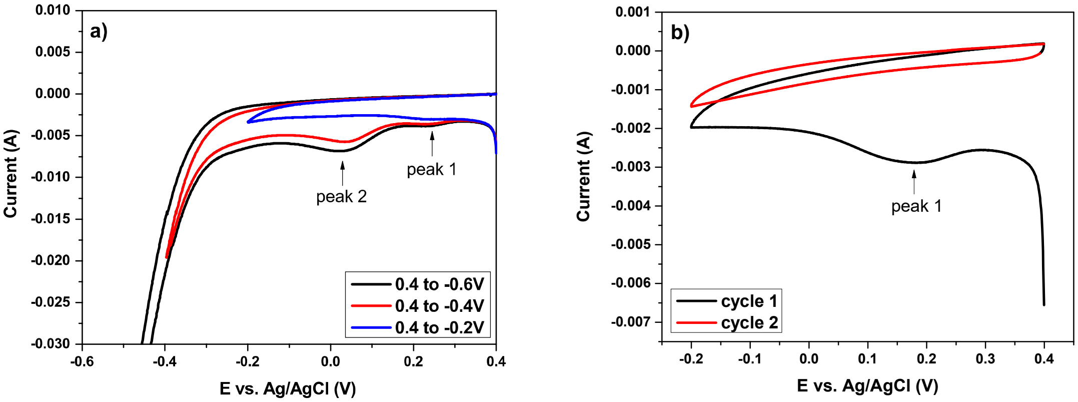

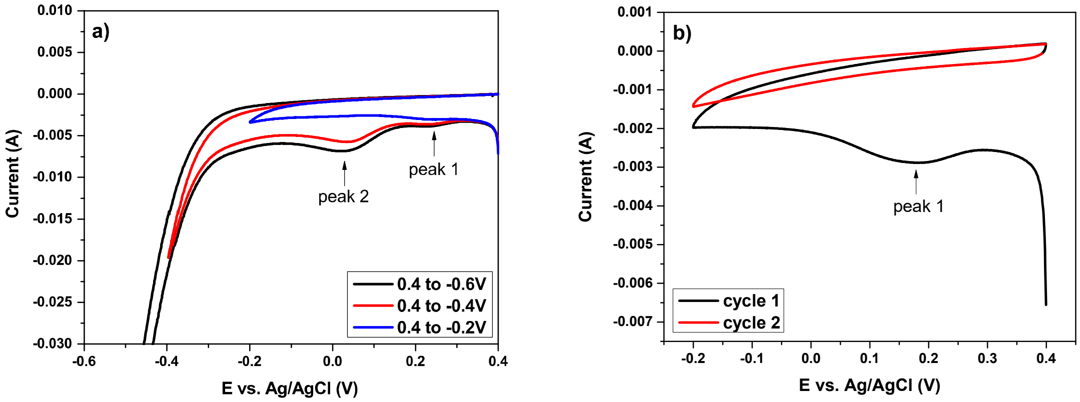

Figure 1b) through the disappearance of the reduction wave of the diazonium salt when more then one cycle is performed.

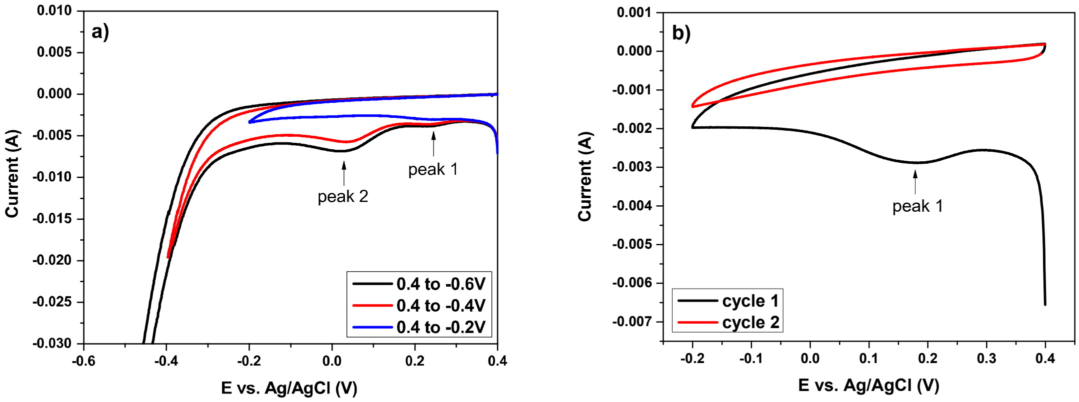

Figure 1: Electrochemical grafting of arylamine layer on gold support a) using three different potential windows for the carried out cyclic voltammetry, and b) two subsequent cycles in the potential window 0.4 to -0.2V. Scan rate 100 mV/s.

The modified gold surfaces were then examined through Atomic Force Microscopy (AFM) (Figure 2b,c and d). For comparison, a control sample of bare gold was also studied (Figure 2a). The AFM images revealed noticeable changes in surface topography after the modification step. The features characteristic for the bare gold surface (Figure 2a) could not be seen after the electrochemical grafting (Figures 2b, c and d), revealing successful coverage of the gold presumably from an arylamine layer. Differences in the topography of the arylimine layer were also observed depending on the potential window used for the modification step. The most uniform and smoothest surface coverage was achieved with the broadest potential window used most likely due to the development of multiple layers of arylamine. The most uniform and smoothest surface coverage was achieved with the shortest potential window used most likely due to the development of a single layer of Ar.

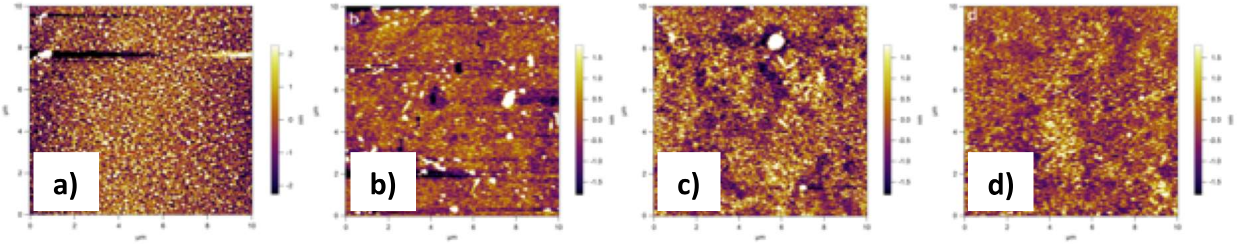

Figure 2: AFM images of gold samples modified via electrochemical grafting of p-phenyleneamine diazonium salt through cyclic voltammetry carried out at three potential windows: a) unmodified gold, b) 0.4 to -0.6 V, c) 0.4 to -0.4 V and d) 0.4 to -0.2 V vs. Ag/AgCl. Size: 10 µm x 10 µm, Rate: 5 µm/s for 5 µm scan, Frequency: 0.2 Hz

The thickness of the arylamine layer strongly influences the conductivity through the layer. A monolayer provides the necessary surface coverage without introducing significant constraints for electron transfer while the deposition of multilayers of arylamine will decrease the conductivity of the material and dramatically hinder the electron transfer rate. Therefore, further analyses were carried out to study the layer composition and thickness. XPS analysis was explored for resolving the surface content and angle resolved XPS was used to determine the thickness of the deposited layer (Figure 3). The angle resolved analysis showed that thicker layers were deposited in potential ranges 0.4 to -0.4 V and 0.4 to -0.6 V vs. Ag/AgCl, confirming the effect of the potential window on the thickness of the deposited arylamine layer. The thinnest arylamine layer (0.33 nm), close to a monolayer, was created when the CV`s potential range was 0.4 to -0.2 V vs. Ag/AgCl. Thus for the subsequent experiments, this electrochemical modification leading to monolayer deposition was applied.

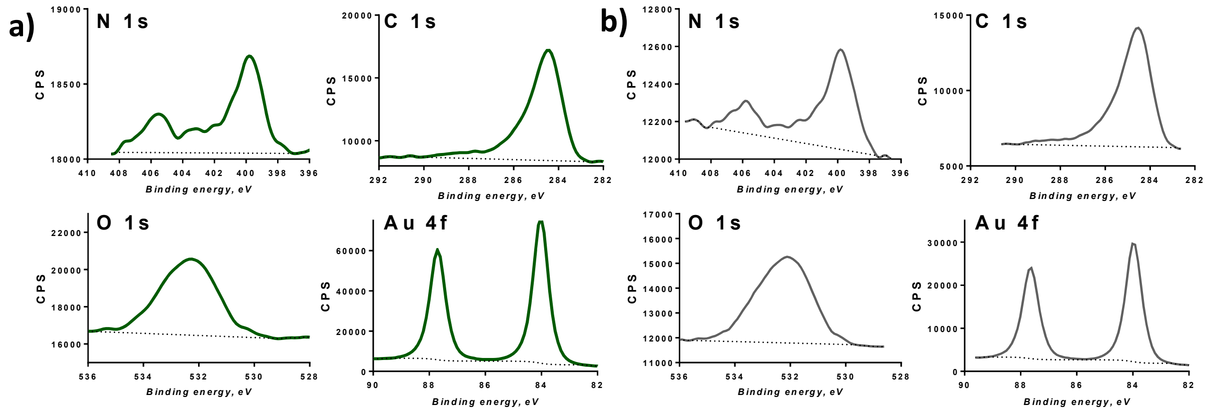

Figure 3: XPS spectra of modified gold surface using one cycle of CV with potential window 0.4 to -0.2 V vs. Ag/AgCl a) 90° TOA, b) 30° TOA. High resolution C 1s, O 1s, N 1s and Au 4f spectral lines are shown. Areas under the peaks of N 1s and Au 4f were used for calculating thickness of arylamine. Elemental composition for 90° TOA is shown in Table 1.

XPS spectra at 90° and 30° TOAs of the monolayer modified gold surface demonstrated the presence of O 1s, C 1s and N 1s along with 4f Au (Figure 3). The appearance of C and mainly N-atoms on the sample surface confirms the success of the electrochemical grafting. The oxygen content for was determined to be 13 % (atomic), the carbon content was 56 % and the N-atoms composed 4.8 % of the surface coverage (Table 1).

The next step was covalent attachment of f-SWNTs on the modified gold surface in a brush-like formation (Scheme 1 (III)). Carbodiimide chemistry was used for this purpose as it has been successfully utilized for nanotube-surface covalent bonding [26]. This approach uses an organic compound containing carbodiimide group to catalyze the formation of amide bond from carboxylic and amine groups [33]. The carbodiimide activates the carboxylic group creating a highly reactive intermediate carboxylic ester, which further reacts with the amine group and creates an amide bond. In order to explore this chemistry and create a covalent bond between CNTs and the solid support, carboxyl-functionalized SWNT were used. The -COOH groups of the SWNTs were attached to the amide groups of the grafted arylamine layer via the utilization of N,N'-dicyclohexylcarbodiimide (DCC) as a homogenous catalyst. Since the carboxyl groups of the modified SWNTs are located at the mouth of the SWNTs, the designed SWNTs-Au assembly had brush-like formation of the CNTs on the support surface.

XPS and AFM analyses were carried out after the attachment of the CNTs to confirm the nanotubes presence and to study the changes in the sample topography. XPS spectra of N 1s, C 1s, O 1s and Au 4f revealed an increase in carbon and oxygen content as a result of the presence of f-SWNTs on the gold surface (Figure 4 and Table 1). The greater increase in oxygen (~13%) than carbon (~5%) is likely due to the location of carboxyl groups at the mouths of the aligned nanotubes. The O-atoms present on the sample surface prior to the SWNTs attachment is most likely due to the atmospheric O_2. In addition, the percentages of N 1s and Au 4f reduction additionally demonstrate an expanded coverage of f-SWNTs over the sample surface.

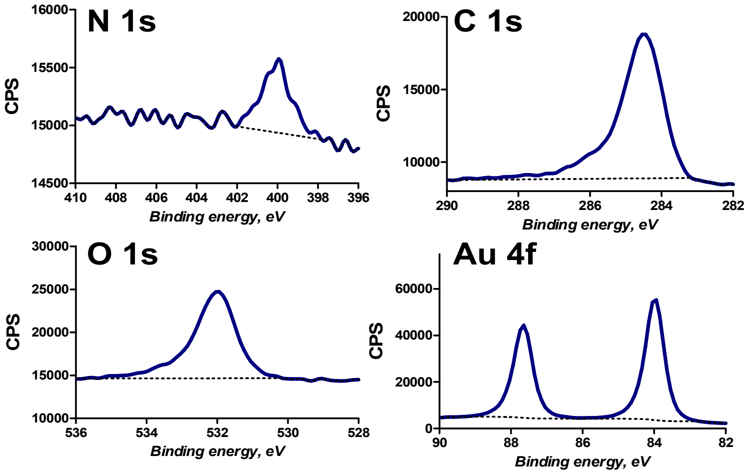

Figure 4: XPS spectra of f-SWNTs on the gold. High resolution C 1s, O 1s, N 1s and Au 4f spectral lines are shown. Elemental composition is shown in Table 1.

Table 1: XPS atomic composition of modified Au support before and after the covalent attachment of f-SWNTs. Data at 90° TOA

Sample	% O 1s	% N 1s	% C 1s	% Au 4f
Au-Arylamine	13.02	4.80	56.06	26.12
Au-SWNTs	26.28	1.67	61.38	10.67

Further surface analyses using AFM demonstrated changes in the surface topography of the sample. The Au-SWNTs surface (Figure 5) showed a much rougher structure in comparison to arylamine- modified gold surface (Figure 2d). The three-dimensional view of the AFM image (Figure 5b) revealed a brush-like construct on the surface with attached CNTs having a relatively short length (< 300 nm).

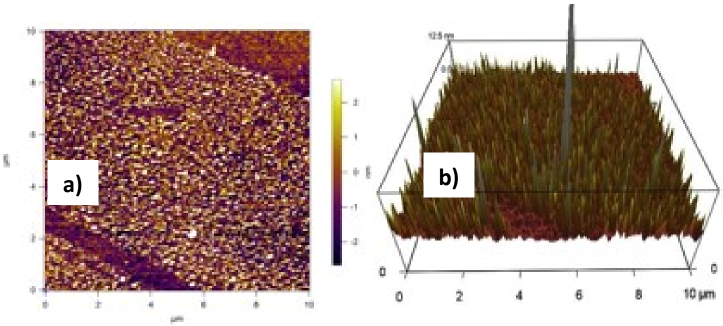

Figure 5: AFM image of Au-SWNTs sample a) 2D and b) 3D view. Size: 10 µm x 10 µm, Rate: 5 µm/s for 5 µm scan, Frequency: 0.2 Hz using super sharp silicon AFM tip.

3.2 Design of DNA scaffold and enzyme immobilization

The family of ZNFs includes a broad group of proteins having extraordinarily diverse functions including DNA recognition, RNA packing, and transcriptional activation, protein bonding and assembly, and lipid binding [34, 35]. A common feature of these proteins is the presence of one or more zinc atoms gripped in between four amino acids (cysteine or histidine), arranged as a tetrahedron around the zinc [35]. ZNFs curls around DNA and binds to the grooves with positioned amino acids inward to read the DNA bases [34, 36]. ZNF 268 plays an essential role in eukaryotic gene expression. It belongs to the Cys_2His_2-like fold group and contains a DNA binding motif, which recognizes and binds to the DNA sequence 5'-GCGTGGGCG-3' with high accuracy and specificity [37]. It has been shown that ZNF 268 interacts with its amino acid residues from the N-terminal portion of the α-helix with three base pair of the DNA scaffold mainly through the guanine residues [38]. The specificity of the ZNF-DNA recognition is provided by side chain-base interactions (Figure 6) [36, 38, 39]. ZNF 268 has been genetically fused to small laccase (SLAC) creating SLAC-3ZNF assembly and since SLAC is a trimer the final assembly has three ZNFs – SLAC-3ZNF. Using surface plasma resonance and magnetic bead capture assay it was demonstrated that the engineered SLAC-3ZNF attaches specifically to target DNA in a catalytically active manner as compared to the enzyme without the ZNF (SLAC-His) [27].

Single-stranded DNA with the following sequence 5'-TTTTTTTTTTTTTTTTTTTTCGCCCACGCTTTTTTTTTTTTTTTTTTTT-3' was used to create a ssDNA-CNT scaffold. The twenty thymine bases on either side of the ZNF specific sequence were utilized to wrap around the CNTs. The middle sequence of the ssDNA was further hybridized with 5'-GCGTGGGCG-3', which served as a docking and binding site for the ZNF module from the fused SLAC-3ZNF.

Figure 6: Overview of the 3ZNF-DNA complex (PDB code 1A1F) [39]. Jmol was used for the visualization: an open-source Java viewer for chemical structures in 3D. http://www.jmol.org/

It has been shown through Molecular Dynamics simulations that all nucleotides can bind to SWNTs in a similar fashion via π-π stacking of the DNA backbone and the SWNTs sidewalls [40]. In our study the success of the DNA hybridization when attached to the CNTs will depend on the strength of the thymine-SWNTs π-π interactions. If the interactions are not strong enough the DNA hybridization will strip the ssDNA from the SWNTs, destroying the DNA scaffold. Therefore, the DNA hybridization was performed before its attachment to the CNTs. The complementary DNA (5'-GCGTGGGCG-3') was marked with Thiol-SS-C3 at the 5' terminus and with Thiol-SS-C6 at the 3' terminus (Scheme 2). The presence of S-atoms, and more specifically the presence of S-S bond, in the complementary DNA sequence allowed the utilization of XPS analysis to determine the success of the DNA hybridization step. The ssDNA was hybridized with its complementary DNA, marked with Thiol-SS-C3 and Thiol-SS-C6, in solution and then wrapped to f-SWNTs suspended in DI water (SWNTs-dsDNA). A suspension of f-SWNTs wrapped with ssDNA (SWNTs-ssDNA) was tested as a control. The samples were washed three times with DI water prior XPS analysis. The results from the XPS study are shown in Table 2: XPS analysis of SWNTs in suspension, wrapped with single stranded (ssDNA) or double stranded (dsDNA) DNA.

$$\overset{\mathrm{O\text{-}GCGTGGGCG\text{-}O}}{\mathrm{OH\text{-}(CH_2)_6\text{-}\mathbf{S}\text{-}\mathbf{S}\text{-}(CH_2)3\text{-}O\text{-}\underset{OH}{P}{=}O \qquad O{=}\underset{OH}{P}\text{-}O\text{-}(CH_2)_3\text{-}\mathbf{S}\text{-}\mathbf{S}\text{-}(CH_2)_3\text{-}OH}}$$

Scheme 2: Composition of Thiol-SS-C3 and Thiol-SS-C6 marked complementary DNA

Table 2: XPS analysis of SWNTs in suspension, wrapped with single stranded (ssDNA) or double stranded (dsDNA) DNA.

Sample	% O 1s	% N 1s	% C 1s	% S 2p	% P 2p
SWNTs-ssDNA	25.77	11.63	58.69	0.00	3.91
SWNTs-dsDNA	38.14	8.43	50.95	0.44	2.05

The presence of phosphorus in the SWNTs-ssDNA and SWNTs-dsDNA XPS spectra reveals the attachment of DNA to the CNTs. At the same time the appearance of S 2p peaks in the SWNTs-dsDNA spectrum is indication for the successful DNA hybridization since S-atoms are present only in the sequence of the complementary DNA.

Once the DNA hybridization and subsequent immobilization on CNTs in suspension was proven, the same approach was explored for the attachment of dsDNA on the aligned CNTs (Scheme 1 (IV). Two samples were composed, one with aligned CNTs on gold support (Au-SWNTs) and another with dsDNA wrapped around the aligned SWNTs, which were covalently attached to the gold substrate (Au-SWNTs-dsDNA). The samples were washed with DI water to remove the excess of unattached DNA and subjected to XPS analysis (Table 3).

Table 3: Results from XPS analysis of aligned SWNTs on Au support with and without dsDNA.

Sample	% O 1s	% N 1s	% C 1s	% P 2p	% S 2p		
					% S-S	% S-C	% S-Ox
Au-SWNTs	13.78	1.57	82.62	0.00	31.8	10.3	57.8
Au-SWNTs-dsDNA	17.88	3.82	75.11	1.19	61.8	24.8	13.4

A detailed examination of S 2p XPS spectra shows the presence of three types of S-bonds: S-S, S-C and S-O$_x$ (Figure 7 and Table 3). The S-C and S-O$_x$ can be due to impurities in the material or to residuals from the solvent (DMSO) used during sample preparation, but the dramatic increase in the amount of S-S bonds can be ascribed to the presence of the Thiol-SS-marker in the dsDNA sequence. Accordingly, along with the appearance of phosphorus in the XPS spectra of the Au-SWNTs-dsDNA sample, we can conclude that dsDNA was successfully attached to the CNTs matrix.

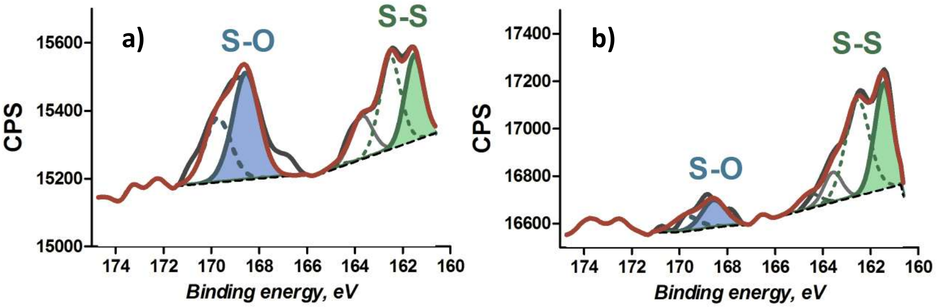

Figure 7: XPS S 2p spectra of a sample composed of aligned SWNTs on midwifed gold support a) without dsDNA and b) with dsDNA wrapped around the CNTs.

After wrapping dsDNA around the Au-SWNTs, SLAC-3ZNF was introduced into the system creating Au-SWNTs-dsDNA-SLAC-3ZNF assemblies (Scheme 1(V)). As mentioned before, the genetically modified SLAC-3ZNF has three ZNF motifs, which allow the enzyme to attach to more than one SWNT or to attach to one and the same SWNT using two of the fused ZNFs. The latter would provide more stable enzyme immobilization and/or better interactions with CNTs.

Since the capability of SLAC–3ZNF to bind to dsDNA have been already proven [27], in this study we only confirmed the presence of SLAC-3ZNF onto the developed assembly using XPS analysis. XPS spectra of the Au-SWNTs-dsDNA-SLAC-3ZNF sample showed the presence of phosphorus and copper atoms (0.43 % and 0.1 %, respectively) (Figure 8). The recorded phosphorus can be due to the presence of DNA and the observed copper can be associated only with the presence of the enzyme. SLAC belongs to the family of multi-copper oxidases named as such based on the incorporation of four and more copper atoms in their active centers. Therefore the presence of Cu 2p spectrum unambiguously demonstrates the success of the enzyme immobilization.

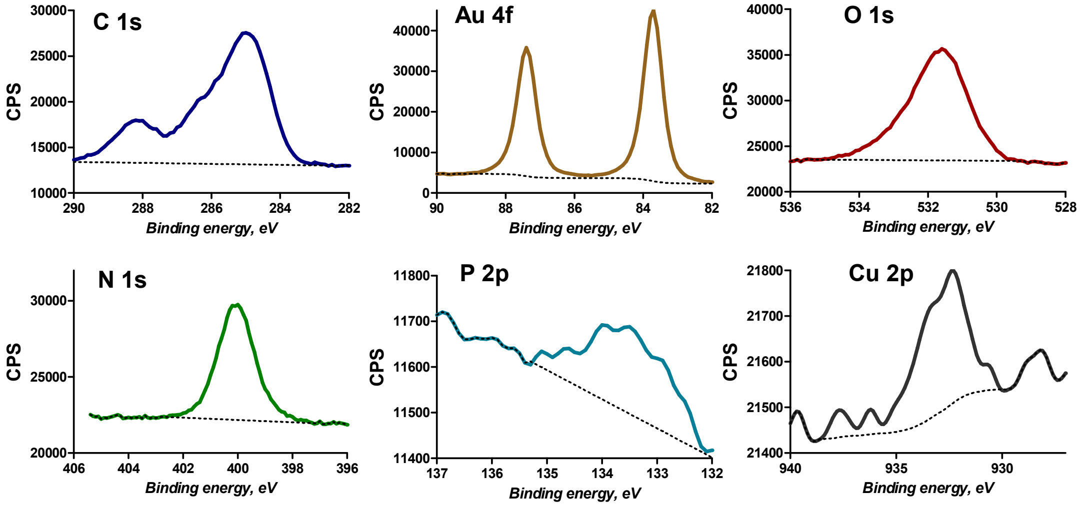

Figure 8: C 1s, Au 4f, O 1s, N 1s, P 2p and Cu 2p XPS spectra of attached SLAC-3ZNF complex onto aligned f-SWNT-arylmine modified gold surface through dsDNA scaffold.

3.3 Enzyme activity and stability

It has already been demonstrated that the SLAC-3ZNF enzyme can oxidize DMF and ABTS [27]. To further study the influence of the immobilization of SLAC-3ZNF onto the designed dsDNA-SWNTs matrix, we monitored the amount of active enzyme attached to the SNWTs-DNA scaffold. For that purpose an activity assay was carried out. f-SWNTs were wrapped with dsDNA in solution of 0.01M phosphate buffer. Low buffer concentration was used to minimize electrostatic interactions between buffer cations and the phosphodiester backbone of DNA and ensure helical wrapping of DNA around the f-SWNTs. SLAC-3ZNF was then added to the f-SWNTs-dsDNA suspension and allowed to immobilize (Fig. 9). The unimmobilized SLAC-3ZNF was removed from the sample by washing and resuspension in phosphate buffer three times. A control containing f-SWNTs with adsorbed SLAC-3ZNF (Fig. 9) was used to compare the enzyme activity after direct enzyme adsorption onto the CNTs and the amount of active enzyme present onto the sample surface when the DNA scaffold was used for enzyme immobilization. The unattached SLAC-3ZNF was also removed from the sample by washing and resuspending it in phosphate buffer three times. 24 hours after preparation, the two samples were washed three times again to remove the detached during the storage enzyme. The samples were resuspended again in phosphate buffer and an aliquotes were taken for carriyng out the activity assay. 100 mM dimethoxyphenyl (DMP) was used as a substrate for the activity assay. The amount of DMP oxidized by the enzyme was monitored by measuring the adsorbance of the DMP with UV-Vis specrometer at 468 nm for five minutes and the amount of enzyme active units (U=1µmol/min of DMP) was calculated based on extintion coefficient of DMP equal to 14,800 M^{-1} cm^{-1}.

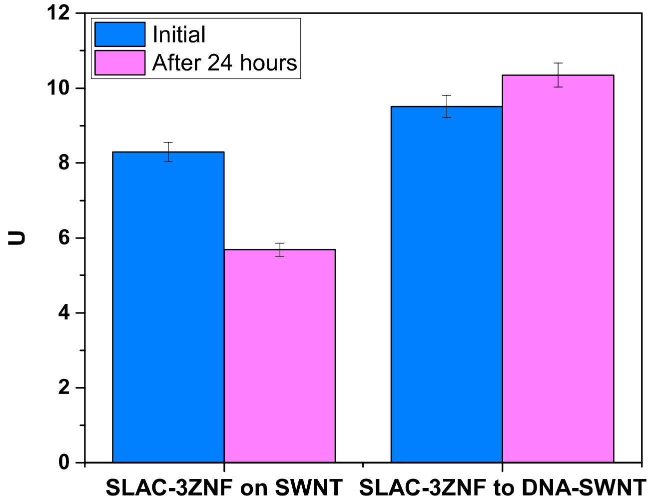

Figure 9: Amount of enzyme active units present for SLAC-3ZNF physically adsorbed onto SWNTs (SLAC-3ZNF on SWNTs) along with SLAC-3ZNF attached to a dsDNA, adsorbed on SWNTs (SLAC-3ZNF to DNA-SWNTs). The samples were prepared in 0.01M phosphate buffer tested after their preparation and 24 hours after being stored at 4°C. Prior to each measurement the samples were washed three times to remove the unattached and detached during storage protein.

The amount of active enzyme immobilized on the SWNTs either through physical adsorption or through the designed DNA scaffold was initially similar (Fig. 9). However, 24 hours after the samples were stored at 4°C, the amount of enzyme active units decreased by approximately 40% for physically adsorbed SLAC-3ZNF and remained unaltered for SLAC-3ZNF attached to dsDNA-SWNT. Thus the active enzyme immobilized through the DNA scaffold after 24 hours of storage was significantly higher ($P<0.002$) than the physicaly adsorbed SLAC-3ZNF. This indicated that enzyme immobilization through dsDNA provides more stable enzyme attachment or leads to preserved enzyme activity.

4. Conclusions

In this study, the design of a three-dimensional carbon nanotube-DNA scaffold for specific immobilization of a single enzyme was demonstrated. This design included the alignment of SWNT to form a brush-type structure on an arylamine modified gold electrode surface where the SWNTs were then wrapped with partially hybridized strands of DNA. The dsDNA was used for the docking of protein engineered SLAC-3ZNF complex. The enzyme immobilization relied on the selectivity of dsDNA-ZNF interactions. Each step of the development of this assembly was discussed in detail and supported through AFM and/or XPS analyses. Finally, an activity assay of the attached through the DNA scaffold SLAC-3ZNF was carried out showing more stable enzyme attachment and preserved enzyme activity.

The engineered SLAC-3ZNF-DNA-CNTs assembly demonstrated here is an essential step in the development of complex three-dimensional bio-nano architectures and a step forward in the design of spatially oriented single- and multi-enzyme assemblies. The incorporation of two or more variants of zinc fingers that bind to different DNA sequences will allow for the precise placement of multiple proteins within nanometer distances, which will be the goal of a future study.

References

[1] Moehlenbrock, M. J., Toby, T. K. T., Pelster, L. N., and Minteer, S. D. (2011) Metabolon Catalysts: An Efficient Model for Multi-enzyme Cascades at Electrode Surfaces, *Chem Cat Chem 3*, 561 – 570.

[2] Zhu, Z., Kin Tam, T., Sun, F., You, C., and Percival Zhang, Y. H. (2014) A high-energy-density sugar biobattery based on a synthetic enzymatic pathway, *Nature communications 5*, 3026.

[3] La Van, D. A., and Cha, J. N. (2006) Approaches for biological and biomimetic energy conversion, *Proceedings of the National Academy of Sciences of the United States of America 103*, 5251-5255.

[4] Idan, O., and Hess, H. (2013) Engineering enzymatic cascades on nanoscale scaffolds, *Current Opinion in Biotechnology 24*.

[5] Atanassov, P., El-Naggar, M. Y., Cosnier, S., and Schroder, U. (2014) Biological Fuel Cells: Cardinal Advances and Critical Challenges, *ChemElectroChem 1*, 1702 – 1704.

[6] Sarma, A. K., Vatsyayan, P., Goswami, P., and Minteer, S. D. (2009) Recent advances in material science for developing enzyme electrodes, *Biosensors and Bioelectronics 24*, 2313-2322.

[7] Cracknell, J., McNamara, T., Lowe, E., Blanford, C. . (2011) Bilirubin oxidase from Myrothecium verrucaria: X-ray determination of the complete crystal structure and a rational surface modification for enhanced electrocatalytic O-2 reduction, *Dalton Transactions 40*, 6668-6675.

[8] Flexer, V., Durand, F., Tsujimura, S., and Mano, N. (2011) Efficient Direct Electron Transfer of PQQ-glucose Dehydrogenase on Carbon Cryogel Electrodes at Neutral pH, *Anal. Chem. 83*, 5721–5727.

[9] Brocato, S., Lau, C., and Atanassov, P. (2012) Mechanistic Study of Direct Electron Transfer in Bilirubin Oxidase, *Electrochimica Acta 61*, 44-49.

[10] Strack, G., Nichols, R., Atanassov, P., Luckarift, H. R., and Johnson, G. R. (2013) Modification of carbon nanotube electrodes with 1-pyrenebutanoic acid, succinimidyl ester for enhanced bioelectrocatalysis, *Methods in molecular biology 1051*, 217-228.

[11] Ramasamy, R. P., Luckarift, H. R., Ivnitski, D. M., Atanassov, P., and Johnson, G. R. (2010) High electrocatalytic activity of tethered multicopper oxidase–carbon nanotube conjugates, *ChemComm 46*, 5977–6188.

[12] Wu, F., and Minteer, S. D. (2013) Fluorescence Characterization of Co-immobilization-Induced Multi-Enzyme Aggregation in a Polymer Matrix Using Förster Resonance Energy Transfer (FRET): Toward the Metabolon Biomimic, *Biomacromolecules 14*, 2739−2749.

[13] Hickey, D. P., Giroud, F., Schmidtke, D. W., Glatzhofer, D. T., and Minteer, S. D. (2013) Enzyme Cascade for Catalyzing Sucrose Oxidation in a Biofuel Cell, *ACS Catal. 3*, 2729−2737.

[14] Wilner, O. I., Weizmann, Y., Gill, R., Lioubashevski, O., Freeman, R., and Willner, I. (2009) Enzyme cascades activated on topologically programmed DNA scaffolds, *Nature Nanotechnology 4*, 249-254.

[15] Kim, Y. H., Campbell, E., Yu, J., Minteer, S. D., and Banta, S. (2013) Complete Oxidation of Methanol in Biobattery Devices Using a Hydrogel Created from Three Modified Dehydrogenases, *Angew. Chem. Int. Ed. 52*, 1437 –1440.

[16] Wheeldon, I. R., Calabrese Barton, S., and Banta, S. (2007) Bioactive Proteinaceous Hydrogels from Designed Bifunctional Building Blocks, *Biomacromolecules 8*, 2990-2994.

[17] Wheeldon, I. R., Gallaway, J. W., Calabrese Barton, S., and Banta, S. (2008) Bioelectrocatalytic Hydrogels from Electron-Conducting Metallopolypeptides Coassembled with Bifunctional Enzymatic Building Blocks, *Proceedings of the National Academy of Sciences of the United States of America 105*, 15275-15280.

[18] Wheeldon, I. R., Campbell, E., and Banta, S. (2009) A Chimeric Fusion Protein Engineered with Disparate Functionalities—Enzymatic Activity and Self–assembly, *J. Mol. Biol. 329*, 129–142.

[19] Feng, W., and Ji, P. (2011) Enzymes immobilized on carbon nanotubes, *Biotechnology advances 29*, 889-895.

[20] Wu, X. E., Guo, Y. Z., Chen, M. Y., and Chen, X. D. (2013) Fabrication of flexible and disposable enzymatic biofuel cells, *Electrochimica Acta 98*, 20-24.

[21] Tamaki, T., Hiraide, A., Asmat, F. B., Ohashi, H., Ito, T., and Yamaguchi, T. (2010) Evaluation of Immobilized Enzyme in a High-Surface-Area Biofuel Cell Electrode Made of Redox-Polymer-Grafted Carbon Black, *Ind. Eng. Chem. Res. 49*, 6394–6398.

[22] Moore, C. M., Akers, N. L., Hill, A. D., Johnson, Z. C., and Minteer, S. D. (2004) Improving the Environment for Immobilized Dehydrogenase Enzymes by Modifying Nafion with Tetraalkylammonium Bromides, *Biomacromolecules 5*, 1241-1247.

[23] Noboru Oyama, T. O., Keiichi Sato, Hisao Yamamoto. (1963) Incorporation of Redox Polymers to Polyelectrolyte-Coated Electrode Surfaces, *ANALYTICAL CHEMISTRY 55*, 1429-1431.

[24] D. Ivnitski, B. B., P. Atanassov and C. Apblett. (2006) Glucose Oxidase Anode for Biofuel Cell Based on Direct Electron Transfer, *Electrochemistry Communications 8*, 1204-1210.

[25] D. Ivnitski, K. A., R.A. Rincón, P. Atanassov, H.R. Luckarift, G.R. Johnson. (2008) Entrapment of Enzymes and Carbon Nanotubes in Biologically Synthesized Silica: Glucose Oxidase-Catalyzed Direct Electron Transfer, *Small 4*, 357-364.

[26] Rawson, F. J., Yeung, C. L., Jackson, S. K., and Mendes, P. M. (2013) Tailoring 3D single-walled carbon nanotubes anchored to indium tin oxide for natural cellular uptake and intracellular sensing, *Nano letters 13*, 1-8.

[27] Szilvay, G. R., Brocato, S., Ivnitski, D., Li, C., De La Iglesia, P., Lau, C., Chi, E., Werner-Washburne, M., Banta, S., and Atanassov, P. (2011) Engineering of a redox protein for DNA-directed assembly, *Chem Commun (Camb) 47*, 7464-7466.

[28] Downard, A. J. (2000) Potential-dependence of self-limited films formed by reduction of aryldiazonium salts at glassy carbon electrodes, *Langmuir 16*, 9680-9682.

[29] Pinson, J. (2012) *Aryl Diazonium Salts: New Coupling Agents in Polymer and Surface Science.*, Wiley-VCH Verlag GmbH & Co. KGaA. .

[30] Pinson, J. (2012) Attachment of organic Layers to Materials Surfaces by Reduction of Diazonium Salts, In *Aryl Diazonium Salts: New Coupling Agents in Polymer and Surface Science* (Chehimi, M. M., Ed.), Wiley-VCH Verlag GmbH & Co. KGaA, Weiheim, Germany.

[31] Lyskawa, J., and Belanger, D. (2006) Direct Modification of a Gold Electrode with Aminophenyl Groups by Electrochemical Reduction of in Situ Generated Aminophenyl Monodiazonium Cations, *Chem. Mater. 18*, 4755-4763.

[32] Paulik, M. (2007) The Modifcation of Gold Surfaces via the Reduction of Aryldiazonium Salts, In *Chemistry*, p 100, Universtiy of Canterbery, University of Canterbery, Chemistry.

[33] Monagle, J. J. (1962) **Carbodiimides. III. Conversion of Isocyanates to Carbodiimides. Catalyst Studies**, *J. Org. Chem 27*, 3851-3855.

[34] Gamsjaeger, R., Liew, C. K., Loughlin, F. E., Crossley, M., and Mackay, J. P. (2007) **Sticky fingers: zinc-fingers as protein-recognition motifs**, *TRENDS in Biochemical Sciences 32*, 63-70.

[35] Laity, J. H., Lee, B. M., and Wright, P. E. (2001) Zinc finger proteins: new insights into structural and functional diversity, *Current Opinion in Structural Biology 11*.

[36] Elrod-Erickson, M., Rould, M. A., Nekludova, l., and Pabo, C. O. (1996) Zif268 protein-DNA complex refined at 1.6 A: a model system for understanding zinc finger-DNA interactions, *Structure 4*, 1171-1180.

[37] Pabo, C. O., Peisach, E., and Grant, R. A. (2001) Design and selection of novel Cys2His2 zinc finger proteins, *Annual review of biochemistry 70*, 313-340.

[38] Pavletich, N. P., and Pabo, C. O. (1991) Zinc Finger-DNA Recognition: Crystal Structure of a Zif268-DNA Complex at 2.1 A, *Science 252*, 809-817.

[39] Elrod-Erickson, M., Benson, T. E., and Pabo, C. O. (1998) High-resolution structures of variant Zif268–DNA complexes: implications for understanding zinc finger–DNA recognition, *Structure 6*, 451–464.

[40] Johnsosn, R. R., Kohlmeyer, A., Johnson, A. T. C., and Klein, M. L. (2009) Free energy landscape of a DNA-carbon nanotube hybrid using replica exchange molecular dymanics, *Nano letters 9*, 537-541.

A Hybrid DNA-Templated Gold Nanocluster For Enhanced Enzymatic Reduction of Oxygen

Introduction

With sources of fossil fuels dwindling, there is an urgent need to find cheap, renewable, and alternate forms of energy using naturally abundant resources such as sunlight, air, and water. Nanostructured materials and enzymatic fuel cells are showing great promise in this respect.1 In enzymatic fuel cells, both the anodic and cathodic reactions are carried out by enzymes acting as bio-electrocatalysts. The enzymes oxidize fuels at the anode while reduction of O2 takes place at the cathode, typically catalyzed by multi-copper oxidases (MCOs).2 The efficiency of these systems depends on how effectively the enzymes communicate with the electrode surface via direct electron transfer (DET) at potentials close to the redox potential of the enzyme.3

Although MCOs have been used as ORR catalysts on various electrode surfaces they suffer from low conversion efficiency primarily due to the lack of effective ET between the electrode surface and the enzyme active site. In addition, there is a need for engineering suitable material architectures that provide a large surface area for good electrical connectivity, substrate accessibility to the enzyme, and yet still retain a biocompatible environment for enzyme immobilization. Overcoming these limitations can enable widespread utilization of enzymatic fuel cells as simplified devices for single-compartment operation under neutral reaction conditions and integration into various scalable systems. To this end, gold nanoparticles (AuNPs) have been used as substrates for immobilization of laccase, which showed enhanced oxygen reduction kinetics by DET.4 However, the electrochemical output of this system still remained poor.

Atomically precise metal nanoclusters (NCs) with a diameter of less than 2 nm and consisting of ~2-200 atoms arranged in well-defined and stable geometric structures are showing important applications across multidisciplinary fields such as sensing, bio-imaging, electronics, photovoltaics, and catalysis.5 Owing to their ultra-small size, NCs possess discrete molecule-like electronic, optical, and electrochemical properties as well as specific packing of atoms on NC surface and the metallic core.6 These unique electronic and structural aspects of NCs play critical roles in fine-tuning their characteristics and bestow them with size-dependent properties that are quite different from those of bulk metals, metal complexes, and metal nanoparticles.

Although bulk gold is inert,7 gold nanoparticles (AuNPs) larger than 2 nm in diameter have been shown to possess interesting catalytic properties when dispersed as ultrafine particles on metal oxide supports.8 Among others, CO and _ENREF_1_ENREF_1hydrocarbon oxidation, hydrogenation, and reduction of nitrogen oxides and oxygen are the most notable examples where AuNPs have been employed as catalysts.8a,9 The high catalytic activity of small Au particles compared to bulk metal has been attributed to several factors, including high surface density of low coordination number Au atoms and less electron density in small Au particles compared to bulk metal.10 Although several studies examined the effect of NP size on catalytic activity,8,9c,11 it was only recently discovered that the catalytically active species in CO oxidation is a bilayer of 10-atom gold nanoclusters (AuNC), ~0.5 nm in diameter.12 Subsequently, several research groups reported catalytic activity of atomically monodisperse, ultrasmall AuNCs (<2 nm) in solution towards oxidation of organic substrates,13 hydrogenation,13a,14 electrocatalytic reduction of CO2,15 and ORR.16 While the reported AuNCs showed a strong size effect on ORR activity, they unfortunately reduced oxygen at low onset potentials (Eonset) [e.g. −0.1 V for Au11, −0.16 V for Au25, −0.2 V for Au55, and −0.25 V for Au140 (vs. Ag/AgCl)] indicating a high overpotential for the reaction.16 In addition, these experiments were exclusively performed in alkaline media. Therefore, efficient ORR catalysts need to be designed with low overpotential and which operate under more environmentally benign aqueous conditions.

Ligands are critical for the synthesis, stabilization and control of electronic properties of metal nanoclusters.17 Over the last decade, DNA has been increasingly used as a ligand to prepare silver,18 copper,19 and platinum20 nanoclusters with interesting luminescent, detection, and catalytic properties.5d,21 Because DNA is a natural nanoscale material with strong affinity for metal cations,22 DNA can template and localize metals to form and stabilize NCs.23 In addition, exquisite control of NC size and the resulting electronic and optical properties has made DNA a natural ligand choice for NC synthesis and their various applications. Finally, the chemistry of DNA-templated NCs can be performed in water and neutral conditions, which is a green and desirable method for technology development as opposed to organic solvents or acidic/alkaline reaction conditions.

Using these advantages of DNA as a ligand for NC synthesis having well-defined materials architectures, and with the wide variety of catalytic applications of AuNCs, we set out to synthesize stable AuNCs using DNA as the ligand and investigate their applications as facilitators of ET in enzymatic fuel cells. While a few examples of DNA-templated gold nanoclusters have been reported,24 their potential applications have been unexplored due to a lack a thorough characterization. We hypothesize that due to the small size, electrochemical activity and unique properties of the AuNCs the DNA-templated AuNC could facilitate ET to the enzyme active site where reduction of O2 takes place and thus lower the overpotential while increasing the electrocatalytic current density for ORR.

Herein we report synthesis and thorough characterization of a new DNA-templated AuNC. We demonstrate the application of this novel material in enzyme-based biofuel cells as facilitator of ET at the enzyme-electrode interface. Composites of the AuNC integrated with carbon nanotubes (CNTs) and bilirubin oxidase (BOD) were immobilized on electrode surfaces for ORR assays. Bilirubin oxidase from Myrothecium verrucaria was chosen as the desired MCO due to its known structure and ready commercial availability. BOD has an ET T1 Cu site, and a catalytic T2/T3 Cu site where the reduction of O2 takes place.25 The relatively high redox potential of BOD26 makes it advantageous for improving its performance towards electrocatalytic oxygen reduction. This unique application of the AuNC as facilitator of ET for ORR demonstrates the beneficial aspects of NC size effects and opens up many possibilities for technology developments in the long term, including biosensors, actuators, and biological fuel cells.

Results and Discussion

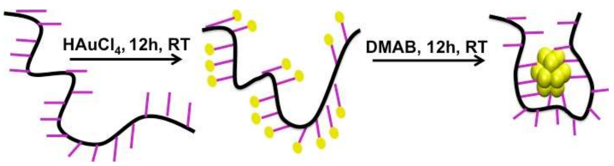

Scheme 1. Synthetic scheme of the AuNC. Black curves represent DNA backbone, pink lines represent DNA bases, individual yellow spheres represent Au(III), while AuNC is shown as the cluster of yellow spheres.

Electronic and secondary structural changes during AuNC formation: DNA-templated AuNC was synthesized according to Scheme 1 (see Materials and Methods for details). To monitor electronic changes occurring during AuNC formation, UV-vis absorption spectroscopy was employed. Incubation of DNA with Au(III) causes a red shift in the λmax of DNA from 261 nm to 266 nm (Figure 1), indicating complexation of Au(III) ions to the functional groups of DNA (likely to nucleobases by Lewis acid-base interactions). Upon reduction of Au(III) and formation of nanoclusters, further spectral changes occur and the λmax subsequently blue-shifts from 266 nm to 264 nm (Figure 1), indicating different electronic transitions in the DNA when the AuNC is formed, compared to the initial Au(III)-DNA complex. Similar trend in spectral shifts was observed during the formation of a DNA-templated AgNC.18a Upon subtracting the DNA contribution from the spectrum of AuNC, the presence of a broad shoulder centered ~394 nm (3.15 eV) was observed (Figure 1, inset). Discrete molecule-like electronic transitions in the range 330-390 nm have been reported for small gold clusters (e.g. Au10-12SG10-12,27 Au11C12,28 Au13[PPh3]4[S(CH2)11CH3]2Cl2,29 u13[PPh3]4[S(CH2)11-CH3]4,29 and Au8PAMAP30), the spectral features of which depend on various factors such as ligand type, geometry, core size, and oxidation states of the clusters.31 Therefore, it is likely that some or all of these factors contribute to the broadness of this shoulder feature in the spectra of the DNA-templated AuNC reported here.

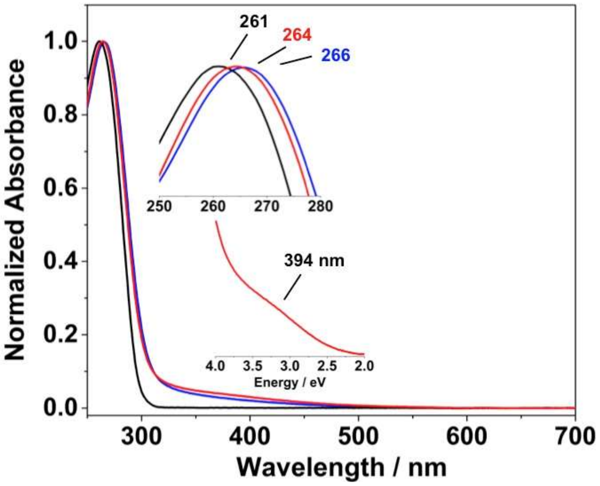

Figure 1. Electronic changes occur during the AuNC formation. UV-vis absorption spectra of solutions containing 15 μM DNA (black line), 15 μM DNA + 225 μM $HAuCl_4$ (blue line), and the as synthesized AuNC (red line) in 20 mM phosphate buffer, 1 mM $Mg(OAc)_2$, pH 7. The top inset shows the clear shifts in the λ_{max} of DNA upon Au(III) complexation and subsequent AuNC formation. The bottom inset shows the spectrum of AuNC after subtraction of the absorption by DNA alone.

To probe whether secondary structural changes occur in the DNA molecule during AuNC formation, we used circular dichroism spectroscopy, which is sensitive to changes in the chirality of ribose sugars. DNA alone shows two positive CD bands at 279 and 219 nm and two negative bands at 244 and 209 nm (Figure 2), respectively. Similar to the electronic absorption spectrum, the CD spectrum also changes upon Au(III) complexation to DNA and subsequent reduction of Au(III) leading to the formation of AuNC (Figure 2), suggesting secondary structural changes in the DNA during these processes. Spectral shifts in both the absorption and CD spectra suggest changes in the electronic transitions and secondary structure of DNA upon Au(III) coordination and subsequent cluster formation process.

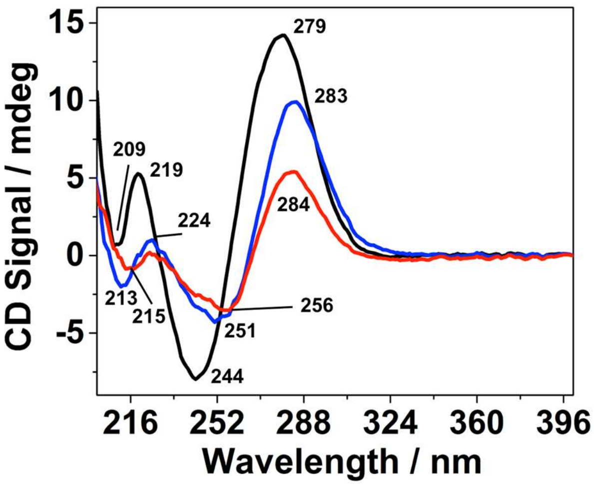

Figure. 2. Secondary structural changes occur during the AuNC formation. CD spectra of solutions containing 100 μM DNA (black line); 150 μM DNA + 2250 μM $HAuCl_4$ (blue line); and the synthesized AuNC (red line).

The AuNC is a small cluster with ~7 Au atoms: Transmission electron microscopy (TEM) analysis was further performed to determine the size of AuNC. The TEM micrograph of the AuNC shows the presence of many small particles with average size of ~0.9 nm in diameter (Figure 3), which is characteristic of small gold clusters.32 The observed apparent polydispersity due to the presence of a few larger particles is originating from electron beam damage of the nanoclusters that causes sintering of the metal, which is a widely observed phenomenon while imaging such small particles.33

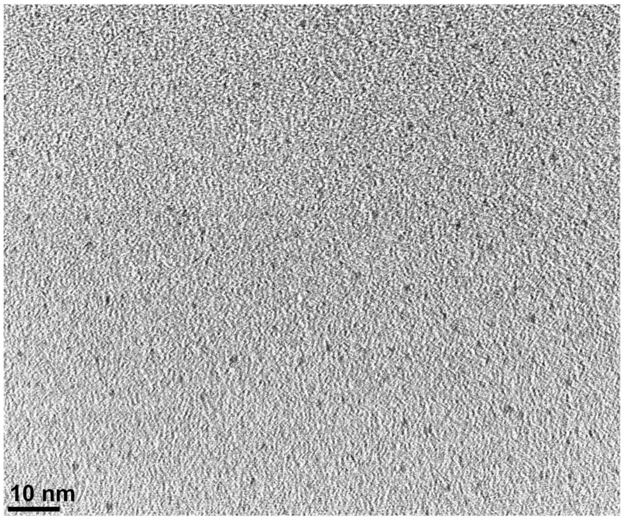

Figure 3. TEM shows small gold clusters. TEM image of the AuNC showing the presence of small clusters with average size of ~0.9 nm in diameter. Scale bar: 10 nm.

The TEM image further proves that the material under study is truly nanocluster in nature and not plasmonic AuNPs (>2 nm in diameter). To determine the number of Au atoms present in the AuNC we performed MALDI-MS of the DNA and the AuNC in both positive and negative ionization modes. The observed molecular weights of the AuNC are 10400 Da and 10524 Da in positive and negative ionization modes, respectively; while those of DNA are 9054 Da and 9196 Da (Figure S1). After subtracting the corresponding DNA, contributions, the total number of Au atoms present in the AuNC was calculated to be ~7 in both positive and negative ionization modes, suggesting that the AuNC is a 7-atom cluster ligated by a single DNA molecule. Although the widths of the AuNC peak within the MALDI spectra are greater than that of DNA alone, it is likely that the extent of ionization of DNA and AuNC are different, giving rise to differences in the observed resolution. Additionally, given that even well characterized and atomically precise thiol protected gold clusters exhibit broad MALDI spectra, the observation of such spectral broadening in the DNA-protected AuNC is not unexpected.16,34 The observed cluster size is smaller than the initial molar ratio of 1:15

(DNA:Au) as some of the added Au(III) produces plasmonic Au particles upon reduction (see Materials and Methods). Furthermore, it is commonly found for DNA-templated nanoclusters that the metal-ligand stoichiometry of the reaction mixture is not maintained within the final product.18a,18c,18d,35

To further probe the composition of the AuNC, we performed energy dispersive X-ray spectroscopy (EDX) analysis to calculate the Au atom count (Figure S2). From intensities of the Au Lα (9.712 keV) and P Kα (2.013 keV) lines, the atomic percentages of P and Au were obtained. From this analysis the number of Au atoms present in one DNA molecule was found to be ~7 (see Materials and Methods for details). While small clusters of 3-13 Au atoms protected by ligands other than DNA have been reported,36 a rigorous analysis of AuNC size and atom count has not been previously performed for any DNA-templated AuNC.

We further inspected the P 2p and Au 4f XPS data to find out the number of gold atoms present in the AuNC. From these data the relative atomic % of P and Au are found to be 3.1% and 0.74%, respectively. Analysis of the data yielded a ~7 atom Au cluster (see Materials and Methods), which is also consistent with the MALDI-MS and EDX data (vide supra) in suggesting the presence of ~7 Au atoms in the AuNC.

The AuNC is a mixed valence cluster: We next investigated whether the clusters possessed both Au(0) and Au(I) oxidation states using X-ray photoelectron spectroscopy (XPS). The Au 4f XPS spectrum of the AuNC sample (Figure 4, blue line) shows an intense and sharp peak at ~85 eV, a less intense and broader peak at ~88.5 eV, and a small peak at ~91 eV. The sharp peak at ~85 eV corresponds to the Au4f7/2 component and the other two peaks correspond to the Au4f5/2 components. Deconvolution of the spectral envelope yielded individual Au species corresponding to different oxidation states. The Au4f7/2 line consists of contributions from a Au(0) species at 84.2 eV (Figure 4, black line) and a Au(I) species at 85 eV (Figure 4, green line) present at a relative population of 0.27:1, respectively.

These data therefore suggest that the DNA-templated AuNC has characteristics of nanoclusters with both Au(0) and Au(I) oxidation states, giving rise to a mixed valence cluster. In addition to both Au(I) and Au(0), a small fraction of residual Au(III) still remains in the sample as observed from the Au 4f7/2 line appearing at 87.1 eV (red dotted line).

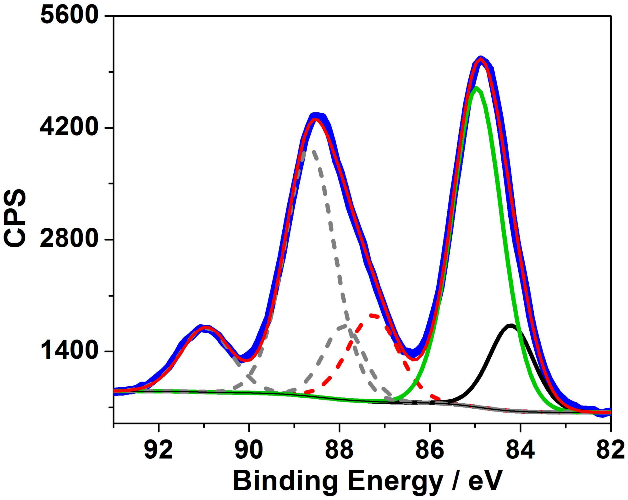

Figure 4. The AuNC consists of both Au(0) and Au(I) oxidation states. Au 4f XPS spectra showing the presence of both Au(0) and Au(I). Blue line: experimental spectrum; red solid line: fitted spectrum; black line: Au4f$_{7/2}$ component of Au(0); green line: Au4f$_{7/2}$ component of Au(I); red dotted line: Au4f$_{7/2}$ component of residual Au(III); gray lines: corresponding Au4f$_{5/2}$ components.

Based upon NMR and EXAFS data of Ag-coordinated DNA, and Raman data on DNA-bound metal ions it is suggested that metal cations bind to DNA through the N7 of purines and N3 of pyrimidines.18a,37 To gain insight as to whether nitrogen atoms of DNA bases are ligating to Au in the AuNC we examined the N1s XPS data. The N1s XPS data shows that the speciation of nitrogen has changed in the AuNC sample compared to metal-free DNA (Figure S3). Specifically, the protonated nitrogen species (401.3 eV) from the DNA bases changes significantly when the AuNC is formed. Measuring the pH of the DNA-only and the AuNC samples (both at pH ~7.0) ensured that deprotonation of the nitrogen was not due to a difference in pH. Although the identity of specific DNA bases that bind to the Au cannot be determined, these data suggest that the AuNC is preferentially formed with ligation from the nitrogens of the DNA bases, the chemical environment of which changes upon binding of gold.

The AuNC displays large Stokes shift with microsecond lifetime: Having established the size and composition of DNA-templated AuNC, we explored whether it was luminescent. At relatively high concentrations (~1 mM), the AuNC showed luminescence with an emission peak at 650 nm (Figure 5, blue line) resulting from a photoexcitation at 470 nm (Figure 5, green line). The large Stokes shift of ~180 nm suggests that the primary origin of this emission is phosphorescence, which was supported by lifetime measurements. Analysis of the luminescence decay curves showed the presence of two emission components with microsecond lifetimes [4.2 μs (89%) and 0.6 μs (11%); Figure S4)]. Such large Stokes shifts and microsecond lifetimes have also been observed in luminescent Au(I) complexes,27a,38 as well as in ligand-protected luminescent AuNCs with glutathione (AuNC@GSH: λex=365nm, λem=610nm),27a D-penicillamine (AuNC@D-Pen: λex=400nm, λem=610nm),5a and dihydrolipoic acid (AuNC@DHLA: λex=490nm, λem=650nm).5b,5c A quantum yield of 2.6x10-3 determined using Ru(bpy)3Cl2 (ϕ=2.8x10-2)39 suggests that the AuNC is weakly luminescent. However, the luminescence quantum yield is comparable to that of glutathione (ϕ=3.5x10-3),5f and tiopronin-protected (ϕ=3x10-3)40 AuNCs and several orders of magnitude greater than dimarcaptosuccinic acid (ϕ=1x10-6),41 and dodecanethiol protected gold clusters (ϕ=4.4x10-5, <3x10-7).42 It has been recently proposed that the origin of luminescence in AuNCs can be attributed to the presence of large fraction of Au(I), and that the AuNCs can be present as a mixed-valence species lying in between luminescent Au(I) complexes and non-luminescent AuNPs.43 To test whether the luminescence in the DNA-templated AuNC is due to the presence of Au(I), the spectral changes were monitored upon reducing the Au(I) in the luminescent AuNC. Addition of 1.0 equivalent (with respect to gold concentration) NaBH4 to a solution of AuNC caused a significant decrease in emission at 650 nm, with ~90% loss of the initial luminescence (Figure S5). This observation suggests that the luminescence of DNA-templated AuNC is associated with the presence of a high fraction of Au(I). Consequently, no luminescence was observed when NaBH4 was used instead of dimethylamine borane

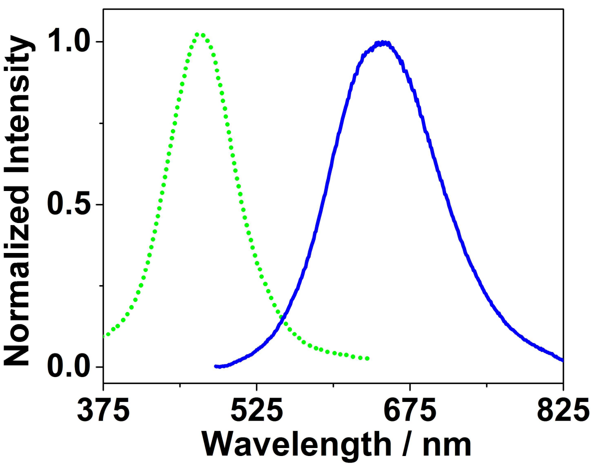

Figure 5. The luminescent AuNC shows large Stokes shift. Excitation spectrum (green line; λ_{em} = 650 nm) and emission spectrum (blue line; λ_{ex} = 470 nm) of ~1 mM AuNC in 20 mM phosphate buffer, 1 mM Mg(OAc)$_2$, pH 7.

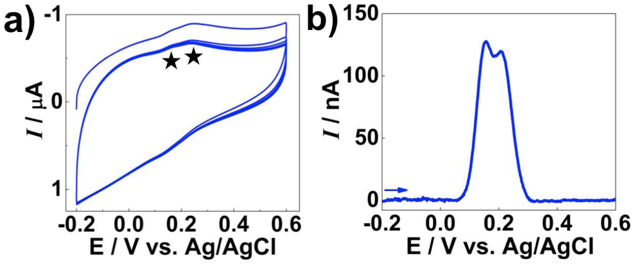

Figure 6. The AuNC is electrochemically active. a) CV scans at a scan rate of 50 mV/s. b) DPV scans in the anodic direction (pulse period = 250 ms, pulse width = 25 ms, amplitude = 25 mV, increment = 2 mV). The concentration of sample solutions were ~0.5 mM AuNC in 50 mM phosphate buffer, 1 mM Mg(OAc)$_2$, pH 7.

(DMAB) as the reductant during the AuNC synthesis. This result corroborates the hypothesis that the presence of Au(I) is critical to the appearance of luminescence in the DNA-templated AuNC.

The AuNC is electrochemically active: Electrochemical properties of the AuNC were assessed by cyclic voltammetry (CV) and differential pulse voltammetry (DPV). Although the CV scans show two poorly defined redox processes (Figure 6a, marked as *), DPV shows two resolved processes occurring at 155 mV and 0.210 V vs. Ag/AgCl, respectively (Figure 6b). From electrochemical studies of monolayer protected AuNCs of various sizes (e.g. Au25(SC6)18,44 Au38(SC2H4Ph)24,45 and Au67(SR)3546), multiple redox processes have been assigned to sequential one-electron oxidation/reduction of the various charge states of the clusters. Here, the two closely spaced potentials are likely associated with two successive one-electron oxidations of the AuNC i.e. two Au(0)/Au(I) processes. As with polynuclear charge-transfer molecules, it is possible that the first oxidation/reduction introduces an overall electronic and charge perturbation that causes the shift of the second process.47

Oxygen reduction activity of AuNC/BOD composites: Motivated by the electrochemical activity and small size of the AuNC, we investigated whether these unique properties can be utilized for enhanced ET between the electrode and the enzyme. BOD was used as an enzyme of choice as it is a well-known enzyme for catalyzing ORR. To test our hypothesis, the AuNC was integrated with BOD by using single-walled carbon nanotubes as a support material. SWNT were dispersed via tetrabutylammonium bromide (TBAB) modified Nafion. TBAB modification causes exchange of the proton from Nafion sulfonic acid group and affords the TBAB salt of Nafion.48 This modification results in an increase in the pore size of the Nafion polymer allowing easy diffusion of substrates and ions to the enzyme active site, and reduces acidity of Nafion, thus making it a more biocompatible polymer for immobilization of the enzyme on the electrode surface.48 DNA-templated AuNC was then mixed with the suspension of SWNT to allow for stacking of the DNA to the SWNT by non-covalent π-π stacking interactions. Next, 1-pyrenebutanoic acid succinimidyl ester (PBSE) was added to the mixture followed by BOD and incubated overnight. While the pyrene groups of PBSE tether to the SWNT by π-π stacking interactions, the succinimidyl ester groups covalently attach to the surface amine groups of the BOD via succinimidyl ester-amine cross-linking chemistry. A schematic of the composite preparation method is shown in Scheme 2. Control composites consisting of i) SWNT and BOD (SWNT/BOD), ii) SWNT, DNA alone, and BOD (SWNT/DNA/BOD), iii) SWNT, plasmonic Au particles (which were produced as the side product from synthesis) and BOD (SWNT/plasmonic Au/BOD) were prepared using similar methods as above but without the AuNC. For electrocatalytic ORR measurements the samples were drop cast on a rotating disk electrode (RDE), dried, and their oxygen reduction activity was tested using linear sweep voltammetry (LSV) with a scan rate of 10 mV/s.

Scheme 2. Schemeatic representaion of composite preparation for ORR assays. AuNC: gold nanocluster, PBSE: 1-pyrenebutanoic acid succinimidyl ester, BOD: bilirubin oxidase, RDE: rotating disk electrode, RE: reference electrode, CE: counter electrode

The experimental potentials from this study will be referred henceforth against two standards Ag/AgCl and RHE, and designated as EAg/AgCl (ERHE). First, we performed electrochemical measurements of SWNT/AuNC/BOD composite under O2 depleted, and dissolved O2 conditions. Under O2-depleted conditions (Figure S6, black line), very low current was observed due to the small amount of oxygen present in the electrolyte solution (~0.66 mg/L). In the presence of dissolved atmospheric O2 (~6.91 mg/L) moderate current was observed for the enzymatic ORR (Figure S6, red line). Below ~0.400 V (1.040 V), the current density decreased because the reaction was limited by the availability of O2 in the electrolyte solution.

Sample	Eonset V vs. Ag/AgCl (V vs. RHE)	E1/2 V vs. Ag/AgCl (V vs. RHE)	Δia (μA/cm2)
SWNT/plasmonic Au/BOD	0.480 (1.120)	0.355 (0.995)	74
SWNT/DNA/BOD	0.485 (1.125)	0.400 (1.040)	197
SWNT/BOD	0.510	0.415	257

	(1.150)	(1.055)	
SWNT/AuNC/BOD	0.525 (1.165)	0.430 (1.070)	412

We next tested electrocatalytic activity of SWNT/AuNC/BOD and two control composites (SWNT/BOD and SWNT/DNA/BOD) in O2–saturated buffer. The SWNT/BOD control composite (Figure 7, gray line) showed catalytic current with Eonset of ~0.510 V (1.150 V), apparent E1/2 of ~0.415 V (1.055 V), and current density [Δi measured as the difference in current between Eonset and the reductive current at 0.300 V (0.940 V)] of ~257 μA/cm2 (Table 1). In contrast, the SWNT/DNA/BOD control composite (Figure 7, blue line) showed a cathodically shifted Eonset at ~0.485 V (1.125 V). In addition, E1/2 decreased to ~0.400 V (1.040) in conjunction with the catalytic current density, which was reduced to ~197 μA/cm2 from ~257 μA/cm2 observed in the SWNT/BOD composite (Table 1). These results suggest that DNA can hinder the interfacial ET from the electrode to the enzyme and thus be detrimental to the ORR (supported by lower current densities with increase in DNA concentration, Figure S7). Remarkably, the presence of the AuNC caused significant changes in the ORR profile displayed by the SWNT/AuNC/BOD composite (Figure 7, red line). First, Eonset was anodically shifted to ~0.525 V (1.165 V) from ~0.510 V (1.150 V) observed using the SWNT/BOD sample, corresponding to a positive shift of ~0.015 V. Second, the electrocatalytic current density was increased to ~412 μA/cm2, an increase of ~155 μA/cm2 compared to SWNT/BOD composite. Finally, the E1/2 increased to ~0.430 V (1.070 V) from that of ~0.415 V (1.055 V) observed using SWNT/BOD (Table 1). These exciting results, therefore, suggest that the presence of AuNC enhances the ORR activity of the enzyme by lowering the overpotential by a significant ~0.015 V with concomitant increase in the kinetics of the reaction, which leads to higher catalytic current densities. We next investigated whether such enhancement of ORR activity by the AuNC is specific to "quantum" clusters. To test this, we performed LSV of SWNT/plasmonic Au/BOD control composite consisting of the SWNT, plasmonic Au particles that were produced as a side product during the cluster synthesis, and BOD. This data (Figure 7, purple line) shows that the Eonset shifts to 0.480 V (1.120 V) as compared to 0.525 V (1.165 V) observed in the presence of AuNC. Further, the E1/2 also significantly shifts to a lower potential of 0.355 V (0.990 V) as compared to 0.430 V (1.070 V) obtained with the SWNT/AuNC/BOD

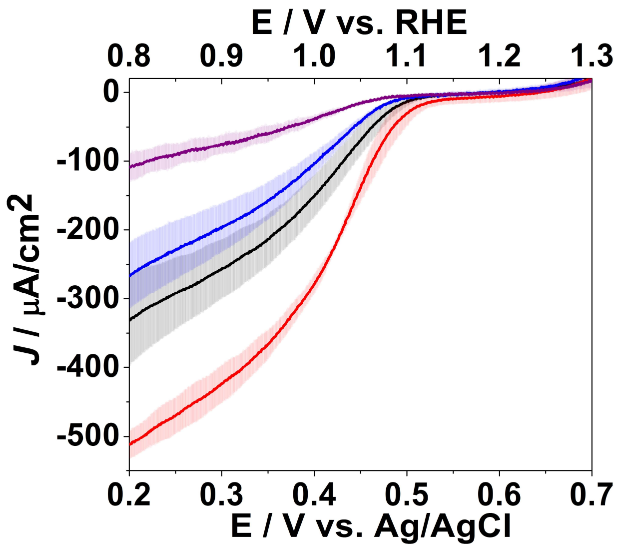

Figure 7. LSV of SWNT/plasmonic Au/BOD (purple line); SWNT/DNA/BOD (blue line); SWNT/BOD (gray line); and SWNT/AuNC/BOD (red line) composite materials in O_2-saturated 0.1M phosphate buffer (pH 7.5). Traces and shaded areas represent the average and standard deviations, respectively, of the data obtained by testing three different samples, prepared and tested independently. Scan rate = 10 mV/s; rotation rate = 1600 rpm

composite with a concomitant reduction of electrocatalytic current density at the electrode (74 μA/cm2 compared to 412 μA/cm2 observed with AuNC). These data, therefore, convincingly suggest that the enhancement of ORR by lowering overpotential by ~0.015 V as well as the enhancement of catalytic current densities in the presence of AuNC is unique to “quantum” clusters, which improved kinetics and thermodynamics of ORR, and cannot be ascribed to the features of plasmonic particles. Such enhancement of ORR activity by the AuNC is the first of its kind reported.

Table 1. Electrochemical results obtained from LSVs in O2-saturated buffer. Potentials vs. RHE in parenthesis.

aΔi is the differential current between the onset potential (Eonset) and the reductive current at 0.300 mV (0.940 V).

The likely mechanism by which the AuNC enhances the ORR performance is by facilitating the ET between the electrode surface and the enzyme active site, which in turn improves the effectiveness of electronic communication. These findings suggest that employment of the AuNC as an enhancer of ET between the electrode surface and the enzyme active site can potentially remove a significant barrier in enzymatic fuel cells, which often suffer from poor performance due to a lack of electronic communication between the electrode and the enzyme active site.

Figure 8. The AuNC enhances ORR by BOD. Potentiostatic polarization curves for MWBP/BOD (black curve); and MWBP/AuNC/BOD (red curve) carried out in 0.1M phosphate buffer (pH 7.5). Standard deviations were calculated from data obtained by testing three different samples, prepared and tested independently.

While the Eonset of the SWNT/AuNC/BOD composite is comparable (Table 1) to that of a BOD on air breathing gas diffusion electrode (GDE) (1.160 V vs. RHE), the observed apparent E1/2 in the current system (Table 1) is higher than that of the GDE (0.920 V vs. RHE).49 In addition, the SWNT/AuNC/BOD composite showed higher Eonset and E1/2 compared to many reported in literature including BOD on spectrographic graphite (Eonset=1.136 V vs. RHE, E1/2=1.036 V vs. RHE),50 and BOD on CNTs (Eonset = 1.149 V vs. RHE, E1/2 = 0.950 V vs. RHE).51 The present system also displays better thermodynamic parameters (Table 1) compared to many Pt-based materials. For example, platinum nanoparticles of various sizes (3-7 nm) reduced O2 with Eonset = 0.870-0.920 V vs. RHE and E1/2 = 0.750 V vs. RHE,52 platinum nanoclusters on genomic DNA and grapheme oxide composites (Ptn/gDNA-GO) showed Eonset = 1.010 V vs. RHE and E1/2 = 0.900 V vs. RHE,20b Pt and Pt/Pd nanotubes as well as graphene supported Pt and Pd catalysts and Pt/Pd nanodendrites showed ORR with E1/2 = 0.850-0.900 V vs. RHE.53 Furthermore, a recently reported Co3O4 nanocrystals on grapheme showed ORR activity with Eonset = 0.880 V vs. RHE and E1/2 = 0.790-0.830 V vs. RHE.54

Further evidence of this unique role of AuNC was obtained from ORR currents measured using a different electrode design. In this case, the electrode material (multi-walled Bucky paper (MWBP)) was first soaked in AuNC solution, followed by PBSE and BOD for the immobilization of the various components (see Materials and Methods for details). The modified MWBP was then placed on a glassy carbon cap electrode and the electrode performance towards ORR was monitored in O2-saturated buffer by measuring potentiostatic polarization curves. The sample containing both AuNC and BOD caused an increase in the ORR current density to 735 μA/cm2 (Figure 8, red line) from that of 493 μA/cm2 obtained using BOD alone (Figure 8, black line), amounting to an increase in current density of ~50%. Therefore, these results also demonstrate that the AuNC is enhancing the performance of BOD by acting as a facilitator of the ET between the electrode surface and the enzyme active site.

Mechanistic insight on 4e− vs. 2e− reduction: To understand whether the presence of the AuNC perturbs the mechanism of ORR by BODs with regards to 2e− vs. 4e− processes, we performed mass and charge balance analysis of rotating ring disk electrode (RRDE) data obtained using the SWNT/AuNC/BOD composite in O2-saturated buffer (Figure S8). From this analysis the number of electrons (n) transferred during O2 reduction can be calculated using the following equation:

$$n = \frac{4}{1 + \left(\frac{i_R}{\eta * i_D}\right)} \qquad (1)$$

where iR is the ring current, iD is the disk current, and η is the collection efficiency at the electrode.55 For RRDE, the collection efficiency is known to be 37%.56 The calculated number of electrons transferred during O2 reduction by SWNT/AuNC/BOD composite was found to be 3.9±0.1. This result indicates that less than 3% of O2 was partially reduced by 2e− to H2O2 (O2+2e−+2H+ → H2O2), while almost all of O2 was reduced to H2O by a 4e− reduction process (O2+4e−+4H+ → 2H2O). These observations lead to the conclusion that the presence of the AuNC did not perturb the mechanism of O2 reduction by BOD,57 and that the SWNT/AuNC/BOD composite material cleanly reduced O2 to H2O with minimal production of reactive oxygen species (ROS).

Conclusions

In conclusion, a new DNA-templated AuNC has been synthesized and thoroughly characterized. While the TEM and EDX analyses show that the AuNC is ~1 nm in diameter and consists of ~7 Au atoms, XPS confirms the presence of both Au(0) and Au(I) oxidation states. The AuNC shows weak photoluminescence with microsecond lifetime and large Stokes shift. The observed phosphorescence can be attributed to the presence of high fraction of Au(I) in the cluster. The AuNC is electrochemically active and enhances the performance of BOD catalyzed enzymatic ORR by lowering the overpotential by ~15 mV, and improving the electronic communication between the electrode and the enzyme active site. RRDE analysis showed that the presence of the AuNC did not perturb the mechanism of O2 reduction, as the AuNC/BOD composite material cleanly reduced O2 to H2O in a 4e− pathway. This unique role as ET enhancers at the enzyme-electrode interface makes the new AuNC as a potential candidate for the development of cathodes for enzymatic fuel cells, thus lifting a critical methodological barrier in biofuel cell design.

Materials and Methods

Synthesis and purification of the AuNC. In a typical synthesis, 15 µM single-stranded DNA (IDT, standard desalting) of sequence ACCCGAACCTGGGCTACCACCCTTAATCCCC was mixed with 225 µM HAuCl4.3H2O (Sigma-Aldrich, ≥99.9% trace metals basis) in a solution of 20 mM phosphate buffer (pH 7), 1 mM Mg(OAc)2 (Fisher Scientific) and equilibrated for 24 h with inverted mixing at room temperature (RT, 23±2 oC). After equilibration, the solution became yellow. Reduction of Au(III) was initiated by addition of 2.25 mM dimethylamine borane (DMAB, Sigma-Aldrich) followed by equilibration at RT for 16 h. At this point, a purple solution was formed indicating the presence of plasmonic Au particles. This solution was then purified by spin filtration using 30 KDa MWCO membranes (Millipore). A yellow solution of the AuNC was collected in the filtrate while the plasmonic Au particles were retained in the membrane. The AuNC solution was stored at 4°C before further use. Whenever necessary, the as-synthesized AuNC was concentrated using 10 KDa MWCO membranes. The highest yield of AuNC was obtained at a maximum reaction volume of ~5 mL. At higher reaction volumes the yield of the AuNC significantly decreased and plasmonic Au particles were formed at a greater extent. For energy dispersive X-ray spectroscopy (EDX) measurements (see below) and to determine the P 2p atomic % from XPS, the AuNC was synthesized in a solution of 50 mM NH4OAc buffer (pH 5.5), 1 mM Mg(OAc)2 to avoid error in measuring the relative ratio of Au:P arising from the presence of P in phosphate buffer.

UV-vis and fluorescence spectroscopy. UV-vis spectra were collected at RT using a Cary 5000 (Agilent) UV-vis NIR spectrophotometer. Fluorescence spectra were collected using wither a Cary Eclipse spectrophotometer or a Horiba Jobin Yvon Fluoromax 4 spectrofluorometer, with an excitation/emission band pass of 5 nm. In lifetime measurements, the spectrofluorometer was coupled with a time-correlated single photon counting (TCSPC) system from Horiba Jobin Yvon. The apparatus was equipped with a pulsed laser diode source (NanoLED) operating at 1 MHz and with excitation centered at 452 nm. Analysis of fluorescence decay profiles was performed with the Horiba DAS6 software. All measurements were performed at RT. Quantum yield of AuNC was determined using Ru(bpy)3Cl2 (λex=470nm, λem=605nm) dissolved in H2O as the standard (ϕ=2.8x10-2).39 Absorbance of both samples was maintained at 0.03-0.12 au. Linear plots were obtained by plotting 5 absorbance values against integrated areas of the emission spectra for these samples excited at 470 nm. The quantum yield of the AuNC sample was obtained to be ϕ=2.6x10-3 using the gradient method.58

CD spectroscopy. CD spectra were collected on a JASCO instrument using a 1 mm path length cuvette. Three scans were collected for each sample.

TEM imaging. Bright-field transmission electron microscopy (TEM) analysis of the AuNC was performed using a FEI Tecnai F30 instrument operating at 200 kV acceleration voltage. A thin carbon-coated (carbon film thickness <10 nm) copper TEM grid (Pacific Grid-Tech, 300 mesh, 3.05 mm O.D., hole size: ~63 µm) was soaked in as-synthesized AuNC solution for 2 h and air-dried before imaging.

MALDI-MS. MALDI data were collected on ABsciex 4800 Plus TOF/TOF MALDI mass spectrometer using both DNA and AuNC samples in both positive and negative ion modes with sinapinic acid (Sigma-Aldrich) as matrix. The AuNC was synthesized using the same DNA stock solution, which was used for MALDI-MS analysis of the DNA-only sample.

EDX measurements. Energy dispersive X-ray spectroscopy (EDX) data were collected at 30 kV acceleration voltage using a FEI Quanta 400 FEG-E-SEM instrument equipped with an EDX system (EDAX Inc.). Data processing was performed using Genesis software. A concentrated sample (~1-2 mM) of the AuNC synthesized in NH4OAc buffer was drop cast and dried on carbon tape. The ratio of gold to phosphorus in the DNA backbone was calculated based on the total atomic % of these two elements determined from the intensities of the Au Lα (9.712 keV) and P Kα (2.013 keV) lines in the EDX spectra of the sample. Contribution from spectral overlap of the Au M line (2.120 keV) to the P Kα line was subtracted. The atomic percentages of these two elements were calculated to be 14 and 59.2, respectively. The total atomic percentage of phosphorus present in the DNA was then used to calculate the number of DNA molecules, determined to be 1.9 (59.2/31) by taking the contributions from 31 P atoms (in this study, the DNA is 31 nucleotides long). As nanoclusters are formed by a single DNA molecule, the number of Au atoms present in the AuNC was found to be ~7.4±1.0 (14/1.9).

XPS data collection and processing. Sample was drop cast on mica surface and air dried before measurements. XPS measurements were performed with a Kratos Axis Ultra DLD X-ray photoelectron spectrometer using a monochromatic Al Kα source operating at 225 W. The data were acquired from 3 different areas in the sample. Survey and high resolution C1s, O1s, N1s, and Au 4f were acquired at 80 and 20 eV pass energy, respectively. Standard operating conditions for good charge compensation were: bias voltage of 3.1 V, filament voltage of −1.0 V, and filament current of 2.1 A. Data analysis and quantification were performed using the CasaXPS software. A linear background was used for C 1s, N 1s, O 1s, and Shirley background for Au 4f spectra. All the spectra were charge referenced to the C 1s at 284.7 eV. Quantification utilized sensitivity factors that were provided by the manufacturer. A 70% Gaussian/30% Lorentzian (GL (30)) line shape was used for the curve fittings.

Atomic % of P and Au obtained from P 2p and Au 4f XPS data were found to be 3.1% and 0.74%, respectively. Upon normalizing the atomic % of P to 1 DNA molecule (which has 31 nucleotides and thus 31 P atoms), we obtain 0.1 as the normalization factor (3.1/31=0.1). After normalizing the atomic % of Au with this normalization factor, the number of Au atoms present in the AuNC is thus calculated to be 7.4 (0.74/0.1=7.4).

Electrochemistry. Cyclic voltammetry (CV) and differential pulse voltammetry (DPV) experiments were performed using a CH Instruments CHI760E potentiostat. A three-electrode setup consisted of a glassy carbon working electrode (3.0 mm disk), a Pt wire auxiliary electrode, and a standard Ag/AgCl reference electrode. Cyclic voltammograms were recorded at scan rates of 10-100 mV s−1 and were let run for at least ten full cycles. The 20 mM phosphate buffer solution (pH 7) containing 1 mM Mg(OAc)2 (used in the AuNC synthesis) was the only electrolyte source. Differential pulse voltammograms were obtained at a pulse period of 250 ms, pulse width of 25 ms, amplitude of 25 mV, and increment of 2 mV. All sample solutions were first deoxygenated and then blanketed with an argon atmosphere throughout the CV and DPV experiments.

Electrochemical measurements for ORR.

1) Preparation of SWNT/AuNC/BOD composite materials: First, a suspension of 1% single-walled carbon nanotubes (SWNT, cheaptubes.com) in 4:1 water:methanol solution and 0.1% tetrabutylammonium bromide (TBAB)-modified Nafion (provided by Prof. Shelley Minteer, University of Utah) in absolute ethanol was made and bath sonicated for 30 min at RT to disperse the SWNT. 5 μL of the AuNC solution was added to 40 μL of the SWNT/TBAB-Nafion suspension and left for 1 h to allow for the stacking of the DNA to the SWNT. Identical luminescence emission spectra of the AuNC

before and after mixing with SWNT/TBAB-Nafion confirmed that the integrity of the AuNC remained intact after stacking with SWNT (Figure S9 Next, 2 μL (4 mg/mL) 1-pyrenebutanoic acid succinimidyl ester (PBSE, Sigma-Aldrich) dissolved in ethanol were introduced to the SWNT/TBAB-Nafion/AuNC mixture and incubated for additional 1 h. After the PBSE adsorption on the SWNT, 2 μL of a 200 mg/mL BOD (Amano Enzyme Inc.) solution in 100 mM phosphate buffer at pH 7.5 was added and the sample was incubated for 16-18 h at 4oC. The composite material was further used for the ORR experiments. Controls consisting of SWNT/BOD, SWNT/DNA/BOD, and SWNT/plasmonic Au/BOD were prepared using same procedure as necessary.

A glassy carbon rotating disk electrode (RDE) (disk area 0.2475 cm2, Pine Instruments) was used. The RDE was cleaned with alumina of increasingly fine grits of 1, 0.3, and 0.05 mm, and rinsed with deionized water. After cleaning the electrode, 10 μL of SWNT/TBAB-Nafion suspension were dropped on the electrode surface and dried under a flow of N2 gas. Next, 10 μL of the composite material (SWNT/BOD, SWNT/DNA/BOD, SWNT/plasmonic Au/BOD or SWNT/AuNC/BOD) was drop cast on the RDE and allowed to air-dry before the electrochemical measurements.

2) Preparation of MWBP electrode: Circular pieces (0.3 mm diameter) of MWBP were cut, immersed in a solution of the AuNC, and left for 1h for attachment of the AuNC with MWBP. The paper discs were then washed with DI water and transferred to a 10 mM solution of PBSE in ethanol. After 1 h, the modified nanotube paper was washed with DI water and placed in solution of BOD (10 mg/mL in 100 mM phosphate buffer, pH 7.5) and incubated at 4°C for 18 h. After enzyme immobilization, the electrodes were washed again with buffer to remove any unattached enzyme. The modified MWBP discs were then placed on a glassy carbon cap electrode and tested in 100 mM phosphate buffer, pH 7.5. A control electrode was prepared the same way except for the use of AuNC.

3) Electrocatalytic measurements: RDE measurements were performed with a WEB30 Pine bi-potentiostat and a rotator from Pine Instruments. A three-electrode setup (glassy carbon working electrode, Pt wire auxiliary electrode, Ag/AgCl reference electrode) was used. The electrolyte was a 100 mM phosphate buffer solution at pH 7.5. Enough time (20 min) was allowed for the system at open circuit conditions to reach equilibrium. Using linear sweep voltammetry (LSV) the disk potential was swept from 0.8 to 0 V at a scan rate of 10 mV/s. At least three sets of independent ORR data were collected from three different preparations of composite samples as well as controls. With each preparation, the ORR currents were measured in electrolyte solutions containing dissolved O2, saturated O2 (purged for 20 min), and depleted O2 (N2 purged for 20 min). Potentiostatic polarization curves of the MWBP/AuNC/BOD and MWBP/BOD electrodes were carried out by applying a constant potential for 300 s, starting from open-circuit potential to 0 V vs. Ag/AgCl, with a step increase of 0.05 V. Potential from Ag/AgCl was converted to RHE using:59

ERHE = Emeasured + 0.197 + 0.059*pH

4) Oxygen reduction reaction current: The electrochemical current (Δi) was calculated by determining the difference in the reductive current at ~0.300 V vs. Ag/AgCl (0.940 V vs. RHE) and the current at the onset potential for oxygen reduction.

5) Mass and charge balance analysis using RRDE: For the mass and charge balance analysis using rotating ring disk electrode (RRDE), the SWNT/AuNC/BOD composite was drop cast on electrode surface, dried, and the ORR activity was measured in 100 mM phosphate buffer at pH 7. Using a bipotentiostat (Pine Instruments), the disk current was swept from 0.800 to 0 V at a scan rate of 10 mV/s while the ring was polarized at 0.800 V. Data analysis was performed according to Eq. 1.

References

(1) a) Qiao, Y.; Li, C. M. J. Mater. Chem. 2011, 21, 4027-4036; b) Zhou, M.; Wang, J. Electroanalysis 2012, 24, 197-209; c) Zebda, A.; Gondran, C.; Le Goff, A.; Holzinger, M.; Cinquin, P.; Cosnier, S. Nat. Commun. 2011, 2, 370; d) Holzinger, M.; Le Goff, A.; Cosnier, S. Electrochim. Acta 2012, 82, 179-190; e) Katz, E.; MacVittie, K. Energy & Environmental Science 2013, 6, 2791-2803; f) Halámková, L.; Halámek, J.; Bocharova, V.; Szczupak, A.; Alfonta, L.; Katz, E. J. Am. Chem. Soc. 2012, 134, 5040-5043; g) Zafar, M. N.; Beden, N.; Leech, D.; Sygmund, C.; Ludwig, R.; Gorton, L. Anal. Bioanal. Chem. 2012, 402, 2069-2077; h) Harreither, W.; Felice, A. K.; Paukner, R.; Gorton, L.; Ludwig, R.; Sygmund, C. Biotechnol. J. 2012, 7, 1359-1366; i) Jia, W.; Valdés-Ramírez, G.; Bandodkar, A. J.; Windmiller, J. R.; Wang, J. Angew. Chem. Int. Ed. 2013, 52, 7233-7236; j) Chen, X.; Li, C.; Grätzel, M.; Kostecki, R.; Mao, S. S. Chem. Soc. Rev. 2012, 41, 7909-7937.

(2) a) Davis, F.; Higson, S. P. Biosens. Bioelectron. 2007, 22, 1224-1235; b) Minteer, S. D.; Liaw, B. Y.; Cooney, M. J. Curr. Opin. Biotechnol. 2007, 18, 228-234; c) Bullen, R. A.; Arnot, T.; Lakeman, J.; Walsh, F. Biosens. Bioelectron. 2006, 21, 2015-2045.

(3) Aricò, A. S.; Bruce, P.; Scrosati, B.; Tarascon, J.-M.; Van Schalkwijk, W. Nat. Mater. 2005, 4, 366-377.

(4) Holland, J. T.; Lau, C.; Brozik, S.; Atanassov, P.; Banta, S. J. Am. Chem. Soc. 2011, 133, 19262-19265.

(5) a) Shang, L.; Dong, S.; Nienhaus, G. U. Nano Today 2011, 6, 401-418; b) Lin, C.-A. J.; Lee, C.-H.; Hsieh, J.-T.; Wang, H.-H.; Li, J. K.; Shen, J.-L.; Chan, W.-H.; Yeh, H.-I.; Chang, W. H. J. Med. Biol. Eng. 2009, 29, 276-283; c) Lin., C.-A. J.; Yang, T.-Y.; Lee, C.-H.; Huang, S. H.; Sperling, R. A.; Zanella, M.; Li, J. K.; Shen, J.-L.; Wang, H.-H.; Yeh, H.-I.; Parak, W. J.; Chang, W. H. ACS Nano 2009, 3, 395-401; d) Li, G.; Jin, R. Acc. Chem. Res. 2013, 46, 1749-1758; e) Wilcoxon, J.; Abrams, B. Chem. Soc. Rev. 2006, 35, 1162-1194; f) Link, S.; Beeby, A.; FitzGerald, S.; El-Sayed, M. A.; Schaaff, T. G.; Whetten, R. L. J. Phys. Chem. B 2002, 106, 3410-3415; g) Proch, S.; Wirth, M.; White, H. S.; Anderson, S. L. J. Am. Chem. Soc. 2013, 135, 3073-3086.

(6) a) Murray, R. W. Chem. Rev. 2008, 108, 2688-2720; b) Walter, M.; Akola, J.; Lopez-Acevedo, O.; Jadzinsky, P. D.; Calero, G.; Ackerson, C. J.; Whetten, R. L.; Grönbeck, H.; Häkkinen, H. Proc. Natl. Acad. Sci. USA 2008, 105, 9157-9162; c) Jadzinsky, P. D.; Calero, G.; Ackerson, C. J.; Bushnell, D. A.; Kornberg, R. D. Science 2007, 318, 430-433; d) Zeng, C.; Qian, H.; Li, T.; Li, G.; Rosi, N. L.; Yoon, B.; Barnett, R. N.; Whetten, R. L.; Landman, U.; Jin, R. Angew. Chem. 2012, 124, 13291-13295; e) Lee, D.; Donkers, R. L.; Wang, G.; Harper, A. S.; Murray, R. W. J. Am. Chem. Soc. 2004, 126, 6193-6199.

(7) Hammer, B.; Norskov, J. Nature 1995, 376, 238-240.

(8) a) Haruta, M.; Daté, M. Appl. Catal., A 2001, 222, 427-437; b) Haruta, M. Catal. Today 1997, 36, 153-166.

(9) a) Boccuzzi, F.; Cerrato, G.; Pinna, F.; Strukul, G. J. Phys. Chem. B 1998, 102, 5733-5736; b) Hayden, B. E.; Pletcher, D.; Suchsland, J. P. Angew. Chem. Int. Ed. 2007, 46, 3530-3532; c) Valden, M.; Lai, X.; Goodman, D. W. Science 1998, 281, 1647-1650; d) Hernández, J.; Solla-Gullón, J.; Herrero, E.; Aldaz, A.; Feliu, J. M. J. Phys. Chem. C 2007, 111, 14078-14083; e) Mohr, C.; Hofmeister, H.; Radnik, J.; Claus, P. J. Am. Chem. Soc. 2003, 125, 1905-1911; f) Hughes, M. D.; Xu,

Y.-J.; Jenkins, P.; McMorn, P.; Landon, P.; Enache, D. I.; Carley, A. F.; Attard, G. A.; Hutchings, G. J.; King, F.; Stitt, E. H.; Johnston, P.; Griffin, K.; Kiely, C. J. Nature 2005, 437, 1132-1135.

(10) van Bokhoven, J. A.; Miller, J. T. J. Phys. Chem. C 2007, 111, 9245-9249.

(11) Tang, W.; Lin, H.; Kleiman-Shwarsctein, A.; Stucky, G. D.; McFarland, E. W. J. Phys. Chem. B 2008, 112, 10515-10519.

(12) Herzing, A. A.; Kiely, C. J.; Carley, A. F.; Landon, P.; Hutchings, G. J. Science 2008, 321, 1331-1335.

(13) a) Zhu, Y.; Qian, H.; Zhu, M.; Jin, R. Adv. Mater. 2010, 22, 1915-1920; b) Liu, Y.; Tsunoyama, H.; Akita, T.; Xie, S.; Tsukuda, T. ACS Catal. 2010, 1, 2-6; c) Xie, S.; Tsunoyama, H.; Kurashige, W.; Negishi, Y.; Tsukuda, T. ACS Catal. 2012, 2, 1519-1523.

(14) Zhu, Y.; Qian, H.; Drake, B. A.; Jin, R. Angew. Chem. Int. Ed. 2010, 49, 1295-1298.

(15) Kauffman, D. R.; Alfonso, D.; Matranga, C.; Qian, H.; Jin, R. J. Am. Chem. Soc. 2012, 134, 10237-10243.

(16) Chen, W.; Chen, S. Angew. Chem. Int. Ed. 2009, 48, 4386-4389.

(17) a) Wu, Z.; Jin, R. Nano Lett. 2010, 10, 2568-2573; b) Xie, J.; Zheng, Y.; Ying, J. Y. J. Am. Chem. Soc. 2009, 31, 888–889.

(18) a) Petty, J. T.; Zheng, J.; Hud, N. V.; Dickson, R. M. J. Am. Chem. Soc. 2004, 126, 5207-5212; b) Zheng, J.; Nicovich, P. R.; Dickson, R. M. Annu. Rev. Phys. Chem. 2007, 58, 409-431; c) O'Neill, P. R.; Velazquez, L. R.; Dunn, D. G.; Gwinn, E. G.; Fygenson, D. K. J. Phys. Chem. B 2009, 113, 4229-4233; d) Schultz, D.; Gwinn, E. G. Chem. Commun. 2012, 48, 5748-5750; e) Sharma, J.; Rocha, R. C.; Phipps, M. L.; Yeh, H. C.; Balatsky, K. A.; Vu, D. M.; Shreve, A. P.; Werner, J. H.; Martinez, J. S. Nanoscale 2012, 4, 4107-4110; f) Sharma, J.; Yeh, H.-C.; Yoo, H.; Werner, J. H.; Martinez, J. S. Chem. Commun. 2010, 46, 3280-3282; g) Yeh, H. C.; Sharma, J.; Han, J. J.; Martinez, J. S.; Werner, J. H. Nano Lett. 2010, 10, 3106-3110.

(19) Jia, X.; Li, J.; Han, L.; Ren, J.; Yang, X.; Wang, E. ACS Nano 2012, 6, 3311-3317.

(20) a) Seidel, R.; Colombi Ciacchi, L.; Weigel, M.; Pompe, W.; Mertig, M. J. Phys. Chem. B 2004, 108, 10801-10811; b) Tiwari, J. N.; Nath, K.; Kumar, S.; Tiwari, R. N.; Kemp, K. C.; Le, N. H.; Youn, D. H.; Lee, J. S.; Kim, K. S. Nat. Commun. 2013, 4, 2221.

(21) Zhu, Y.; Qian, H.; Jin, R. J. Mater. Chem. 2011, 21, 6793.

(22) a) Pinheiro, A. V.; Han, D.; Shih, W. M.; Yan, H. Nat. Nanotech. 2011, 6, 763-772; b) Seeman, N. C. Mol. Biotechnol. 2007, 37, 246-257.

(23) Mertig, M.; Colombi Ciacchi, L.; Seidel, R.; Pompe, W.; De Vita, A. Nano Lett. 2002, 2, 841-844.

(24) a) Kennedy, T. A.; MacLean, J. L.; Liu, J. Chem. Commun. 2012, 48, 6845-6847; b) Liu, G.; Shao, Y.; Ma, K.; Cui, Q.; Wu, F.; Xu, S. Gold Bull. 2012, 45, 69-74; c) Liu, G.; Shao, Y.; Wu, F.; Xu, S.; Peng, J.; Liu, L. Nanotechnology 2013, 24, 015503.

(25) a) Solomon, E. I.; Heppner, D. E.; Johnston, E. M.; Ginsbach, J. W.; Cirera, J.; Qayyum, M.; Kieber-Emmons, M. T.; Kjaergaard, C. H.; Hadt, R. G.; Tian, L. Chem. Rev. 2014, 114, 3659-3853; b)

Liu, J.; Chakraborty, S.; Hosseinzadeh, P.; Yu, Y.; Tian, S.; Petrik, I.; Bhagi, A.; Lu, Y. Chem. Rev. 2014, 114, 4366-4469.

(26) Ivnitski, D. M.; Khripin, C.; Luckarift, H. R.; Johnson, G. R.; Atanassov, P. Electrochim. Acta 2010, 55, 7385-7393.

(27) a) Luo, Z.; Yuan, X.; Yu, Y.; Zhang, Q.; Leong, D. T.; Lee, J. Y.; Xie, J. J. Am. Chem. Soc. 2012, 134, 16662-16670; b) Negishi, Y.; Nobusada, K.; Tsukuda, T. J. Am. Chem. Soc. 2005, 127, 5261-5270.

(28) Yang, Y.; Chen, S. Nano Lett. 2003, 3, 75-79.

(29) a) Menard, L. D.; Xu, H.; Gao, S.-P.; Twesten, R. D.; Harper, A. S.; Song, Y.; Wang, G.; Douglas, A. D.; Yang, J. C.; Frenkel, A. I. J. Phys. Chem. B 2006, 110, 14564-14573; b) Menard, L. D.; Gao, S.-P.; Xu, H.; Twesten, R. D.; Harper, A. S.; Song, Y.; Wang, G.; Douglas, A. D.; Yang, J. C.; Frenkel, A. I. J. Phys. Chem. B 2006, 110, 12874-12883.

(30) Zheng, J.; Petty, J. T.; Dickson, R. M. J. Am. Chem. Soc. 2003, 125, 7780-7781.

(31) a) Jaw, H. R. C.; Mason, W. R. Inorg. Chem. 1991, 30, 275-278; b) Hall, K. P.; Theoblad, B. R. C.; Gilmour, D. I.; Mingos, D. M. P.; Welch, A. J. J. Chem. Soc., Chem. Commun. 1982, 528-530; c) Bartlett, P. A.; Bauer, B.; Singer, S. J. Am. Chem. Soc. 1978, 100, 5085-5089.

(32) Zheng, J.; Zhang, C.; Dickson, R. M. Phys. Rev. Lett. 2004, 93, 077402.

(33) a) Ramasamy, P.; Guha, S.; Shibu, E. S.; Sreeprasad, T. S.; Bag, S.; Banerjee, A.; Pradeep, T. J. Mater. Chem. 2009, 19, 8456-8462; b) Levi-Kalisman, Y.; Jadzinsky, P. D.; Kalisman, N.; Tsunoyama, H.; Tsukuda, T.; Bushnell, D. A.; Kornberg, R. D. J. Am. Chem. Soc. 2011, 133, 2976-2982.

(34) Qian, H.; Jin, R. Chem. Mater. 2011, 23, 2209-2217.

(35) Petty, J. T.; Fan, C.; Story, S. P.; Sengupta, B.; Iyer, A. S.; Prudowsky, Z.; Dickson, R. M. J. Phys. Chem. Lett. 2010, 1, 2524-2529.

(36) a) Santiago Gonzalez, B.; Rodriguez, M. J.; Blanco, C.; Rivas, J.; Lopez-Quintela, M. A.; Gaspar Martinho, J. M. Nano Lett. 2010, 10, 4217-4221; b) Guliamov, O.; Frenkel, A. I.; Menard, L. D.; Nuzzo, R. G.; Kronik, L. J. Am. Chem. Soc. 2007, 129, 10978-10979.

(37) a) Sengupta, B.; Ritchie, C. M.; Buckman, J. G.; Johnsen, K. R.; Goodwin, P. M.; Petty, J. T. J. Phys. Chem. C 2008, 112, 18776-18782; b) Ritchie, C. M.; Johnsen, K. R.; Kiser, J. R.; Antoku, Y.; Dickson, R. M.; Petty, J. T. The Journal of Physical Chemistry C 2007, 111, 175-181; c) Neidig, M. L.; Sharma, J.; Yeh, H.-C.; Martinez, J. S.; Conradson, S. D.; Shreve, A. P. J. Am. Chem. Soc. 2011, 133, 11837-11839; d) Duguid, J.; Bloomfield, V. A.; Benevides, J.; Thomas Jr, G. J. Biophys. J. 1993, 65, 1916.

(38) a) Yam, V. W. W.; Cheng, E. C. C.; Zhou, Z. Y. Angew. Chem. Int. Ed. 2000, 39, 1683-1685; b) White-Morris, R. L.; Olmstead, M. M.; Jiang, F.; Tinti, D. S.; Balch, A. L. J. Am. Chem. Soc. 2002, 124, 2327-2336; c) Cha, S.-H.; Kim, J.-U.; Kim, K.-H.; Lee, J.-C. Chem. Mater. 2007, 19, 6297-6303.

(39) Brouwer, A. M. Pure and Appl. Chem. 2011, 83, 2213-2228.

(40) Huang, T.; Murray, R. W. J. Phys. Chem. B 2001, 105, 12498-12502.

(41) Negishi, Y.; Tsukuda, T. Chem. Phys. Lett. 2004, 383, 161-165.

(42) Bigioni, T.; Whetten, R.; Dag, Ö. J. Phys. Chem. B 2000, 104, 6983-6986.

(43) Chen, S.; Wang, S.; Zhong, J.; Song, Y.; Zhang, J.; Sheng, H.; Pei, Y.; Zhu, M. Angew. Chem. Int. Ed. 2015, 54, 3145-3149.

(44) Garcia-Raya, D.; Madueno, R.; Blazquez, M.; Pineda, T. J. Phys. Chem. C. 2009, 113, 8756-8761.

(45) Qian, H.; Zhu, Y.; Jin, R. ACS Nano 2009, 3, 3795-3803.

(46) Nimmala, P. R.; Yoon, B.; Whetten, R. L.; Landman, U.; Dass, A. J. Phys. Chem. A 2013, 117, 504-517.

(47) Zanello, P. Inorganic Electrochemistry: Theory, Practice, and Application; Royal Society of Chemistry, 2003.

(48) Moore, C. M.; Akers, N. L.; Hill, A. D.; Johnson, Z. C.; Minteer, S. D. Biomacromolecules 2004, 5, 1241-1247.

(49) Gupta, G.; Lau, C.; Rajendran, V.; Colon, F.; Branch, B.; Ivnitski, D.; Atanassov, P. Electrochem. Commun. 2011, 13, 247-249.

(50) Shleev, S.; El Kasmi, A.; Ruzgas, T.; Gorton, L. Electrochem. Commun. 2004, 6, 934-939.

(51) a) Ramasamy, R. P.; Luckarift, H. R.; Ivnitski, D. M.; Atanassov, P. B.; Johnson, G. R. Chem. Commun. 2010, 46, 6045-6047; b) Weigel, M. C.; Tritscher, E.; Lisdat, F. Electrochem. Commun. 2007, 9, 689-693.

(52) Wang, C.; Daimon, H.; Onodera, T.; Koda, T.; Sun, S. Angew. Chem. Int. Ed. 2008, 47, 3588-3591.

(53) a) Chen, Z.; Waje, M.; Li, W.; Yan, Y. Angew. Chem. Int. Ed. 2007, 46, 4060-4063; b) Seo, M. H.; Choi, S. M.; Kim, H. J.; Kim, W. B. Electrochem. Commun. 2011, 13, 182-185; c) Lim, B.; Jiang, M.; Camargo, P. H.; Cho, E. C.; Tao, J.; Lu, X.; Zhu, Y.; Xia, Y. science 2009, 324, 1302-1305.

(54) Liang, Y.; Li, Y.; Wang, H.; Zhou, J.; Wang, J.; Regier, T.; Dai, H. Nature materials 2011, 10, 780-786.

(55) a) Hsueh, K. L.; Chin, D. T.; Srinivasan, S. J. Electroanal. Chem. Interf. Electrochem. 1983, 153, 79-95; b) Brett, C. M. A.; Brett, A. M. O. Electrochemistry Principles, Methods and Applications; Oxford University Press Inc.: New York, NY, 1993.

(56) Pine Research Instrumentation E7 Series ThinGap RRDEs Dimensions, R.; NC.

(57) Brocato, S.; Lau, C.; Atanassov, P. Electrochim. Acta 2012, 61, 44-49.

(58) Williams, A. T. R.; Winfield, S. A.; Miller, J. N. Analyst 1983, 108, 1067-1071.

(59) Bard, A. J.; Faulkner, L. R. Electrochemical methods: fundamentals and applications; Wiley New York, 1980; Vol. 2.

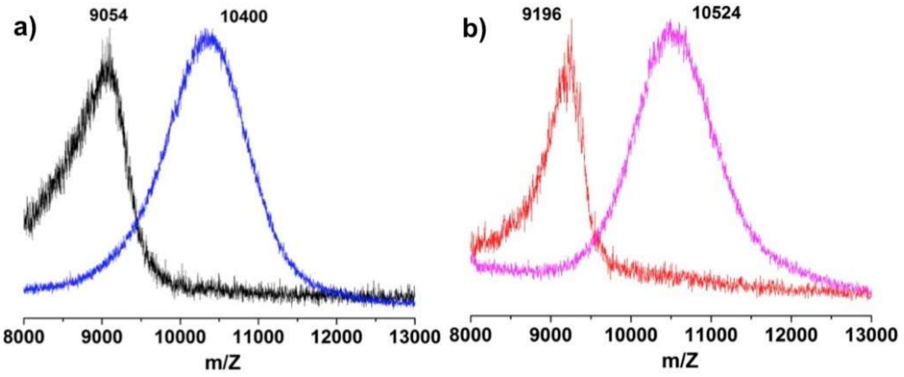

Figure S1. MALDI-MS of DNA and AuNC in sinapinic acid matrix measured in negative a) and positive b) ionization modes. After subtracting the molecular weight of corresponding DNA the number of Au atoms was calculated to be 6.8 and 6.7, respectively indicating ~7 Au atom cluster.

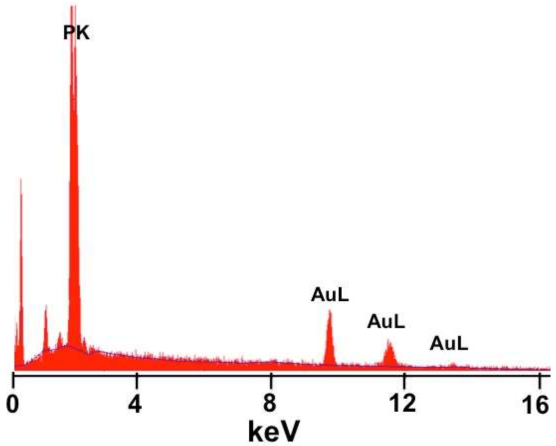

Figure S2. Representative EDX data showing the PK and AuL lines of the AuNC synthesized in 50 mM NH4OAc, 1mM Mg(OAc)2, pH 5.5 and dried on carbon tape. Background signal was corrected before quantifying the atomic percentage of P (59.2%) and Au (14%) from the intensities of P Kα (2.013 keV) and Au Lα (9.712 keV) lines. The total atomic % of P was then divided by the number of P groups present in DNA, which is 31 in this case. Thus, 1.9 DNA molecules were calculated (59.2/31). Since there is one DNA molecule that forms the AuNC, the atomic% of Au was normalized to 1 DNA molecule (14/1.9 = 7.4), yielding the Au:DNA ratio of 7.4±1.0 (standard deviation obtained from 4 independent sample preparations). A similar estimate of cluster size was obtained from MALDI-MS.

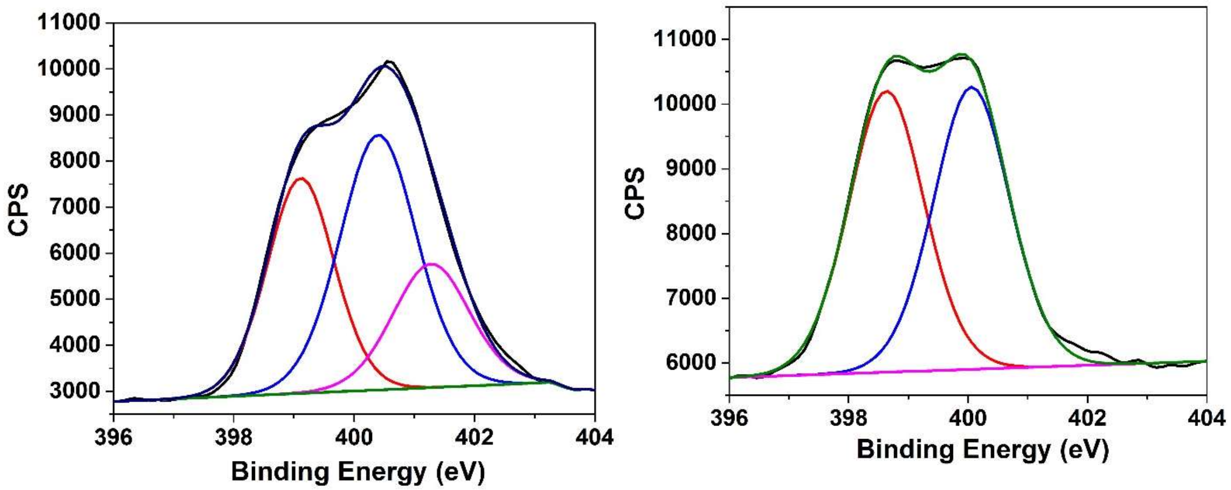

Figure S3. N 1sS XPS data of DNA (top), and AuNC (bottom). For DNA black curve: experimental data; dark blue curve: fit; red, blue, and purple curves: individual deconvoluted components; green line: background. For AuNC: black curve: experimental data; green curve: fit; blue and red curves: individual deconvoluted components; purple line: background. It can be clearly seen that the relative% of amine (398.8 eV), and amide (400.3 eV) peaks changes between the DNA and the AuNC samples. Additionally, the protonated nitrogen species (401.3 eV) also changes in the AuNC sample compared to DNA.

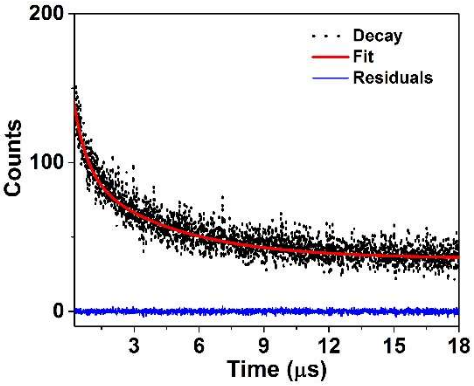

Figure S4. Luminescence lifetime decay curves of ~1 mM solution of AuNC in 20 mM phosphate buffer, 1 mM Mg(OAc)2, pH 7. Data was fit to a bi-exponential function. From this analysis, the lifetimes were obtained to be 4.2 μs and 0.6 μs with relative amplitudes of 89% and 11%, respectively.

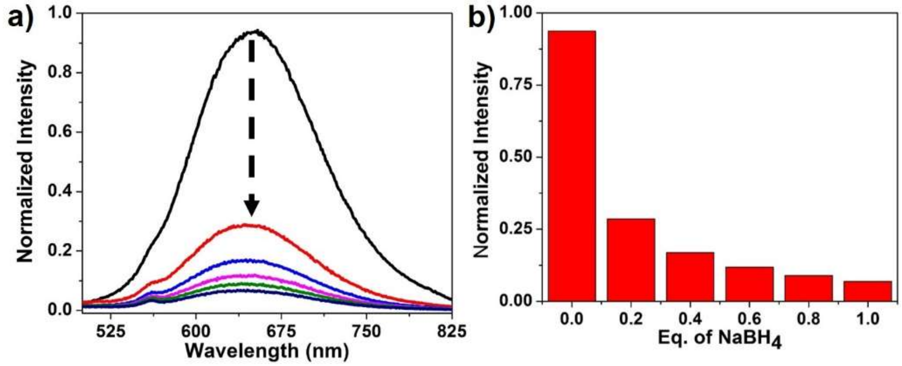

Figure S5. Effect of NaBH4 on the luminescence of the AuNC. Addition of up to 1 equivalents of NaBH4 to a solution of ~1 mM AuNC (a) in 20 mM phosphate buffer, 1 mM Mg(OAc)2 causes ~90% decrease in the luminescence emission of AuNC as shown in bar graph (b). This observation is attributed to the reduction of surface Au(I) present in the AuNC and suggests the importance of surface Au(I) in the resulting luminescence.

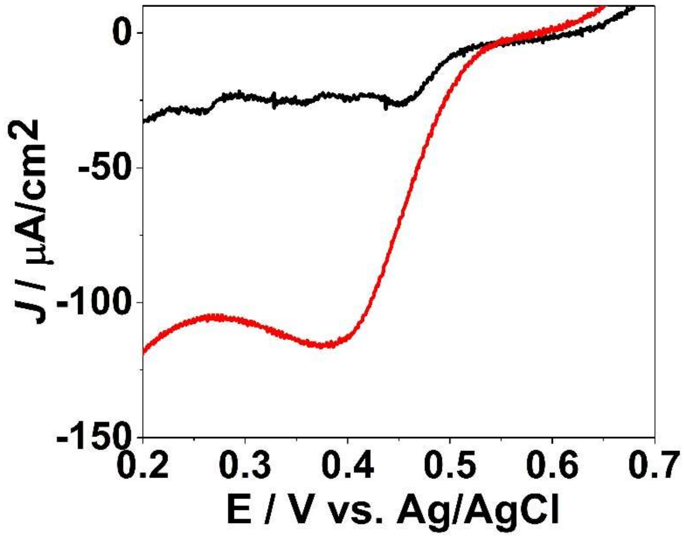

Figure S6. LSVs of AuNC/SWNT/BOD composite in O2-depleted (black line, trace amounts of O2), and dissolved O2 (red line) in 0.1 M phosphate buffer (pH 7.5) obtained at a scan rate of 10 mV/s and electrode rotation rate of 1600 rpm. An onset potential of ~0.510 V, E1/2 of ~0.460 V vs. Ag/AgCl, and electrochemical current density of ~96 μA/cm2 was measured from the dissolved O2 data. The current densities decreased below ~0.4 V as the reaction was limited by the availability of O2 in the electrolyte solution.

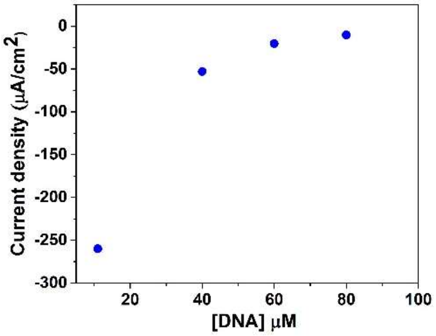

Figure S7. Effect of DNA concentration on current density (derived from LSV measurements with 10mV/s; electrode rotation rate = 1600 rpm).of SWNT/DNA/BOD composite materials in O2-saturated 0.1M phosphate buffer pH 7.5.

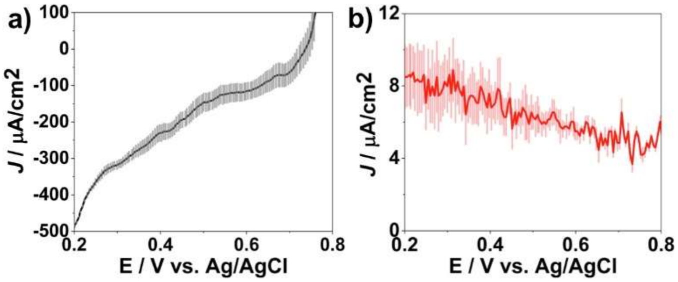

Figure S8. Rotating ring disk electrode (RRDE) measurements of SWNT/AuNC/BOD composites performed in O2-saturated 0.1 M phosphate buffer, pH 7.5. Disk potential was swept from 0.8 V to 0 V while the ring was held at a constant potential of 0.8 V vs. Ag/AgCl. Resulting disk and ring currents are shown in a) and b) respectively. Shaded areas represent standard deviation from three independent measurements.

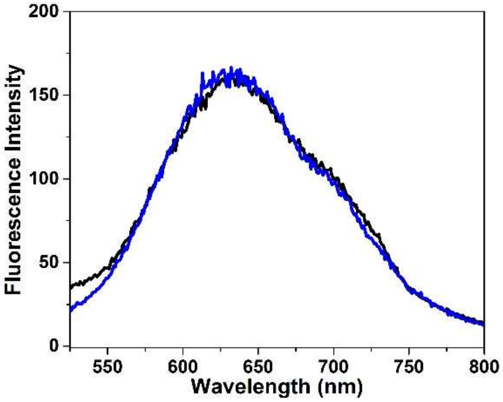

Figure S9. Emission spectra of solutions containing the AuNC (blue curve), and AuNC mixed with SWNTs/TBAB-Nafion (black curve) collected with photo excitation at 470 nm. Similar emission peak maxima confirm that the presence of SWNTs/TBAB-Nafion does not perturb the integrity of the AuNC.

Electrochemical Enhancement of Small Laccase DNA Complex with DNA-Templated Gold Nanoclusters

1. Introduction

In the face of today's rapidly growing energy demands accompanied by limited, non-renewable supplies, development of novel energy alternatives that are both renewable and inexpensive has become more important than ever. Researches have explored the use of nanoscale materials and biomolecules as potential alternatives to established energy technologies [1, 2]. Combining redox enzymes with various nanomaterials has been an extensively studied aspect of biomimetic energy for many years and has shown great promise in replacing current technology. In contrast to traditional fuel cells, which use metals such as platinum for catalysis, enzymatic fuel cells (EFCs) use both oxidizing and reducing enzymes at the anode and cathode surfaces, respectively. There are several benefits to EFCs such as renewability, use of inexpensive fuel and catalyst, high level of selectivity towards fuel, mild pH and temperature operating conditions (pH 5-8, 25-27°C), and lack of fuel crossover and poisoning [3, 4]. Therefore, EFCs appear to be an attractive alternative to conventional energy means. However, EFCs still suffer from several problems including low efficiency and stability [5, 6]. Overcoming these limitations in order to make them more viable for potential applications is an ongoing challenge for researchers.

Finding proper immobilization strategies that will not negatively affect the structural integrity of the enzyme(s) over time or interfere with the electron transfer between enzymes' active centers and the electrode surface continues to be a challenging aspect of developing efficient and stable enzymatic fuel cells. Immobilization of enzymes is advantageous in EFC when compared to free enzymes since the immobilization of the enzyme reduces electron loss; yields higher recovery rates and often times results in improved stability of the enzyme under electrocatalytic conditions [7, 8]. Single or multiples enzymes are often immobilized on various nanomaterials through physical adsorption either directly to the material or in concert with polymers [9, 10 11], bio-molecules [12-14], surfactants, or by tethering [15]. Carbon nanotubes (CNTs) in particular are an ideal material for enzyme immobilization due of their high surface to volume ratio, comparable size to enzymes and their interesting electronic properties [16-20].

One challenging aspect associated with EFCs is the low power density that results from single enzyme utilization. Therefore, novel methods for multi-enzyme cascades (MECs) must be developed and implemented to remove this drawback. Metabolic processes observed in nature carry out complex fuel oxidation and reduction reactions through the use of MECs. The capability to reproduce these processes would help to ensure high-level of fuel processing and allow for highly efficient and stable EFCs [3, 21-23]. Complete fuel oxidation using MECs was first reported by Palmore et al. [24] where the complete oxidation of methanol to carbon dioxide was carried out via a system of alcohol dehydrogenase, aldehyde dehydrogenase and formate dehydrogenase. Since then, methods for MEC development and improved EFC performance have been extensively studied [21, 23, 25]; however researchers are yet to develop EFCs that match stability and performance of conventional fuel cells.

Immobilization of artificially produced MECs require methods that direct enzyme orientation in such a way that reduces diffusion losses by creating efficient catalytic pathways, much like in nature [22]. This cannot be achieved using nanotubes alone where, during immobilization the enzyme orientation could not be controlled and is highly dependent on the properties of the enzymes themselves. One possible method, DNA directed self-assembly, has shown to not only alleviate many stability issues but allow for regulation of enzyme orientation and position from one enzyme to the next [21]. Additionally, transcription factors called zinc fingers (ZnFs) have been commonly used for specific DNA-binding of biomolecules. As a result of their highly selective DNA binding capability to given DNA sequences and the customization of the DNA-binding domain, ZnFs are ideal for use in controlled enzyme immobilization [26-30]. In our previous study, we explored the concept of zinc finger binding with DNA/CNT scaffolds as a possible method for enzyme immobilization catalyzing oxygen reduction reaction (ORR) [31]. Multi-copper oxidases (MCOs) are the most commonly used enzymes for catalyzing enzymatic ORR. One enzyme in particular, small laccase (SLAC), was chosen as a proof of concept for single enzyme immobilization due to its high thermal and pH stability (up to pH 9.4), and high catalytic activity [32-34]. The genetic engineering of trimeric SLAC fused with the three zinc finger domains (SLAC-3ZnF), specifically ZnF268 has allowed for controlled docking of the enzyme conjugate with DNA [31, 35]. The position of the SLAC active centers in the protein molecule and the presence of ZnF for the immobilization do not allow rapid electron transfer from the electrode surface to the T1 center of the enzyme and thus limits the electrochemical efficiency of the system. Therefore, to decrease the electron transfer tunneling distance and improve the electron transfer rate in this study we explored the addition of metal nanoparticles to the SLAC-ZnF conjugate. The metal particles are bound to sequence specific DNA constructs to be recognized by SLAC-bound zinc finger domains.

In this study, we have incorporated the use of gold nanoclusters (AuNCs) as means for enhanced electron transfer and overall improved EFC performance with ZnF directed immobilization of SLAC on DNA-CNT architecture (**Error! Reference source not found.**). Although bulk gold is inert, gold nanoparticles (AuNPs) have been shown to act as catalysts in several reductive reactions including ORR [36-42]. It was recently reported that a DNA-templated AuNC (D3AuNC) on CNT facilitated the electron transfer during bilirubin oxidase catalyzed reduction of O_2 to H_2O [43]. The goal of this research was to develop a stable architecture for SLAC-3ZnF binding in the presence of DNA-templated AuNCs and demonstrate improved electron transfer and therefore higher ORR rate. The AuNCs were synthesized using the DNA template (D3). A ZnF recognition sequence was hybridized at the DNA sequence (D3ZnF-ZnFH), and poly T tails at both ends were used for CNT wrapping. The resulting product (D3ZnF-ZnFH-AuNC) was immobilized on SWNTs and used for SLAC-3ZnF attachment.

We believe enzyme immobilization in this manner will lead to future multi-enzyme cascade development that would allow for very controlled and customizable systems for two or more enzymes. The latter will allow the design of systems with maximized power densities and lower overpotential for electrocatalysis. Herein we demonstrate that the D3AuNCs, when co-assembled with SLAC-3ZnF and SWNTs, improve both the ORR reaction kinetics and electron transfer from the electrode to the active site of SLAC.

2. Materials and Methods

2.1 Reagents

HDPlas™ single-wall/double-wall carbon nanotubes 99 wt% (diameter = 1-2 nm, length = 3-30µm) were purchased from cheaptubes.com. Custom oligomer sequences were ordered from Integrated DNA Technologies, Inc. Tetrabutylammonium bromide (TBAB-Nafion) was provided by Professor Shelley Minteer (University of Utah, Salt Lake City, UT). Lyophilized SLAC-3ZNF was expressed and purified as previously reported [31].

Synthesis and purification of DNA-templated AuNC containing zinc finger recognition sequence

We designed a DNA sequence bearing the NC forming sequence, ZnF recognition sequence, and poly-T tails to enhance wrapping of the DNA with CNTs. The full-length sequence thus designed is represented as D3D$_Z$:

5'-TTTTTTTTTTTTTTTTTTTTTTTTTTTTTTACCCGAACCTGGGCTACCACCCTTAAT
CCCCCGCACCCGCTTTTTTTTTTTTTTTTTTTTTTTTTTTTTT-3'

where the nanocluster forming sequence, as reported previously, [43] is shown in red, and the zinc finger recognition sequence in blue. We employed two approaches to synthesize the NC. In one approach we first synthesized the NC with D3D$_Z$ followed by subsequent hybridization of D3D$_Z$NC with the complimentary zinc finger recognition sequence H: 5'-GCGGGTGCG-3' (T_m = 43.8°C). The hybridized sequence containing the cluster is represented here as D3D$_Z$NCH, implying that first the NC is synthesized with D3D$_Z$, followed by hybridization. In the second approach, we first hybridized the zinc finger sequence followed by NC synthesis. The final cluster sample thus prepared is represented as D3D$_Z$HNC.

2.2.1 Preparation of D3D$_Z$NCH

For AuNC synthesis, 15 µM D3D$_Z$ was equilibrated with 225 µM $HAuCl_4.3H_2O$ (Sigma-Aldrich, ≥ 99% trace metal basis) for ~18 h in 20 mM phosphate buffer pH 7 and 1 mM $Mg(OAc)_2$ (Fisher Scientific) solution at 22°C. Upon equilibration, the solution color changed from colorless to light yellow. Cluster formation was initiated by addition of 2.25 mM dimethylamine borane (Sigma-Aldrich) as reducing agent followed by equilibration for additional 18 h at 22°C. At the end a light purple color solution was formed which was purified by spin filtration through 50 kDa MWCO membranes (Millipore). The light purple solution was retained in the membrane indicating the presence of a small amount of plasmonic Au particles. Pure NC was obtained as a light yellow color solution in the filtrate. An equimolar solution containing 91 μM D3D$_Z$NC and H (concentrations determined based on $\varepsilon_{260} = 838.1$ mM^{-1}cm^{-1} of D3D$_Z$ and 83.9 mM^{-1}cm^{-1} for H as provided by IDT) was hybridized by heating the mixture at 80°C for 5 min in hybridization buffer (30 mM HEPES pH 7.5, 100 mM KOAc) followed by slow cooling to 4°C. The final hybridized solution was then buffer exchanged to 20 mM phosphate buffer pH 7 with 1 mM Mg(OAc)$_2$ using 10 kDa MWCO membranes and stored at 4°C until further use.

2.2.2 Preparation of D3D$_Z$HNC

The hybridization of D3D$_Z$ and H was performed as described above. After hybridization, the sample was buffer exchanged to 20 mM phosphate buffer pH 7 with 1 mM Mg(OAc)$_2$. Synthesis and purification of NC was performed using similar conditions as described above except that this time the temperature was maintained at 4°C to ensure that the hybridization is maintained at all times during cluster synthesis.

2.3 SLAC-3ZnF Control Composites

Two control composites without NC were made in order to observe the effect of the NC on enhancing the electro-catalytic activity of SLAC-3ZnF represented by SZ$_3$ (**Table 5**) with and without the zinc finger recognition sequence.

2.3.1. SWNTs mixture

All samples were made with a mixture of 1.5% SWNT and 0.1% TBAB-Nafion in a 4:1 water to EtOH. The SWNT suspension was sonicated for 30 minutes to disperse the tubes. SLAC-3ZnF was suspended at an initial 67mg/ml in 0.01M potassium phosphate buffer (pH 7.5) for use in all samples.

2.3.2. Preparation of SLAC-3ZnF on SWNT-TBAB scaffold

SLAC-3ZnF immobilized through direct adsorption on SWNT was prepared with 10μl SLAC-3ZnF and 40μl SWNT mixture described above. Samples were allowed to incubate for 24 h at 4°C prior to testing.

2.3.3. Preparation of SLAC-3ZnF with Zinc Finger DNA Recognition Sequence

For control samples with DNA but no NC, we designed DNA with the zinc finger recognition sequence and poly T tails for efficient wrapping of CNTs. The sequence is represented by D$_Z$:

5'-TTTTTTTTTTTTTTTTTTTTTTTTCGCCCACGCTTTTTTTTTTTTTTTTTTTTTTT-3'

where zinc finger sequence is in blue. The sequence was hybridized with the complimentary H 5'-GCGTGGGCG-3'. The resulting hybrid is represented by D$_Z$H. DNA was stored at 4°C until ready for use. 5μl of D$_Z$H (10 mg/ml) was then suspended with 40μl of SWNT mixture, gently mixed and allowed to equilibrate for 12 hours at 4°C. 10μl SLAC-3ZnF was added to the suspension and left to incubate for 24 hours at 4°C. The final molar concentrations of DNA and SLAC-3ZnF were approximately 51.45 and 243.99 μM, respectively.

2.4 Development of SLAC-3ZnF Composites with NC

Samples containing NC with and without zinc finger recognition sequence were prepared to compare the effect of the recognition sequence on directing the SLAC-3ZnF to the DNA-NC and the resulting electrocatalytic performance of the composite. All samples were prepared with 1.5% SWNT 0.1% TBAB-Nafion mixture (initial concentration) and 67mg/ml (initial concentration) SLAC-3ZnF suspensions prepared as the control samples.

2.4.1 Preparation of SLAC-3ZnF with D3NC

We first combined 5 μl D3NC with a 40 μl SWNT mixture and left to allow for D3NC to attach to the nanotubes for 12 hours at 4°C before adding 10 μl SLAC-3ZnF suspension. Samples were left to incubate overnight for 24 hours at 4°C.

2.4.2 Preparation of SLAC-3ZnF with D3D$_Z$NCH

Samples containing zinc finger recognition sequences hybridized prior to NC synthesis were made by first mixing 5μl D3D$_Z$NCH with 40μl SWNT mixture and left for 12 hours at 4°C. 10μl SLAC-3ZnF was then added to each samples and allowed to incubate for 24 hours at 4°C.

2.4.3 Preparation of SLAC-3ZnF with D3D$_Z$HNC

Samples containing zinc finger recognition sequences hybridized after NC synthesis were made by first mixing either 5μl D3D$_Z$HNC with 40μl SWNT mixture and left for 12 hours at 4°C. 10μl SLAC-3ZnF was added to each samples and allowed to incubate for 24 hours at 4°C.

2.5 MALDI-MS

MALDI-MS data were collected on ABSciex 4800 Plus TOF/TOF MALDI mass spectrometer using sinapinic acid (Sigma-Aldrich) as the matrix. Molecular weight of D3D$_Z$NC sample was determined to be ~32221 Da indicating the formation of ~10 atom gold cluster (MW of D3D$_Z$ = 30264 Da).

2.6 Electrochemical Measurement

Open circuit potentials (OCP) were run for 30 minutes or until stable.

Linear sweep voltammetry (LSV) was performed on all SZ$_3$/SWNT composites using a Princeton Instruments rotating disk electrode (RDE) with 0.2465cm^2 glassy carbon electrode and Versa Stat MC equipped with Pine Company Instruments rotating motor and control box. The RDE was polished prior to each use with 0.05 mm alumina and rinsed with deionized water. 20 μl of each SZ$_3$/SWNT composite was dropped on the RDE and allowed to air dry at 4°C. Reduction currents were measured at rotation rates 1600, 1200, 800, 400 and 0 rotations per minute (rpm) from applied potential of 0.8 to -0.6 V with a scan rate of 100 mV/s with RDE submerged in 0.1 KPB (pH 7.5).

Testing was done under dissolved, saturated or depleted O_2 environment. Depleted and saturated O_2 was achieved by purging the buffer with compressed N_2 or O_2, respectively, for a minimum of 20 minutes prior to testing. Ag/AgCl and platinum wire electrodes were used as reference and counter electrodes, respectively. The swept potential was represented both versus Ag/AgCl and reversible hydrogen electrode (RHE).

Potentiostatic polarization curves were carried out by chronoamperometric (CA) measurements starting from OCP to -0.2V vs. Ag/AgCl with a step of 50mV. The samples tested were placed on a small glassy carbon cap electrode (GCCE). GCCE was polished before each use with 0.05 mm alumina and rinsed with DI water. 5μl of the samples were dropped on 0.085 cm^2 multi-walled carbon nanotubes buckypaper (BP) electrodes, placed on GCCE and allowed to air dry at 4°C. The GCCE was submerged in 0.1 M KPB (pH 7.5) and tested using Ag/AgCl reference and platinum wire counter electrodes. Potentials were held for 300 seconds each from OCP to -0.25 V at 0.05V increments in saturated O_2 electrolyte. Conversion to RHE for both LVS and CA were done using $E_{RHE} = E_{Ag/AgCl} + 0.059pH + E^{o}_{Ag/AgCl}$ with $E^{o}_{Ag/AgCl} = 0.197$ V.

2.7 Table of DNA Templates and Enzyme Composites

The following table show the description of each component and abbreviations used for the purpose of simplification:

Table 4: Description of DNA Sequences

Name	Description	Nucleotide Sequence 5' to 3'
D3	NC Template	ACCCGAACCTGGGCTACCACCCTTAATCCCC
D3Dz	ZnF Recognition with NC Template	ACCCGAACCTGGGCTACCACCCTTAATCCCCCGCACCCGC
DzH	ZnF Recognition Sequence	CGCCCACGC-Poly T GCGTGGGCG
Poly-T	Poly Thymine Tail	TTTTTTTTTTTTTTTTTTTTTTTTTTTTTT

Table 5: Description of SLAC-3ZnF composites

Composites	Description
SWNT	Single-walled carbon nanotubes

D$_Z$H	ZnF hybrid recognition sequence wrapped with no AuNC
SZ$_3$1	SLAC-3ZnF directly adsorbed on SWNT
SZ$_3$2	SLAC-3ZnF bound by ZnF recognition sequence on SWNT
SZ$_3$NC	AuNC without ZnF recognition sequence
SZ$_3$NC1	ZnF hybrid recognition hybridization after AuNC synthesis
SZ$_3$NC2	ZnF hybrid recognition hybridization prior to AuNC synthesis

3. Results and Discussion

3.1 XPS characterization of D3D$_z$NCH and D3D$_z$HNC shows the presence of primarily Au(I) oxidation state

We used x-ray photoelectron spectroscopy (XPS) to probe the oxidation state of Au in the NC samples. Both the D3D$_z$NCH and D3D$_z$HNC samples display intense peaks at 84.9 eV, 88.6 eV (Figure 1a: D3D$_z$NCH), and 84.7 eV, 88.4 eV (Figure 1b: D3D$_z$HNC), corresponding to the Au 4f$_{7/2}$ and Au 4f$_{5/2}$ components, respectively (Figure 1, blue lines). Deconvolution of the spectral envelope yielded single Au(I) species (Figure 1: green lines for Au 4f$_{7/2}$ and gray dotted lines for Au 4f$_{5/2}$ components) corresponding to 86% and 92% of total Au in D3D$_z$NCH and D3D$_z$HNC, respectively. The remaining Au is present as some residual unreduced Au(III) species (Figure 1: dotted magenta lines for Au 4f$_{7/2}$ at 87 eV and gray dotted lines for Au 4f$_{5/2}$ at 90.6 eV).

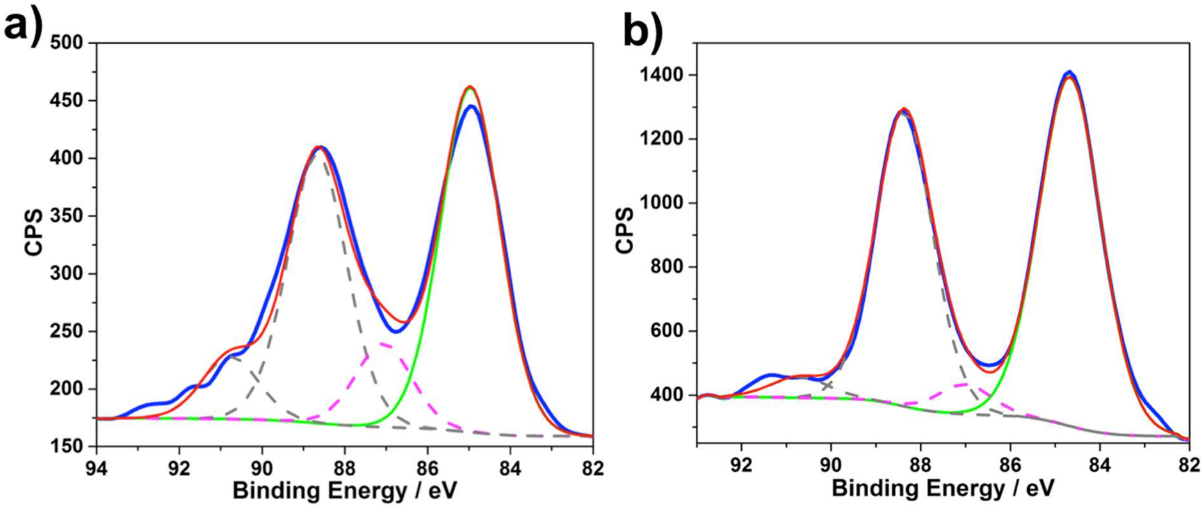

Figure 1. The AuNCs consist of primarily Au(I) oxidation state in both D3D$_Z$HG1 (a) and D3D$_Z$HG2 (b) samples. Experimental data: blue curves, simulated data: red curves, Au 4f$_{7/2}$ for Au(I) is shown as green lines, residual Au(III) species is shown as dotted magenta lines. The corresponding Au 4f$_{5/2}$ components are shown as gray dotted lines.

3.2 Electrochemical Analysis of SLAC-3ZnF Composites

Recently we reported the design of a directed immobilization of SLAC-3ZnF using the high specificity of the ZnF binding to a specific DNA sequence. Although the catalytic activity in terms of 2,6-dimethoxyphenol (DMP) reduction was shown for both SZ$_3$1 and SZ$_3$2 [31], it was discovered that electrochemical activity towards ORR for of these composites is poor. It was posited that the impeded electron transfer was in part due to increased distance of the enzyme active centers from the SWNT scaffolds resulting in poor electrocatalytic performance by SLAC. Encouraged by a recent study where a D3AuNC was shown to improve the electrocatalytic performance of bilirubin oxidase (BOD) in catalyzing ORR while not affecting the 4e$^-$ reduction of O_2 to H_2O[34], we hypothesized that by using gold nanoclusters the ORR reaction kinetics and electron transfer could be improved in the SLAC-3ZnF system.

3.2.1 The presence of AuNC significantly increases the kinetics and thermodynamics of laccase catalyzed ORR

In order to study the effectiveness of NCs on improving the electron transfer we performed linear sweep voltammetry (LSV) experiments on five different SLAC composites employing different immobilization methods. We tested each composite in 0.1 M KPB under dissolved (~6.91 mg/L), saturated (8.66 mg/L), and depleted (~0.66 mg/L) O_2 environments at 1600 rpm, respectively. Under depleted O_2 conditions only modest currents were observed (Figure SI).

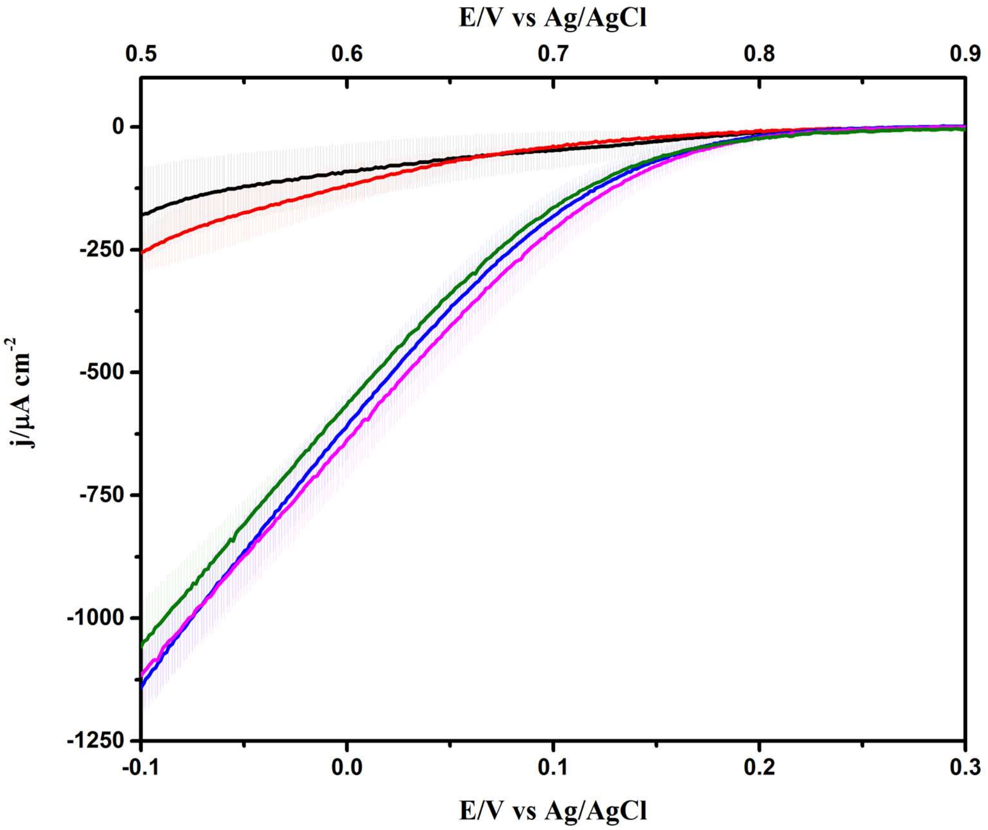

Figure 4 and **Table 6** show the results from each sample tested under saturated O_2 conditions. First we tested the control composites SZ_31 and SZ_32. Both of these samples demonstrated (**Figure 4**, black, red lines) modest catalytic activity even in the presence of saturated O_2 with low onset potentials (E_{onset}) of = 0.130V (vs. Ag/AgCl) and 0.113 V, and current densities of 141 μA/cm^2 and 222 μA/cm^2 (**Table 6**) for SZ_31, and SZ_32, respectively. It is noteworthy that these engineered SLAC-zinc finger composites irrespective of the presence of the zinc-finger recognition DNA sequence, causes significant lowering of the ORR onset potential compared to SLAC alone (0.595V vs. Ag/AgCl) [32]. These results, therefore, suggest that the presence of zinc finger domain causes significant lowering of electrocatalytic activity of laccase presumably by hindering efficient electron transfer from the electrode to the enzyme active site. However, the presence of the AuNC caused significant changes in the ORR profile displayed by the SZ_3NC/SWNT composites (**Figure 4**, magenta, blue and green lines). In all of these cases the presence of much more positive onset potentials of ORR was observed. First, the **SZ_3NC** (**Figure 4**, green line) composite, which, despite lacking the zinc finger recognition sequence in the cluster-bearing DNA [43], displays an E_{onset} of 0.225 V and electrocatalytic current density of 1050 μA/cm^2 (**Table 6**), suggesting that the presence of the AuNC enhances the thermodynamics by lowering overpotential by ~0.112 V, and kinetics by enhancing the electrocatalytic current density ~828 mV as compared to the SZ_32 composite. In the presence of the zinc finger recognition sequence on the AuNC-bearing DNA, further enhancements in E_{onset} and electrocatalytic current densities were observed in the SZ_3NC1

(**Figure 4**, magenta line) and SZ$_3$NC2 (**Figure 4**, blue line) composites. For these samples E$_{onset}$ of 0.252 V and 0.240 V, and electrocatalytic current densities of 1137 µA/cm^2, 1114 µA/cm^2 (**Table 6**) were observed for SZ$_3$NC1, and SZ$_3$NC2, respectively. These results, therefore, suggest that the presence of the zinc-finger recognition sequence in the cluster forming DNA improves the molecular recognition of the engineered SLAC-zinc finger protein conjugate with the AuNC, resulting in lower overpotential (~25 mV) and improved current density by ~90 µA/cm^2. Overall, the SZ$_3$NC1, and SZ$_3$NC2 composites display an improved E$_{onset}$ and lower overpotential by ~0.140 V and ~5-fold increase current density compared to the samples lacking the AuNC. These results, suggest that the presence of NC enhances the ORR activity of SLAC by lowering the overpotential and increasing the kinetics of the reaction, similar to what was observed for the effect of AuNC on enhanced ORR activity of bilirubin oxidase [43].

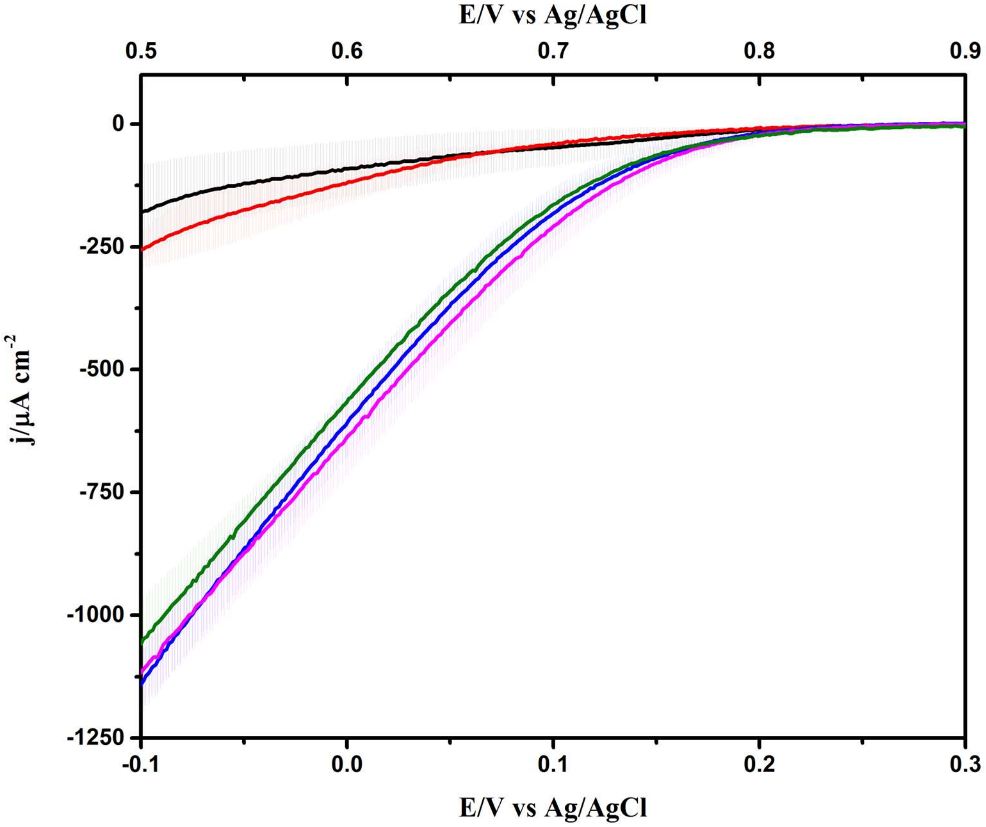

Figure 4: LSV of SZ$_3$1 (SZ$_3$/SWNT: black); SZ$_3$2 (SZ$_3$/D$_Z$H/SWNT: red); **SZ$_3$NC1** (SZ$_3$/D3D$_z$NCH/SWNT: magenta); **SZ$_3$NC2** (SZ$_3$/D3D$_z$HNC/SWNT: blue); and **SZ$_3$NC** (SZ$_3$/D3G/SWNT: green) composites in O$_2$ saturated 0.1 M potassium phosphate buffer (pH 7.5). Three individually prepared samples of each composite were tested and averaged. Standard deviation represented by the shaded areas. Potential sweep vs. Ag/AgCl was performed from 0.8 to -0.6V, scan rate=0.01V/s; and rotation rate (ω)= 1600 rpm. The potential was also converted to RHE using $E_{RHE} = E_{Ag/AgCl} + 0.059pH \quad E^{o}_{Ag/AgCl}$ with $E^{o}_{Ag/AgCl} = 0.179\ V$.

Table 6: LSV Electrochemical Results of SLAC-3ZnF/SWNT Composites in O_2-Saturated Buffer.

Composite	**E_{onset}/V vs Ag/AgCl (V vs RHE)**	**Δj/μA/cm^2**
SZ_31	0.130 (0.752)	141
SZ_32	0.113 (0.735)	222
SZ_3NC	0.225 (0.847)	1050
SZ_3NC1	0.252 (0.874)	1137
SZ_3NC2	0.240 (0.877)	1114

Potentials vs. RHE are in parenthesis. Δj is the differential current density between the current at the onset potential and the current at -0.1 V.

3.3.2 Polarization curve for SLAC-3ZnF immobilized on ZnF recognition DNA shows the presence of AuNC enhances electrocatalytic current density

We performed potentiostatic polarization curves of the SZ_3/NCs-DNA composites to evaluate the applicability of these novel composites as cathodes for ORR. For this purpose, we used a different cathode design approach. Composite materials of SZ_32, SZ_3NC1 and SZ_3NC2 were dropped on circular disk of multi-walled carbon nanotubes or buckypaper. The buckypaper electrodes were then placed on glassy carbon cap electrode and allowed to air dry at 4°C. The polarization curves were carried out under saturated O_2 conditions to minimize the mass transfer limitations. The resulting polarization curves show an increase in current density from ~100 μA/cm^2 for SZ_32 (**Figure 5**, red line) to ~300 μA/cm^2 for SZ_3NC1 (**Figure 5**, magenta line), and ~210μA/cm^2 for SZ_3NC2 (**Figure 5**, blue line). These data support the LSV measurements where improved current density was seen in presence of AuNC, further corroborating the role of AuNC in enhancing the kinetics of SLAC-catalyzed ORR. It can be noted from both the LSV (**Figure 4** and **Table 6**) and polarization measurements that when the NCs were synthesized prior to DNA hybridization a higher E_{onset} and current densities were recorded.

Figure 5: Polarization curves for SZ$_3$2 (*SZ$_3$/D$_Z$H/SWNT:* red), SZ$_3$NC1 (SZ$_3$/D3D$_z$NCH/SWNT: magenta), and SZ$_3$NC2 (SZ$_3$/D3D$_z$NCH/SWNT: blue).

As we described previously [43], the likely mechanism by which the NC enhances the ORR activity of the SLAC/SWNTs composites is by facilitating the electron transfer of the enzyme from the poised electrode surface presumably due to the electrochemical activity of the NCs and the decreased electron traveling distance.

4 Conclusion

Despite our previous study showing improved stability and activity for 2,6-dimethoxyphenol reduction for SLAC-3ZnF docked on a DNA/SWNT consisting of the zinc finger recognition sequence [31], SLAC-3ZnF has consistently displayed poor electrocatalytic activity when compared to unmodified SLAC [32] where onset potentials and current densities obtained are low. This is likely caused by an increased distance of active centers from the electrode surfaces[32]. Encouraged by previous success using DNA-templated gold nanoclusters for enhanced ORR of bilirubin oxidase [43], we incorporated D3NC into the previously designed DNA sequences [31] to improve electron transfer rates and reaction kinetics of oxygen reduction reaction carried out by SLAC-3ZnF.

In this study, we reported the effects of the synthesis of DNA-templated gold nanoclusters with addition of ZnF recognition DNA. AuNC synthesis was confirmed by using MALDI-MS and XPS analysis. Linear sweep voltammetry and chronoamperometry, along with rotating disk electrodes and glassy carbon cap electrodes, were used to determine the onset potentials of ORR and current densities of the system. We showed dramatically increased current densities when the electron transfer was facilitated by the presence of the AuNC, where current densities showed a 4-fold increase with LSV; and 2- and 3-fold increases with chronoamperometric measurements. It was also observed that the SLAC-3ZnF/AuNCs-DNA composite with synthesized AuNCs prior to DNA hybridization had higher current density than when synthesized after hybridization. This result implies that the timing of ZnF recognition DNA hybridization before or after AuNC synthesis may affect the concentration of resulting AuNC. Reasons for this are not certain, but a possible cause may be interference of the hybridizing fragment with AuNC synthesis where the free DNA fragment may hybridize with the AuNC-template as well as the ZnF recognition sequence within the longer strand.

Although the precise mechanism for electron transfer using AuNC in conjunction with SLAC-3ZnF is still unknown, we hypothesize that AuNC may act to mediate electron transfer between the electrode and enzyme, significantly increasing the current densities achieved by the biocathode. In

Figure 6, we show a proposed general mechanism for electron transfer and ORR for docked SLAC-3ZnF on the ZnF recognition portion (blue) of the designed DNA/SWNT scaffold. In this mechanism, we show AuNC acting as a mediator for electron transfer between the electrode surface to the enzyme active center of one subunit of the SLAC-3ZnF.

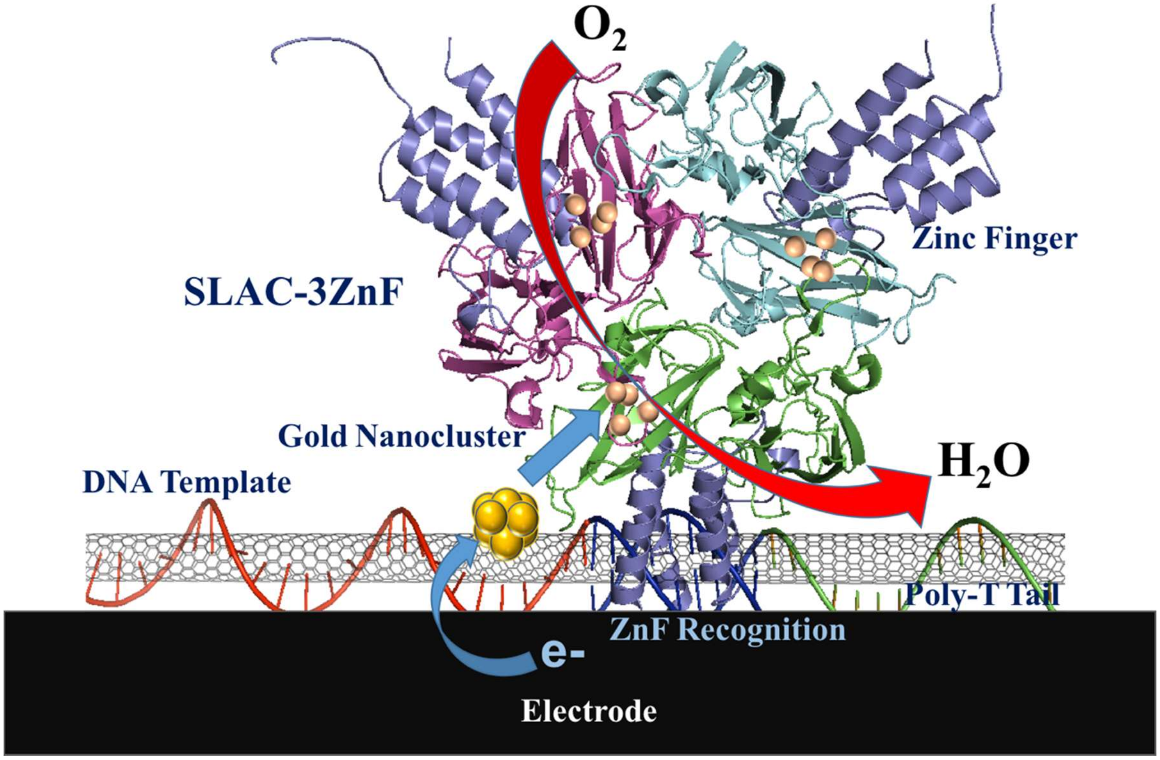

Figure 6: Oxygen reduction to water by SLAC-3ZnF via gold nanocluster mediated electron transfer.

Given the results of this study, we conclude that the AuNC facilitates electron transfer and enhances ORR reducing the effect of increased distances between active centers and electrode surfaces and possible hindrance of the ZnF domain. This concept may be applied to similar systems with various enzymes immobilized using DNA and ZnF leading to bioanodes and biocathodes with excellent catalyst stability, longer fuel cell lifetimes and improved power density.

References:

[1] La Van, D. A., and Cha, J. N. (2006) Approaches for biological and biomimetic energy conversion, *Proceedings of the National Academy of Sciences of the United States of America 103*, 5251-5255.

[2] Idan, O., and Hess, H. (2013) Engineering enzymatic cascades on nanoscale scaffolds, *Current Opinion in Biotechnology 24*.

[3] Meredith, M. T., and Minteer, S. D. (2012) Biofuel cells: enhanced enzymatic bioelectrocatalysis, *Annual review of analytical chemistry 5*, 157-179.

[4] Arechederra, R. L., Treu, B. L., and Minteer, S. D. (2007) Development of glycerol/O2 biofuel cell, *Journal of Power Sources 173*, 156-161.

[5] Kim, J., Grate, J. W., and Wang, P. (2006) Nanostructures for enzyme stabilization, *Chemical Engineering Science 61*, 1017-1026.

[6] Atanassov, P., and Apblett, C. (2007) Enzymatic biofuel cells for micropower source applications, *Abstr Pap Am Chem S 234*.

[7] Mateo, C., Palomo, J. M., Fernandez-Lorente, G., Guisan, J. M., and Fernanez-Lafuente, R. (2007) Improvement of enzyme activity, stability and selectivity via immobization techniques, *Enzyme and Microbial Technology 40*, 1451-1463.

[8] Sheldon, R. A. (2007) Enzyme immobilization: The quest for optimum performance, *Adv Synth Catal 349*, 1289-1307.

[9] Sarma, A. K., Vatsyayan, P., Goswami, P., and Minteer, S. D. (2009) Recent advances in material science for developing enzyme electrodes, *Biosensors and Bioelectronics 24*, 2313-2322.

[10] Cracknell, J., McNamara, T., Lowe, E., Blanford, C. . (2011) Bilirubin oxidase from Myrothecium verrucaria: X-ray determination of the complete crystal structure and a rational surface modification for enhanced electrocatalytic O-2 reduction, *Dalton Transactions 40*, 6668-6675.

[11] Wu, F., and Minteer, S. D. (2013) Fluorescence Characterization of Co-immobilization-Induced Multi-Enzyme Aggregation in a Polymer Matrix Using Förster Resonance Energy Transfer (FRET): Toward the Metabolon Biomimic, *Biomacromolecules 14*, 2739-2749.

[12] Niemeyer, C. M., Koehler, J., and Wuerdemann, C. (2002) DNA-directed assembly of bienzymic complexes from in vivo biotinylated NAD(P)H:FMN oxidoreductase and luciferase, *Chembiochem 3*, 242-245.

[13] Li, C., Yang, K., Zhang, Y., Tang, H., Yan, F., Tan, L., Xie, Q., and Yao, S. (2011) Highly biocompatible multi-walled carbon nanotube-chitosan nanoparticle hybrids as protein carriers, *Acta biomaterialia 7*, 3070-3077.

[14] Jiang, L., Wang, R., Li, X., Jiang, L., and Lu, G. (2005) Electrochemical oxidation behavior of nitrite on a chitosan-carboxylated multiwall carbon nanotube modified electrode, *Electrochemistry Communications 7*, 597-601.

[15] Lopez, R. J., Babanova, S., Ulyanova, Y., Singhal, S., and Atanassov, P. (2014) Improved Interfacial Electron Transfer in Modified Bilirubin Oxidase Biocathodes, *ChemElectroChem 1*, 241-248.

[16] Kim, B. C., Zhao, X., Ahn, H. K., Kim, J. H., Lee, H. J., Kim, K. W., Nair, S., Hsiao, E., Jia, H., Oh, M. K., Sang, B. I., Kim, B. S., Kim, S. H., Kwon, Y., Ha, S., Gu, M. B., Wang, P., and Kim, J. (2011) Highly stable enzyme precipitate coatings and their electrochemical applications, *Biosensors & bioelectronics 26*, 1980-1986.

[17] Wang, Q., Wang, W., Lei, J., Xu, N., Gao, F., and Ju, H. (2013) Fluorescence quenching of carbon nitride nanosheet through its interaction with DNA for versatile fluorescence sensing, *Anal Chem 85*, 12182-12188.

[18] Wooten, M., Karra, S., Zhang, M., and Gorski, W. (2014) On the direct electron transfer, sensing, and enzyme activity in the glucose oxidase/carbon nanotubes system, *Anal Chem 86*, 752-757.

[19] Feng, W., and Ji, P. (2011) Enzymes immobilized on carbon nanotubes, *Biotechnology advances 29*, 889-895.

[20] Mundaca, R. A., Moreno-Guzman, M., Eguilaz, M., Yanez-Sedeno, P., and Pingarron, J. M. (2012) Enzyme biosensor for androsterone based on 3alpha-hydroxysteroid dehydrogenase immobilized onto a carbon nanotubes/ionic liquid/NAD+ composite electrode, *Talanta 99*, 697-702.

[21] Jia, F., Narasimhan, B., and Mallapragada, S. (2014) Materials-based strategies for multi-enzyme immobilization and co-localization: A review, *Biotechnology and bioengineering 111*, 209-222.

[22] Minteer, S. D., Liaw, B. Y., and Cooney, M. J. (2007) Enzyme-based biofuel cells, *Curr Opin Biotechnol 18*, 228-234.

[23] Zhu, Z., Sun, F., Zhang, X., and Zhang, Y. H. (2012) Deep oxidation of glucose in enzymatic fuel cells through a synthetic enzymatic pathway containing a cascade of two thermostable dehydrogenases, *Biosensors & bioelectronics 36*, 110-115.

[24] Palmore, G. T. R., Bertschy, H., Bergens, S. H., and Whitesides, G. M. (1998) A methanol/dioxygen biofuel cell that uses NAD(+)-dependent dehydrogenases as catalysts: application of an electro-enzymatic method to regenerate nicotinamide adenine dinucleotide at low overpotentials, *Journal of Electroanalytical Chemistry 443*, 155-161.

[25] Gamella, M., Campuzano, S., Conzuelo, F., Curiel, J. A., Munoz, R., Reviejo, A. J., and Pingarron, J. M. (2010) Integrated multienzyme electrochemical biosensors for monitoring malolactic fermentation in wines, *Talanta 81*, 925-933.

[26] Elrod-Erickson, M., Rould, M. A., Nekludova, l., and Pabo, C. O. (1996) Zif268 protein-DNA complex refined at 1.6 A: a model system for understanding zinc finger-DNA interactions, *Structure 4*, 1171-1180.

[27] Jacobs, G. H. (1992) Determination of the base recognition positions of zinc fingers from sequence analysis, *The EMBO journal 11*, 4507-4517.

[28] Pabo, C. O., Peisach, E., and Grant, R. A. (2001) Design and selection of novel Cys2His2 zinc finger proteins, *Annual review of biochemistry 70*, 313-340.

[29] Isalan, M. (2012) Zinc-finger nucleases: how to play two good hands, *Nat Methods 9*, 32-34.

[30] Hurt, J. A., Thibodeau, S. A., Hirsh, A. S., Pabo, C. O., and Joung, J. K. (2003) Highly specific zinc finger proteins obtained by directed domain shuffling and cell-based

selection, *Proceedings of the National Academy of Sciences of the United States of America 100*, 12271-12276.

[31] Hjelm, R. M., Garcia, K. E., Babanova, S., Artyushkova, K., Matanovic, I., Banta, S., and Atanassov, P. (2016) Functional interfaces for biomimetic energy harvesting: CNTs-DNA matrix for enzyme assembly, *Biochimica et biophysica acta*.

[32] Gallaway, J., Wheeldon, I., Rincon, R., Atanassov, P., Banta, S., and Barton, S. C. (2008) Oxygen-reducing enzyme cathodes produced from SLAC, a small laccase from Streptomyces coelicolor, *Biosensors & bioelectronics 23*, 1229-1235.

[33] Machczynski, M. C., Vijgenboom, E., Samyn, B., and Canters, G. W. (2004) Characterization of SLAC: a small laccase from Streptomyces coelicolor with unprecedented activity, *Protein Sci 13*, 2388-2397.

[34] Barton, S. C., Gallaway, J., and Atanassov, P. (2004) Enzymatic biofuel cells for implantable and microscale devices, *Chem Rev 104*, 4867-4886.

[35] Szilvay, G. R., Brocato, S., Ivnitski, D., Li, C., De La Iglesia, P., Lau, C., Chi, E., Werner-Washburne, M., Banta, S., and Atanassov, P. (2011) Engineering of a redox protein for DNA-directed assembly, *Chem Commun (Camb) 47*, 7464-7466.

[36] Haruta, M., and Date, M. (2001) Advances in the catalysis of Au nanoparticles, *Appl Catal a-Gen 222*, 427-437.

[37] Boccuzzi, F., Cerrato, G., Pinna, F., and Strukul, G. (1998) FTIR, UV−Vis, and HRTEM Study of Au/ZrO2 Catalyst: Reduced Reactivity in the CO−O2 Reaction of Electron-Deficient Gold Sites Present on the Used Samples, *The Journal of Physical Chemistry B 102*, 5733-5736.

[38] Hayden, B. E., Pletcher, D., and Suchsland, J. P. (2007) Enhanced activity for electrocatalytic oxidation of carbon monoxide on titania-supported gold nanoparticles, *Angew Chem Int Ed Engl 46*, 3530-3532.

[39] Valden, M., Lai, X., and Goodman, D. W. (1998) Onset of catalytic activity of gold clusters on titania with the appearance of nonmetallic properties, *Science 281*, 1647-1650.

[40] Hernandez, J., Solla-Gullon, J., Herrero, E., Aldaz, A., and Feliu, J. M. (2007) Electrochemistry of shape-controlled catalysts: Oxygen reduction reaction on cubic gold nanoparticles, *J Phys Chem C 111*, 14078-14083.

[41] Mohr, C., Hofmeister, H., Radnik, J., and Claus, P. (2003) Identification of active sites in gold-catalyzed hydrogenation of acrolein, *Journal of the American Chemical Society 125*, 1905-1911.

[42] Hughes, M. D., and Xu, Y.-J. (2005) Tunable gold catalysts for selective hydrocarbon oxidation under mild conditions, *Nature 437*.

[43] Chakraborty, S., Babanova, S., Rocha, R. C., Desireddy, A., Artyushkova, K., Boncella, A. E., Atanassov, P., and Martinez, J. S. (2015) A Hybrid DNA-Templated Gold Nanocluster For Enhanced Enzymatic Reduction of Oxygen, *Journal of the American Chemical Society 137*, 11678-11687.

Malate Dehydrogenase and Citrate Synthase on Modified Multi-Walled Carbon Nanotubes for Mediated L-Malate Oxidation

Introduction

The TCA cycle is an important part of the natural metabolic mechanism responsible for producing energy, adenosine triphosphate (ATP) regulation and certain biosynthesis building blocks. In eukaryotes, the TCA cycle begins within the mitochondria as pyruvate is converted to oxaloacetate and acetyl coenzyme A (acetyl coA) by pyruvate carboxylase (PCB) and pyruvate dehydrogenase (PDH), respectively. Oxaloacetate and acetyl-CoA then bind to citrate synthase (CS) forming citrate. The cycle ends when oxaloacetate is regenerated by the oxidation of L-malate by malate dehydrogenase (MDH) and the oxidized form of nicotinamide adenine dinucleotide (NAD^+). Resulting NADH molecules are then transported into the oxidative phosphorylation cycle. Several NAD-dependent redox enzymes are responsible for the oxidation of intermediate products throughout the cycle.

The enzyme that completes the TCA cycle, MDH, has been one enzyme of interest due its electrochemical properties, general instability in aqueous solution and NAD dependence. MDH catalyzes the reversible oxidation of L-malate to oxaloacetate in the presence of NAD^+. Oxaloacetate is then channeled through citrate synthase and used with acetyl-CoA to produce citrate. The formation of an MDH/CS complex and channeling of oxaloacetate through it has been shown through mathematical and experimentally means [1, 2]. Given this evidence along with evidence of MDH/CS complex formation, it would logical to conclude that additional means for enzyme orientation would not be necessary when using sequential enzymes and would simplify methods used for optimizing reaction pathways due to lowered risk to structural integrity. However, because naturally occurring MECs are unstable and dissociate quickly, finding methods for increased stabilization are a necessary step in producing EFCs that can compete against the current energy technology.

Immobilization on nanomaterials is one area that has been extensively researched to address stability issues. Nanomaterials are ideal for this purpose due to their comparable to enzymes size, nanomaterials structural and electronic properties, and ability to interact with biological molecules[3-18]. For MECs, numerous co-localization techniques have been explored for EFCs including entrapment, covalent bonding, direct-physical adsorption and cross-linking using biomolecules, polymers and surfactant [19]. However, choosing the best method is highly dependent on enzyme properties. Direct adsorption onto some nanomaterials can lead to denaturing of the enzyme resulting in loss of function. PBSE and biomolecules like chitosan (chit) have also been used for immobilization of enzyme on nanomaterials in sensors and EFCs [11, 20-25].

For the purposes of this study, we focused on the incorporation of nanomaterials, specifically multi-walled carbon nanotubes (MWNTs) for stabilization and increased electron transfer to electrode surfaces of PMG-modified MWNT Buckypaper (PMG-BP). Our goal was to identify methods in which the native structure and therefor oxidative function of the MDH with CS are not negatively impacted. Two methods that we address here for MDH/CS co-localization include entrapment via deacylated chit or tethering with PBSE. These two methods differ significantly in enzyme interaction but both have been shown to produce stable scaffolds for immobilization on nanotubes. We report hereon the effects of concentration and applied potential on each immobilization method in the presence of CS.

Reagents

Malic acid (No. M1000), aconitase (porcine heart, lyophilized powder, No. A5384), citrate synthase (porcine heart, $(NH_4)_2SO_4$ suspension, No. C3269), β-nicotinamide adenine dinucleotide hydrate (No N7004), chitosan (No. 03312A7) and 1-pyrenebutanoic acid succinimidyl ester (PBSE, No. MKBQ6358V) were purchased from Sigma Aldrich (St. Louis, MO). Citrate synthase (CS) was purified using centrifugation to remove from $(NH_4)_2SO_4$ immediately prior to use. Malate dehydrogenase (porcine heart, lyophilized powder, No. 18670) was obtained from Affymetrix USB products (Cleveland, OH) and used as received. Multi-walled carbon nanotubes (MWNT) were obtained from www.cheaptubes.com (Cambridgeport, VT). Tetrabutylammonium bromide (TBAB-Nafion) was provided by Professor Shelley Minteer (University of Utah, Salt Lake City, UT)

Materials

A Reference 600^{TM} poteniostat/galvanostat/ZRA from Gamry Instruments (Warminster, PA) was used for all electrochemical methods. Cells for electrode testing were constructed from a proprietary polypropylene cell with graphite plate current collector provided by CFD Research Corporation (CRDRC, Huntsville, AL), 3M KCl Ag/AgCl reference and platinum wire counter electrodes. The Buckypaper (BP) for electrodes (20 gsm, M and C-grade mixture) was purchased from Nanotech Labs Composites (Yadkinville, NC).

Electrode Preparation Protocol

Polymerization of Methylene Green Film on BP

Electropolymerization was used for depositing a PMG film onto the carbon nanotube paper. To accomplish this, first, a buffer solution of 0.6mM methylene green (MG) in 0.1M potassium phosphate buffer (KPB, pH 7) and 0.1M potassium nitrate (KNO_3) was prepared and purged with compressed nitrogen (N_2) for 15 minutes to remove oxygen. Working electrodes were made from high conductivity, c/m-grade blend MWNT Buckypaper (BP) cut to approximately 1.77 cm^2 each. Reduced hydrophobicity was achieved through brief treatment with isopropyl alcohol (IPA) and then rinsed with DI water immediately prior to film deposition. A standard three-electrode cell using Ag/AgCl reference electrode, stainless steel mesh counter electrode and BP electrode was set up with 15 ml MG solution with N_2 purging. Polymerization was carried out through 10 cyclic voltammetry cycles with an applied potential range of -0.5 to 1.3V at a scan rate of 50 mV/s resulting in the deposition of a PMG layer on the BP surface (PMG-BP). Each PMG-BP electrode was thoroughly washed with DI water and air-dried.

Chitosan/MWNT Composite Preparation

All enzymes immobilized on MWNT using entrapment with chitosan were done in a 95 % chitosan to 5% MWNT mixture (Chit/MWNT). Deacylation of medium weight chitosan to 95% was carried out through autoclaving for 20 minutes at 121°C and 15 psi in 45% NaOH solution and dry vacuumed for 24 hours [23, 26]. A 1% deacylated chitosan in 0.25 acetic acid (Chit, pH 6) suspension was prepared and stored at 4°C. From this suspension, a mixture of MWNT and chitosan with a 2.5 wt.% MWNT was made (Chit/MWNT). The mixture was stored at 4°C and stirred immediately prior to use to ensure uniform distribution and prevent polymerization while at room temperature.

Malate Dehydrogenase Entrapment with Chitosan/MWNT

1.5 mg of MDH were combined with 150µl of Chit/MWNT mixture and left to incubate at 4°C for 30 minutes. Samples were then transferred and distributed on prepared PMG-BP electrodes and left to air dry overnight at 4°C.

Malate Dehydrogenase and Citrate Synthase Entrapment with Chitosan/MWNT

138 µl of CS suspension in ammonium sulfate (9 mg/ml) was centrifuged at 1000xg for 10 minutes to remove CS from solution. The resulting pellet (~1.28 mg CS) was combined with 1.5 mg MDH and then immediately and carefully mixed with 150 µl Chit/MWNT mixture (MCChit). The mixture was allowed to incubate for 30 min at 4°C before being transferred and distributed on the prepared PMG-BP electrodes.

PBSE /MWNT Composite Preparation

For all PBSE/MWNT samples, 2.5%wt MWNT with 0.1 % TBAB-Nafion, were suspended in 0.1M KPB (pH 7.5), placed under water sonication for 30 minutes and stored at room temperature. 4 mg/ml PBSE in ethanol (EtOH) suspension was prepared using water sonication. Suspensions of PBSE and 2.5%wt MWNT (20% PBSE, 80% MWNT) were combined, briefly mixed using a vortex mixer and left for 1 hour at 23° C to combine.

Malate Dehydrogenase Cross-Linkage with PBSE on MWNT

1.5 mg of MDH were combined with 200 µl of MWNT-PBSE suspension and left to incubate at 4°C for 18 hours (MP). Samples were then transferred and distributed on prepared PMG-BP electrodes and left to air dry at 4°C before testing.

Malate Dehydrogenase and Citrate Synthase Cross-Linkage on MWNT with PBSE

As with chit/MWNT samples, 138µl of CS suspension in ammonium sulfate (9 mg/ml) was centrifuged at 1000xg for 10 minutes to remove CS from solution. The resulting pellet was combined with 1.5mg MDH and then carefully mixed with 200µl of the PBSE-MWNT mixture (MCP). The mixture was allowed to incubate for 24 hours at 4°C before being transferred and dried on the prepared PMG-BP electrodes (**Figure 7**).

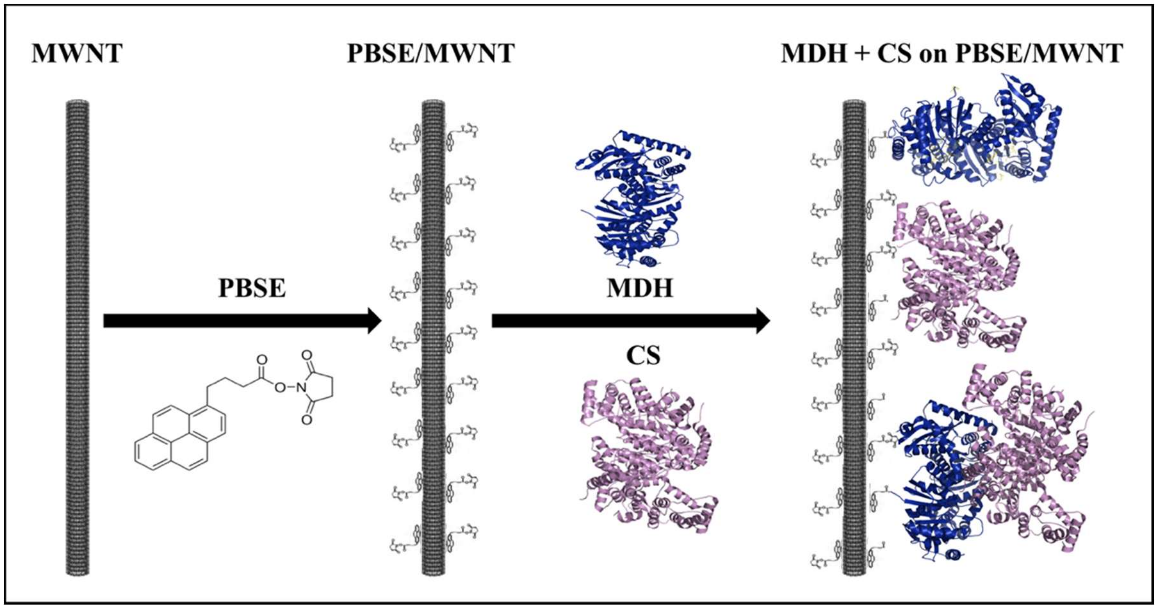

Figure 7: Representation of possible MDH and CS orientation cross-linked to MWNT with PBSE

Electrochemical Measurement

Cells were assembled using prepared electrodes placed on graphite plate electrodes and secured against a polypropylene cell for all composites. All potentials were tested against Ag/AgCl reference with a platinum wire counter electrode. 1.75M L-malate solution was prepared from L-malic acid in DI water and adjusted to pH 7.4 with concentrated NaOH for use with all measurements. For cells with MDH only, approximately 2.6ml of a solutions containing 0.1 KPB, 0.1 KCl and 5 mM NAD^+ (pH 7.4) solution was transferred into the poly-propylene cells. For cells with MDH and CS, a solution of 0.1M KPB, 0.1 M KCl, 5 mM NAD^+ and 1 mM Acetyl Co-A (pH 7.4) was transferred into the poly-propylene cells. Cells were checked for air bubbles in the solution and on the electrode surface prior to running any measurements. An open circuit potentials (OCP) measurement was run for 1 hour or until voltage was stable for each electrode.

Kinetic-Concentration Measurement

After OCP measurements were complete, chronoamperometry (CA) was used to measure current at increasing concentrations of L-malate. Prior to L-malate addition, CA was left to stabilize to where a steady-state current was observed. Aliquots of L-malate were then added at 300 second intervals until a concentration of 0.1M was reached. Results were plotted as current (i) versus L-malate concentration ([M]).

Michaelis-Menten equation (Eq. 21) was used to determine parameters for MP, MCP and MChit electrodes and bi-hill equation was used to determine MCChit parameters (Eq. 22).

$$\boldsymbol{i = \frac{i_{max}[M]}{K_M+[M]}} \qquad \text{(Eq. 1)}$$

$$\boldsymbol{i = P_m \frac{1+\left(\frac{K_a}{[M]}\right)^{H_a}}{1+\left(\frac{K_i}{[M]}\right)^{H_i}}} \qquad \text{(Eq. 2)}$$

Where i is the reaction rate or current (μA) at [M]; i_{max} is the maximum current reached by the system, [M] is the concentration of L-malate; K_M is the concentration at ½ i_{max}; P_m is the peak current observed; K_a is the L-malate concentration at ½ P_m during activation; K_i is the L-malate concentration at ½ P_m during inhibition; and H_a and H_i are the hill coefficients for activation and inhibition, respectively.

Polarization Measurement of Electrodes

150μl of L-malate solution (final concentration of approximately 0.1M) was added to cell prior to start of the polarization measurements. Each sample was measured for 300 seconds at a constant potential from -0.35 to 0.35V at 0.05V increments. Resulting current density (j) were plotted against the applied potential (E).

Results and Discussion

Electropolymerization of PMG on MWNT Type "Buckypaper"

The use of PMG for NAD^+ regeneration has been extensively studied [27-30] and been implemented for use in NAD dependent DH-based electrodes due to its effectiveness in reducing overpotential [4, 24, 31-34]. Previous studies have demonstrated the usefulness of various immobilization techniques in conjunction with mediators such as PMG for the regeneration of NAD^+ using MDH in anodic electrodes [24, 26, 31]. These studies addressed the issue of NAD^+ regeneration for reducing overpotential and improving the overall statistics of the electrode. We have chosen PMG for the modification of MWNT type BP for the purpose of NAD^+ regeneration in MDH and MDH/CS electrodes immobilized through PBSE/MWNT and Chit/MWNT scaffolds. The electrodes were modified prior to enzyme/scaffold addition using cyclic voltammetry as described earlier. The number of cycles and range used was determined based on prior SWNT PB modification with PMG film [31].

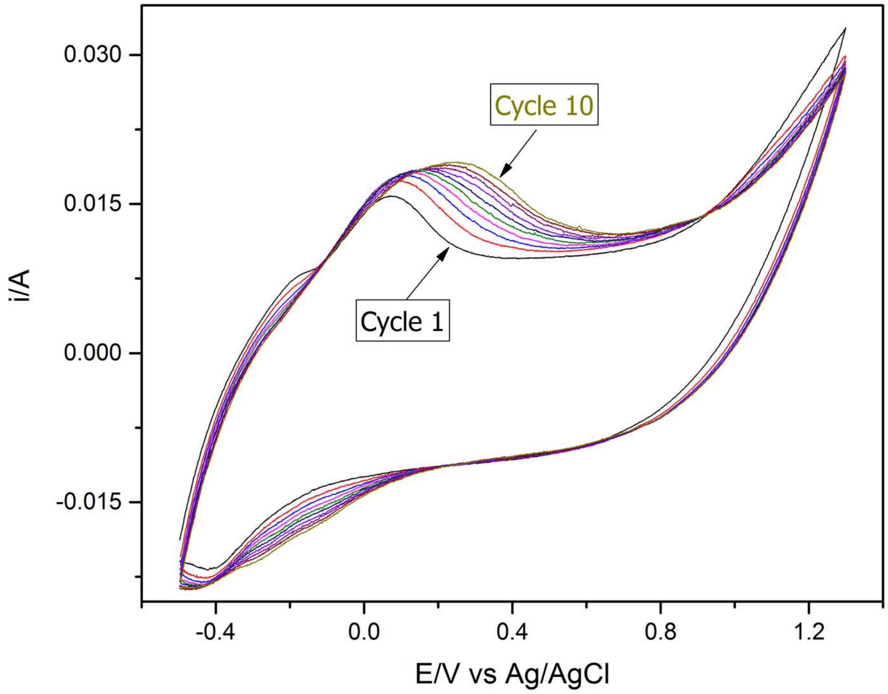

Figure 8: Representative cyclic voltammogram results for poly-methylene green deposition on MWNT type BP. 10 cycles were carried out consecutively from an applied potential range of -0.5 to 1.3 V with a 50 mV/s scan rate. Cycle 1 and cycle 2 are indicated here and are evidence of altered surface composition.

Ten CV cycles from -0.5 to 1.3 V were run to form the PMG film. The voltammetry results were typical for PMG deposition observed in previous studies (**Figure 8**) [24, 31, 35] and is evidence of MG polymerization on the surface of BP. The peak observed at approximately -0.2V, which represents the un-polymerized MG reduces with each cycle applied until no longer present at cycle 10; while the polymerization peak at approximate 0.1V shifts and becomes increasingly present.

L-Malate Oxidation by MDH-Based PMG-PB Electrodes

In order to study the affects of CS interaction with MDH and immobilization techniques for co-localization on fuel cell oxidation potentials, two methods were utilized. The first was to immobilize MDH alone and in the presence of CS using entrapment via chit-modified MWNT. The second was to use covalent crosslinking to MWNT via PBSE, for a direct comparison. Coenzyme/KBP solutions, PBSE, chit, MWNT and enzyme concentrations were held constant throughout experiments and were the same for all composites. Deacylated chit was chosen as one method because it has been shown to be an optimal structure for enzyme immobilization [23, 36, 37] and ability to solubilize carbon nanotubes [38, 39]. PBSE was chosen because it forms an amide bond with proteins using primary amines and pi-stacks on nanotubes structures.

For composites containing both MDH and CS, we added each enzyme simultaneously to allow for equal interaction time between enzymes and scaffolds. The goal was to see how L-malate oxidation would be affected when MDH was in complex with or in possible competition for immobilization with CS depending on the method used. The resulting composites were deposited on the prepared PMG-BP and measured by applying a constant potential of 0.3V with increasing concentrations of L-malate (**Figure 9**). Comparing the two MDH immobilization methods, PBSE or chitosan, we saw that the maximum current (i_{max}) reached with PBSE/MWNT (i_{max}=11.1 ± 0.2 μA) was twice higher than Chit/MWNT (i_{max}=5.7 ± 0.2 μA) and the corresponding apparent Michaelis-Menten constant, K_{Mapp}, for MChit was 1.2 times higher in comparison to the PBSE tethering technique (**Figure 9**, **Table 7**). The higher K_M value for MChit suggests lower binding affinity of L-malate to MDH although it may be due to mass transport inhibition of L-malate through chitosan.

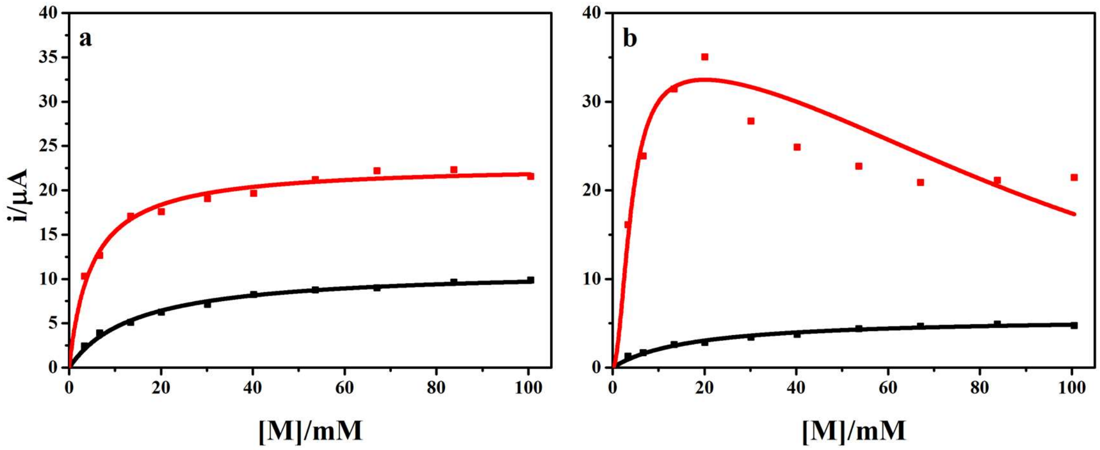

Figure 9: Current (i) versus L-malate concentration [M] of MDH (black) and MDH/CS (red) enzyme systems on a) PBSE/MWNT and b) Chit/MWNT, respectively. Each sample was measured at an applied potential of 0.3V vs Ag/AgCl and successive L-malate aliquots (1.75 M, pH 7.4) were added at 300 second intervals until steady-state current was observed.

electrodes behavior deviates form the Michaelis-Menten model used to fit all other electrodes resembling inhibition-like behavior at [M]>20mM. A bi-hill equation fit was used to determine P_m and K_a and estimate the binding affinity for L-malate (**Figure 9**). While there is a two-fold increase in i_{max} of MCP in relation to MP, at P_m (P_m=35.0 μA) of MCChit, at approximately [M]=20mM was two times higher than observed at the same malate concentration for MCP (i_{20mM}=17.5μA) (**Table 7**) indicating higher conversion efficiency for the MCChit electrodes. The i_{max} for MCChit is also 12 times higher than observed with MChit electrodes. At [M] between 20 and 40 mM, product inhibition behavior is seen where current decreases from 35.0μA to 24.9 μA before reaching apparent saturation. This inhibition effect is most likely a result of the binding of citrate to an allosteric site of MDH as proposed previously. The latter is possible due to the presence of CS in the artificially created MDH/CS metabolon. K_a of MCChit was compared to K_M of MP, MCP and MChit. For MDH only electrodes, K_M for MP and MChit were approximately 14.5mM and 17.3mM, respectfully. The binding affinity increased with addition of CS to the MDH on PBSE and chitosan where K_M reduced to 4.9mM and $K_a = 3.7$mM (**Table 7**).

There are several factors that may account for this behavior seen in entrapment versus covalent crosslinking:

1. Since there is evidence for MDH and CS complex formation through residue cross-linking and the likely involvement of C- and N- termini in surface interfaces [40], and PBSE forms amide bonds from reaction between primary amine in the proteins and its ester group; the close proximity of the N- and C-termini may be interfered with due to reaction with the ester and primary amine for cross-linking to carbon nanotubes leading to fewer MDH/CS complex present at MWNT surfaces.
2. CS and MDH may be competing for binding to PBSE.
3. The deacylation of chitosan where acyl groups ($-COCH_3$) are removed increases amine groups and makes it less reactive to nucleophilic attack from primary amines on proteins. The reaction with the resulting amine with carboxyl groups at the C-terminus is non-spontaneous and would require heat in order to create a bond. Therefor, it is unlikely that the protein complex would be disrupted by chitosan and more likely to have higher amounts of MDH/CS interaction than with amide bonding.
4. Although, lower activity of enzymes immobilized in chitosan versus free enzymes has been reported and thought to be a result of the lowered mass transport of substrates through the porous structure [23]; at low [M], mass transport is likely not as hindered. In addition, citrate may bind to an allosteric binding site in the MDH, shifting equilibrium in favor of oxaloacetate/NADH production resulting in increased reaction rate [1, 2] therefor a higher current detected.
5. Saturation of CS with citrate inhibits oxaloacetate binding to the enzyme, resulting in a higher concentration of free oxaloacetate [Ox] in the buffer solution. High [Ox] inhibits L-malate oxidation by MDH [Kitto, 1966 #148].

The results from this study show that in the presence of CS, the oxidation of L-malate through MDH is enhanced. The data suggests that MDH/CS complex formation may not be as favored with PBSE as with chitosan scaffolds. This would suggest that chitosan is a more appropriate method for MDH/CS immobilization than covalent tethering at low substrate concentrations. The increase in recorded current of MDH/CS using PBSE may however still be evidence of MDH/CS complex formation.

Table 7: Summary of concentration study parameters obtained for chronoamperometry measurements of PMG-BP electrodes.

Electrode	Composition	K_M (mM)	i_{max} (μA)
MP	MDH immobilized on PBSE/MWNT	14.5	11.1 ± 0.2
MCP	MDH and CS immobilized on PBSE/MWNT	4.90	22.7 ± 0.4
MChit	MDH immobilized in a Chit/MWNT	17.2	5.66 ± 0.2
MCChit	MDH and CS immobilized in a chit/MWNT	K_a=3.7	P_m=35.01

Polarization Curves of MDH-Based PMG-BP Electrodes

A potentiostatic polarization curves were also carried out to support the results of the concentration experiment. A series of chronoamperometry measurements were performed for 300 seconds each to study the behavior of the system at incremental potential increase. The resulting current density (j) for the anodes was plotted versus the applied potential (**Figure 10**). The results from the polarization curves supported the concentration data with CS containing electrodes out-performing the MDH electrodes by 2-fold increase in current density. Both single enzyme and two-enzyme electrodes showed similar current densities. At 0.3 V, j is approximately 17.4 ± 1.5 μA/cm^2 for MP, 14.6 ± 1.2 μA/cm^2 for MChit, 28 ± 1.4 μA/cm^2 for MCChit and 29 ± 0.6 μA/cm^2 for MCP.

Figure 10: Anodic polarization curve of MDH (black) and MDH/CS (red) enzymes on a) PBSE/SWNT and b) Chit/MWNT scaffolds in, respectively. Potentials were applied from -0.35 to 0.35V at 0.05V increments.

Conclusion

In this study, the affects of CS presence on oxidation of L-malate by MDH using two methods of immobilization, tethering with PBSE and entrapment in deacylated chitosan on MWNT were tested using chronoamperometry. BP electrode surfaces were first prepared using poly-(methylene green) modification. Prepared MP, MCP, MChit, MCChit were deposited on the PMG-BP and tested for oxidation potential of L-malate by MDH. It was observed that in the presence of CS, the MDH-based electrodes performance was significantly improved showing a 2-fold increase in current density. This may support the hypothesis that citrate plays a roll in MDH regulation

References

[1] Fahien, L. A., et al. (1988) Regulation of Malate Dehydrogenase Acitivity by Glutamate, Citrate, alpha-Ketoglutarate, and Multienzymes Interaction., *Journal of biological chemistry 263*, 10687-10697.

[2] Mullinax, T. R., Mock, J. N., McEvily, A. J., and Harrison, J. H. (1982) Regulation of mitochondrial malate dehydrogenase. Evidence for an allosteric citrate-binding site, *J Biol Chem 257*, 13233-13239.

[3] Feng, W., and Ji, P. (2011) Enzymes immobilized on carbon nanotubes, *Biotechnology advances 29*, 889-895.

[4] Fenga, P. G., Cardoso, F. P., Aquino Neto, S., and De Andrade, A. R. (2013) Multiwalled carbon nanotubes to improve ethanol/air biofuel cells, *Electrochimica Acta 106*, 109-113.

[5] Holzinger, M., Le Goff, A., and Cosnier, S. (2012) Carbon nanotube/enzyme biofuel cells, *Electrochimica Acta 82*, 179-190.

[6] Jacobs, C. B., Peairs, M. J., and Venton, B. J. (2010) Review: Carbon nanotube based electrochemical sensors for biomolecules, *Anal Chim Acta 662*, 105-127.

[7] Jiang, L., Wang, R., Li, X., Jiang, L., and Lu, G. (2005) Electrochemical oxidation behavior of nitrite on a chitosan-carboxylated multiwall carbon nanotube modified electrode, *Electrochemistry Communications 7*, 597-601.

[8] D. Ivnitski, K. A., R.A. Rincón, P. Atanassov, H.R. Luckarift, G.R. Johnson. (2008) Entrapment of Enzymes and Carbon Nanotubes in Biologically Synthesized Silica: Glucose Oxidase-Catalyzed Direct Electron Transfer, *Small 4*, 357-364.

[9] Kim, J., Grate, J. W., and Wang, P. (2008) Nanobiocatalysis and its potential applications, *Trends in biotechnology 26*, 639-646.

[10] Kim, J., Grate, J. W., and Wang, P. (2006) Nanostructures for enzyme stabilization, *Chemical Engineering Science 61*, 1017-1026.

[11] Li, C., Yang, K., Zhang, Y., Tang, H., Yan, F., Tan, L., Xie, Q., and Yao, S. (2011) Highly biocompatible multi-walled carbon nanotube-chitosan nanoparticle hybrids as protein carriers, *Acta biomaterialia 7*, 3070-3077.

[12] Lynch, I., and Dawson, K. A. (2008) Protein-nanoparticle interactions, *Nano Today 3*, 40-47.

[13] Rajalakshmi, N., Ryu, H., Shaijumon, M., and Ramaprabhu, S. (2005) Performance of polymer electrolyte membrane fuel cells with carbon nanotubes as oxygen reduction catalyst support material, *Journal of Power Sources 140*, 250-257.

[14] Rotkin, S. V., and Snyder, S. E. Theory of Electronic and Optical Properties of DNA-SWNT hybrids, In *Carbon Nanotubes and Related Structures: Synthesis, Characterization, Functionalization, and Applications* (Friedrich-Alexander-Universität, and Erlangen-Nürnberg, Eds.), Wiley-VCH Verlag GmbH & Co. KGaA, Weinheim, Weinheim Germany.

[15] Smart, S. K., Cassady, A. I., Lu, G. Q., and Martin, D. J. (2006) The biocompatibility of carbon nanotubes, *Carbon 44*, 1034-1047.

[16] Wang, X., Li, W., Chen, Z., Waje, M., and Yan, Y. (2006) Durability investigation of carbon nanotube as catalyst support for proton exchange membrane fuel cell, *Journal of Power Sources 158*, 154-159.

[17] Zheng, M., Jagota, A., Semke, E. D., Diner, B. A., McLean, R. S., Lustig, S. R., Richardson, R. E., and Tassi, N. G. (2003) DNA-assisted dispersion and separation of carbon nanotubes, *Nature materials 2*, 338-342.

[18] Zheng, M., Jagota, A., Strano, M. S., Santos, A. P., Barone, P., Chou, S. G., Diner, B. A., Dresselhaus, M. S., McLean, R. S., Onoa, G. B., Samsonidze, G. G., Semke, E. D., Usrey, M., and Walls, D. J. (2003) Structure-based carbon nanotube sorting by sequence-dependent DNA assembly, *Science 302*, 1545-1548.

[19] Jia, F., Narasimhan, B., and Mallapragada, S. (2014) Materials-based strategies for multi-enzyme immobilization and co-localization: A review, *Biotechnology and bioengineering 111*, 209-222.

[20] Liu, M., Zhang, Y., Wu, C., Xiong, S., and Zhou, C. (2012) Chitosan/halloysite nanotubes bionanocomposites: structure, mechanical properties and biocompatibility, *International journal of biological macromolecules 51*, 566-575.

[21] Xiang, C., Zou, Y., Sun, L. X., and Xu, F. (2007) Direct electrochemistry and electrocatalysis of cytochrome c immobilized on gold nanoparticles-chitosan-carbon nanotubes-modified electrode, *Talanta 74*, 206-211.

[22] Li, J., Liu, Q., Liu, Y., Liu, S., and Yao, S. (2005) DNA biosensor based on chitosan film doped with carbon nanotubes, *Analytical biochemistry 346*, 107-114.

[23] Sjoholm, K. H., Cooney, M., and Minteer, S. D. (2009) Effects of degree of deacetylation on enzyme immobilization in hydrophobically modified chitosan, *Carbohyd Polym 77*, 420-424.

[24] Rincón, R. A., Lau, C., Garcia, K. E., and Atanassov, P. (2011) Flow-through 3D biofuel cell anode for NAD+-dependent enzymes, *Electrochimica Acta 56*, 2503-2509.

[25] Liu, X., Peng, Y., Qu, X., Ai, S., Han, R., and Zhu, X. (2011) Multi-walled carbon nanotube-chitosan/poly(amidoamine)/DNA nanocomposite modified gold electrode for determination of dopamine and uric acid under coexistence of ascorbic acid, *J Electroanal Chem 654*, 72-78.

[26] Lau, C., Martin, G., Minteer, S. D., and Cooney, M. J. (2010) Development of a Chitosan Scaffold Electrode for Fuel Cell Applications, *Electroanalysis 22*, 793-798.

[27] Arechederra, M. N., Jenkins, C., Rincón, R. A., Artyushkova, K., Atanassov, P., and Minteer, S. D. (2010) Chemical polymerization and electrochemical characterization of thiazines for NADH electrocatalysis applications, *Electrochimica Acta 55*, 6659-6664.

[28] Li, H., Wen, H., and Calabrese Barton, S. (2012) NADH Oxidation Catalyzed by Electropolymerized Azines on Carbon Nanotube Modified Electrodes, *Electroanalysis 24*, 398-406.

[29] Li, H., Worley, K. E., and Calabrese Barton, S. (2012) Quantitative Analysis of Bioactive NAD+Regenerated by NADH Electro-oxidation, *ACS Catalysis 2*, 2572-2576.

[30] Svoboda, V., Cooney, M., Liaw, B. Y., Minteer, S., Piles, E., Lehnert, D., Calabrese Barton, S., Rincon, R., and Atanassov, P. (2008) Standardized Characterization of Electrocatalytic Electrodes, *Electroanalysis 20*, 1099-1109.

[31] Narvaez Villarrubia, C. W., Rincon, R. A., Radhakrishnan, V. K., Davis, V., and Atanassov, P. (2011) Methylene green electrodeposited on SWNTs-based "bucky" papers for NADH and l-malate oxidation, *ACS applied materials & interfaces 3*, 2402-2409.

[32] Kar, P., Wen, H., Li, H., Minteer, S. D., and Calabrese Barton, S. (2011) Simulation of Multistep Enzyme-Catalyzed Methanol Oxidation in Biofuel Cells, *Journal of The Electrochemical Society 158*, B580.

[33] Yu, J., Rasmussen, M., and Minteer, S. D. (2013) Effects of Carbon Nanotube Paper Properties on Enzymatic Bioanodes, *Electroanalysis 25*, 1130-1134.

[34] Blackwell, A. E., Moehlenbrock, M. J., Worsham, J. R., and Minteer, S. D. (2009) Comparison of Electropolymerized Thiazine Dyes as an Electrocatalyst in Enzymatic Biofuel Cells and Self Powered Sensors, *Journal of Nanoscience and Nanotechnology 9*, 1714-1721.

[35] Barsan, M. M., Pinto, E. M., and Brett, C. M. A. (2008) Electrosynthesis and electrochemical characterisation of phenazine polymers for application in biosensors, *Electrochimica Acta 53*, 3973-3982.

[36] Klotzbach, T., Watt, M., Ansari, Y., and Minteer, S. (2006) Effects of hydrophobic modification of chitosan and Nafion on transport properties, ion-exchange capacities, and enzyme immobilization, *Journal of Membrane Science 282*, 276-283.

[37] Klotzbach, T. L., Watt, M., Ansari, Y., and Minteer, S. D. (2008) Improving the microenvironment for enzyme immobilization at electrodes by hydrophobically modifying chitosan and Nafion® polymers, *Journal of Membrane Science 311*, 81-88.

[38] Kim, S. W., Kim, T., Kim, Y. S., Choi, H. S., Lim, H. J., Yang, S. J., and Park, C. R. (2012) Surface modifications for the effective dispersion of carbon nanotubes in solvents and polymers, *Carbon 50*, 3-33.

[39] Zhang, M., Smith, A., and Gorski, W. (2004) Carbon nanotube-chitosan system for electrochemical sensing based on dehydrogenase enzymes, *Anal Chem 76*, 5045-5050.

[40] Wu, F., and Minteer, S. (2015) Krebs cycle metabolon: structural evidence of substrate channeling revealed by cross-linking and mass spectrometry, *Angew Chem Int Ed Engl 54*, 1851-1854.

Computation Design for Protein Self-Assembly

Introduction and Background

While top-down and bottom-up approaches to constructing nanomaterials have made great advances in recent years, no approach yet allows the predictable design of novel functional materials patterned from the nano to macro scale with atomic level accuracy. Such a method would greatly reduce time spent on initial research and development efforts, and in so doing, both increase the rate at which we are able to engineer new advanced materials and decrease the cost. Nature offers many examples of such exquisite structures, but engineering new ones rivaling these natural specimens has proven to be a challenging problem.

Bottom-up approaches possess the inherent advantage of being defined at the atomic level, but also present the challenge of predicting the structures and interactions of complex molecular systems. The relative simplicity of DNA and its stereotyped interactions has made it a focus of bottom-up approaches in recent years. While many arbitrary nanoscale two- and three-dimensional structures have now been designed using DNA, these materials have presented limitations with regard to the precision and low-error rate required for nanoscale manufacturing applications [1]. Proteins, on the other hand, generally fold into precisely defined native states with a high degree of accuracy and reproducibility and, as is demonstrated in their use in a wide range of structural components in nature, large protein assemblies can be very robust materials [2, 3]. Despite these advantages, the field of protein-based nanotechnology has been hindered by the relative complexity of proteins and their interactions. Our recent success in designing symmetric protein assemblies with atomic-level accuracy demonstrates the ability to overcome these limitations and opens the door to a new generation of protein-based nanomaterials [4-7].

Natural protein assemblies – and in fact nearly all naturally occurring structures composed of multiple copies of the same or similar building blocks – are assembled according to underlying principles of symmetry [8]. In symmetric architectures, chemically identical subunits find themselves in identical environments by making equivalent contacts with their neighbors. An important consequence is that only a small number of distinct types of interactions or subunit interfaces are required to hold symmetric assemblies together. This observation in fact best explains the prevalence of symmetric architectures in nature: they are easier or more likely to evolve. It also lays out fundamental ideas for how to think about the problem of designing self-assembling protein molecules: a building block must be designed to contain a certain number of symmetric interaction interfaces in some geometrically defined orientation. During the last three years we have used the NSF DMREF funding to exploit this principle to design both open (unbounded) and closed (bounded) symmetric assemblies. We summarize this work in the following section.

I Results from AFOSR Work

With AFOSR funding, the Baker lab has made several significant advances in the design of self-assembling protein nanomaterials. First, we developed general methods for modeling symmetric open and closed architectures within the publicly available and widely distributed Rosetta protein design software, allowing the design of two-component self-assembling tetrahedral nanocages [5]. We designed five 24-subunit cage-like protein nanomaterials in two distinct symmetric architectures and experimentally demonstrated that their structures are in close agreement with the computational design models (**Figure 1**).

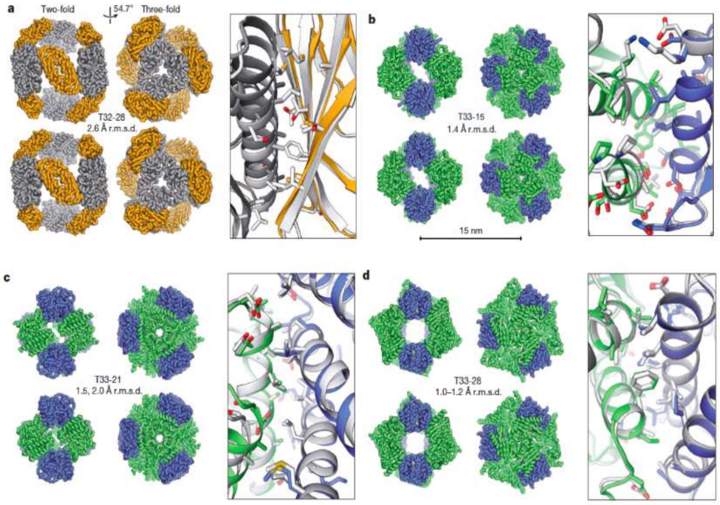

Figure 1 | Crystal structures of designed two-component protein nanomaterials. The computational design models (top) and X-ray crystal structures (bottom) are shown at left for T32-28 (a), T33-15 (b), T33-21 (c) and T33-28 (d). Views of each material are shown to scale along the two-fold and three-fold tetrahedral symmetry axes (scale bar at center, 15 nm). At right, overlays of the designed interfaces in the design models (white) and crystal structures (gray, orange, green and blue) are shown.

While these designed tetrahedra are important proofs of concept, the internal volume of such structures is too small for applications such as isolating enzyme systems inside their cavities. We therefore focused subsequent nanocage design work on developing approaches for designing self-assembling icosahedra with much larger interiors. We generalized the methods previously used to enable design of a 60-subunit, one-component (homomeric) protein icosahedron. Electron microscopy characterization of the designed protein expressed in *E. coli* revealed a homogenous population of icosahedral particles nearly identical to the design model (**Figure 2**). The particles are stable in 6.7 M guanidine hydrochloride (GuHCl) up to 80 °C, and undergo extremely abrupt but reversible disassembly between 2 M and 2.25 M guanidine thiocyanate (GITC). The icosahedron is robust to genetic fusions: one or two copies of superfolder green fluorescent protein (GFP) can be fused to each of the 60 subunits to create highly fluorescent standard candles for light microscopy [9], and a designed protein pentamer can be placed in the center of each of its twelve pentameric faces to potentially gate macromolecule access to the nanocage interior.

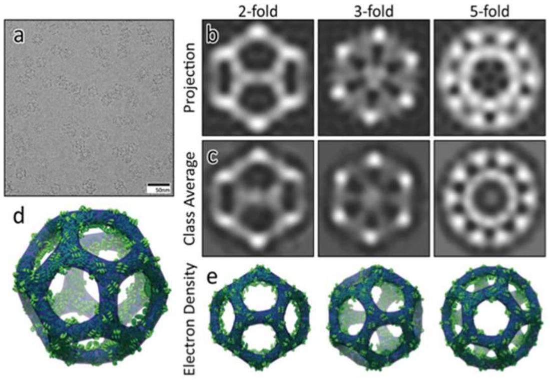

Figure 2 | Cryo-electron microscopy of a designed one-component icosahedron. a) Field of view micrographs showing monodisperse particles. b-c) Class averages along all three symmetry axes match projection images generated from the computational design model. d-e) Calculated density (blue) matches the design model (green) very well.

F

We then went on to computationally design and experimentally characterize co-assembling two-component 120 subunit icosahedral protein nanostructures with molecular weights (1.8 to 2.8 MDa) and dimensions (24 to 40 nm diameter) comparable to small viral capsids (Nature, in press). To achieve this capability, we generalized the symmetric architecture description within Rosetta to enable design of self-assembling two-component icosahedra (**Figure 3**).

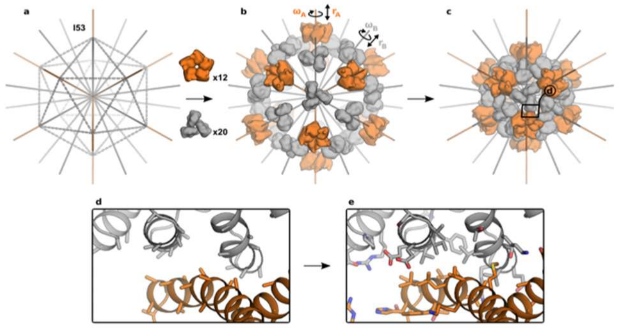

Figure 3 | Computational method for designing two-component self-assembling icosahedra. a) Icosahedral symmetry showing 5-fold (orange) and 3-fold (grey) axes. b-c) Components are aligned along their symmetry axes, and displacement and rotation is sampled. d-e) New protein-protein interfaces are designed between the subunits to drive self-assembly.

Ten designs spanning three distinct icosahedral architectures were found to form materials closely matching the design models. Comprising 120 subunits each, the designed icosahedra have molecular weights (1.8 to 2.8 MDa) and dimensions (240 to 400 Å diameter) comparable to those of small viral capsids (**Figure 4**). Electron microscopy, SAXS, and X-ray crystallography showed that ten designs spanning three distinct icosahedral architectures formed materials closely matching the design models. *In vitro* assembly of independently purified components revealed rapid assembly rates comparable to viral capsids and enabled controlled packaging of molecular cargo via charge complementarity. The ability to design megadalton-scale materials with atomic-level accuracy and controllable assembly opens the door to a new generation of genetically programmable protein-based molecular machines. The ability to design such large and complex structures with atomic-level accuracy presents exciting opportunities for a broad range of applications, including vaccines, targeted delivery, and bioenergy. A manuscript describing this work is in press at *Science* (See Ref below).

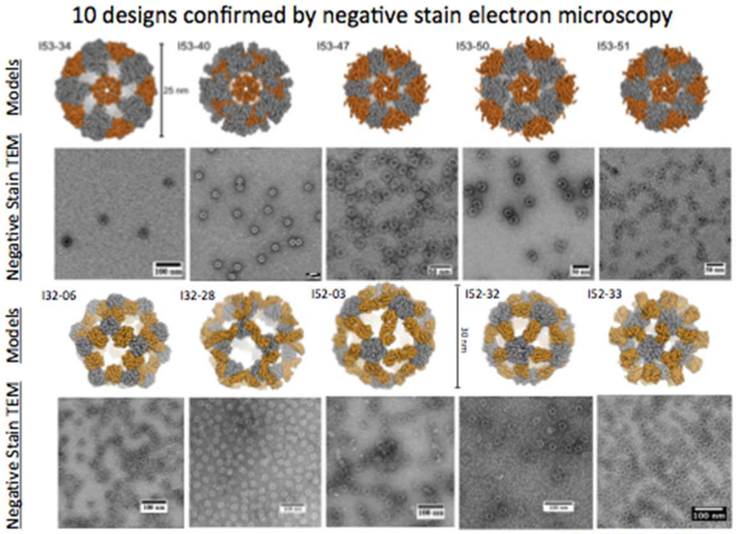

Shane Gonen, Tamir Gonen

Figure 4 | Electron microscopy of designed two-component icosahedra. TEM reveals homogenous fields of self-assembling two-component (gray and gold) icosahedral protein particles that match their respective design structures. The naming scheme for these protein nanoparticles is "I" for icosahedron, followed by the symmetry operator for components one and two (e.g., "I52" denotes an icosahedron with 5-fold and 2-fold symmetric components) and a unique identification number (e.g., "-03" is the third design in a series).

Next, we showed that our computational approach can also be used to design two-dimensional (2D) protein arrays (**Figure 5**). Protein homo-oligomers were placed into one of the seventeen 2D layer groups, the degrees of freedom of the lattice were sampled to identify configurations with shape-complementary interacting surfaces, and the interaction energy was minimized using sequence design calculations. We used the method to design proteins that self-assemble into layer groups P 3 2 1, P 4 2(1) 2, and P 6. Projection maps of micrometer-scale arrays, assembled both in vitro and in vivo, are consistent with the design models and display the target layer group symmetry. Such programmable 2D protein lattices should enable new approaches to structure determination, sensing, and nanomaterial engineering. This work was published in *Science* [10].

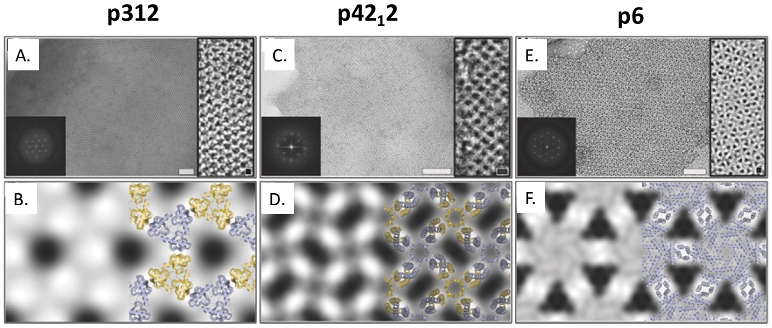

Figure 5 | Computationally designed proteins that self-assemble into unbound 2D arrays. We demonstrate one-component protein arrays with p312 (A and B), p4212 (C and D), and p6 (E and F) point symmetries. From top (A, C, E) to bottom (B, D, F) we show transmission electron micrographs of partially purified protein arrays expressed in E. coli, calculated Fourier transform electron diffraction patterns from the EM images, the calculated electron density map from Fourier transform data (inset), and superposition of the electron density map with the computer model for the designed

With AFOSR funding, we have also continued to refine and expand our computational design methods. In order to increase the percentage of designs passing our criteria for experimental testing, we have modified the energy function and search algorithms used during the initial docking stage of our design process to favor protein backbone configurations matching those of commonly observed interaction motifs found in high-resolution crystal structures in the Protein Data Bank, and have enabled the side chain conformations from these "motifs" to be added into our library of side chain conformations used during design. In addition, we have developed new algorithms to aid in the final refinement stages of the design process, bringing us closer to having a fully automated Rosetta design pipeline. We have also tested multiple methods of improving the solubility of our designs via redesign of solvent-exposed side chains. As published recently in *Protein Science*, redesign of side chains to increase the net charge on the individual components led to a variant of one of our designed two-component tetrahedra with significantly increased soluble yield [11]. This enabled us to determine the crystal structure of the design, which we were unable to obtain previously due to low yield of soluble protein. The crystal structure was found to match closely with our design model.

With the aforementioned breakthroughs in near atomic level accurate protein design of mega-dalton multi-component self assembling protein architectures, we next set out on a new endeavor to design such materials using fully de novo designed proteins of various topologies with atomic accuracy[12-14]. We have focused much of the *de novo* design effort on proteins composed of repeated modules similar to interlocking Lego® blocks. Such "repeat proteins" are common in the natural world, serving biological functions ranging from sensors to structural scaffolds. As a stepping stone to building nanomaterials from robust de novo designed building blocks we have developed general methods for designing novel idealized repeat proteins [12]. We have used these methods to investigate the space of folded structures that can be generated by tandem repetition of a simple helix–loop–helix–loop structural motif.

Eighty-three designs with sequences unrelated to known repeat proteins were experimentally characterized. Of these, 53 were monomeric and stable at 95 °C, and 43 had solution X-ray scattering spectra consistent with the design models. Crystal structures of 15 designs spanning a broad range of curvatures were in close agreement with the design models, with root mean square deviations ranging from 0.7 to 2.5 Å (**Figure 6**). Our results show that existing repeat proteins occupy only a small fraction of the available conformation space, and that it is possible to design totally new proteins with precisely specified geometries that go far beyond what nature has achieved. These results open up a wide array of new possibilities for biomolecular engineering.

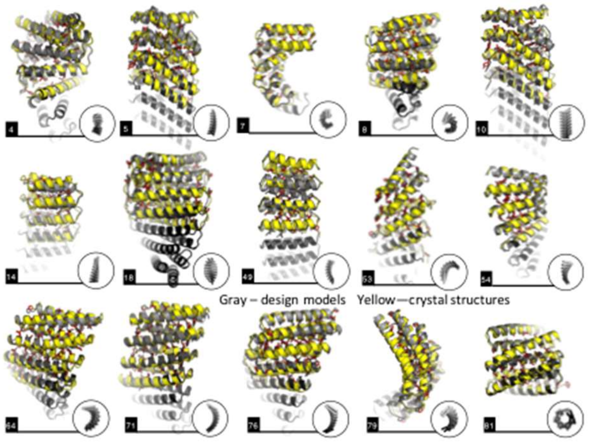

Figure 6 I Accurate design of *de novo* repeat protein architectures. Crystal structures of fifteen repeat protein designs are in close agreement with the design models. Crystal structures are in yellow, and the design models in gray. Insets in circles show the overall shape of the repeat protein. Hydrophobic side chain conformations observed in the crystal structures (red) are largely captured by the designs.

The design of protein-protein interfaces used to achieve self-assembling materials shown in Figures 1-5, and the interfaces between helical repeats shown in Figure 6 has largely been based on hydrophobic interactions found in natural protein-protein assemblies. We can also now design protein-protein interfaces with the logic of hydrogen bond networks such as those found in DNA [15], with the advantage of allowing self-assembling proteins to behave better in aqueous environments. Our first success in design of hydrogen bond networks was in the *de novo* design of small molecule binding proteins and biosensors where precisely positioned hydrogen bond donors or acceptors can provide the specificity and selectivity for high affinity binding to a small molecule target [16, 17]. More recently we have succeeded in developing computational Rosetta design methods (HBnet algorithms) for designing a wide range of protein homo-oligomers with specificity determined by modular arrays of central hydrogen bond networks. We used the approach to design dimers, trimers, and tetramers consisting of two concentric rings of helices, including previously not seen triangular, square, and supercoiled topologies. X-ray crystallography confirms that the structures overall, and the hydrogen bond networks in particular, are nearly identical to the design models, and the networks confer interaction specificity in vivo. The ability to design extensive hydrogen bond networks with atomic accuracy is a milestone for protein design and enables the programming of protein interaction specificity for a broad range of synthetic biology applications, including those that are responsive to changes in the chemistry of an aqueous environment (e.g. pH dependent switches).

Our recent results with one-component layers [10], two-component icosahedra, and modular repeat proteins represent major achievements in the field of nanomaterials. These results take us far beyond our initial proof of principle design targets, indicating that our overall approach and computational design methodologies are also likely to be successful when applied to the remaining symmetric architectures predicted by our theoretical rule set outline (described below). Furthermore, as our methods continue to improve, the rate at which we are able to create novel, successful designs is also increasing. In addition to a number of new designs that are currently being characterized, including two-component layers and three-component crystals, our improved methods have enabled us to more than double the number of successful designs created and confirmed year over year. Just as the manufacturing industry was revolutionized by creating interchangeable parts designed to precise specifications; custom designed protein modules with the right twist, turns, symmetric junctions, tuned linkers, and matched interfaces for modular self-assembly is a bold new direction for bioengineering nanomaterials.

With this vision in mind, we have designed, produced and validated a large number (50-100) of self-assembling protein nanopore scaffolds that are computationally predicted to be highly tolerant of follow-on modification to impart the ability to insert the nanopores into lipid-bilayer membranes and to sculpt their inner pores to impart biomolecule binding specificity. We are now applying Rosetta design protocols for self-assembling protein nanostructures designed *de novo* with either (i) hydrophobic protein-protein interfaces or (ii) interfaces based on hydrogen bond networks using HBnet [REF]. Protein nanopore assemblages can be produced either by in vitro mixing of purified recombinant components in solution (e.g., mixing purified single components of a multi-component assembly) or by expression in E. coli to achieve nanopore insertion into membranes with control features to ensure they do not kill the cells expressing them [18]. Once the nanopores are purified, they can then be subjected to detailed biophysical studies to corroborate that the designed materials have homogeneous nanostructures, and that the desired architecture has been achieved.

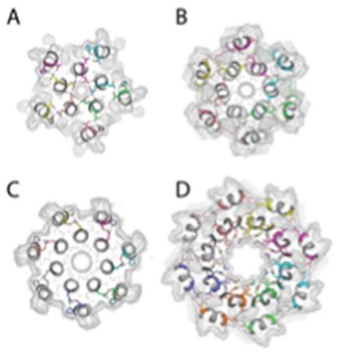

Figure 7 I Preliminary results on water-soluble porous helical bundle oligomers. Residues that form hydrogen bond networks are colored. (A) pentameric, (B) hexameric, (C) heptameric, and (D) octameric helical bundle oligomers define central channels with internal diameters ranging from approximately 5 Å to 15 Å.

Preliminary data demonstrates that we can build self-assembling porous oligomers using HBNet out of helical hairpin monomer subunits (**Figure 7**). The backbones of subunits consist of a short loop-connected inner and outer helix produced by varying the parameters in the Crick coiled coil-generating equations. HBNet was then used to search these backbones for hydrogen bond networks spanning the intermolecular interface. Rosetta sequence design calculations were carried out to optimize rotamers at the remaining residue positions in the context of the cyclic symmetry of the oligomer. Rosetta structure prediction calculations were used to investigate the extent to which the final designed sequences encode the desired structure; if the lowest-energy structures were similar to the design models, the designs were synthesized and experimentally characterized. Using this approach, porous helical bundle oligomers have been successfully created which define central channels with internal diameters ranging from approximately 5 Å for a pentamer to 15 Å for an octamer (**Figure 7**).

Finally, as a theoretical foundation for the aforementioned design work, we have used group theory to work out the geometric rules for assembling protein-based materials by combining together two symmetries (e.g., from two oligomers in a two-component design approach). The rules for designing closed cages were published earlier [19, 20]. The rules for designing extended two-dimensional layers have been worked out (**Table 1**) and will be published this year in a review article *in Current Opinion in Structural Biology*. A total of 36 distinct possibilities are articulated that can be formed by the combination of two oligomeric point groups (additional possibilities based on one-component systems related by a screw axis are not included in this number). For each entry we articulate the rigid body degrees of freedom that are available for relating the second symmetric oligomer to the first. For instance, the p422 layer design obtained by combining C2 and D2 requires the following relationship: 90°x, 45°z, shift[a,b,0]. The rotations describe how the second component symmetry (C2) must be rotated from its canonical orientation. The shift describes the translational degrees of freedom (two distances a and b in this case) for positioning the center of the second symmetry. This table of rules and degree-of-freedom specifications will make it possible for other researchers in the field to exploit the symmetry-based strategies we have developed in our work. Not listed here are rules for 79 three-dimensional crystalline materials that can be constructed following the same principles.

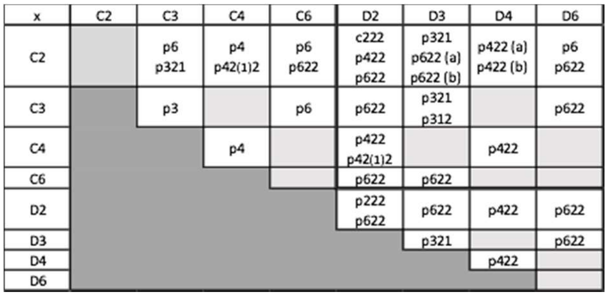

x	C2	C3	C4	C6	D2	D3	D4	D6
C2		p6 p321	p4 p42(1)2	p6 p622	c222 p422 p622	p321 p622 (a) p622 (b)	p422 (a) p422 (b)	p6 p622
C3		p3		p6	p622	p321 p312		p622
C4			p4		p422 p42(1)2		p422	
C6					p622	p622		
D2					p222 p622	p622	p422	p622
D3						p321		p622
D4							p422	
D6								

Table 1. Rules for creating extended 2D protein layers by combining two separate symmetries. Each entry describes a 2D layer group that can be formed by combining two simpler (finite) point group symmetries. The two component symmetries can derive from the separate point group symmetries of two types of oligomers in a two-component design strategy, or from the symmetry of a single oligomer in a one-component strategy combined with a symmetry group describing how multiple copies of that oligomer are related to each other. The two symmetry components must have specific orientations relative to each other, and non-coincident origins, following constraints that have been articulated for each case. Among the possible symmetries, three have been demonstrated in our recent work [10] and another was demonstrated earlier by Sinclair, *et al.* [21].

Summary

The information content embedded in protein polymers far exceeds traditional low complexity plastics and metals that make up all modern machines and materials. From light harvesting to gap junctions and ion channels, to spider web and silk, natural proteins have solved all of the problems faced during evolution. As fantastic as these natural proteins are, we know that evolution has only sampled a tiny fraction of structures, sequences, and functions that proteins are capable of achieving. Over the last several years, the Baker group has developed general computational design methods with Rosetta allowing the design of single- and two-component self-assembling protein nanomaterials with open 2-dimensional (**Figure 5**) and closed 3-dimensional architectures (**Figures 1-4**) in a growing variety of experimentally validated symmetries [4, 5, 10, 11]. For example, we have designed, produced and validated ten different two-component self-assembling icosahedral protein structures. These icosahedra span three distinct architectures, comprising of 120 subunits each, with molecular weights (1.8 to 2.8 MDa) and dimensions (240 to 400 Å diameter) comparable to those of small viral capsids, and all were found to form materials closely matching the design models. We have extended our design capabilities now into totally de novo designed proteins (**Figures 6-7**). In aggregate, with AFOSR funding we have made significant breakthroughs in computational protein design which lay the groundwork for computational design of 3D architectures that confine enzymes and enzyme systems to specific surfaces, orientations, and associated with chemical channels to achieve new molecular energy conversion systems planned for the next funding period.

References

1. Ko SH, Du K, Liddle JA: **Quantum-dot fluorescence lifetime engineering with DNA origami constructs**. *Angewandte Chemie* 2013, **52**(4):1193-1197. PMC#
2. Presenda A, Allred DB, Baneyx F, Schwartz DT, Sarikaya M: **Stability of S-layer proteins for electrochemical nanofabrication**. *Colloids Surf B Biointerfaces* 2007, **57**(2):256-261. PMC#
3. Goodsell DS, Olson AJ: **Structural symmetry and protein function**. *Annu Rev Biophys Biomol Struct* 2000, **29**:105-153. PMC#
4. King NP, Sheffler W, Sawaya MR, Vollmar BS, Sumida JP, Andre I, Gonen T, Yeates TO, Baker D: **Computational design of self-assembling protein nanomaterials with atomic level accuracy**. *Science* 2012, **336**(6085):1171-1174. PMC#
5. King NP, Bale JB, Sheffler W, McNamara DE, Gonen S, Gonen T, Yeates TO, Baker D: **Accurate design of co-assembling multi-component protein nanomaterials**. *Nature* 2014, **510**(7503):103-108. PMC#
6. Lai YT, Cascio D, Yeates TO: **Structure of a 16-nm cage designed by using protein oligomers**. *Science* 2012, **336**(6085):1129. PMC#
7. Lai YT, Reading E, Hura GL, Tsai KL, Laganowsky A, Asturias FJ, Tainer JA, Robinson CV, Yeates TO: **Structure of a designed protein cage that self-assembles into a highly porous cube**. *Nat Chem* 2014, **6**(12):1065-1071. PMC#PMC4239666
8. Ahnert SE, Marsh JA, Hernandez H, Robinson CV, Teichmann SA: **Principles of assembly reveal a periodic table of protein complexes**. *Science* 2015, **350**(6266):aaa2245. PMC#
9. Hsia Y, Bale JB, Gonen S, Shi D, Sheffler W, Fong KK, Nattermann U, Xu C, Huang PS, Ravichandran R, Yi S, Davis TN, Gonen T, King NP, Baker D: **Design of a hyperstable 60-subunit protein icosahedron**. *Nature* 2016. PMC#
10. Gonen S, DiMaio F, Gonen T, Baker D: **Design of ordered two-dimensional arrays mediated by noncovalent protein-protein interfaces**. *Science* 2015, **348**(6241):1365-1368. PMC#
11. Bale JB, Park RU, Liu Y, Gonen S, Gonen T, Cascio D, King NP, Yeates TO, Baker D: **Structure of a designed tetrahedral protein assembly variant engineered to have improved soluble expression**. *Protein science : a publication of the Protein Society* 2015, **24**(10):1695-1701. PMC#PMC4594668

12. Brunette TJ, Parmeggiani F, Huang PS, Bhabha G, Ekiert DC, Tsutakawa SE, Hura GL, Tainer JA, Baker D: **Exploring the repeat protein universe through computational protein design**. *Nature* 2015, **528**(7583):580-584. PMC#
13. Huang PS, Feldmeier K, Parmeggiani F, Fernandez Velasco DA, Hocker B, Baker D: **De novo design of a four-fold symmetric TIM-barrel protein with atomic-level accuracy**. *Nature chemical biology* 2016, **12**(1):29-34. PMC#PMC4684731
14. Huang PS, Oberdorfer G, Xu C, Pei XY, Nannenga BL, Rogers JM, DiMaio F, Gonen T, Luisi B, Baker D: **High thermodynamic stability of parametrically designed helical bundles**. *Science* 2014, **346**(6208):481-485. PMC#
15. Boyken SE, Chen Z, Groves B, Langan RA, Oberdorfer G, Ford A, Gilmore JM, Xu C, DiMaio F, Pereira JH, Sankaran B, Seelig G, Zwart PH, Baker D: **De novo design of protein homo-oligomers with modular hydrogen-bond network-mediated specificity**. *Science* 2016, **352**(6286):680-687. PMC#
16. Tinberg CE, Khare SD, Dou J, Doyle L, Nelson JW, Schena A, Jankowski W, Kalodimos CG, Johnsson K, Stoddard BL, Baker D: **Computational design of ligand-binding proteins with high affinity and selectivity**. *Nature* 2013, **501**(7466):212-216. PMC#3898436
17. Griss R, Schena A, Reymond L, Patiny L, Werner D, Tinberg CE, Baker D, Johnsson K: **Bioluminescent sensor proteins for point-of-care therapeutic drug monitoring**. *Nature chemical biology* 2014, **10**(7):598-603. PMC#
18. Gurnev PA, Nestorovich EM: **Channel-forming bacterial toxins in biosensing and macromolecule delivery**. *Toxins (Basel)* 2014, **6**(8):2483-2540. PMC#PMC4147595
19. Padilla JE, Colovos C, Yeates TO: **Nanohedra: using symmetry to design self assembling protein cages, layers, crystals, and filaments**. *Proceedings of the National Academy of Sciences of the United States of America* 2001, **98**(5):2217-2221. PMC#PMC30118
20. Lai YT, King NP, Yeates TO: **Principles for designing ordered protein assemblies**. *Trends Cell Biol* 2012, **22**(12):653-661. PMC#
21. Sinclair JC, Davies KM, Venien-Bryan C, Noble ME: **Generation of protein lattices by fusing proteins with matching rotational symmetry**. *Nat Nanotechnol* 2011, **6**(9):558-562. PMC#

Doubling the cross-linking interface of a rationally-designed beta roll peptide for calcium-dependent proteinaceous hydrogel formation

Introduction

Protein-based biopolymer hydrogels composed of three-dimensionally cross-linked macroscopic networks have been widely investigated for a host of applications in the biomedical field because of their biocompatibility, predictable erosion rates, and tunable viscoelastic properties.[1-5] Several excellent reviews are available that detail protein and peptide-based self-assembly strategies.[6-11] Biomolecules with the ability to respond “intelligently” to external stimuli such as pH, temperature, ionic strength or light are often incorporated into monomeric polymer building blocks to trigger or disrupt self-assembly through a variety of mechanisms.[12-14] Calmodulin, elastin-like polypeptides, and α-helical leucine zipper domains have been used to actuate hydrogel formation in response to environmental cues, leading to successful implementation into microfluidic systems, biosensors, and vehicles for controlled release.[1,5,15-20]

We have previously reported a rationally designed peptide based on the beta roll (β-roll) domain that functions as a stimulus-responsive cross-linker for calcium dependent hydrogel formation.[21] The β-roll scaffold was taken from the block V repeats-in-toxin (RTX) domain of adenylate cyclase from *Bordetella pertussis*.[22] It is a modular, repeating polypeptide that undergoes a reversible structural rearrangement in response to calcium. The peptide is apparently intrinsically disordered in the absence of calcium and folds into a β-roll in calcium rich environments consisting of two parallel β-sheet faces separated by flexible turn regions (Figure 1a).[22,23] Conserved aspartic acid residues in the turn regions are responsible for coordinating calcium ions. Only a C-terminal capping group is required for calcium-induced folding of the polypeptides.[24,25]

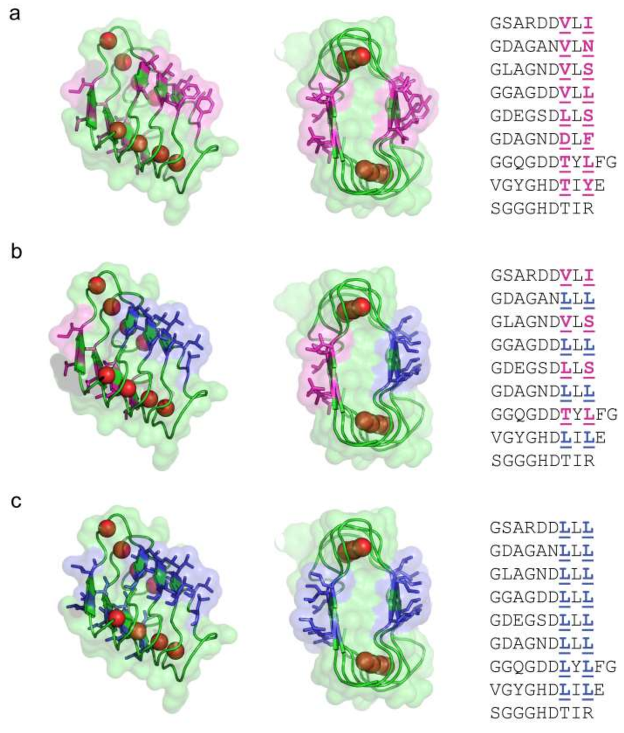

Figure 1. Homology models for WT and mutant β-roll domains with primary sequences. Homology models for WTβ (a), Leuβ (b), and DLeuβ (c) domains were generated with SWISS-MODEL (Swiss Institute of Bioinformatics) using a β-roll-containing lipase as a template (PDB 2Z8X). Side and top-down views are given for each construct in the folded conformation with the red spheres representing bound calcium ions. The side chains of the surface exposed residues are highlighted and underlined in the primary sequences. The amino acids in magenta represent the wild-type residues and the blue amino acids represent the rational leucine mutations. All images were rendered in PyMOL.

Each β-sheet face in the folded conformation contains eight residues with solvent exposed side chains that project radially away from the hydrophobic core. In our previous study, we mutated one β-sheet face to contain leucine residues at these eight positions (Figure 1b). We fused the mutant leucine β-roll (Leuβ) to a self-assembling α-helical leucine zipper domain (H) and a randomly coiled hydrophilic linker (S) which is included to provide flexibility and prevent aggregation. Both H and S domains have been extensively characterized previously.[26-28] Without calcium, the helices form tetrameric coiled-coil bundles, but the β-roll domains remain unstructured, delocalizing the leucine-rich patches and prohibiting HS-Leuβ supramolecular self-assembly. After calcium binding, the β-roll folds and the leucine-rich faces are exposed creating a hydrophobic driving force for oligomerization (Figure 2a). The resulting calcium-responsive hydrogel networks have been characterized using a variety of techniques.[21]

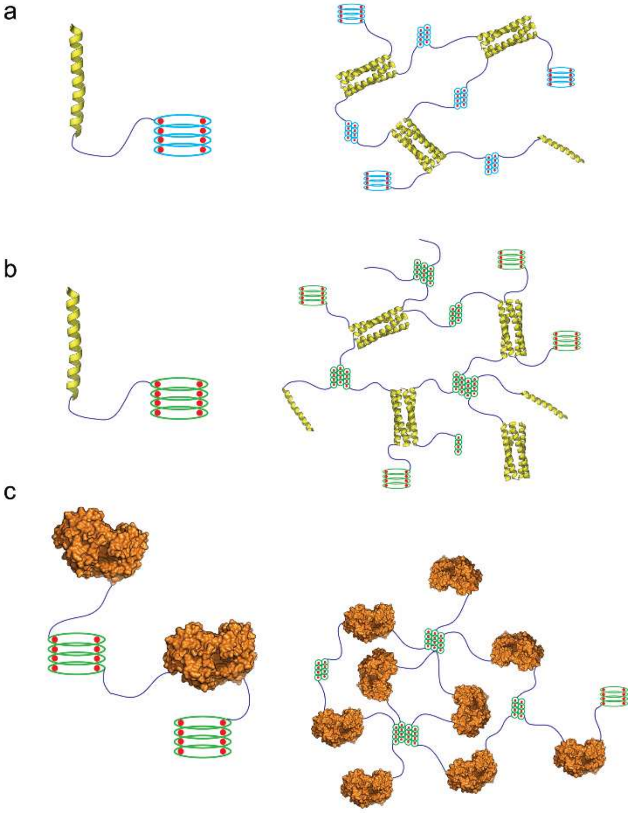

Figure 2. Monomeric polymer building blocks and assembled hydrogel networks. All cartoons represent β-roll domains in the folded conformation after calcium (red) binding. (a) HS-Leuβ monomer composed of an α-helical leucine zipper (yellow), a randomly coiled linker (purple), and the mutant Leuβ (light blue). The assembled network depicts an association number of 2 for

Leuβ. (b) HS-DLeuβ monomer composed of an α-helix, linker, and DLeuβ mutant (green). Association numbers of > 2 are depicted. (c) MBP-DLeuβ-MBP-DLeuβ monomer. The DLeuβ can achieve higher oligomerization states and does not require cross-linking provided by the helical bundles. MBP is a monomeric protein and does not naturally self-assemble. Alpha-helices and MBP were rendered in PyMOL using PDB files 1GCL and 1YTV, respectively.

In this study, we have expanded this approach by further engineering the Leuβ peptide to increase its cross-linking capacity. The folded β-roll domain consists of two β-sheet faces, each with eight solvent exposed residues. We have now rationally engineered a "double-faced" leucine β-roll peptide (DLeuβ) such that all sixteen positions are leucines (Figure 1c). This should enable cross-linking on both sides of the folded construct simultaneously, thereby increasing the potential oligomerization state and cross-linking density (Figure 2b). Previously, Leuβ domains were approximated to have an association number of 2 (Figure 2a), which required significant protein concentrations (60 mg/mL) and additional cross-linking moieties to assemble into supramolecular networks. We hypothesize that DLeuβ will self-assemble at lower weight percentages as concentration dependent sol-gel transition and oligomerization state of the cross-linking domain are directly related.[28] Further, DLeuβ should be able to induce calcium-dependent self-assembly without the additional cross-linking provided by the α-helical leucine zippers. Circular dichroism (CD), fluorescence resonance energy transfer (FRET) and bis-ANS binding were used to ensure DLeuβ folds in a similar manner as the wild type β-roll (WTβ) and Leuβ in response to calcium. The mechanical properties of HS-DLeuβ were analyzed using a microrheology technique and compared to results obtained previously for HS-WTβ and HS-Leuβ.[21] Finally, the utility of the DLeuβ as a stand-alone cross-linking domain was assessed by creating fusions to maltose binding protein (MBP) and analyzing the resulting hydrogel networks (Figure 2c).

Experimental Section

Materials

Amylose resin, the MBP expression kit, and all enzymes for DNA cloning were purchased from New England Biolabs (Ipswich, MA). Isopropyl β-D-1-thiogalactopyranoside (IPTG) and ampicillin sodium salt were purchased from Gold Biotechnology (St. Louis, MO). Amicon centrifugal filters were purchased from Millipore (Billerica, MA). All materials for polyacrylamide gel electrophoresis (PAGE) experiments as well as 1 μm Nile Red FluoSpheres for particle tracking were purchased from Life Technologies (Grand Island, NY). All oligonucleotides were purchased from Integrated DNA Technologies (Coralville, IA). BL21 *E. coli* cells were purchased from Bioline (Taunton, MA). All other reagents were purchased from Sigma-Aldrich (Sr. Louis, MO) unless otherwise stated.

Cloning into the pMAL expression plasmid

Cloning and expression of the WTβ and Leuβ constructs have been described previously.[21] The DLeuβ peptide was assembled by annealing and extending two overlapping oligonucleotides encoding for the entire gene. The C-terminal cap of the β-roll domain was amplified from the pDLE-9-cyaA plasmid, a gift from Dr. Daniel Ladant (Institut Pasteur, Paris, France), and appended to the DLeuβ gene by overlap extension PCR.[22] KpnI and HindIII restriction sites were added for ligation into a modified pMAL plasmid containing a self-cleaving intein, a gift from Dr. David Wood (Ohio State University, Columbus, OH).[29] DLeuβ was also cloned into the same pMAL-Intein backbone modified with an α-helical domain (H) and a soluble linker (S) from the pQE9AC10Acys plasmid, a gift from Dr. David Tirrell (California Institute of Technology, Pasadena, CA).[26] The resultant constructs, pMAL-Intein-DLeuβ and pMAL-Intein-HS-DLeuβ were transformed into BL21 *E. coli* cells for expression.

Concatemers of MBP and DLeuβ (Figure 2c) were cloned into the pMAL-c4e vector backbone. DLeuβ with the C-terminal cap was amplified out of pMAL-Intein-DLeuβ construct and cloned using EcoRI and BamHI restriction sites. MBP was amplified from the pMAL-c4e construct and inserted after DLeuβ-Cap via BamHI and SalI restriction sites. Lastly, the second DLeuβ-Cap was amplified and cloned using SalI and HindIII restriction sites, resulting in the final construct: pMAL-MBP-DLeuβ-MBP-DLeuβ. During this cloning process, we also created the construct pMAL-MBP-DLeuβ to be used as a negative control.

Expression & Purification of DLeu Constructs

All DLeuβ constructs were expressed identically in Terrific Broth (TB) supplemented with 100 µg/mL ampicillin and 2 g/L D-glucose. Saturated 10 mL overnight cultures containing the appropriate transformed cells were diluted in 1 L of sterilized TB and grown at 37 °C and shaken at 220 RPM. Once the optical density (OD) at 600 nm reached 0.6, protein expression was induced with IPTG to a final concentration of 0.3 mM. Expression was carried out for either 5 h at 37 °C or 16 h at 25 °C after which cells were harvested via centrifugation at 5,000 x g for 10 min. Cell pellets were resuspended in 50 mL MBP column buffer (20mM Tris-HCl, 200mM NaCl, 1 mM EDTA, pH 7.4) per L of culture. Expressed protein was liberated from the cells by microtip sonication for 6 min on ice (Sonicator 3000, QSonica, Newtown, CT). Cell debris and insoluble protein were collected via centrifugation at 15,000 x g for 30 min and discarded. Soluble protein was diluted five-fold in MBP column buffer and loaded onto equilibrated amylose resin drip columns. The columns were washed to remove any nonspecifically bound protein. MBP-DLeuβ and the concatemers were eluted with maltose and further purified on a Superdex HiLoad 16/60 size exclusion chromatography column (GE Healthcare). Columns containing proteins with the intein domain were saturated with intein cleaving buffer (137 mM NaCl, 2.7 mM KCl, 8.1 mM Na_2HPO_4, 1.76 mM KH_2PO_4, 40 mM bis-Tris, 2 mM EDTA, pH 6.2), capped, and incubated at 37 °C for 12-16 h. Cleaved fusion proteins were eluted with 50mL of MBP column buffer and concentrated using either 10 or 30 kDa MWCO centrifugal filter devices. The samples were buffer exchanged into 20 mM bis-Tris, 25 mM NaCl, pH 6.0 and loaded onto a 16/10 Q FF ion exchange column (GE Healthcare). Target proteins were eluted using a linear NaCl gradient from 25 mM to 500 mM NaCl over 20 column volumes. Protein concentration was determined by absorbance at 280 nm using calculated extinction coefficients. Purified protein fractions were pooled, concentrated, and buffer exchanged into the appropriate assay buffer. Purity and molecular weight for HS hydrogel forming constructs were confirmed by SDS-PAGE and MALDI-MS.

Circular Dichroism Spectroscopy

100 µM β-roll samples were loaded into a 0.1 mm path length quartz cuvette and analyzed on a J-815 CD spectrometer (Jasco, Easton, MD). The temperature was held constant at 25 °C by a Peltier junction temperature controller. Samples were incubated in the presence or absence of $CaCl_2$ prior to analysis. All experiments were performed in triplicate in 50 mM Tris

pH 7.4. Titration data were fit to the Hill equation using SigmaPlot (Systat Software, San Jose, CA) nonlinear regression software.

Bis-ANS Dye Binding

1 μM β-roll samples were prepared in 50 mM Tris pH 7.4 in the presence and absence of 50 mM $CaCl_2$ prior to the addition of 5 μg / mL bis-ANS dye. Samples were loaded into a 1 cm path length UV cuvette and analyzed on a SpectraMax M2 cuvette reader (Molecular Devices, Sunnyvale, CA). Fluorescence emission was monitored from 420 nm to 600 nm following excitation at 390 nm. All measurements were performed in triplicate.

Fluorescence Resonance Energy Transfer (FRET)

1 μM β-roll samples were prepared in 20 mM PIPES pH 6.8 supplemented with 120 mM NaCl and 10 mM KCl. A terbium (III) chloride stock solution was prepared in the same buffer. β-roll samples were titrated with increasing amounts of terbium in 96 well microtiter plates and incubated at 25 °C for 30 min prior to analysis. Tyrosine residues in the β-roll domain were excited at 282 nm and the fluorescence emission from bound terbium ions was monitored at 545 nm. All data were collected in triplicate.

Hydrogel Preparation

All β-roll samples were prepared in a similar manner. 500 μL of diluted protein samples were lyophilized in 5 mM Tris pH 7.4 supplemented with $CaCl_2$ or $MgCl_2$. Self-assembly was initiated by reconstituting the lyophilized protein in 1/10 the original volume resulting in 4-6 wt% protein in 50 mM Tris pH 7.4. Mechanical mixing, vortexing, and centrifugation were used to ensure all of the lyophilized protein was rehydrated. Samples were allowed to set at room temperature for 30 min prior to analysis.

Microrheology

Passive microrheology experiments were performed as previously described with minor modifications.[21] When rehydrating lyophilized protein for particle tracking experiments, ddH_2O was supplemented with 1μm FluoSpheres conjugated with Nile Red. The samples were mixed, loaded onto a glass slide and sealed with a coverslip. Particle motion was tracked using an Olympus IX81 motorized inverted microscope with a 40 X objective. A high-speed Hamamatsu C9300 digital camera was used to record individual particle trajectories at an exposure time of 33 ms. 300 frames of video were recorded at 30 frames per second for each run. 3 runs were recorded per sample to ensure a good statistical average. All runs were recorded on a ThorLabs air table to eliminate ambient vibrational noise. All videos were analyzed using MetaMorph software and converted to TIFF stacks in ImageJ.[30] Particle tracking and rheological analysis were completed in Interactive Data Language (IDL) software using algorithms created by Crocker et al.[31-34] Mean square displacement (MSD) plots were generated and used to compare the mechanical properties of the prepared samples.

Results

DLeuβ Characterization

The rationally designed "double-faced" leucine β-roll was expressed, purified, and characterized by CD, bis-ANS dye binding, and terbium binding assays to evaluate its response to calcium and self-assembly capability. We have previously characterized the WTβ and Leuβ using these same techniques.[21] 100 μM samples of purified protein were analyzed by CD in the presence and absence of 10 mM $CaCl_2$. The resulting spectra are shown in Figure 3a-c for WTβ, Leuβ, and DLeuβ constructs, respectively. All three proteins demonstrated similar conformational changes in response to calcium. In calcium-free environments, the spectra exhibited large negative peaks at 198 nm, which is indicative of randomly coiled peptide. Significant changes in secondary structure were observed in 10 mM $CaCl_2$ for all β-roll domains. A random coil to β-sheet transition was evidenced by the emergence a negative peak at 218 nm and is consistent with previous reports.[24] Slight variations in the CD spectra were most likely caused by small amounts of contamination in the samples from the recombination expression process. A titration was performed by monitoring the CD signal at 218 nm over a range of $CaCl_2$ concentrations to elucidate the calcium binding parameters for each peptide (Figure 3d). The data were fit to the Hill equation and the resulting parameters are summarized in Table 1. Leuβ and DLeuβ bound calcium with affinities similar to the wild type peptide and all constructs exhibited cooperative binding with Hill coefficients (n_H) > 1.

Bis-ANS is a commonly used molecular probe that binds to protein surfaces through hydrophobic interactions causing in an increase in fluorescence.[35] It can be used to detect changes in protein structure and has been previously used to examine the structural transition of β-roll peptides in response to calcium binding.[21,24] Purified DLeuβ was incubated with bis-ANS in the presence and absence of calcium. Significant increases in fluorescence were observed in the calcium-rich samples indicating a disordered to folded transition.

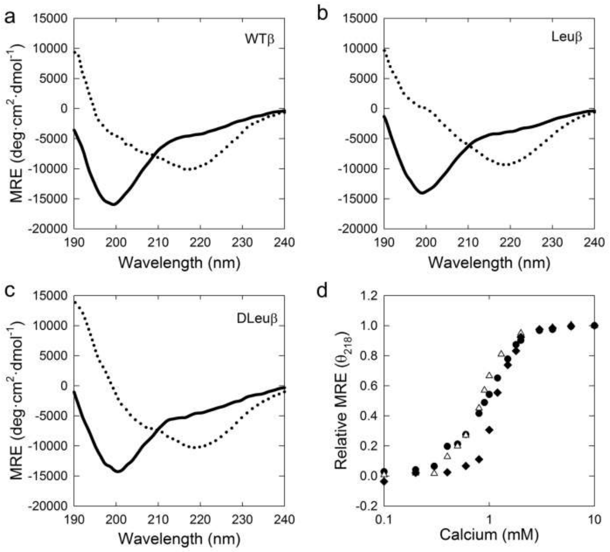

Figure 3. β-roll CD characterization. Mean residue ellipticity (MRE) were plotted over a range of wavelengths for WTβ (a), Leuβ (b), and DLeuβ (c) in the presence (• • •) and absence (—) of 10 mM $CaCl_2$. (d) Relative MRE at 218 nm for WTβ (●), Leuβ (Δ), and DLeuβ (♦) were plotted over a range of calcium concentrations. All data were collected in triplicate in 50 mM Tris pH 7.4. Titration data were fit to the Hill equation using non-linear regression software. The calcium binding parameters are summarized in Table 1.

Construct	K_D (mM)	n_H	R^2

WT	0.91 ± 0.02	2.3 ± 0.1	0.997
Leu	0.82 ± 0.01	3.1 ± 0.1	0.998
DLeu	1.18 ± 0.02	4.6 ± 0.3	0.998

Table 1 – Calcium binding properties for WTβ, Leuβ, and DLeuβ peptides.

Terbium, a fluorescent calcium analog, was shown previously to trigger β-roll folding.[21,24] In the folded conformation, bound terbium ions are in close proximity to a tyrosine residue in the 7th repeat of the β-roll. Excitation of the tyrosine residue results in a fluorescence emission from the terbium ion proportional to the distance between the two.[36] A terbium titration was performed while monitoring this fluorescence emission. While this does not directly report calcium-induced folding, it is consistent with the CD and bis-ANS data suggesting that the DLeuβ mutant retains its intrinsic stimulus-responsive conformational behavior.

HS-DLeuβ Microrheology

An α-helical leucine zipper domain (H) and an unstructured hydrophilic linker (S) were appended to the N-terminus of the DLeuβ (Figure 2b). We previously demonstrated that this N-terminal fusion does not interfere with β-roll folding in response to calcium.[21] Self-assembly into non-covalently cross-linked supramolecular networks was analyzed by passive microrheology. Time averaged mean square displacements (MSD) of 1 μm fluorescent particles embedded into the samples were calculated over a range of lag times. The dynamics of the embedded particles report the mechanical properties of the surrounding microenvironment. In a purely viscous fluid, the tracer particles are allowed to freely diffuse and the MSD scales linearly with the lag time (τ). In an elastic medium, the MSD becomes independent of lag time and is characterized by a pronounced plateau over a sampled time domain.[32,37] [33] Initial experiments were conducted at 6 wt%, the concentration at which HS-Leuβ self-assembles in calcium rich environments. It should also be noted that 6 wt% HS-WTβ remained viscous regardless of the calcium concentration in our previous study.[21] The results from the 6 wt% experiments are provided in Figure 4. HS-DLeuβ remained viscous in 50 mM $MgCl_2$ at 6 wt% and assembled into elastic network in the presence of 50 mM $CaCl_2$ over the explored time domain (Figure 4a). An image of the assembled hydrogel is provided in Figure 4e.

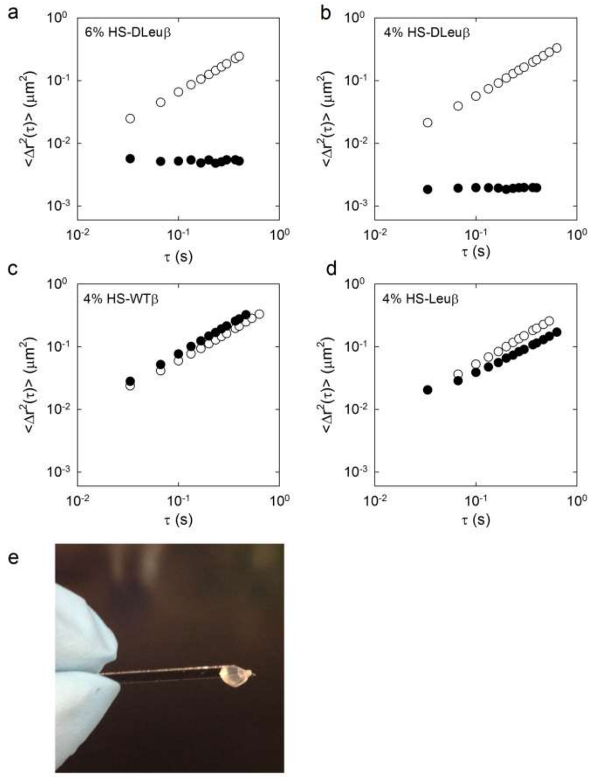

Figure 4. Time averaged MSD measurements for HS-β-roll constructs. 6 wt% (60 mg/mL) HS-DLeuβ MSD measurements in the presence of 50 mM magnesium (○) and 50 mM calcium (●) are given in panel (a). Identical experiments were performed at 4 wt% (40 mg/mL) for HS-DLeuβ (b), HS-WTβ (c), and HS-Leuβ (d). Only the HS-DLeuβ construct underwent a sol-gel transition in response to calcium at 4 wt%. Panel (e) shows an image of 6 wt% HS-DLeuβ in 50 mM $CaCl_2$ suspended on a glass coverslip.

The rheology experiments were repeated at lower weight percentages to explore the lower critical protein concentration required for HS-DLeuβ self-assembly. The results at 4 wt% are shown in Figure 4b-d. Again, the HS-WTβ construct remained viscous in both magnesium and calcium rich solutions (Figure 4c). HS-Leuβ appeared largely viscous in both magnesium and calcium as well (Figure 4d). HS-DLeuβ remained viscous in magnesium and self-assembled into an elastic network over the sampled time domain in the presence of calcium (Figure 4b), similar to that observed at 6 wt%.

To further explore the utility of the DLeuβ peptide and to take full advantage of the dynamic conformational response of the β-roll domain, we characterized the mechanical properties of 6 wt% HS-DLeuβ at varying calcium concentrations. Since self-assembly is mediated by β-roll folding, viscoelastic intermediate materials should be generated by using calcium concentrations in the dynamic range of β-roll folding. Figure 5 demonstrates the transition of 6 wt% HS-DLeuβ from largely viscous at low calcium concentrations to largely elastic at 10 mM calcium in the time range sampled. Interestingly, a viscoelastic intermediate was observed at 5 mM calcium.

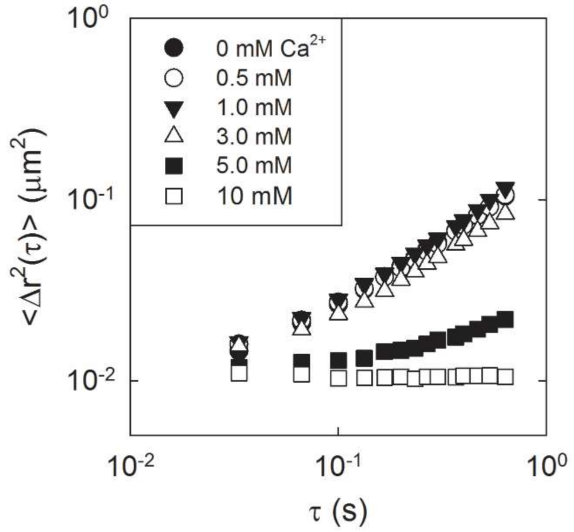

Figure 5. Time averaged MSD measurements at various calcium concentrations for HS-DLeuβ. 6 wt% (60 mg/mL) HS-DLeuβ samples were prepared in increasing $CaCl_2$ concentrations. The MSD measurements in 0 mM (●), 0.5 mM (○), 1.0 mM (▼), 3.0 mM (△), 5.0 mM (■), and 10 mM (□) calcium are given. A transition from linear increases in MSD with respect to lag time in low calcium concentrations to a more pronounced plateau at higher calcium concentrations was observed.

MBP-DLeuβ Concatemer Microrheology

In order to assess the utility of DLeuβ as a stand-alone cross-linking domain, we genetically constructed concatemers of DLeuβ and MBP. The monomeric block is shown in Figure 2c. In this case, the linkers are either composed of a poly-asparagine linker at the C-terminus of MBP or the unstructured capping group at the C-terminus of DLeuβ. Significantly higher weight percentages were required (21.3 wt%) to maintain the same molar concentration of cross-linking content used in the 6 wt% HS-β-roll experiments. Rheological analysis was performed as described above and the results are provided in Figure 6a. A clear sol-gel transition was observed in the presence of calcium, demonstrated by the lag time independence of the MSD, when compared to the magnesium control. A photograph of the cross-linked hydrogel suspended on a glass coverslip is provided in Figure 6c. Rheological analyses were also performed on samples with identical molar cross-linking content as the 4 wt% HS-β-roll experiments (14.2 wt%), and similar results were obtained. The MSD of samples prepared in the absence of calcium remained largely linear with respect to lag time while samples prepared in 50 mM calcium self-assembled into hydrogel networks in the time scales explored (Figure 6b).

To supplement this data, the rheological properties of a truncated monomeric unit containing only one cross-linking domain (MBP-DLeuβ) were tested in the presence and absence of calcium at 21.3 wt% and 14.2 wt%. As expected, these samples remained visually viscous, regardless of protein or calcium concentration, which is consistent with the MSD data.

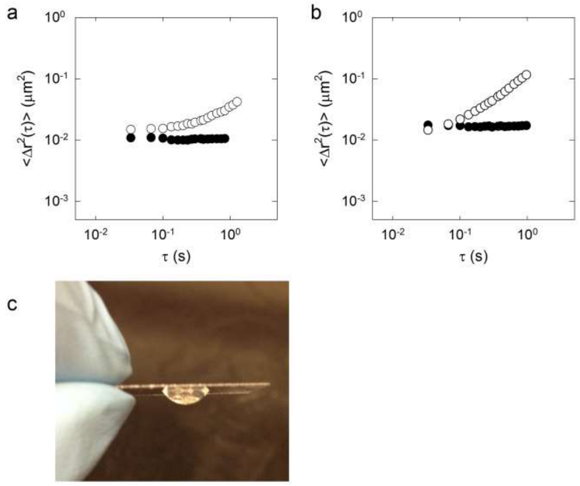

Figure 6. Time averaged MSD measurements for DLeuβ-MBP concatemers. Panel (a) provides MSD measurements for 21.3 wt% DLeuβ-MPB concatemers in the presence of 50 mM magnesium (○) and 50 mM calcium (●). The increased weight percentage was necessary to normalize the molar cross-linking content to the 6 wt% samples described previously. Panel (b) shows an identical experiment performed at 14.2 wt%, normalized to the molar cross-linking content of the 4 wt% samples described in Figure 4. Panel (c) shows an image of 21.3 wt% DLeuβ-MBP concatemer in the presence of 50 mM calcium suspended on a glass coverslip.

Discussion

In this work, we have rationally engineered a stimulus-responsive cross-linking peptide by exploiting the calcium induced conformational change intrinsic to the β-roll domain. The Leuβ and DLeuβ peptides require low millimolar concentrations of calcium to trigger self-assembly, which affords tight control over the gelation process. Additionally, viscoelastic properties can be allosterically regulated by simply adjusting the calcium concentration. Several biophysical techniques were used to investigate the structural responses of the mutant peptides to calcium, the lower critical protein concentration required for self-assembly, and the mechanical properties of the resulting supramolecular networks.

We have shown previously that mutating one face of the β-roll peptide (Leuβ) has minimal impact on the affinity for calcium or the structural rearrangement induced upon calcium binding.[21] By mutating both faces to contain leucine residues (DLeuβ), we have substantially increased the solvent exposed hydrophobic surface area of the folded construct. Despite the significant increase in hydrophobicity, no observable effects on protein solubility were detected for DLeuβ when compared to the other two constructs. Similar CD spectra were obtained in the presence and absence of 10 mM calcium for all three β-roll peptides indicating a disordered to β-sheet transition (Figure 3a-c). CD titration data were fit to the Hill equation, which assumes a two state binding model (disordered and folded) and multiple calcium binding sites. Fits from the titration data yielded similar affinities for calcium (~1 mM), however larger variations in the Hill coefficients, a measure of ligand binding cooperativity, were observed. Interestingly, both mutants bind calcium with a higher cooperativity than WTβ (Table 1), however the relationship between solvent exposed hydrophobicity and Hill coefficient is not entirely clear. The data suggested that higher calcium concentrations were required to initiate folding, especially for the double mutant. The increased hydrophobicity of the DLeuβ may non-specifically stabilize the peptide in the disordered conformation.

Bis-ANS dye binding experiments were used to supplement the CD data and ensure the DLeuβ mutant retained the calcium binding properties intrinsic to the WTβ domain. Significant increases in fluorescence emission were detected in calcium rich solutions as compared to spectra obtained in the absence of calcium. This increase in fluorescence can be attributed to an increase in hydrophobic surface area amenable to dye binding caused by calcium-induced folding. These results are in agreement with previously reported data for WTβ and Leuβ.[21,24] Terbium binding assays were also conducted to further ensure the performance of the DLeuβ mutant. Increases in fluorescence emission were observed with increasing terbium concentration, plateauing around 200 μM. Near identical hyperbolic responses were observed for WTβ and Leuβ.[21] However, it is important to note that while terbium acts as a calcium analog, it does not directly report calcium affinity. Taken together, the CD, bis-ANS, and terbium binding data suggest that all three constructs bind calcium in a similar manner resulting in a transition from a disordered state to a spatially organized β-roll structure.

After the preliminary characterization was completed, the self-assembly capabilities of DLeuβ were assessed by two separate approaches. First we expanded our previous study by appending an α-helical leucine zipper domain (H) and a soluble linker (S) to the N-terminus of DLeuβ (Figure 2b). Microrheology experiments performed at 6 wt% confirmed HS-DLeuβ self-assembly into an elastic network in 50 mM $CaCl_2$ while remaining a viscous liquid in 50 mM $MgCl_2$ in the time domain explored (Figure 4a). These experiments verified what we have previously observed with Leuβ. In the absence of calcium, the data are consistent with a viscous solution, meaning the tracer particles can freely diffuse through the medium and $<r^2(\tau)>$ increases linearly with τ. The helical domains can assemble into tetrameric coiled-coil bundles, but the unstructured β-roll domains prohibit the formation of an elastic network. In response to increasing calcium concentrations, the designed β-roll domains begin to fold thus providing a driving force for self-assembly. The viscosity of the medium increases causing a markedly slower growth rate of MSD vs. τ and a pronounced plateau in the observable time range. In 50 mM $CaCl_2$, we expect the β-roll domains to be fully folded thus localizing the leucine side chains into a structurally well-defined surface suitable for cross-linking.

In our earlier work, the Leuβ peptide contained leucine residues on only one face of the folded β-helix which yielded a potential association number of 2 (Figure 2a).[21] This required protein concentrations of 60 mg/mL (6 wt%) to induce self-assembly. At lower concentrations, there were not enough cross-links to sustain an elastic network. We hypothesized that by designing a β-roll peptide with cross-linking interfaces on both sides of the folded construct, the oligomerization state could potentially be increased (Figure 2b). Association numbers higher than 2 should facilitate self-assembly at lower protein concentrations. To investigate this, we prepared 40 mg/mL (4 wt%) samples of HS-WTβ, HS-Leuβ, and HS-DLeuβ. Self-assembly was observed only for the HS-DLeuβ sample in calcium. All constructs remained viscous in the magnesium controls (Figure 4). HS-WTβ and HS-Leuβ MSD plots were indicative of a viscous medium in the presence of calcium as well. These rheological experiments suggest that DLeuβ has a higher association number than the Leuβ construct. At protein concentrations below 4 wt%, HS-DLeuβ assembled into several small elastic aggregates, but they did not constitute the entire volume, indicating fluctuations in local protein concentration (data not shown).

We next investigated the potential of the DLeuβ cross-linking domain to allosterically regulate the mechanical properties of a 6 wt% gel. Samples were incubated in increasing concentrations of calcium and the resultant MSD plots are provided in Figure 5. A clear transition was observed from a characteristically viscous medium at low calcium to an elastic medium at 10 mM calcium over the time domain sampled. The 5 mM calcium sample displayed characteristics of each limiting rheological behavior, i.e. linear MSD growth with τ and limited fluctuation of MSD amplitude, particularly at small lag times. This is indicative of a viscoelastic intermediate in the given time scales.[37] We have previously observed this phenomena with the HS-Leuβ construct, however, the transition from a viscous medium to a hydrogel occurred over a broader range of calcium concentrations.[21] A strong correlation can be drawn between the calcium binding parameters of the two mutants and the allosteric regulation of the mechanical properties. The Leuβ peptide binds calcium cooperatively with a Hill coefficient of 3.1 as compared to 4.6 for DLeuβ. This means DLeuβ undergoes the structural transition from unfolded to folded over a more narrow range of calcium concentrations (Figure 3d), which is reflected in the sharp change in mechanical properties in Figure 5. The structural transition of Leuβ occurs over a broader range of calcium concentrations giving rise to a broader range of viscoelastic intermediates. These results further confirm our hypothesis that self-assembly is driven by β-roll folding.

To further test the utility of the DLeuβ as a stimulus responsive cross-linking domain, we constructed concatemers of DLeuβ and MBP (Figure 2c), eliminating the α-helical leucine zipper domains. The microrheology results indicate similar calcium dependent self-assembly properties as seen with the HS constructs (Figure 6). Both 21.3 wt% and 14.2 wt% samples in magnesium had significantly more viscoelastic character than the corresponding HS samples (Figure 6a,b). In order to normalize the molar cross-linking content between the HS and concatemer experiments, significantly higher protein concentrations were required due to the large size of MBP. However, a clear transition in mechanical properties was still observed for the concatemer samples at both weight percentages tested (Figure 6a,b). These results demonstrated that the DLeuβ mutant has the ability to create enough elastically effective associations to actuate self-assembly in the presence of calcium, without depending on additional cross-linking provided by the leucine zipper domains. A lower critical protein concentration for self-assembly was determined to be approximately 14 wt% (adjusted for molar cross-linking content), which is in agreement with the HS experiments discussed above (data not shown).

The DLeuβ peptide is considerably different from other stimulus-responsive protein-associating domains used for hydrogel cross-linking. β-roll domains do not naturally participate in self-assembly or biomolecular recognition; the self-assembly capabilities were rationally designed and engineered into the stimulus-responsive scaffold itself. More commonly, a naturally associating domain is placed in an environment which destabilizes the cross-linking interactions such as higher pH, temperature or by addition of denaturation agents. In contrast, the DLeuβ can be easily modulated from disordered to structured and, in turn, viscous to elastic by simply adjusting the calcium concentration. This may also offer a convenient strategy to encapsulate protein domains or cells inside a β-roll cross-linked hydrogel. Encapsulation targets can be incubated with soluble β-roll cross-linking domains after which calcium can be added to trigger macromolecular assembly, trapping protein or cells inside. Catalytically active proteins can also be genetically inserted in between β-roll cross-linking domains to create bifunctional stimulus responsive enzymatic hydrogels. Future experiments are planned to investigate erosion rates, reversibility of self-assembly and to further elucidate the mechanical properties of the β-roll hydrogels. While the microrheology experiments clearly demonstrate a sol-gel transition, the values of the storage and loss moduli have yet to be determined. Traditional oscillatory shear rheology over a larger time domain should provide more accurate measurements of the viscoelastic properties of these new materials.

Conclusions

In this work, we have described a calcium responsive β-roll peptide with the ability to induce self-assembly into supramolecular networks. The β-roll scaffold was modified to create two hydrophobic surfaces suitable for cross-linking which are available only after calcium-induced structural rearrangement of the peptide. We have characterized the self-assembly capabilities of this domain by fusing an α-helical leucine zipper to the N-terminus and completing microrheology analysis. These chimeras were shown to self-assemble only in the presence of calcium. DLeuβ was also shown to self-assemble at lower protein concentrations than the single-faced mutant, indicating a higher association number. Furthermore, we have demonstrated the ability of the DLeuβ peptide to induce self-assembly without the additional cross-links provided by the leucine zipper by evaluating concatemers of DLeuβ and MBP. Thus we showed that Dleuβ can serve as a new cross-linking domain, capable of hydrogel formation, which can be allosterically-regulated via alteration of calcium concentrations.

References

(1) Banta, S.; Wheeldon, I. R.; Blenner, M. *Annu. Rev. Biomed. Eng.* **2010**, *12*, 167-186.

(2) Glassman, M. J.; Chan, J.; Olsen, B. D. *Adv. Funct. Mater.* **2013**, *23* (*9*), 1182-1193.

(3) Kim, M.; Tang, S.; Olsen, B. D. *J. Polym. Sci., Part B: Polym. Phys.* **2013**, *51* (*7*), 587-601.

(4) Sui, Z.; King, W. J.; Murphy, W. L. *Adv. Funct. Mater.* **2008**, *18* (*12*), 1824-1831.

(5) Jonker, A. M.; Löwik, D. W.; van Hest, J. C. *Chem. Mater.* **2012**, *24* (*12*), 759-773.

(6) Kopeček, J. *Biomaterials* **2007**, *28* (*34*), 5185-5192.

(7) Kopeček, J.; Yang, J. *Acta Biomater.* **2009**, *5* (*3*), 805-816.

(8) Zhang, S. *Nat. Biotechnol.* **2003**, *21* (*10*), 1171-1178.

(9) Zhang, S.; Marini, D. M.; Hwang, W.; Santoso, S. *Curr. Opin. Chem. Biol.* **2002**, *6* (*6*), 865-871.

(10) Cui, H.; Webber, M. J.; Stupp, S. I. *Pept. Sci.* **2010**, *94* (*1*), 1-18.

(11) Krishna, O. D.; Kiick, K. L. *Pept. Sci.* **2010**, *94* (*1*), 32-48.

(12) Grove, T. Z.; Osuji, C. O.; Forster, J. D.; Dufresne, E. R.; Regan, L. *J. Am. Chem. Soc.* **2010**, *132* (*40*), 14024-14026.

(13) Collier, J. H.; Hu, B.-H.; Ruberti, J. W.; Zhang, J.; Shum, P.; Thompson, D. H.; Messersmith, P. B. *J. Am. Chem. Soc.* **2001**, *123* (*38*), 9463-9464.

(14) Mart, R. J.; Osborne, R. D.; Stevens, M. M.; Ulijn, R. V. *Soft Matter* **2006**, *2* (*10*), 822-835.

(15) Bysell, H.; Månsson, R.; Hansson, P.; Malmsten, M. *Adv. Drug Deliv. Rev.* **2011**, *63* (*13*), 1172-1185.

(16) Ehrick, J. D.; Deo, S. K.; Browning, T. W.; Bachas, L. G.; Madou, M. J.; Daunert, S. *Nat. Mater.* **2005**, *4* (*4*), 298-302.

(17) Hendrickson, G. R.; Lyon, L. A. *Soft Matter* **2009**, *5* (*1*), 29-35.

(18) Wheeldon, I. Protein Engineering Strategies for Modular, Responsive, and Spatially Organized Biomaterials. In *Tissue and Organ Regeneration: Advances in Micro-and*

Nanotechnology; Zhang, L.G., Khademhosseini, A., Webster, T., Eds.; CRC Press: Boca Raton, **2014**; pp 265-294.

(19) Ehrick, J. D.; Stokes, S.; Bachas-Daunert, S.; Moschou, E. A.; Deo, S. K.; Bachas, L. G.; Daunert, S. *Adv. Mater.* **2007**, *19* (*22*), 4024-4027.

(20) Murphy, W. L.; Dillmore, W. S.; Modica, J.; Mrksich, M. *Angew. Chem. Int. Ed.* **2007**, *46* (*17*), 3066-3069.

(21) Dooley, K.; Kim, Y. H.; Lu, H. D.; Tu, R.; Banta, S. *Biomacromolecules* **2012**, *13* (*6*), 1758-1764.

(22) Bauche, C.; Chenal, A.; Knapp, O.; Bodenreider, C.; Benz, R.; Chaffotte, A.; Ladant, D. *J. Biol. Chem.* **2006**, *281* (*25*), 16914-16926.

(23) Chenal, A.; Guijarro, J. I.; Raynal, B.; Delepierre, M.; Ladant, D. *J. Biol. Chem.* **2009**, *284* (*3*), 1781-1789.

(24) Blenner, M. A.; Shur, O.; Szilvay, G. R.; Cropek, D. M.; Banta, S. *J. Mol. Biol.* **2010**, *400* (*2*), 244-256.

(25) Szilvay, G. R.; Blenner, M. A.; Shur, O.; Cropek, D. M.; Banta, S. *Biochemistry* **2009**, *48* (*47*), 11273-11282.

(26) Shen, W.; Lammertink, R. G.; Sakata, J. K.; Kornfield, J. A.; Tirrell, D. A. *Macromolecules* **2005**, *38* (*9*), 3909-3916.

(27) Shen, W.; Zhang, K.; Kornfield, J. A.; Tirrell, D. A. *Nat. Mater.* **2006**, *5* (*2*), 153-158.

(28) Xu, C.; Breedveld, V.; Kopeček, J. *Biomacromolecules* **2005**, *6* (*3*), 1739-1749.

(29) Fong, B. A.; Wu, W.-Y.; Wood, D. W. *Trends Biotechnol.* **2010**, *28* (*5*), 272-279.

(30) Abràmoff, M. D.; Magalhães, P. J.; Ram, S. J. *Biophotonics* **2004**, *11*(*7*), 36-43.

(31) Mason, T.; Ganesan, K.; Van Zanten, J.; Wirtz, D.; Kuo, S. *Phys. Rev. Lett.* **1997**, *79* (*17*), 3282-3285.

(32) Mason, T. G.; Weitz, D. *Phys. Rev. Lett.* **1995**, *74* (*7*), 1250-1253.

(33) Crocker, J. C.; Valentine, M. T.; Weeks, E. R.; Gisler, T.; Kaplan, P. D.; Yodh, A. G.; Weitz, D. A. *Phys. Rev. Lett.* **2000**, *85* (*4*), 888-891.

(34) Crocker, J. C.; Grier, D. G. *J. Colloid Interface Sci.* **1996**, *179* (*1*), 298-310.

(35) Hawe, A.; Sutter, M.; Jiskoot, W. *Pharm. Res.* **2008**, *25* (*7*), 1487-1499.

(36) Allen, J. E.; McLendon, G. L. *Biochem. Biophys. Res. Commun.* **2006**, *349* (*4*), 1264-1268.

(37) Petka, W. A.; Harden, J. L.; McGrath, K. P.; Wirtz, D.; Tirrell, D. A. *Science* **1998**, *281* (*5375*), 389-392.

The TCA Cycle Metabolon

Metabolons are multi-enzyme complexes formed through various interactions including covalent linkages, electrostatic forces, hydrophobic interactions, hydrogen bonding and Van der Waals interactions. Based on their robustness, metabolons can be generally classified into static and dynamic complexes.[1, 2] Static complexes are tightly associated through stronger bonding and more resistant to environmental alterations. Therefore, they are isolatable, for example, PDH complex and αKDH complex. On the contrary, dynamic complexes are held by much weaker forces. These type of metabolons are usually observed in highly progressive pathways with numerous metabolic crossroads, such as glycolysis and the TCA cycle. Transient association allows their quick reorganization in response to any external stimuli. In these complexes, intermediary metabolites are not always strongly bound as in static complexes but locally accumulated around metabolons to form discrete "pools", which is in fact a wise strategy to overcome limited solvation in cells. It also facilitates the preferential delivery of intermediates for specific products and control of metabolic flux.[2-4] Although the mechanism for metabolon formation is not fully understood, it is believed that the unique cellular community supported by structural scaffolds (filament and microtubule) is essential in stabilizing dynamic complexes. *In vivo*, proteins are very concentrated and the aqueous phase is highly viscous as half of water molecules are in the bound state and 30% of space is occupied by macromolecules. This so-called volume-excluding effect promotes not only protein-protein interactions but also protein-scaffold interactions, resulting in compartmentalization of metabolic pathways.[2, 5, 6] In the meantime, small metabolites may also place a non-negligible effect on the stability of these loosely associated complexes.[7] Therefore, membrane disruption and protein dilution during isolation and purification often lead to instant dissociation of dynamic metabolons.

Compared to stable multifunctional proteins or multi-enzyme complexes, dynamic metabolons always require special considerations on several criteria to minimize or overcome adverse effects during isolation. First of all, relatively gentle cell disruption is needed to recover enzyme associations. Second, dilution factors can be compensated by adding in volume-excluding agents like polyethylene glycol (PEG) or accumulating in ammonium sulfate-induced coprecipitation. Third, all enzyme activities for a metabolic pathway should be cofractionated during each isolation step. Finally, specific protein-protein interactions (not random aggregation) are conserved after isolation.[7] Despite all technical difficulties, since the last couple of decades a number of metabolons have been isolated from nucleic acid biosynthesis, protein biosynthesis, glycogen biosynthesis, purine and pyrimidine biosynthesis, amino acid metabolism, lipid and steroid biosynthesis, glycolysis, TCA cycle, fatty acid oxidation, electron transport chain, antibiotic biosynthesis, urea cycle and cyclic AMP degradation.[3]

We have experimentally demonstrated the existence of the TCA cycle metabolon by identifying all eight enzymes through *in vivo* cross-linking and mass spectrometry. Using distance constraints derived from cross-links, we propose two models for the wild-type mMDH-CS-ACO complex and a two-fold symmetric octamer composed of two mMDH dimers, one CS dimer, and two ACO monomers. Analysis of surface electrostatic potential of the model shows that rearrangement of surface charge patterns upon protein-protein association leads to forming a continuous positively charged zone across their interface. This would consequently facilitate directed transport of carboxylate substrates from one active site to the next. Until this work, direct observation of substrate channeling remained a big hurdle in metabolon research even though simulation work has built a theoretical foundation for its metabolic implications. Our investigation of natural TCA cycle metabolons gains structural insight into the organization of wild-type enzymes within the mitochondrial matrix, and provides an orientation option (MCA1) for engineered TCA cycle metabolon to achieve substrate channeling in vitro.

To our knowledge, little work has been done so far on artificial TCA cycle metabolon except the fusion mMDH-CS complex made by the Srere group nearly 20 years ago.[8, 9] Besides hybridizing the two enzymes by fusing terminus together, now we may engineer a complex retaining the naturally occurring structure and featuring substrate channeling. In this work, we combined site-specific modification with XL-MS and protein docking and structurally evaluated the engineered mMDH-CS complex and compared the structure to the native complex that we had also evaluated in this project. Furthermore, substrate channeling in the artificial metabolon was characterized from a kinetic perspective.

Formation of mMDH-CS Complex *In Vitro*

In vitro cross-linking of mMDH-CS interactions was done together with ACO as to simulate the situation in natural metabolon. As shown in Figure 1, intense protein bands appeared near the starting wells after cross-linking, indicating the formation of large aggregates, in which mMDH, CS and ACO were identified by mass spectrometry. In mitochondria, cross-linking of all the TCA cycle enzymes *in situ* generated a huge complex. Being different in solution, the three enzymes would have more freedom to assemble into higher-ordered complexes, which might be the association of enzyme multimers, or the aggregation of mMDH-CS-ACO complexes.

Structural Comparison of WT/Recombinant mMDH-CS Complex to Natural Metabolon

Interactions between WT mMDH and WT CS in dilute solution can occur at random regions, which are shown in Figure 2. A number of docked models were found to meet our selection criteria. Each model exhibited quite distinct conformation orientation and interface from the others. Among them, one candidate (highlighted in red square) showed up as the most promising structure. In the case of recombinant enzymes, protein-protein interactions appeared relatively simple. According to mass spectrometric identification and protein docking, only one structure was hit and its conformation orientation looked very similar as the natural metabolon. A structural comparison is illustrated in Figure 3. In WT complex, mMDH was flipped by approximately 90 degrees around the axis parallel to the original interface in natural metabolon, and consequently one of its N-terminus was buried between enzymes. Meanwhile, all the other terminus went away from the interface. This flipping might be unfavorable for directed OAA transport, because that the cleft between two subunits where L-malate and OAA are accommodated was now facing oppositely and open to the bulk solution. The average distance between active sites was also increased from 35 Å in natural metabolon to 46 Å.

In contrast to WT complex, recombinant complex exhibited some rational behavior in dilute solution. Although mMDH rotated around the axis perpendicular to the interface by approximately 30 degrees, the final structure maintained most of the natural features. First of all, no terminus were buried in the interface due to hindrance from additional tags. Second, terminus located around the interface were not altered and they were kept in almost unchanged relative orientations. Thirdly, the two tagged N-terminus of mMDH were extended into the open space. More importantly, the activity cleft in mMDH was still facing towards CS not the bulk solution, and the average distance between active sites was only 30 Å. It worth mentioning that the interface surface area in recombinant mMDH-CS complex was 12500 Å^2, suggesting that it may be more thermodynamically favorable than the natural metabolon.

Proof of Enhanced OAA Channeling in Recombinant mMDH-CS Complex

Slightly different from the simulation for natural metabolon at pH 7.8, pH value used for calculation of surface ESP of mMDH-CS complex in solution was set at 7.4, which was the medium pH. As depicted in Figure 4, positively charged continuous bands formed across the binding interfaces in both WT and recombinant complexes. In WT complex, the band was quite long and broad with the majority of one side surface covered. Although flipping of mMDH increased the distance between active sites, OAA channeling may still happen within the positively charged pathway. In recombinant complex, the band area was significantly smaller, only encompassing the active site clefts and binding interface. This is definitely favored by the restricted orientation of tagged enzymes. With route length shorter, transport of OAA in recombinant mMDH-CS complex would be faster than in WT complex.

To prove the predicted kinetic advantage in engineered metabolon, transient time of coupled reactions was measured by stopped flow methods, and the absorbance changed with time has been shown in Figure 5. It can be seen that the coupled conversion from L-malate to citrate underwent fast kinetics and the transient time (τ) was always no more than 1 s. For WT complex, τ was around 292.6 ms. After terminal modification, τ was drastically reduced by 90% to about 29.6 ms, which strongly agrees with the simulated results. In recombinant complex, OAA may be directly transported from either one of the mMDH active sites to CS by passing much shorter surface distances.

As a negative control to recombinant complex, disrupted channeling was realized by replacing key residues contributing to rearrangement of electrostatic potentials. First we calculated the surface ESP after replacing the positively charged arginines on CS by neutral alanine. Simulation result (Figure 4) showed that the electrostatic connection of active sites was completely broken apart, and the surface ESP of the whole complex became more positive upon neutralization of following CS arginines: 65, 67, 229, 324, 329 and 334. To experimentally demonstrate site-directed mutagenesis-induced channeling disruption, we finally substituted CS Arg65 by Ala65. As a result, coupled reaction rate significantly decreased with the transient time increased to nearly 1 s (Figure 5). Such huge decline in catalytic performance of recombinant mMDH-CS complex implied the crucial role of CS Arg65 in metabolon formation.

Conclusion

In this section, we have reconstituted an artificial TCA cycle metabolon in solution with recombinant mMDH and CS and revealed that peptide-tagged N- and C-terminus in this specific situation can help orient protein-protein interactions in a more restricted manner by structural invesigation. The resultant structure also shows its feasibility in further scaffoled assembly. Simulation and fast kinetic study have demonstrated a significantly enhanced OAA channeling in engineered metabolon compared to WT mMDH-CS complex. In alanine scanning, CS Arg65 turns out to be a key residue in formation of metabolon and substrate channeling. Although the result we have obtained so far is very preliminary, it at least points out a direction that we can follow in fabricating metabolon mimic *in vitro*. This is the first attempt of making an extracellular TCA cycle metabolon based on naturally formed structure in combination of mass spectrometry, computer simulation and protein engineering. Ongoing efforts in near future will be devoted to more convincing experimental proof of substrate channeling from competitive coupled assay, and mapping of dominant residues in channeling construction by site-directed mutagenesis, which will also give us some deeper insight into the nature of the TCA cycle metabolon.

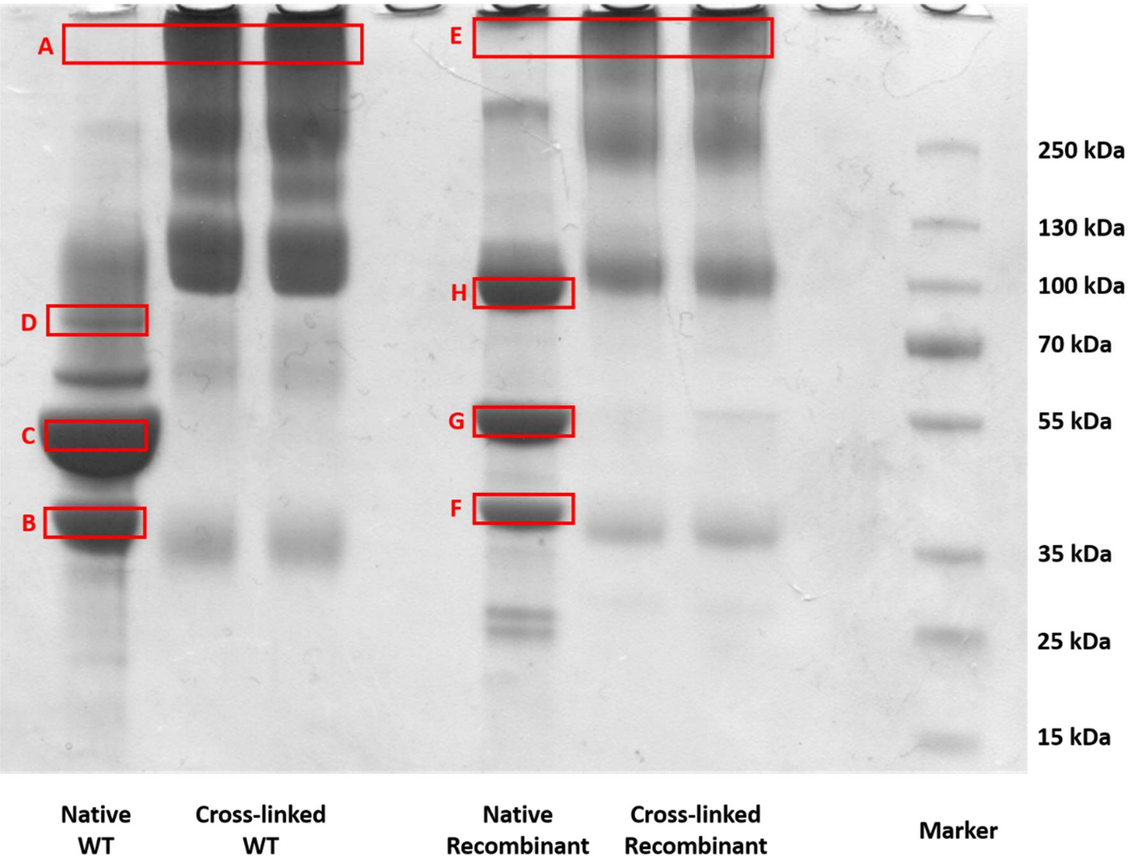

Figure 1 Reducing SDS PAGE of cross-linked and native (non-cross-linked) mMDH-CS-ACO complex *in vitro*. Bands in red squares were cut for digestion and mass spectrometric analysis: (A) cross-linked large WT mMDH-CS-ACO complex, (B) native WT mMDH subunit, (C) native WT CS subunit, (D) native WT ACO, (E) cross-linked large recombinant mMDH-CS-ACO complex, (F) native recombinant mMDH subunit, (G) native recombinant CS subunit, (H) native recombinant ACO.

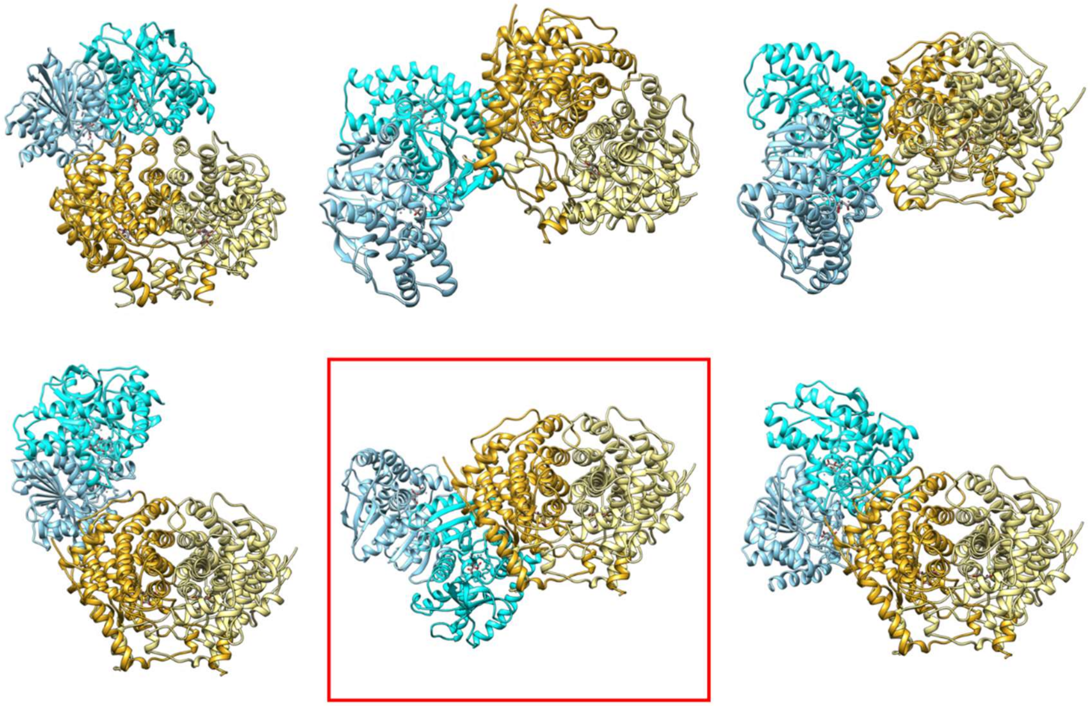

Figure 2 List of all possible docked structures for WT mMDH-CS complex. The two chains of CS are colored in goldenrod and khaki. The two chains of mMDH are colored in sky blue and cyan. The most promising structure is highlighted by the red square.

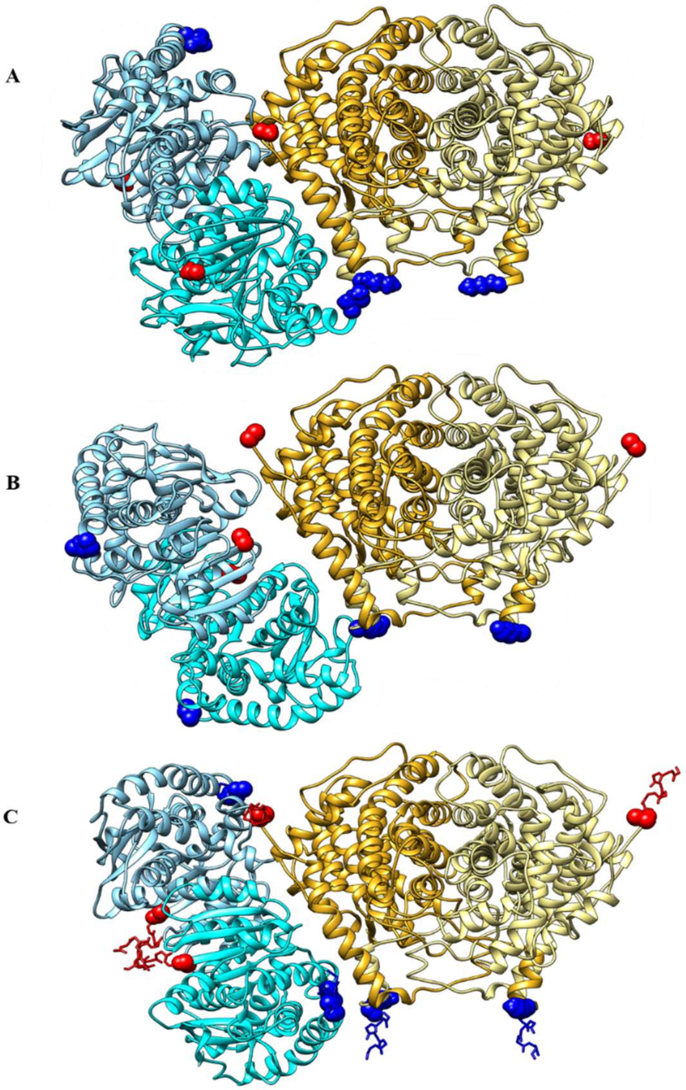

Figure 3 Docked structures of natural TCA cycle metabolon (**A**), *in vitro* WT mMDH-CS complex (**B**) and recombinant mMDH-CS complex (**C**). N-terminus are represented by red spheres. C-terminus are represented by blue spheres. FLAG-tags are represented by red sticks. HexHis-tags are represented by blue sticks.

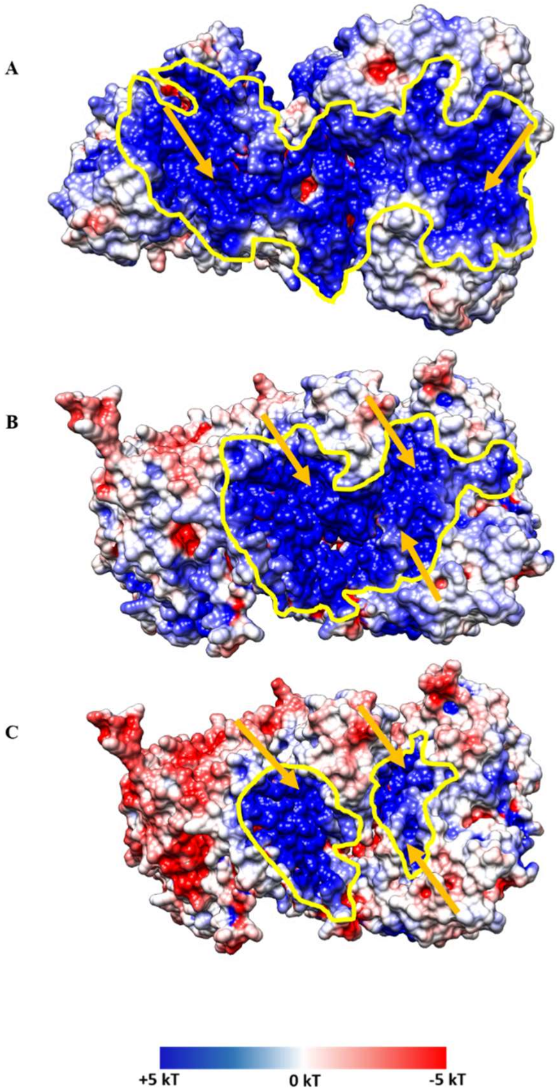

Figure 4 Simulated electrostatic channeling in WT (**A**), recombinant (**B**) and alanine-scanned (**C**) mMDH-CS complex. Calculation of surface ESP was done at pH 7.4. Active sites are denoted by orange arrows and electrostatic channels are highlighted by yellow edges. Negatively charged, positively charged and neutral regions are colored in red, blue and white.

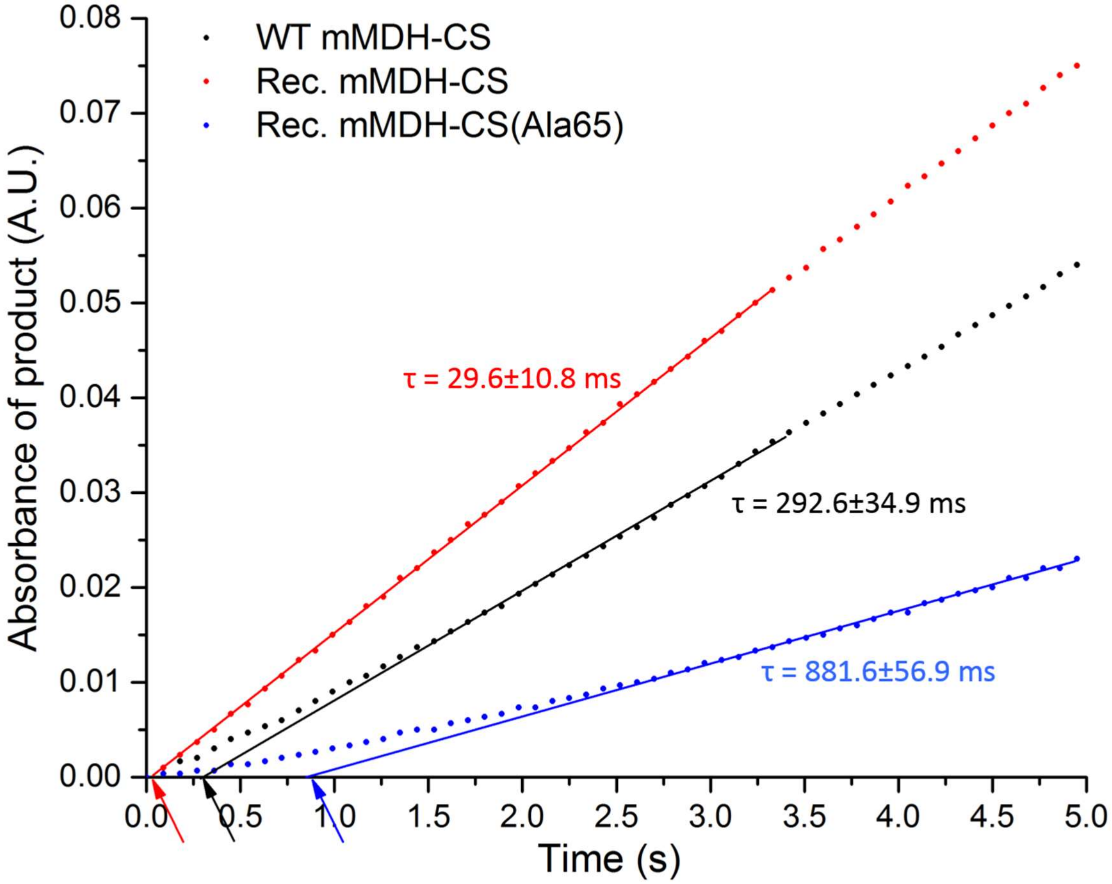

Figure 5 Change of product absorbance at 412 nm over time (dots) in coupled enzymatic reactions from L-malate to citrate. Straight solid lines were drawn at the steady state phase where maximum production rate was achieved, and extrapolated to the time axis. Intervals denoted by arrows were the transient time (τ) for each mMDH-CS complex.

The ETC Metabolon

The electron transport chain (ETC) is a group of five membrane enzymes that are the driving force for the conversion of energy in mitochondria. The ETC enzymes shuttle electrons through their substrates, NADH, ubiquinone, and cytochrome c, producing a proton gradient along the inner membrane of the mitochondria to produce ATP.[10] As the individual complexes were purified and studied, Complexes I and III, and Complexes III and IV were found to be associated in purified fractions.[11-13] These new developments led to changing the model from a fluid to solid description, where the enzyme complexes aggregate together in the membrane.[14] Figure 6(A) shows a scheme of one of the possible solid organizations of the ETC chain through various interactions.

Three enzymes form a supercomplex, where Complex I, dimer Complex III, and various copies of Complex IV are electrostatically, hydrophobically, structurally, and catalytically connected in a stoichiometric assembly referred to as a respirasome.[15-18] The ETC supercomplex was first studied by blue native gel electrophoresis by Schagger et al.,[19, 20]

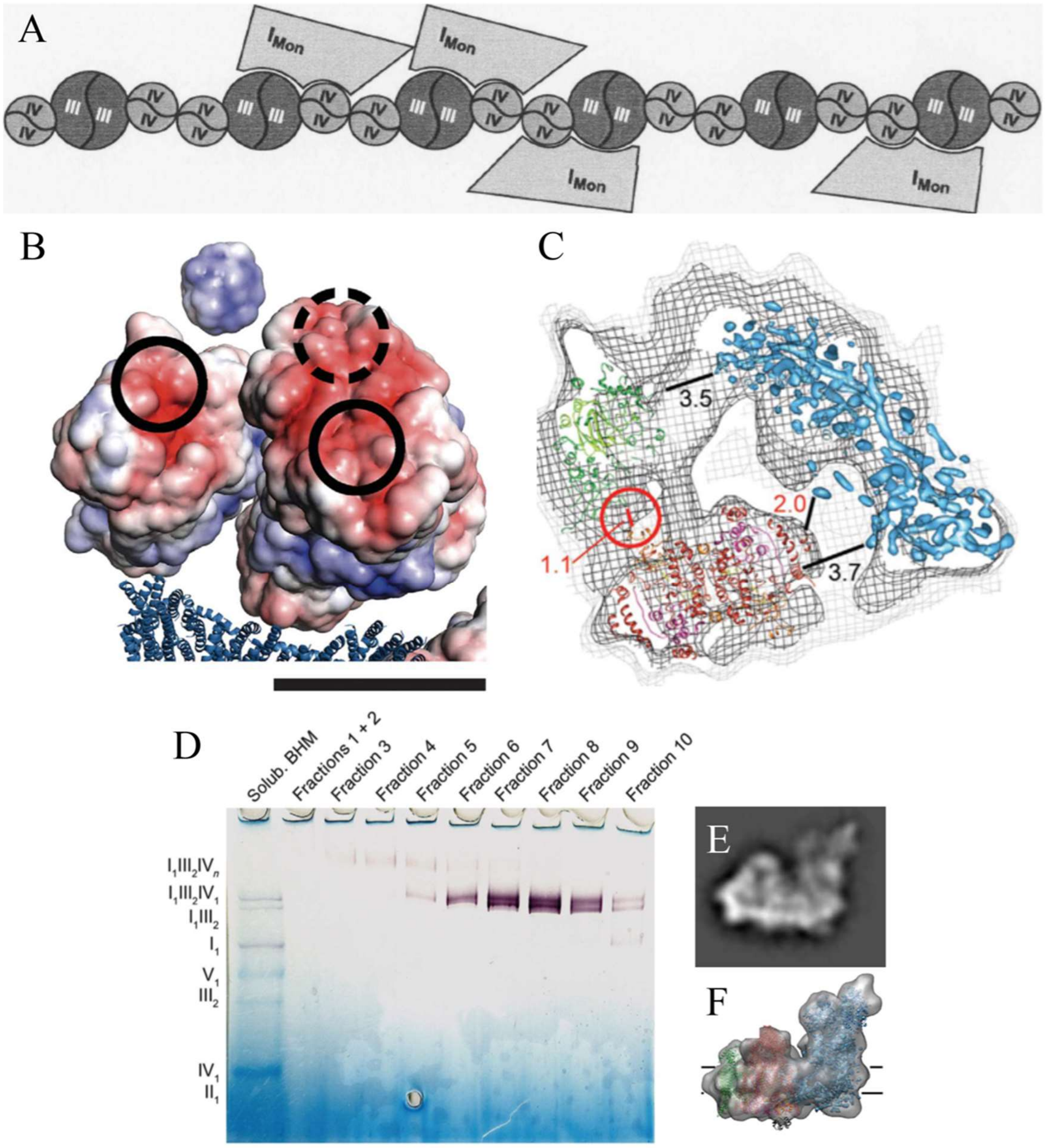

Figure 6. (A) Organizational scheme of electron transport chain organization in the mitochondrial inner membrane depicting the complexation of the enzymes.[18] Reprinted with permission The Journal of Biological Chemistry, 276, 37861-37867. American Society for Biochemistry and Molecular Biology, 2001. (B) Surface charge potentials and cytochrome c binding positions of Complex III, Complex IV, and cytochrome c. (Red, negative charge; Blue, positive; White, neutral) Scale bar 10 nm. (C) Electron microscopy topography slice and X-ray structures of distances in the supercomplex formation.[21] (D) Blue Native gel with NADH activity staining and (E) Cyro-transmission electron micrograph of the purified supercomplex. (F) Transmission electron micrograph space model of the complexes at the inner membrane near the lipid

headgroups of the intermembrane space.[21] Reproduced with permission from The EMBO Journal, 2011, 30, 4652–4664. Copyright John Wiley and Sons 2011.

leading to the descriptions and statistics of bound enzymes by the gel separations. Studies suggested that Complex I is part of almost all supercomplexes, Complex III is bound 50%, and Complex IV is loosely bound at 15% of the time, describing a weak binding of the supercomplexes after the purification and electrophoretic separations.[18] Multiple studies on kinetic analysis, gene knockouts, and electron microscopy have provided more insight into the specific interactions, stability, and catalytic enhancement.[22-25] This enzyme cascade can be described as a metabolon, which has protein-protein and electrostatic interactions for minimal substrate diffusion into the bulk solution. The substrate channeling of ubiquinone and cytochrome c provides for efficient electron transfer between complexes by substrate mediators, passed between the enzymes in the membrane and the membrane interface. [26] Figure 6 (B and C) shows the surface potentials for the cytochrome c binding sites for Complex III and IV, as well as the distances between the ETC enzymes in the membrane. The formation of the supercomplexes in the mitochondrial inner membrane increases the efficacy of substrate channeling, which leads to higher overall enzymatic catalytic rate for cellular respiration.[18, 27] For kinetic studies, the electron transport chain was examined by flux control analysis, where individual enzyme inhibition can have an effect on the overall kinetic activity of the complex. Complex I and III were found to have a large impact on the electron flux in the supercomplex and Complex IV did not, which demonstrate that Complex I and III have substrate channeling of ubiquinone but cytochrome c was claimed not to channel in the intermembrane space for beef heart mitochondria. Potato mitochondrial proteins showed that Complex IV had a much higher flux control coefficient.[23] Although another study theorized cytochrome c binding to both Complex III and Complex IV, many characteristics of the operation of the ETC supercomplex are unanswered by *in vitro* studies. Studying the supercomplex in a biomimic structure in a membrane environment will allow more insights into the activity and electron transport properties of these important enzymes. It will provide knowledge about biological energy conversion that can be used as inspiration for other energy applications or challenges.

ETC purification in literature

The first purifications of the supercomplexes occurred with detergent solubilization, at a concentration where complexes would retain their native protein-protein interactions.[11-13] Schagger et al. determined that mild, non-ionic detergents, such as Digitonin and Triton X-100^{TM}, were optimal for the largest intact supercomplexes.[19] Dudkina et al. purified the supercomplex by solubilization and utilized a sucrose gradient to separate the different supercomplexes based on their density and molecular weight for cryo-transmission electron microscopy analysis. Stroh et al. purified the supercomplex by solubilization and application to protein mixed ion exchange and gel filtration chromatography.[28] The ETC supercomplexes can be purified by common protein isolation techniques as long as the detergent concentration is kept constant to retain native acitivty and conformation. Althoff et al. reconstituted the supercomplex with an amphipol, A8-35, by utilizing cyclodextrin complexation to remove digitonin and separate the reconstituted supercomplexes by a sucrose gradient. Figures 6 D, E, and F display the native gel of the purified supercomplex, along with the cryo-transmission electron micrograph and corresponding space and crystal structure model produced from the microscopy.

Lipid bilayer electrodes for transmembrane enzymes

While soluble enzymes can be immobilized on electrodes, integral membrane enzymes need the structural support of a lipid bilayer to retain their activity. Integral enzymes have been a challenging area to study because of their lipophilic nature, leading to new developments in electrode architectures. Advancements have been made to incorporate membrane-bound enzymes into lipid bilayers by supported, tethered, and polymer cushioned membrane architectures upon solid surfaces.[29-31] Using supported and tethered lipid bilayers has become more common for bioelectrocatalysis studies of membrane proteins in fundamental bioelectrochemistry. [32, 33] The lipid bilayer membranes allow for the study of enzymatic bioelectrocatalysis on an electrode in an *in vitro* environment but with retained native function. With increased interest in studying metabolic and cellular processes in a natural state, tethered lipid bilayers permit in depth studies of enzymatic redox complexes that are important to many cellular energetic processes.

Recent studies have detailed the bioelectrochemistry of the individual complexes in various designs, but the entire ETC supercomplex has not been electrochemically evaluated.[34-37] While structural, kinetic, and genetic evidence prove the formation of the ETC supercomplex,[23, 24, 38] characterization of the bioelectrocatalysis of the three mitochondrial complexes together on an electrode has never been attempted. By purifying and reconstituting the ETC metabolon into a tethered lipid bilayer on a gold electrode, we can construct a mitochondrial inner membrane biomimic and characterize the bioelectrocatalysis of the electron transport chain with its substrates. The tethered lipid bilayer will have a hydrated layer, next to the electrode, that will enable native enzymatic activity and diffusion of the supercomplex substrate cytochrome c. Table 1 lists the half reactions and the corresponding potentials to the reactions that can take place in the ETC metabolon enzymes and surrounding environment. Complex III has a heme c_1 and Complex IV has a binuclear copper Cu_A in subunits that extends into the intermembrane space, in the hydrated space that could be in close contact with the electrode to study direct electron transport from these enzymes. Figure 7 shows a schematic of the proposed electrode architecture with the tethered lipid bilayer and the ETC metabolon. I propose with this biomimic, the direct and/or mediated electron transfer and enhanced bioelectrocatalysis of the ETC metabolon can be determined.

Table 1 Standard Reduction Potentials for ETC Biological Half-Reactions at pH 7

Reduction Half-Reaction	**E°'(V) vs. Ag|AgCl (sat'd)**
$\frac{1}{2}O_2 + 2H^+ + 2\,e^- \rightarrow H_2O$	0.617
$Fe^{3+} + e^- \rightarrow Fe^{2+}$	0.572
Cytochrome a_3(Fe^{3+})+ e^- → cytochrome a_3(Fe^{2+})	0.151
Cytochrome a(Fe^{3+})+ e^- → cytochrome a(Fe^{2+})	0.091
Rieske Fe-S(Fe^{3+})+ e^- → Rieske Fe-S(Fe^{2+})	0.081
Cytochrome c(Fe^{3+})+ e^- → cytochrome c(Fe^{2+})	0.055
Cytochrome c_1(Fe^{3+})+ e^- → cytochrome c_1(Fe^{2+})	0.021

UQH × + $H^1 + e^- \rightarrow UQH_2$ (UQ=coenzyme Q)	-0.009
UQ + 2 $H^+ + 2\,e^- \rightarrow UQH_2$	-0.139
Cytochrome $b_H(Fe^{3+}) + e^- \rightarrow$ cytochrome $b_H(Fe^{2+})$	-0.149
UQ + $H^+ + e^- \rightarrow$ UQH ×	-0.169
$[FAD] + 2\,H^+ + 2\,e^- \rightarrow [FADH_2]$	-0.196
Cytochrome $b_L(Fe^{3+}) + e^- \rightarrow$ cytochrome $b_L(Fe^{2+})$	-0.299
$FMN + 2\,H^+ + 2\,e^- \rightarrow FMNH_2$	-0.418
$FAD + 2\,H^+ + 2\,e^- \rightarrow FADH_2$	-0.418
$NAD^+ + 2\,H^+ + 2\,e^- \rightarrow NADH + H^+$	-0.519

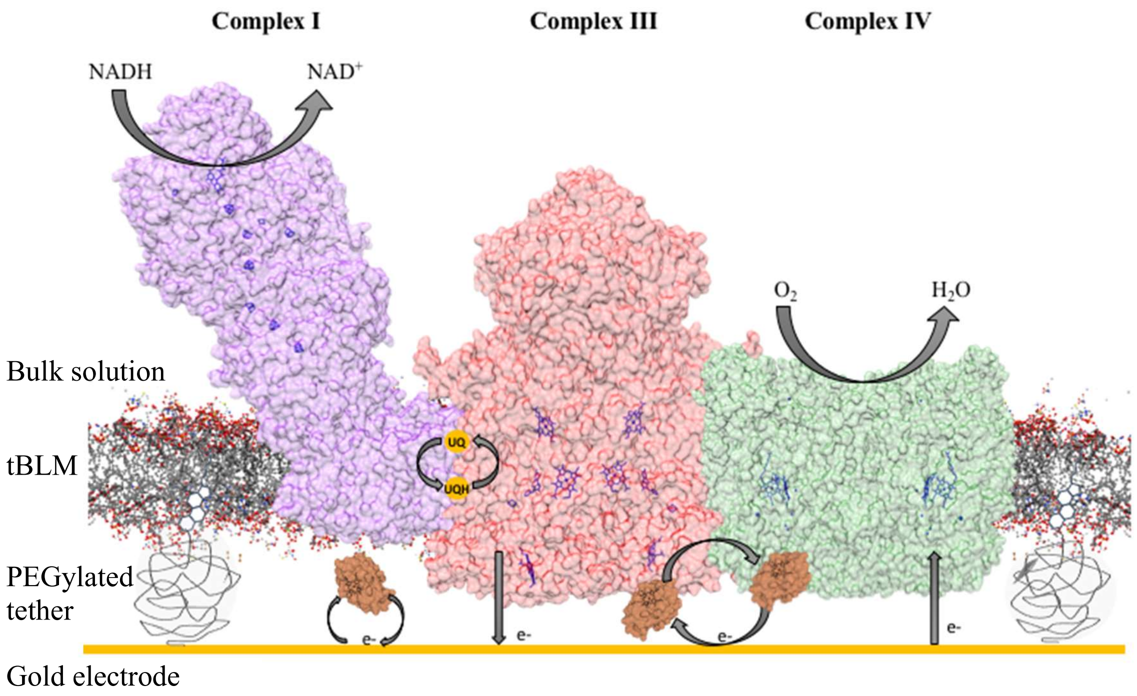

Figure 7. Tethered lipid bilayer scheme for ETC metabolon bioelectrocatalysis. The scheme depicts the preferred orientation of the metabolon into the tethered bilayer with NADH oxidation and oxygen reduction taking place in the bulk solution while cytochrome c oxidation/reduction takes place in the hydrated space of the tethered bilayer near the electrode surface.

Purification of the ETC Metabolon

A purification procedure for the mitochondrial ETC metabolon was developed by combining multiple literature procedures to achieve an isolated if not pure supercomplex in the active state. The purification of the ETC supercomplex was monitored by activity assays for Complex I for NADH oxidation, Complex III for cytochrome c reduction, and Complex IV for cytochrome c oxidation. Table 2 displays the activity of each fraction of the sucrose gradient. The ultracentrifuge gradient was utilized to separate the supercomplex by the density of the sucrose. The denser supercomplexes will settle in the higher percentage sucrose fractions while the single enzymes are separated at the lower percentages of sucrose. The fractions have high NADH activity in the first seven fractions. Complex III activity is highest in fractions 4-8. Complex IV activity is highest in fractions 6-8 as it is less dense. The first several fractions show high activity for all three complexes. Fractions

1-6 were concentrated to remove the sucrose and purified by the gel filtration column.

Table 2. Specific activity assays for the sucrose gradients fractions for purification of the supercomplex. (U/mg)

Fraction	Complex I	Complex III	Complex IV	mg/ml protein
1	39.79	0.83	1.10	0.33
2	46.74	0.95	0.68	0.19
3	35.29	0.78	0.41	0.21
4	43.86	12.24	1.16	0.02
5	41.71	2.32	1.90	0.41
6	15.28	3.76	2.68	0.10
7	18.92	6.66	5.87	0.32
8	2.30	3.71	3.33	0.36
9	7.71	1.16	1.71	0.44
10	4.26	0.025	1.09	0.64

Fractions 6-10 show high Complex III and Complex IV activity, indicating alternative

combinations of the complexes. The sucrose can have a stabilizing effect on the supercomplexes, enabling high activity after purification. Table 3 displays the activity of the purified fractions from the column for the first purification. Fraction 2 and 4 showed the highest activity for all three complexes, although Fraction 1 had the highest activity for the complexes upon reconstitution in bilayer lipids in Table 4, while the rest of the fractions follow the same trend. Reconstitution into the bilayer mixture of lipids should improve the activity of the enzymes, with the cardiolipin to stabilize the membrane protein structure. The importance of the inner membrane lipid cardiolipin and substrate ubiquinone are demonstrated in the assays of Table 5. The reconstituted enzymes lost a large amount of activity in Complexes III and IV with the removal of the lipid cardiolipin. Complex IV has 50% less activity without ubiquinone substrate for Complex III, but is not as affected compared to the removal of cardiolipin, which eliminates 98% of the activity. This demonstrates the established link between cardiolipin and ETC enzyme stabilization.[39] Table 6 shows the second purification of the ETC metabolon with the sucrose gradient

Table 3. Specific activity assays for the purified fractions after gel filtration for first purification. (U/mg)

Fraction	Complex I	Complex III	Complex IV	mg/mL protein
		μmol*min/mg protein		
Sucrose gradient concentrate	0.81	0.59	0.58	-
1	1.46	3.23	3.17	0.05
2	3.09	6.53	6.41	0.06
3	5.61	2.52	2.47	0.12
4	5.60	6.52	6.40	0.09
5	3.25	1.67	0.82	0.77
6	0.24	3.92	3.85	0.02

Table 4. Specific activity of purified fractions of reconstituted proteoliposomes for first purification. (U/mg)

Fraction	Complex I	Complex III	Complex IV	mg/mL protein
		μmol*min/mg protein		
1	6.1	2.7	2.3	0.01
2	4.1	0.9	4.7	0.02
3	10.5	1.9	5.4	0.01
4	6.5	0.8	8.2	0.02
5	1.0	0.1	12.2	0.15
6	14.0	0.7	20.2	0.01

Table 5. Specific activity of proteoliposomes with and without cardiolipin (CL) and ubiquinone (UQ). (U/mg)

Fraction	CIII	CIV	mg/ml protein
2	1.35 ± 0.09	0.39 ± 0.06	0.136

2 (-CL)	0.40 ± 0.01	0.02 ± 0.01	0.153
2 (-UQ)	0.46 ± 0.20	0.15 ± 0.04	0.167

Table 6. Specific activity of sucrose gradient and purified fractions for second purification.

Sucrose gradient fractions	Complex I	Complex III	Complex IV
		µmol*min/mL	
1 & 2	27.0 ± 3.7	0.08 ± 0.01	0.55 ± 0.17
3 & 4	51.5 ± 3.2	0.74 ± 0.14	3.18 ± 0.20
5 & 6	9.1 ± 0.6	0.18 ± 0.04	3.42 ± 0.38
Combined 1-6	22.4 ± 3.1	0.43 ± 0.05	2.13 ± 0.21

Column fractions	**Complex I**	**Complex III**	**Complex IV**	**mg/mL protein**
		µmol*min/mg protein		
1	10.5 ± 3.1	0.06 ± 0.02	0.48 ± 0.06	0.79
2	13.9 ± 1.2	0.24 ± 0.07	0.76 ± 0.06	0.24
3	14.2 ± 0.9	0.19 ± 0.06	0.75 ± 0.17	0.32
4	12.3 ± 2.0	0.57 ± 0.12	1.04 ± 0.20	0.67
5	9.5 ± 1.2	0.15 ± 0.07	1.11 ± 0.01	2.6
6	3.6 ± 0.3	0.09 ± 0.03	0.49 ± 0.04	7.1
7	4.0 ± 0.2	0.05 ± 0.03	0.51 ± 0.02	7.0
8	13.5 ± 1.7	0.04 ± 0.01	0.57 ± 0.10	1.6
9	6.4 ± 0.8	0.10 ± 0.01	0.66 ± 0.12	2.0
10	10.2 ± 2.5	0.04 ± 0.01	0.82 ± 0.01	1.2

and column purified fractions. The assays demonstrate the same trend of enzymatic activity as Table 1 and 2 for the ETC supercomplex purification. The most active fractions were used to be reconstituted for electrochemical analysis.

Figure 8 depicts the activity of the purified fractions with a low ionic strength buffer (12 mM) with 25 µM oxidized and reduced cytochrome c, inhibition with sodium azide (Complex IV) and azoxystrobin (Complex III), and solubilization with β-docedyl maltoside (DDM). The addition of azoxystrobin shows the slight increase in cytochrome c oxidation from Complex IV. The addition of azide shows the increased cytochrome c reduction for the activity of Complex III, showing the presence of both Complex III and

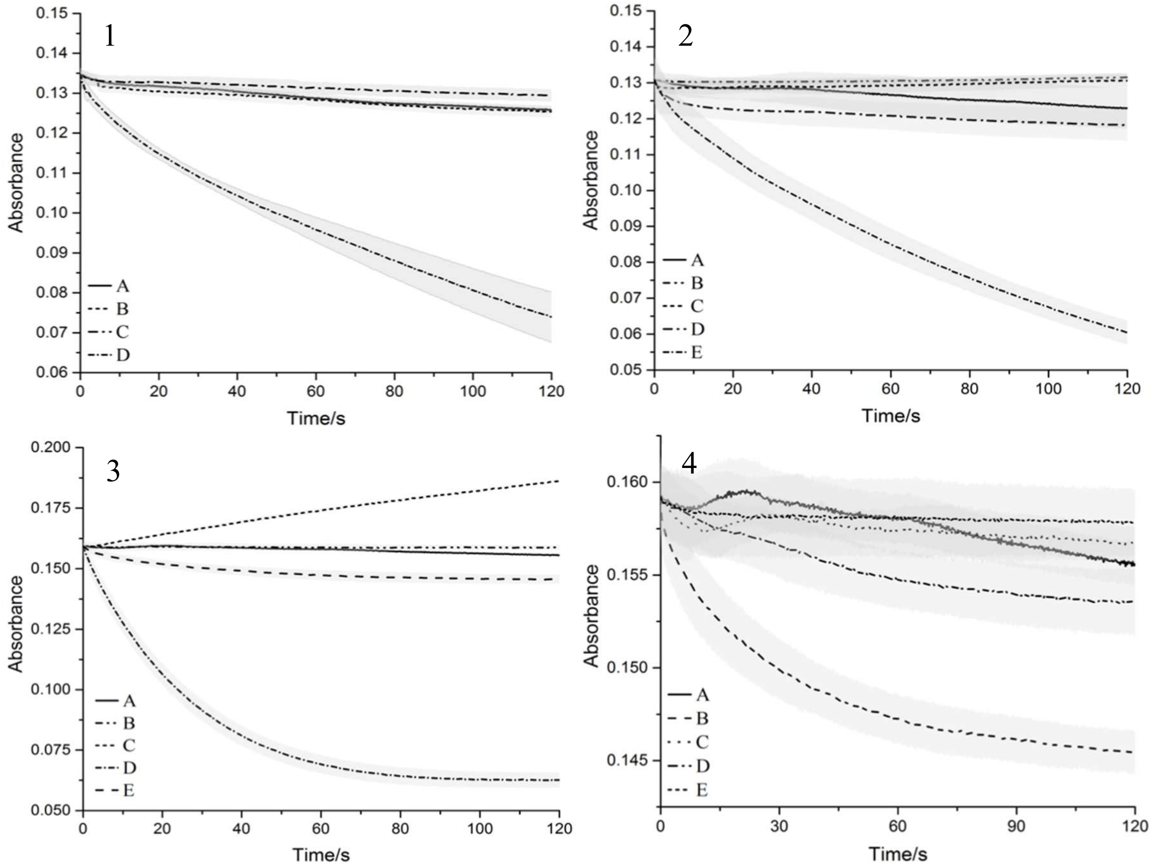

Figure 8. Injection activity assays for purified metabolon fractions. Shaded areas indicate standard deviation with n=3.

(1) Fraction #1 (A) 20 mM Tris HCl, pH 8, 25 μM oxidized cytochrome c; (B) A + 180 μM sodium azide; (C) A + 40 μM Azoxystrobin; (D) 20 mM Tris HCl, pH 8, 25 μM reduced cytochrome c.
(2) Fraction #4 (A) 20 mM Tris HCl, pH 8, 25 μM oxidized cytochrome c; (B) A + β-Docedyl Maltoside (C) A + 180 μM sodium azide; (D) A + 40 μM Azoxystrobin; (E) 20 mM Tris HCl, pH 8, 25 μM reduced cytochrome c.

(3) Fraction #5 (A) 20 mM Tris HCl, pH 8, 25 μM oxidized cytochrome c; (B) A + β-Docedyl Maltoside (C) A + 180 μM sodium azide; (D) 20 mM Tris HCl, pH 8, 25 μM reduced cytochrome c; (E) A + 40 μM Azoxystrobin.
(4) Fraction #5 (A) 20 mM Tris HCl, pH 8, 25 μM oxidized cytochrome c; (B) A + 90 mM KCl (C) 20 mM Tris HCl, pH 8, 200 mM Mannitol, 70 mM sucrose, 1 mg/ml BSA, 25 μM oxidized cytochrome c; (D) 20 mM Tris HCl, pH 8, 200 mM Mannitol, 70 mM sucrose, 1 mg/ml BSA, 8 μM oxidized cytochrome c; (E) 20 mM Tris HCl, pH 8, 8 μM oxidized cytochrome c.

IV. Fractions 1 and 4 has slight activity for Complex III and high Complex IV, which is in line with the noted differences in the turnover of the complexes. Solubilization with DDM leads to the slight decrease in overall oxidase activity, showing that the detergent breaks some of the protein-protein interactions of this complex. The addition of potassium chloride, to increase the ionic strength, increases the oxidase activity showing that ionic strength will increase the diffusion of cytochrome c in the buffer and therefore the number of collisions with the complexes. Assays in the presence of a crowding buffer showed some improvement in the activity, while the addition of polyethylene glycol precipitated the protein. These assays show the presence of the three complexes and how their activities are dependent on each other in different buffer environments with salt and crowding reagents.

Electrochemical Characterization of DSPE-PEG2K-PDP Enzyme

Bilayer

The preparation of the electrode surface is done by cleaning the polycrystalline gold disk in acid solutions to remove any organic impurities at the surface before monolayer deposition. Thiols are known to have spontaneous adsorption at the gold surface, creating a Au-S bond.[40] A monolayer on the surface of the electrode will remove any interfacial capacitance and have electronic blocking properties.[41, 42] β-mercaptoethanol monolayers will make the gold surface hydrophilic to assure adsorption of the liposomes and to eliminate any denaturation of the protein. The DSPE-PEG2K-PDP (pyridyl dithio propionate) will bind to the gold surface, becoming the tether for the proteoliposomes to fuse to form a bilayer. Gold disc electrodes were characterized by cyclic voltammetry as a bare gold electrode, the self assembled monolayer, bilayer, and a protein modified bilayer in buffer shown in Figure 9 (top). The preparation of the electrode shows the formation of the self-assembled monolayer by the elimination of the current and capacitance at the electrode surface. The capacitance will increase slightly with an addition of a bilayer fused with the PEGylated lipids, demonstrated by the increase in the current. Each electrode was characterized by cyclic voltammetry after the incubation of the self-assembled monolayer. Control electrodes were made by modifying an electrode with bilayer lipids without proteins. Based on this technique of bilayer formation by dropcasting, fusion by evaporation, and large protein incorporation, the bilayer will contain defects and will not be electrically sealing.[43] Cytochrome c is a redox active protein that serves as the electron shuttle for the ETC enzymes between Complex III and IV. This redox protein was examined to determine its electrochemistry with the bilayer and response on the surface of the electrode. Figure 9 (bottom) shows the cyclic voltammograms of oxidized cytochrome on the bilayer electrode and shows the linear response to concentration, void of any catalytic reaction with oxygen or ubiquinone in the membrane. The cyclic voltammograms show a diffusion limited response, where the cytochrome c can diffuse between the tethered lipid bilayer and the electrode surface within the hydrated layer. The E_{pc} is at ~ 0 mV (vs. Ag|AgCl) and the E_{pa} is at ~ +180 mV (vs. Ag|AgCl), demonstrating a quasi-reversible reaction on the electrode surface with a measured E^{o} of +90 mV (vs. Ag|AgCl).

The electron transport chain enzymes are large transmembrane proteins that extend aboveand below the lipid bilayer. Complex III and IV have redox active subunits that extend into the intermembrane space ~30 Å and ~32 Å respectively.[44, 45] Their substrate,

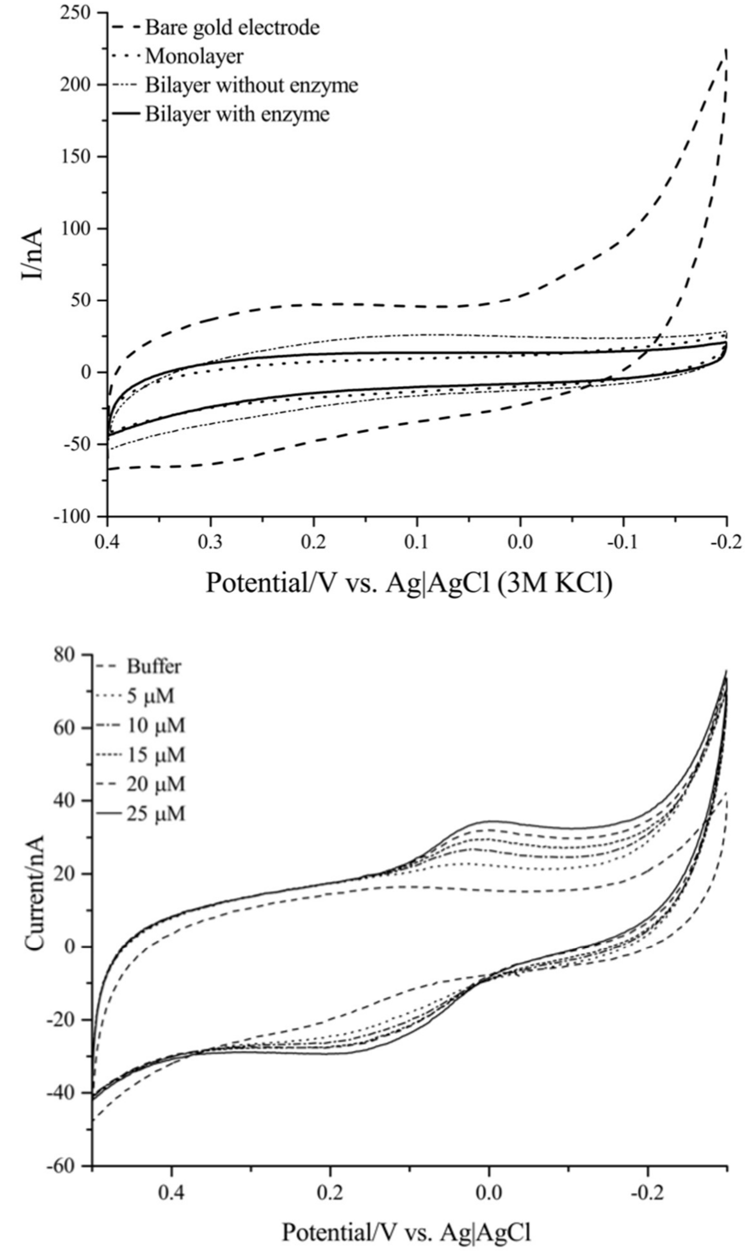

Figure 9. (Top) Cyclic voltammograms of a bare gold electrode, gold electrode with a monolayer, and gold electrode with a protein bilayer. (Bottom) Control bilayer electrode with increasing concentrations of oxidized cytochrome c. 10 mM potassium phosphate, pH 7.5, 70 mM potassium chloride. Scan rate 5 mV/s.

cytochrome c, has a diameter of ~34 Å.[46] A tethered lipid bilayer will allow the retention of native conformation and activity of the enzymes to determine the bioelectrochemical responses. DSPE-PEG2k-PDP was chosen for the tether link, because it has been studied extensively.[47, 48] Knoll et al. immobilized the PEGylated lipid tether in a bilayer on gold and measured the distances between the distinct groups by neutron scattering.[49] The PEGylated chain makes a ~60 Å hydrated space between the gold surface and the head groups of the lipids. The lipid bilayer itself makes up a ~25 Å space before the bulk solution. This architecture will allow for the fluid movement of the lipid bilayer and insertion of the transmembrane complexes. Cytochrome c is be able to freely diffuse between the electrode, lipid bilayer, and complexes. It is assumed that the tethered bilayer formed on the surface is not perfectly insulating and will have defects that allow the diffusion of cytochrome c into the hydrated space.[43] The buffer and ionic strength was chosen for the optimal electron transfer rate of cytochrome c with the enzymes.[50, 51]

Metabolon proteoliposomes were immobilized onto the electrode by drop casting onto the electrode surface. The proteoliposomes were allowed to evaporate to decrease the inner volume of the vesicles, collapse and then rehydrated with a low ionic strength buffer with calcium to induce fusion into the tethered bilayer.[52] A CV in buffer in the absence of the substrate shows no redox signal appears from enzymatic redox cofactors heme c_1 from Complex III or the binuclear copper Cu_A from Complex IV, which would be closest to the electrode surface. The protein subunits might not be orientated enough to facilitate direct electron transfer with a distance too large for electron tunneling or hopping. The redox peak could be buried beneath the capacitance of the monolayer on the surface and the bilayer with a very small current. By using the surface area of the metabolon (670 nm^2)[16] and Complex IV (99 nm^2)[53] in the membrane, theoretical calculations can be made to determine the moles of enzyme that could possibly be found on the surface of the electrode area ($3.1x10^{12}$ nm^2). With a weight ratio of lipids to proteins at 5:1, the ETC metabolon complex and Complex IV could be found at a surface concentration of 50 attomoles and 160 attomoles in a complete tethered bilayer. If no lipids were present, the metabolon could be found at 16 femtomoles and Complex IV at 50 femtomoles. With these numbers, the charge of the redox peak can be calculated by the $\Gamma = Q/nFA$ where Γ is the number of moles cm^{-2}, Q is the charge obtained by integrating the redox peak, n is the number of electrons involved in the reaction, F is Faraday's constant (96,485 $Cmol^{-1}$) and A is the electrochemically available surface area (0.031 cm^{-2}). These concentrations would provide a redox response between 0.15 pA (lowest) and 0.30 nA (highest) assuming a one electron reaction. Therefore it is not surprising that a response is not observed.

The bioelectrocatalytic response of the ETC metabolon in the presence of increasing concentrations of oxidized cytochrome c in buffer is shown in Figure 10 (top). The cyclic voltammetry shows a sigmoidal catalytic reduction current response with increasing substrate concentrations, demonstrating that the enzyme kinetics are rate limiting.[54] If the substrate was limiting, the response would show a more diffusion limited response similar to the cytochrome c control. The current response can be related to the enzyme concentration and its catalytic rate on the electrode. This response demonstrates mediated bioelectrocatalysis with cytochrome c for electron transfer. Previous reports have shown cytochrome c can mediate Complex IV oxygen reduction reaction since the enzyme is not close enough or orientated for direct electron transfer. The potentials of Complex IV's Cu_A subunit and Complex III's heme c_1 are within 50 mV of each other, the electrochemical mediation is facile, and as well as being the natural electron transfer molecule in the membrane. The onset potential of the reduction at 0.150 V (vs. Ag|AgCl) corresponds to the potential of cytochrome c with a bilayer control. The electrochemical reaction reduces the cytochrome c where the electrons are passed to Complex IV to reduce oxygen to water.

Kinetics were determined by measuring the limiting current, I_{lim}, at -0.100 V. Non-linear regression was utilized to determine the Michaelis-Menten kinetics with cyclic voltammetry. The metabolon sample produced an average I_{max} of 1,584 nA and a Michaelis Menten constant, K_M, of 83 μM (based on 2 replicates). A high K_M indicates a weak affinity or binding of the substrate, and a low K_M has a stronger affinity or binding of the substrate. Although the buffer solution was purged by nitrogen, the small amounts of oxygen left would be enough for the Complex IV concentration on the electrode. Inhibition of enzymes is a useful tool to determine the responsible enzymes contributing to the current response in this system. Complex IV is inhibited by sodium azide, where it binds to the heme a_3-Cu_B complex inhibiting oxygen reduction to water. Sodium azide was used instead of the common sodium cyanide, because it was not electrochemically active on the gold electrode. The addition of sodium azide in the presence of oxidized cytochrome c lowers the catalytically current, indicating the inhibition of Complex IV in the metabolon. This produces a diffusion limited response with a high sodium azide concentration, with the potential corresponding the control peak of cytochrome c shown in Figure 10 (bottom). A metabolon fraction, reconstituted without ubiquinone in the lipids, showed a decrease in the limiting current compared to the sample containing ubiquinone, with an average I_{max} of 718 nA and K_M of 67 μM. This data proves the need for the substrate ubiquinone and the

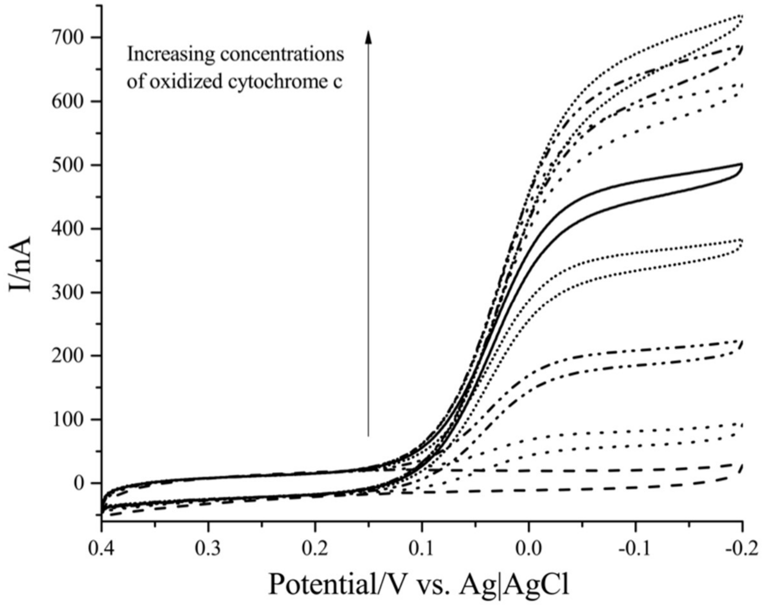

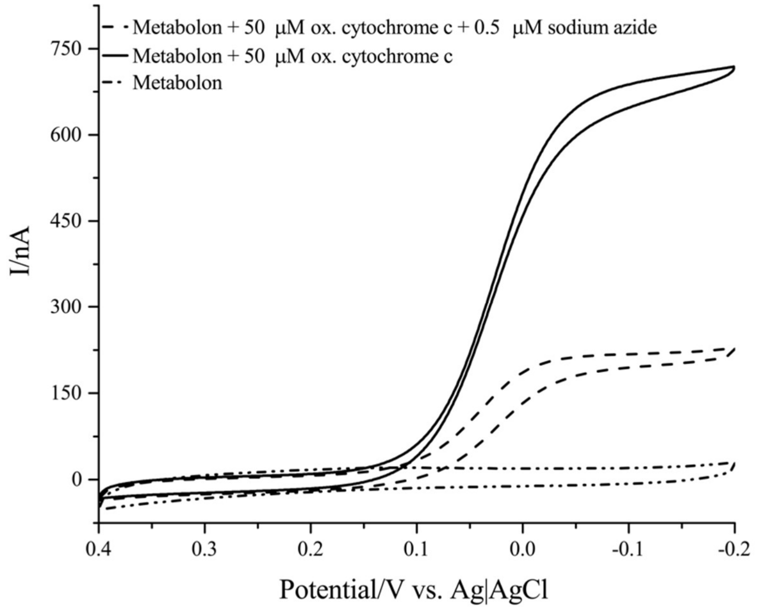

Figure 10 (Top) Representative cyclic voltammograms of ETC metabolon with increasing concentrations of 0-50 µM oxidized cytochrome c. (Bottom) Inhibition of metabolon with sodium 5 µM azide. 10 mM potassium phosphate buffer, 70 mM sodium chloride, pH 7.5. Scan rate 5 mV/s.

participation of Complex III in the bioelectrocatalytic response with oxidized cytochrome c. Theoretically, the addition of NADH should improve the current response of the metabolon kinetics as NADH provides the electrons to shuttle through the enzymatic chain. The addition of NADH (with or without the presence of cytochrome c) did not increase or change the current response of the metabolon sample.

Complex IV proteoliposomes were examined as a positive control to compare to the metabolon bioelectrocatalysis. In the absence of reduced cytochrome c, the response was the same as the metabolon, no redox peaks were present from the enzymes. With the addition of reduced cytochrome c, the current response is the same as the metabolon with oxidized cytochrome c, a sigmoidal catalytic reduction current. This provides evidence that Complex IV is part of the bioelectrocatalysis in the metabolon complex, where it is oxidized by Complex IV to be reduced again at the electrode surface. The data shows the Michaelis Menten response of Complex IV with reduced cytochrome c and Complex IV inhibition with sodium azide. Non linear regression for Complex IV provided a I_{max} of 398± 25 nA and a K_M of 34 ± 4 µM. Figure 11 (top) compares the catalytic response of Complex IV with reduced cytochrome c and metabolon with oxidized cytochrome c. Table 8 lists the kinetic parameters of the cyclic voltammetry experiments. Because the cyclic voltammograms do not show a redox peak for any of the enzymes, the surface concentration of the electroactive species cannot be determined. The current difference in the metabolon and Complex IV electrodes cannot be compared without the enzyme concentrations and catalytic rate of each sample.

Amperometry experiments were performed to examine at the enzyme kinetics at steady state conditions and the inhibition of the different complexes, eliminating the

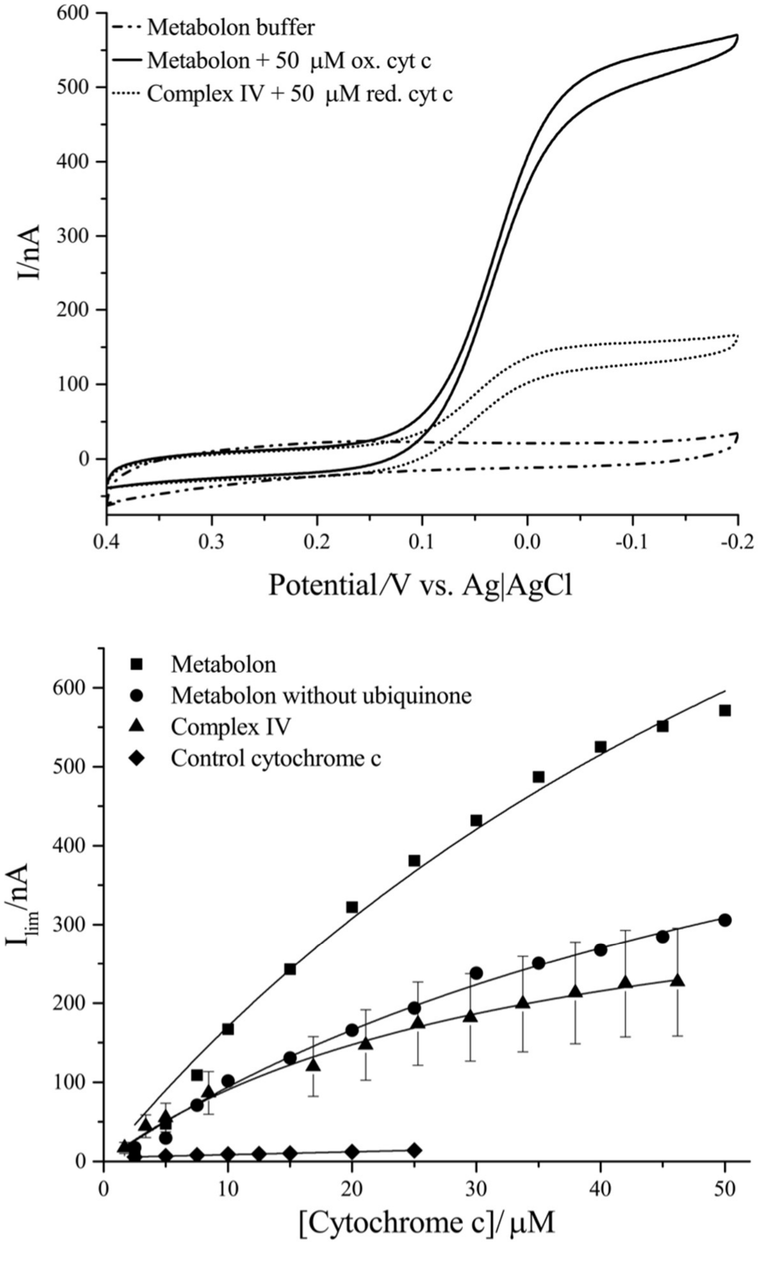

Figure 11. (Top) Comparison cyclic voltammograms of metabolon with oxidized cytochrome c and Complex IV with reduced cytochrome c. (Bottom) Concentration profiles of ETC metabolon with and without ubiquinone and cytochrome c oxidase with oxidized and reduced cytochrome c respectively.

Table 8. Kinetic data for cyclic voltammetry of ETC metabolon and Complex IV.

	I_{max} (nA)	K_M (μM)	R^2	n
Metabolon (average)	1584	83		2
Metabolon w/o UQ (average)	718	67		2
Complex IV	398 ± 25	34 ± 4	0.9930	3

capacitive effects of the bilayer. The potential was held at E_{app} of -50 mV (vs Ag|AgCl), more negative than the half wave potential of 25 mV (vs. Ag|AgCl). Raw amperometric data with the metabolon sample showed a gradual increase in the current response before stabilizing with injections of oxidized cytochrome c in the buffer in Figure 12 (top). The black arrows indicate where the injections were added for cytochrome c or the inhibitors. The catalytic current increases over a long period of time and is dependent on the kinetics of the enzymes and their respective turnover numbers. The kinetic response had an I_{max} of 367 ± 27 nA and a K_M of 14.6 ± 2.0 μM oxidized cytochrome c.

Enzymatic inhibition of Complex III was initiated by the addition of micromolar concentrations of azoxystrobin, which inhibits the ubiquinone binding site Q_o, preventing the electron transfer to the Rieske iron sulfur protein to the heme c_1 subunit to cytochrome c. The injection of azoxystrobin (at time 330 minutes) shows a slow decrease in the reductive current, showing that Complex III contributes to the current response. Additions of sodium azide was added to determine the kinetics of the inhibition of the metabolon by the response of Complex IV. The response was immediate after injection and formed a kinetic response with additional injections of inhibitor. The response gave an I_{max} of inhibition at 162 ± 3 nA and a K_i of 130 ± 6 μM sodium azide. Amperometry with Complex IV demonstrated large gradual increase in current with the addition reduced cytochrome c in Figure 12 (bottom). The response gave an I_{max} of inhibition at 98 ± 4 nA and a K_i of 249 ± 22 μM sodium azide. The catalytic current and inhibition responses can be seen in Figure 12 and kinetic data in Tables 9 and 10. The maximum metabolon current was inhibited by almost 55% and Complex IV by 50%, which it can be possible the residual current is another enzyme contribution or electrolysis of the enzyme by cytochrome c

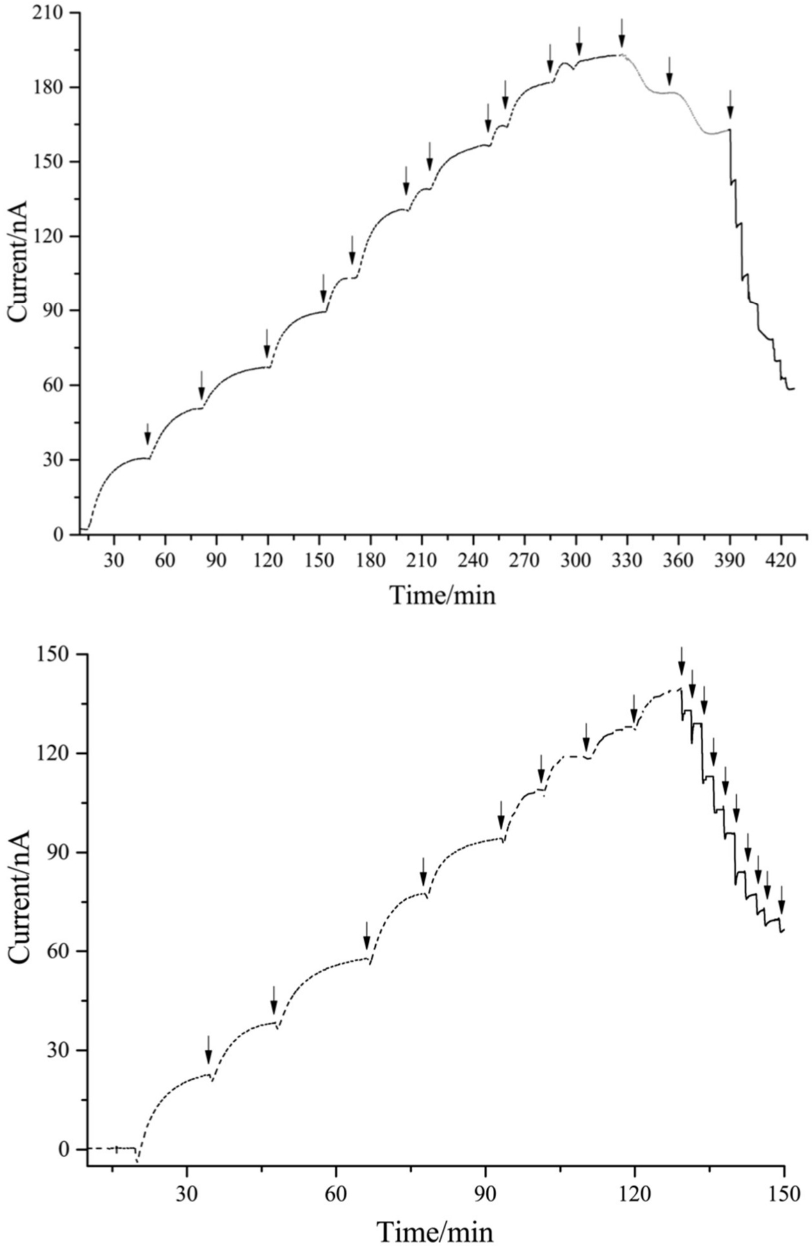

Figure 12. (Top) Raw amperometric current data of ETC metabolon with increasing oxidized cytochrome c injections. Injections of azoxystrobin (in methanol) and sodium azide start at 330 minutes and 380 minutes. (Bottom) Raw amperometric current data of cytochrome c oxidase with increasing injections of reduced cytochrome c and inhibition with azide at 130 minutes. Potential was held at -0.050 V. 10 mM potassium phosphate buffer, pH 7.5, 70 mM sodium chloride.

Table 9. Kinetic data for amperometry of enzymes

	I_{max} (nA)	K_M (μM)	R^2	n
Metabolon	367 ± 27	14.6 ± 2.0	0.9911	3
Complex IV	205 ± 7	11.1± 0.8	0.9976	3

Table 10. Kinetic inhibition data of sodium azide for amperometry of enzymes.

	I_{max} (nA)	K_i (μM)	R^2	n
Metabolon	162 ± 3	130 ± 6	0.9987	3
Complex IV	98 ± 4	249 ± 22	0.9964	3

without catalytic current. If the supercomplex was intact, then the inhibition of the end of the enzyme chain would have a large impact on the electron flux. Inhibition with sodium azide demonstrated a lower Ki, or more sensitive, for the metabolon electrode, where Complex IV activity has a large impact on the metabolon current response.

While the experiments show bioelectrocatalytic currents for Complex IV and the ETC metabolon, the cyclic voltammetry experiments were not reproducible with repeated trials and similar reconstituted fractions at any current magnitude. The cyclic voltammetry was performed on multiple metabolon electrodes, while only two were active with high currents. Repeated experiments with other active metabolon samples did not yield similar results and had error larger than 25% RSD. The proteoliposomes could be adsorbed to the surface but not fused into a complete bilayer. The long chain PEGylated tether could make the bilayer too fluid for stable positions as enzymes diffuse laterally and the bilayer moves away from the electrode surface. The enzymes have the ability to diffuse laterally and change positions in the bilayer because the enzymes are not tethered directly to the surface. With those assumptions of instability of the present tether, new directions were started with a different bilayer tether to provide more reproducible bioelectrocatalysis results.

Electrochemical Characterization of CHOL-PEG1K-NHS

Enzyme Bilayer

Cholesterol-PEG1K-n-Hydroxylsuccinimide (NHS) was used as a shorter and more stable connection of the lipid bilayer to the electrode. With a shorter chain, the diameter of the PEG group in a mushroom formation is 44.8 Å.[48] This smaller PEG linker could provide closer contact for the enzymes to the electrodes and more lipid/enzyme stability with a cholesterol anchor.[55] The new tether required a different immobilization procedure, because it has a NHS functional group instead of a sulfur group. Cysteamine was added to the β-mercaptoethanol monolayer at a 1:10 ratio to complete the reaction with the succidimide of the tether molecule. Bilayer formation with proteoliposomes was the same procedure, described previously. Control experiments were performed with lipid bilayers without enzyme to determine the current response with cytochrome c with the different tether in Figure 13. The cyclic voltammograms show a surface confined redox response in the smaller hydrated space of the cholesterol tether. The response was linear with concentrations of cytochrome c until ~5 μM where the current reponse levels out, indicating possible saturation of the protein at the surface. The E_{pc} was at ~ 20 mV (vs. Ag|AgCl) and E_{pa} was at ~ 50 mV (vs. Ag|AgCl) with a E^{o} at 35 mV (vs. Ag|AgCl), more reversible than the previous cytochrome c controls with the PEGylated lipid tether. The shorter cholesterol tether could trap the cytochrome c towards the electrode surface.

Cyclic voltammetry responses for the metabolon were similar to the previous PEGylated lipid tether experiments with sigmoidal catalytic reduction currents in Figure 14. The metabolon response had half wave potential of $E_{1/2}$ of 75 mV (vs. Ag|AgCl), an I_{max} of 310 ± 13 nA and a K_M of 6.3 ± 0.5 μM oxidized cytochrome c in Table 11. One large difference with the cholesterol tether was that the concentration allowed for cytochrome c bioelectrocatalysis was at a lower magnitude for the kinetic properties of the bioelectrocatalysis. Larger concentrations did not increase the current but rather saturated

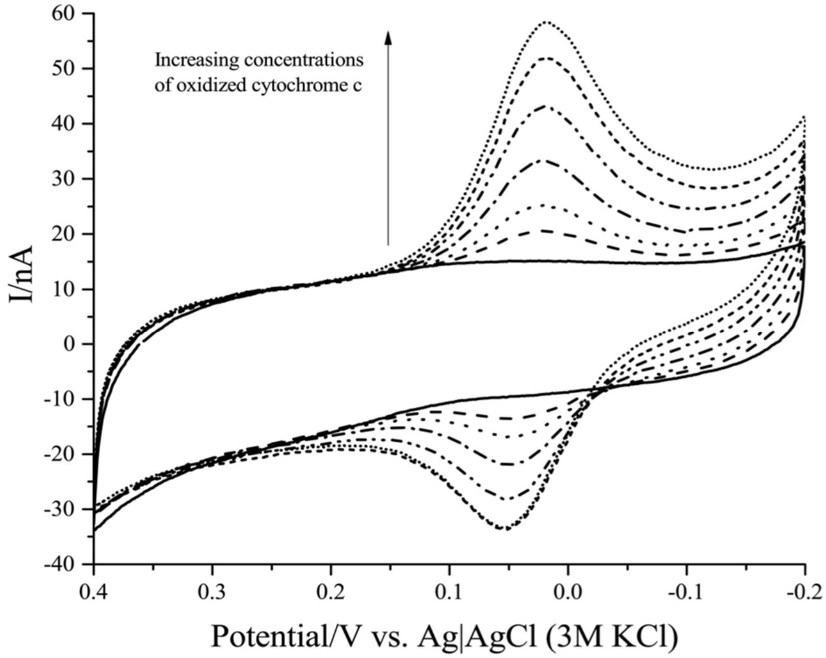

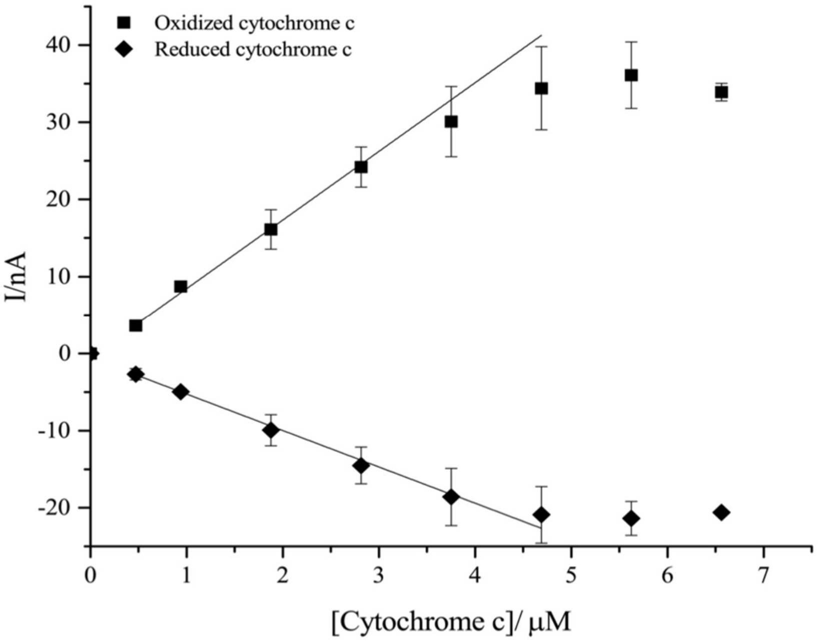

Figure 13. (Top) Representative cyclic voltammograms of oxidized cytochrome c with bilayer modified electrode. (Bottom) Peak current data for cytochrome c oxidation and reduction. 10 mM potassium phosphate buffer, pH 7.5, 70 mM potassium chloride. Scan rate 5 mV/s.

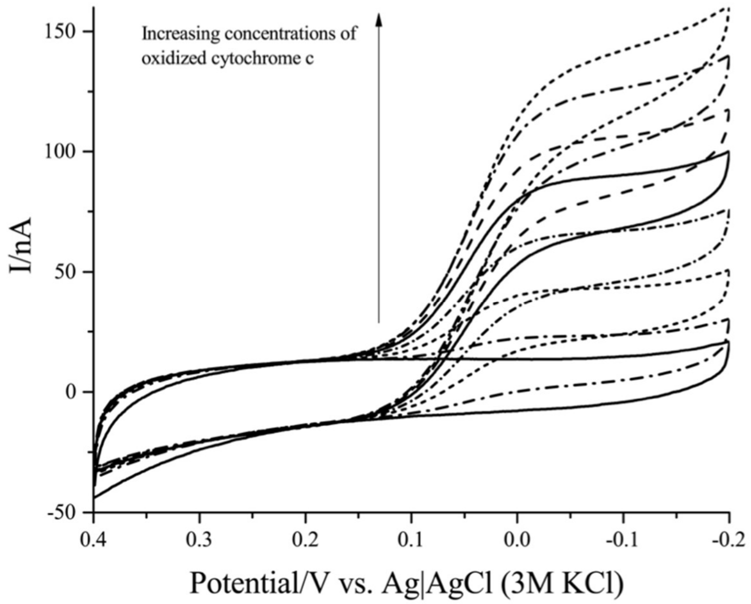

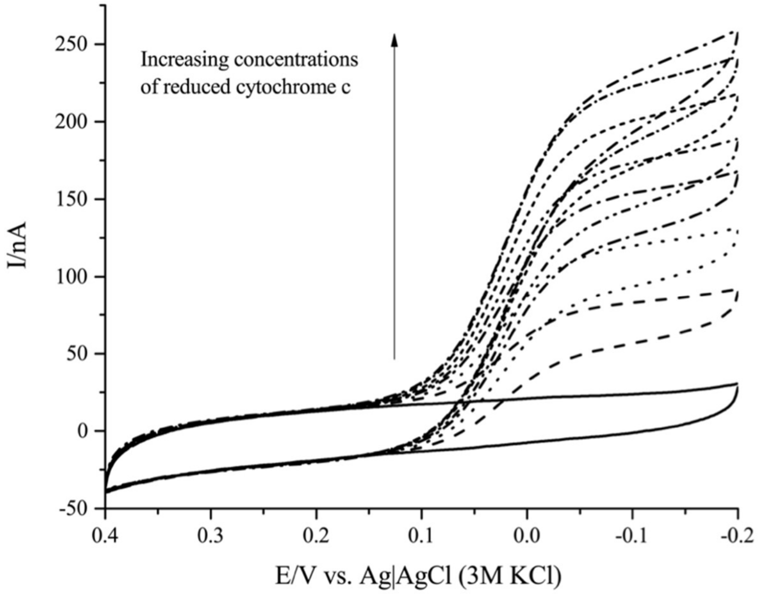

Figure 14. (Top) Representative ETC metabolon cyclic voltammograms with increasing oxidized (0-5 μM) cytochrome c concentrations. (Bottom) Representative cytochrome c oxidase cyclic voltammograms with increasing reduced (0-5 μM) cytochrome c concentrations. 10 mM potassium phosphate buffer, pH 7.5, 70 mM potassium chloride. Scan rate 5 mV/s.

Table 11. Kinetic data for cyclic voltammetry of enzymes.

	I_{max} (nA)	K_M (μM)	R^2	n
Metabolon	310 ± 13	6.3 ± 0.5	0.9967	4
Complex IV	189 ± 2	0.55 ± 0.02	0.9992	3

or inhibited activity. This difference could indicate that cytochrome c is limited in the diffusion into or out of the hydrated layer and may be more bound to the enzymes. Like the previous set, NADH addition to the buffer did not affect the catalytic current response. With injections of sodium azide in the presence of oxidized cytochrome with the metabolon sample, the limiting current decreased and became more diffusion limited, showing the inhibition of Complex IV. The Complex IV response had a half wave potential of $E_{1/2}$ of 50 mV (vs. Ag|AgCl), an I_{max} of 189 ± 2 nA and a K_M of 0.55 ± 0.02 μM reduced cytochrome c. The dramatic change in the kinetics for Complex IV with the cholesterol tether questions whether cytochrome c actually diffuses in and out of the bilayer or has a tighter binding with enzyme, not leaving the binding pocket of Complex IV.

The amperometric experiments were held at a more negative E_{appl} -100 mV. The experiments had same response for kinetics with oxidized and reduced cytochrome c, although the current response was much higher for the metabolon electrode. The metabolon response had an I_{max} of 231 ± 19 nA and a K_M of 4.9 ± 0.7 μM oxidized cytochrome c in Table 12, similar to the cyclic voltammetry responses. The inhibition of the metabolon sample with injections of axozystrobin showed a decrease in current but does not completely level out to a steady state to effectively quantitate the kinetics. Injections with sodium azide produced the same effect as cytochrome c oxidase and was more sensitive for the metabolon sample, almost completely inhibited by 100 μM sodium azide with I_{max} of inhibition at 163 ± 3 nA and a K_i of 42± 2 μM sodium azide in Table 13. The inhibiton had more affect on the current, eliminating the catalytic current by almost 70%. This shows that the metabolon is more sensitive to the inhibition of the Complex IV, because it has some control over the activity of the enzymes together and the source of the bioelectrocatalytic response. Complex IV had the same amperometric response with an I_{max} of 300 ± 16 nA and a K_M of 0.64 ± 0.04 μM reduced cytochrome c. For inhibition with sodium azide, it produced an I_{max} of inhibition at 143 ± 3 nA and a K_i of 130 ± 7 μM sodium azide in Table 13. Overall the difference in the tethering agent for the lipid bilayer sheds light on how the mediation with its substrate is affected by the loss in space of the hydrated layer.

Conclusion

By isolating the complex, the activities of the individual complexes can provide valuable information about the complex formation of the enzymes, the control of the overall activity by inhibition and how different buffer/environmental conditions affect the supercomplex activity. With inhibition with either azoxystrobin and azide, Complex III and Complex IV activity in the metabolon can be seen in the same sample. The addition of a crowding buffer and increasing the ionic strength shows slight improvement in the activity of the overall complex. The metabolon can then be reconstituted into proteoliposomes in preparation for electrochemical studies.

	I_{max} (nA)	K_M (μM)	R^2	n
Metabolon	231 ± 19	4.9 ± 0.7	0.9898	4
Complex IV	300 ± 6	0.64 ± 0.04	0.9949	4

Table 12. Kinetic data for amperometry of enzymes.

	I_{max} (nA)	K_i (μM)	R^2	n
Metabolon	163 ± 3	42 ± 2	0.9973	4

Table 13. Kinetic inhibition data for amperometry of enzymes.	Complex IV	143 ± 3	130 ± 7	0.9952	3

A tethered lipid bilayer has been developed to immobilize the large proteins of the ETC metabolon. Surface characterization experiments gave a glimpse into the immobilization of the enzymes, monitoring the mass deposited on the electrode and the cyclic effects of the mass by the applied potentials by QCM-D. Vesicle fusion is an important step that was demonstrated by proteoliposomes that were able to fuse together or stay adsorbed to the surface, limiting the amount of catalytic current that is measured. AFM and helium ion microscopy brought detail to the surface of the electrode, showing that prepared lipid bilayers are not complete, but rather lipid rafts or aggregated protein leaving large areas of surface without enzymes.

The development of this mitochondrial inner membrane biomimic has led to the study of the bioelectrocatalysis of the ETC metabolon on the electrode surface. By dropcasting on the electrode, the proteoliposomes need a fusing agent in calcium or an ionic strength change to burst the vesicles to fuse and form the tethered lipid bilayer. When using the DSPE-PEG2k-PDP, the enzymes showed very high currents up to 1.5 mA. The removal of a key substrate in the bilayer dropped the current by 50%. The positive control of Complex IV only produced 25% of the current at 400 nA, indicating a large amount of the current produced is by the flux of the entire chain, but was not reproducible after multiple attempts. The lipid bilayer could be too fluid with the large PEGylated layer, allowing the enzymes or the enzyme bound substrate to have a more transient connection with the electrode. Inhibition with azoxystrobin and sodium azide on the metabolon samples shows that Complex III and IV are part of the bioelectrocatalytic response decreasing the catalytic current by 50%. The cholesterol PEGylated tether showed a more reproducible response, possibly by the smaller hydrated layer to eliminate diffusional effects of the enzymes in the bilayer. The difference between the tethers was evident in the catalytic concentrations of cytochrome c, which decreased by 1-2 orders of magnitude for Complex IV.

Between both PEGylated tethers, the bioelectrocatalytic response is mediated by the substrate of cytochrome c. The potentials of cytochrome c, cytochrome c_1, and the binuclear copper center are within 50 mV of each other so it is difficult to determine if direct electron transport is possible without detecting a redox peak in buffer. By varying different conditions, the kinetics and inhibition responses can be monitored and reveal more information about the electron flux and activity of the enzymes in this formation and as an important metabolic cascade. Future efforts will explore more in depth studies with concentrations of ubiquinone, ionic strength conditions to differ the diffusion of cytochrome c, lipid content to aggregate or spread out the enzymes, and other possible enzymes such as ATP Synthase to learn more about this bioenergetics pathway and apply the knowledge to other biological energy applications such as biofuel cells.

DNA as a Scaffold for Forming Artificial Metabolons

An important factor that affects the biocatalytic activity of an enzyme cascade is the diffusion efficiency of intermediate substrates from one enzyme to another. In nature, enzyme cascades utilized in metabolic pathways are highly organized to form supercomplexes termed "metabolon" that can facilitate substrate channelling, which in turn increases the pathway efficiency. Inspired by this phenomenon, researchers used small crosslinkers such as dimethyl suberimidate, glutaraldehyde or bis-maleimides for synthesizing enzyme conjugates. The utilization of these conjugates instead of free enzymes in the anode led to the improvement of BFC performance and biosensor sensitivity. However the usage of small crosslinkers suffers from several drawbacks such as low conjugation yield, homo-crosslinking issue and especially, no control over the spatial arrangement of enzyme components. Therefore, the employment of methods to assemble enzyme cascades with better control over the interenzyme distance might help to further improve biofuel cell (BFC) performance and biosensor sensitivity.

In recent years, various strategies have been developed for *in vitro* construction of multi-enzyme cascades to enhance the catalytic activity. Among them, the utilization of DNA as a structural scaffold is a powerful method for assembly of enzyme cascades. Due to the programmability of DNA hybridization and the predictability of its secondary structure, DNA provide versatile and addressable platforms to precisely organize enzyme components at nanometer scale. Previous studies have shown that the assembly of multi-enzyme systems on various DNA scaffolds such as simple double helix, 2D arrays or DNA origami resulted in the enhancement of catalytic activity. However, most of these studies used the common enzymatic pair glucose oxidase (GOx)/horseradish peroxidase (HRP) as a model system. Similar study on enzyme cascades that can potentially be incorporated in BFC or biosensors remains unexplored. In this paper, we investigate the possibility of using DNA as a scaffold for assembly of the invertase (Inv)/glucose oxidase (GOx) enzyme cascade to improve its bioelectrocatalytic efficiency.

The Inv/GOx cascade uses sucrose as a substrate that is first hydrolysed by Inv to form D-glucose, which can be subsequently oxidized by GOx . We chose this enzymatic pair for our study because of several reasons. First, the cascade contains only one redox active enzyme (GOx), therefore, the bioelectrocatalysis of GOx can be directly used to compare the output activity of the assembled and non-assembled cascades. On the other hand, that comparison of cascades consisting of two or more sequential oxidative enzymes might be more complicated, since all enzymes will contribute to the outcome bioelectrocatalysis signal of the systems. In addition, the electrochemical response of the Inv/GOx pair is well studied, since it has been used to design biosensor for sucrose detection and construct an efficient BFC.

To assemble Inv and GOx on a DNA scaffold, these enzymes were first conjugated with DNA 1 and 2, respectively, by using sulfo-EMCS crosslinking reagent as previously described. The quantification of functionalized enzymes showed the average number of DNA per protein is 1.8 for GOx and 8 for Inv, which is in good agreement with literature values. Because our ultimate goal is studying the bioelectrocatalytic activity of the Inv/GOx enzyme pair when immobilized on the electrode surface, an ideal DNA scaffold used to assemble this cascade should be small to not affect the enzyme loading capacity. Therefore, our initial attempt is using a simple single-stranded DNA 3 containing two domains that can hybridize with 1 and 2 and are flanked by 10 bases. The activity of the enzyme pair was examined by a DCPIP assay with sucrose as a substrate. In this assay, sucrose is hydrolyzed by Inv to from glucose and fructose. Then, the reaction between glucose and DCPIP is catalyzed by GOx to form gluconolactone and the colourless reduced DCPIP. Thus, the activity of GOx can be determined by monitoring the decrease of DCPIP maximum absorbance (550nm at pH 5.5). Unfortunately, we did not observe any increase in activity of the Inv/GOx cascade when assembled on the DNA scaffold 3.

Recent simulation study suggest that the organization of multiple enzyme pairs on a scaffold can increase the activity, because this construct provides multiple enzyme targets for intermediate substrates. Therefore, in our next experiment, we attempt to examine a DNA scaffold that allows positioning multiple Inv/GOx pairs. For this purpose, we chose a long single stranded DNA generated by rolling circle amplification (RCA template), that is previously utilized by Wilner and co-workers for assembly of the GOx/HRP cascade. This study showed that the hybridization of the RCA template with DNA-modified enzymes is highly efficient and one template can positions approximately 200 enzyme pairs. The RCA template was synthesized as described and confirmed by agarose gel electrophoresis. To our delight, we observe 2±0.3 folds increase in the activity of the Inv/GOx cascade in the presence of the RCA template. A control experiment showed that the presence of a random DNA (40mer) that does not hybridize with 1 and 2 resulted in no change in the activity of the cascade. The activity enhancement in the presence of the RCA template is most likely due to the close proximity of the two enzymes on the DNA scaffolds allowing effective diffusion of the intermediate substrate to the second enzyme. Another possibility for the enhancement effect is the interaction of substrates with DNA scaffold as proposed recently. However, the activity of GOx-1 did not change in the presence of the RCA template, suggesting that is not the case in our experimental conditions.

Comparing to the GOx/HRP cascade, the activity enhancement of the Inv/GOx cascade is lower when assembled on the same DNA template. In agreement with previous observations, this result suggests that the "kinetic balance" among enzyme components might play an important role in the activation of enzyme cascades positioned on a scaffold. Our recent study showed that the hydrolysis of sucrose by Inv is rate-limiting step in the cascade. However the analysis of the overall kinetic in our system might be challenging because there are multiple enzyme pairs on a DNA template allowing the intermediate substrate interacts with various number of the second enzyme. In addition, the product of sucrose hydrolysis is α-D-glucose that undergo mutoration to β-D-glucose, and the latter compound is an even better substrate for GOx than the former ones. Moreover, Inv and GOx operate synergistically since Inv is inhibited by its products, thus, the increase in activity of GOx might also enhance the Inv activity. Additional stimulation work might be helpful to understand the overall kinetic of the system. Another product of sucrose hydrolysis is D-fructose that can be consumed by fructose dehydrogenase enzyme (FDH). Since FDH has relative high activity toward both fructose anomers (α, β forms), the Inv/FDH cascade might be a better option for kinetic analysis. However, we found that FDH does not tolerate with DNA modification and it lost about 80% of the native activity when functionalized with DNA. Nevertheless, the increase in activity of the Inv/GOx when assembled on the RCA template is evident and this triggered us to investigate the bioelectrocatalysis of this system when immobilized on the electrode surface.

For electrochemical studies, the Inv/GOx cascade was immobilized on a carbon paper electrode by using Fc-C6-LPEI hydrogel polymer as described in our previous report. The hydrogel polymer contains the redox active ferrocene moiety, which plays a role as an electron mediator, since GOx does not perform direct electron transfer to the electrode. The fabrication of electrodes was described in the supporting information. The electrochemical characterization of

Inv/GOx electrodes was studied using a conventional three-electrode set up with saturated calomel and Pt mess as a reference and counter electrodes, respectively. A cyclic voltametry (CV) experiment was first carried out to determine the oxidation potential of the Inv/GOx/Fc-C6-LPEI film. Amperometric response of Inv/GOx electrodes was investigated at the potential that is 50 mV higher than the oxidation potential of the film. The current allows to reach stable and sucrose was added from 1M stock solution. The results indicated that the presence of the RCA template leads to 50-100% increase in the current density of the Inv/GOx electrodes depending on the sucrose concentration. That enhancement effect is more pronounced at low concentration of sucrose. This is not surprised since the bioelectrocatalytic rate of GOx will be approaching to V_{max} when increasing the concentration of substrate. In addition, the fact that Inv inhibited by its products might also contribute to that effect. Overall, the observation here is in concert with our previous finding that a cross-linked enzyme cascade can enhance the bioelectrocatalysis comparing to free enzyme system.

We next investigate the performance of sucrose/O_2 biofuel cells with carbon paper anodes constructed from RCA-assembled or non-assembled Inv/GOx cascade. The cathode used in all biofuel cells is an air-breathing platinum electrode to ensure the anode is the limiting electrode. The characteristics of these biofuel cells is summarized in Table 1. In all biofuel cells, the current density is decreased when the potential reaching short circuit (0 V), probably due to the diffusion limit of the substrate to the electrode. Nevertheless, we observed a 40% increase in maximum current density of the RCA-assembled Inv/GOx biofuel cell comparing to that of free bienzyme biofuel cell at 50 mM concentration of the sucrose fuel. Similar to the amperometric experiments described above, this enhancement effect also more pronounced at low concentration of sucrose. For example, only 10% increase in the maximum current density was observed when these biofuel cells were tested at 100 mM sucrose. However, the measurement of power density of the assembled- and non-assembled Inv/GOx biofuel cells gave almost the same values at two sucrose concentrations studied. We postulated that the slow current response of the Inv/GOx cascade might be the reason for this result. As shown in the amperometric experiments, the Inv/GOx electrodes require up to 3h to reach the steady-state current; while the biofuel cells test only takes 15 minutes. Therefore, future study on DNA-assembled enzyme cascade should focus on enzyme systems that have fast current response, ideally in minute scale, to detect the difference in power density of assembled- and non-assembled cascade.

Conclusions

In conclusion, we investigated the utilization of DNA to assemble the Inv/GOx cascade to improve the bioelectrocatalytic activity. Our preliminary results showed that the DNA-assemble cascade have higher activity than the free cascade, both in solution and in immobilized state on the electrode surface. The study presented here indicates that DNA is a promising structural scaffold for assembly of enzyme cascades to enhance their bioelectrocatalysis, which in turn improve the performance of biofuel cells. Our future work will focus on utilizing this strategy for different enzyme cascades that contain more than two enzyme and carrying out fluorescent microscopy study to better understand the structure of DNA-assembled enzyme cascade immobilized on the electrode surface.

References

[1] Ovadi J, Srere PA. Macromolecular compartmentation and channeling. Int Rev Cytol 2000;192:255-80.

[2] Ovadi J, Srere PA. Metabolic Consequences of Enzyme Interactions Cell Biochem Funct 1996;14:249-58.
[3] Minteer SD. Alcoholic Fuels. Boca Raton, FL: CRC Press; 2006. p. 273.
[4] Oaks A, Bidwell RGS. Compartmentation of intermediary metabolites. Annue Rev Plant Physiol 1970;21:43-66.
[5] Araiza-Olivera D. Metabolic optimization by enzyme-enzyme and enzyme-cytoskeleton associations. In: Bubulya P, editor. Cell Metabolism - Cell Homestasis and Stress Response. Rijeka: InTech; 2012. p. 101-14.
[6] Srere PA, Knull HR. Location-location-location. TIBS 1998;23:319-20.
[7] Srere PA, Mathews CK. Purification of multienzyme complexes. Method Enzymol 1990;182:539-51.
[8] Elcock AH, McCammon JA. Evidence for electrostatic channeling in a fusion protein of malate dehydrogenase and citrate synthase. Biochemistry 1996;35:12652-8.
[9] Shatalin K, Lebreton S, Rault-Leonardon M, Velot C, Srere PA. Electrostatic channeling of oxaloacetate in a fusion protein of porcine citrate synthase and porcine mitochondrial malate dehydrogenase. Biochemistry 1999;38:881-9.
[10] Siedow JN, Umbach AL. Plant Mitochondrial Electron Transfer and Molecular Biology. The Plant Cell 1995;7:821-31.
[11] Hatefi Y, Haavik AG, Griffiths DE. Studies on the electron transfer system. XL. Preparation and properties of mitochondrial DPNH-coenzyme Q reductase. Journal of Biological Chemistry 1962;237:1676-80.
[12] Hatefi Y. The mitochondrial electron transport and oxidative phosphorylation system. Annual Reviews in Biochemistry 1985;54:1015-69.
[13] Ragan CI, Heron C. The interaction between mitochondrial NADH-ubiquinone oxidoreductase and ubiquinol-cytochrome c oxidoreductase. Evidence for stoicheiometric association. Biochemical Journal 1978;174:783-90.
[14] Hackenbrock CR, Chazotte B, Gupte SS. The random collision model and a critical assessment of diffusion and collision in mitochondrial electron transport. Journal of Bioenergetics and Biomembranes 1986;18:331-68.
[15] Rees D. Electrostatic influence on energetics of electron transfer reactions. Proceedings of the National Academy of Sciences 1985;82:3082-5.
[16] Althoff T, Mills DJ, Popot JL, Kuhlbrandt W. Arrangement of electron transport chain components in bovine mitochondrial supercomplex I1III2IV1. The EMBO journal 2011;30:4652-64.
[17] Chaban Y, Boekema EJ, Dudkina NV. Structures of mitochondrial oxidative phosphorylation supercomplexes and mechanisms for their stabilisation. Biochimica et biophysica acta 2014;1837:418-26.
[18] Schagger H, Pfeiffer K. The ratio of oxidative phosphorylation complexes I-V in bovine heart mitochondria and the composition of respiratory chain supercomplexes. Journal of Biological Chemistry 2001;276:37861-7.
[19] Schagger H, Pfeiffer K. Supercomplexes in the respiratory chains of yeast and mammalian mitochondria. The EMBO journal 2000;19:1777-83.
[20] Schägger H, von Jagow G. Blue native electrophoresis for isolation of membrane protein complexes in enzymatically active form. Analytical Biochemistry 1991;199:223-31.

[21] Althoff T, Mills DJ, Popot J-L, Kühlbrandt W. Arrangement of electron transport chain components in bovine mitochondrial supercomplex I1III2IV1. The EMBO journal 2011;30:4652-64.
[22] Lapuente-Brun E, Moreno-Loshuertos R, Acin-Perez R, Latorre-Pellicer A, Colas C, Balsa E, et al. Supercomplex Assembly Determines Electron Flux in the Mitochondrial Electron Transport Chain. Science 2013;340:1567-70.
[23] Bianchi C, Genova ML, Parenti Castelli G, Lenaz G. The Mitochondrial Respiratory Chain Is Partially Organized in a Supercomplex Assembly: Kinetic Evidence Using Flux Control Analysis Journal of Biological Chemistry 2004;279:36562-9.
[24] Genova ML, Baracca A, Biondi A, Casalena G, Faccioli M, Falasca AI, et al. Is supercomplex organization of the respiratory chain required for optimal electron transfer activity? Biochimica et Biophysica Acta (BBA) - Bioenergetics 2008;1777:740-6.
[25] Genova ML, Lenaz G. Functional role of mitochondrial respiratory supercomplexes. Biochimica et Biophysica Acta (BBA) - Bioenergetics 2014;1837:427-43.
[26] Srere PA. Complexes of Sequential Metabolic Enzymes. Annu Rev Biochem 1987;56:89-124.
[27] Schafer E, Dencher NA, Vonck J, Parcej DN. Three-dimensional structure of the respiratory chain supercomplex I1III2IV1 from bovine heart mitochondria. Biochemistry 2007;46:12579-85.
[28] Stroh A. Assembly of Respiratory Complexes I, III, and IV into NADH Oxidase Supercomplex Stabilizes Complex I in Paracoccus denitrificans. Journal of Biological Chemistry 2003;279:5000-7.
[29] Wagner ML, Tamm LK. Tethered polymer-supported planar lipid bilayers for reconstitution of integral membrane proteins: silane-polyethyleneglycol-lipid as a cushion and covalent linker. Biophysical journal 2000;79:1400-14.
[30] Ataka K, Giess F, Knoll W, Naumann R, Haber-Pohlmeier S, Richter B, et al. Oriented attachment and membrane reconstitution of His-tagged cytochrome c oxidase to a gold electrode: in situ monitoring by surface-enhanced infrared absorption spectroscopy. Journal of the American Chemical Society 2004;126:16199-206.
[31] Jeuken LJ, Connell SD, Henderson PJ, Gennis RB, Evans SD, Bushby RJ. Redox enzymes in tethered membranes. Journal of the American Chemical Society 2006;128:1711-6.
[32] Jeuken LJC, Jones AK, Chapman SK, Cecchini G, Armstrong FA. Electron-Transfer Mechanisms through Biological Redox Chains in Multicenter Enzymes. Journal of the American Chemical Society 2002;124:5702-13.
[33] Roger M, de Poulpiquet A, Ciaccafava A, Ilbert M, Guiral M, Giudici-Orticoni MT, et al. Reconstitution of supramolecular organization involved in energy metabolism at electrochemical interfaces for biosensing and bioenergy production. Analytical and Bioanalytical Chemistry 2013;406:1011-27.
[34] Gutierrez-Sanz O, Olea D, Pita M, Batista AP, Alonso A, Pereira MM, et al. Reconstitution of respiratory complex I on a biomimetic membrane supported on gold electrodes. Langmuir : the ACS journal of surfaces and colloids 2014;30:9007-15.
[35] Zu Y, Shannon RJ, Hirst J. Reversible, Electrochemical Interconversion of NADH and NAD+by the Catalytic (Iλ) Subcomplex of Mitochondrial NADH:Ubiquinone Oxidoreductase (Complex I). Journal of the American Chemical Society 2003;125:6020-1.
[36] Pelster LN, Minteer SD. Ubiquinol-cytochrome c reductase (Complex III) electrochemistry at multi-walled carbon nanotubes/Nafion modified glassy carbon electrodes. Electrochimica Acta 2012;82:214-7.

[37] Friedrich MG, Robertson JWF, Walz D, Knoll W, Naumann RLC. Electronic Wiring of a Multi-Redox Site Membrane Protein in a Biomimetic Surface Architecture. Biophysical journal 2008;94:3698-705.
[38] Acín-Pérez R, Fernández-Silva P, Peleato ML, Pérez-Martos A, Enriquez JA. Respiratory Active Mitochondrial Supercomplexes. Molecular Cell 2008;32:529-39.
[39] Pfeiffer K, Gohil V, Stuart RA, Hunte C, Brandt U, Greenberg ML, et al. Cardiolipin stabilizes respiratory chain supercomplexes. Journal of Biological Chemistry 2003;278:52873-80.
[40] Love JC, Estroff LA, Kriebel JK, Nuzzo RG, Whitesides GM. Self-Assembled Monolayers of Thiolates on Metals as a Form of Nanotechnology. Chemical Reviews 2005;105:1103-70.
[41] Góes MS, Rahman H, Ryall J, Davis JJ, Bueno PR. A Dielectric Model of Self-Assembled Monolayer Interfaces by Capacitive Spectroscopy†. Langmuir : the ACS journal of surfaces and colloids 2012;28:9689-99.
[42] Boubour E, Lennox RB. Insulating Properties of Self-Assembled Monolayers Monitored by Impedance Spectroscopy. Langmuir : the ACS journal of surfaces and colloids 2000;16:4222-8.
[43] Valincius G, Mickevicius M. Tethered Phospholipid Bilayer Membranes. Advances in Planar Lipid Bilayers and Liposomes 2015;21:27-61.
[44] Wingfield P, Arad T, Leonard K, Weiss H. Membrane crystals of ubiquinone:cytochrome c reductase from Neurospora mitochondria. Nature 1979;280:696-7.
[45] Fuller SD, Capaldi RA, Henderson R. Structure of cytochrome c oxidase in deoxycholate-derived two-dimensional crystals. J Mol Biol 1979;134:305-27.
[46] Oellerich S, Lecomte S, Paternostre M, Heimburg T, Hildebrandt P. Peripheral and Integral Binding of Cytochromecto Phospholipids Vesicles. The Journal of Physical Chemistry B 2004;108:3871-8.
[47] Munro JC, Frank CW. Adsorption of Lipid-Functionalized Poly(ethylene glycol) to Gold Surfaces as a Cushion for Polymer-Supported Lipid Bilayers. Langmuir : the ACS journal of surfaces and colloids 2004;20:3339-49.
[48] Munro JC, Frank CW. In Situ Formation and Characterization of Poly(ethylene glycol)-Supported Lipid Bilayers on Gold Surfaces. Langmuir : the ACS journal of surfaces and colloids 2004;20:10567-75.
[49] Knoll W, Naumann R, Friedrich M, Robertson JWF, Lösche M, Heinrich F, et al. Solid supported lipid membranes: New concepts for the biomimetic functionalization of solid surfaces. Biointerphases 2008;3:FA125.
[50] Gupte S, Wu ES, Hoechli L, Hoechli M, Jacobson K, Sowers AE, et al. Relationship between lateral diffusion, collision frequency, and electron transfer of mitochondrial inner membrane oxidation-reduction components. Proceedngs of the National Academy of Sciences 1984;81:2606-10.
[51] Gupte SS, Hackenbrock CR. The role of cytochrome c diffusion in mitochondrial electron transport. Journal of Biological Chemistry 1988;263:5248-53.
[52] Hernández VA, Lendeckel U, Scholz F. Electrochemistry of Adhesion and Spreading of Lipid Vesicles on Electrodes2013.
[53] Iwata S, Ostermeier C, Ludwig B, Michel H. Structure at 2.8 Å resolution of cytochrome c oxidase from Paracoccus denitrificans. Nature 1995;376:660-9.
[54] Kano K, Ikeda T. Fundamentals and Practices of Mediated Bioelectrocatalysis. Analytical Sciences 2000;16:1013-21.

[55] Schneider H, Hochli M, Hackenbrock CR. Relationship between the density distribution of intramembrane particles and electron transfer in the mitochondrial inner membrane as revealed by cholesterol incorporation. Journal of Cell Biology 1982;94:387-93.

Metabolon formation and substrate channeling in recombinant TCA cycle enzymes

Abstract

Supramolecular assembly of enzymes into metabolon structures is thought to enable efficient transport of reactants between active sites via substrate channeling. Recombinant versions of porcine citrate synthtase (CS), mitochondrial malate dehydrogenase (mMDH) and aconitase (Aco) were found to adopt a homogeneous native-like metabolon structure *in vitro*. Site-directed mutagenesis performed on highly conserved arginine residues located in the channel connecting mMDH and CS active sites led to the identification of CS(R65A) which retained high catalytic efficiency. Substrate channeling between the CS mutant and mMDH is severely impaired and the overall channeling probability decreased from 0.99 to 0.023, which would have important implications on the control of flux in central carbon metabolism.

Introduction

Enzymes frequently function in sequential, multi-step cascades and the co-localization of the enzymes in self-assembling clusters is often observed.[1-3] The term "metabolon" has been used describe these non-covalent structural enzyme complexes.[4] These arrangements enable substrates to be channeled between active sites without escaping into the medium.[5] When the intermediate transport is not 100% efficient, leaky channeling can occur, but the intermediates are sequestered enough to prevent equilibrium with the surroundings.[5-7]

Substrate channeling within metabolons results in several metabolic advantages. High local substrate concentrations enable better fluxes through a pathway, despite unfavorable equilibrium constants. Intermediates can be protected from the bulk phase, hindering competition from alternative pathways and protecting the cell from toxicity. These effects on the mass transport allow the enzymes to operate at high efficiencies even when the average concentrations of intermediates in the bulk phase are low, resulting in the improvement of overall catalytic efficiency of the metabolic process.[6-10]

Metabolons exist in many pathways, including glycolysis, fatty acid oxidation, amino acid metabolism, lipid biosynthesis and the tricarboxylic acid (TCA) cycle.[5,11] Several enzymes of the TCA cycle participate in metabolon formation, including citrate synthase (CS), mitochondrial malate dehydrogenase (mMDH) and aconitase (Aco).[12-15] Since they play a central role in cellular energy generation, metabolons of the TCA cycle have been well-studied.[16-23] The CS/mMDH interactions are of particular interest since the free oxaloacetate (OAA) intermediate concentration in the cell is thought to be too low to sustain the experimentally determined cycle rate and the mMDH reaction has an unfavorable equilibrium constant in the forward direction of the cycle.[20,23]

Most metabolon investigations employ indirect techniques to infer channeling.[8,14,21] Fundamental characterizations of substrate channeling have focused on enclosed channels such as the tunneling that occurs in tryptophan synthase.[24-26] However, the bounded diffusion mechanism within the metabolon is more relevant to most biological systems. And, it is becoming clear that these "leaky channeling" systems are inspiring new approaches in biocatalysis where coupled reaction/transport systems are being engineered with biomimetic substrate channeling pathways.[7]

Results and Discussion

The TCA cycle enzymes are a canonical example of the importance of substrate channeling. Characterizing the leaky channeling within this system has been difficult due to limited experimental tools. Recently, the first structural evidence for natural metabolon formation and subsequent electrostatic substrate channeling within these enzymes was obtained, by resolving the three-dimensional structure of the mMDH-CS-Aco complex by *in vivo* chemical cross-linking, mass spectrometry and protein docking.[27] Here, we characterize a synthetic metabolon formed *in vitro* by three recombinant versions of these enzymes of the cycle, which form a similar conformation as the natural complex *in vivo*. Substrate channeling is further investigated by site-directed mutagenesis and channeling can be significantly impaired by a single site-directed mutation.

The mMDH and CS enzymes are dimers composed of identical subunits, weighing 34 kDa and 49 kDa respectively, whereas the next enzyme, Aco (85 kDa), is monomeric.[28-30] mMDH catalyzes the reversible NAD(H)-dependent conversion of L-malate and OAA. CS converts OAA and acetyl coenzyme A (acetyl-CoA) to citrate and Coenzyme A (CoA). Aco catalyzes the dehydration-rehydration of citrate to iso-citrate, with cis-aconitate being the intermediate. These enzymes have been individually characterized, with porcine heart being the most extensively studied variants, which share >95% sequence homology with bovine heart enzymes. Here, three different enzyme groups were investigated: native tissue enzymes isolated from the intact bovine mitochondria, commercially available wild-type enzymes and recombinantly produced enzymes. Codon optimized synthetic genes coding for porcine heart mMDH, CS and Aco were expressed in *E. coli*. Enzymes were purified to >90% (Figure S1) and the protein yields were 5 mg/L, 75 mg/L and 50 mg/L for mMDH, CS and Aco, respectively.

Recombinant metabolons assembled *in vitro* exhibit only one of the wild-type metabolon conformations. Over the last decade, cross-linking/mass spectrometry analysis has been a common and standardized technique for studying protein complexes that can't be evaluated by X-ray or NMR analysis.[31,32] *In vitro* chemical cross-linking of protein-protein interactions between recombinant mMDH and CS was performed in the presence of Aco. SDS-PAGE analysis of commercial and recombinant enzyme mixtures demonstrated the formation of higher-ordered complexes after incubation with DSG, indicated by a set of intense bands above 100 kDa (Figure S2). In-gel tryptic digestion was conducted on the large complex bands, and the extracted peptide fragments were analyzed by liquid chromatography-tandem mass spectrometry (LC-MS/MS).

In the mitochondrial matrix, compartmentalized TCA cycle enzymes diffuse slowly, and their dynamic association is stabilized by the crowded environment. On the contrary, the apparent diffusion coefficient of enzymes in dilute solution is approximately two orders of magnitude higher, and the random molecular collision occurs much faster[11,33-36] than DSG cross-linking chemistry, so it is not possible to isolate and purify a stable in-vitro complex without cross-linking and there are minimal experimental artificats from random molecular collisions without strong intermolecular interactions. However, the in-vitro system only contains the three enzymes mMDH-CS-Aco, so the mass spectrometric data analysis and protein docking is easier, because the identity of all of the enzymes participating in the complex are known. Matching experimentally detected tryptic peptides to protein databases using the *Mascot* search engine identified the three enzymes in both cross-linked and non-cross-linked sample bands (Table S1). Cross-linked peptide candidates were determined by comparing cross-linked and non-cross-linked mass spectra, and matching additional masses after cross-linking to a manually-built theoretical mass database. Using the distance restraint (25 Å) on potentially DSG-linked residues (Figure S3), a hybrid protein docking method was utilized to elucidate the interactions between mMDH and CS *in vitro*.

For the complexes of commercial enzymes, a number of structures were found to meet the selection criteria and bear at least three identified cross- links (Figure S4). These structures exhibited distinct conformations, implying that mMDH and CS without any modifications interact in a random manner in dilute solution. Compared to the native tissue mitochondrial TCA cycle metabolon (Figure 1a), one model of the complex of commercial mMDH-CS showed up with the most structural similarity. In this structure (Fig. 1b), three DSG cross-links (matching three MS speaks, Table S2) were obtained between mMDH Lys 191, Lys 277, Lys 283 and CS Lys 325. The α-helices of CS at Ala1-His 28 and Ser426-Lys437 are buried in the interface that covers the inter-subunit domain of mMDH. Compared to the native tissue mitochondrial metabolon *in vivo*, however, mMDH is flipped around the axis parallel to the binding interface by about 180 degrees. As a result, the two N-termini of mMDH are in close proximity with CS while the C-termini are pointing outward. This flipping may be less favorable for channeling of OAA, as the mMDH active site clefts are open to the bulk phase and separated from CS active sites by a longer distance (73 Å) than that in the native tissue mitochondrial metabolon (35 Å).[27]

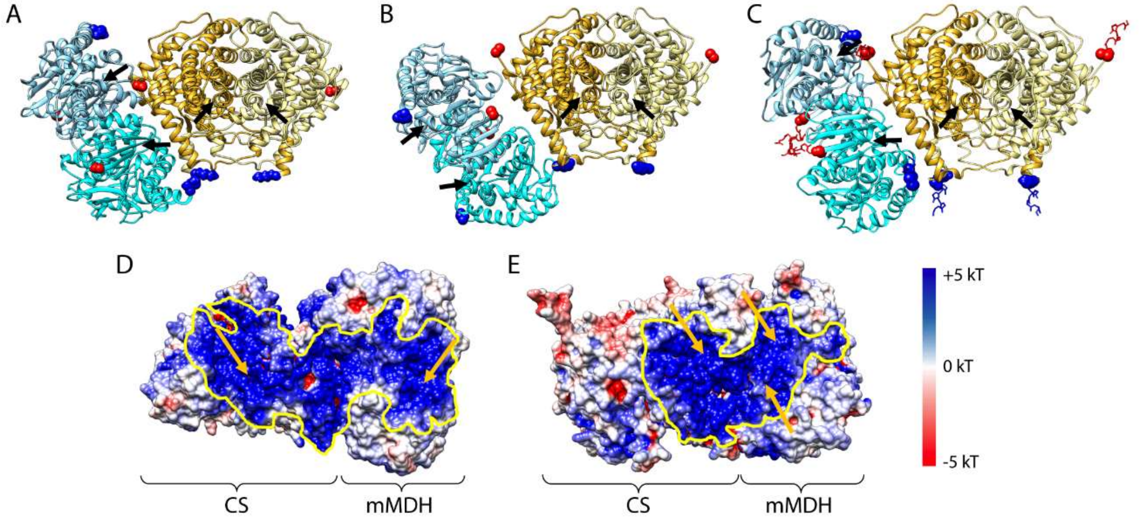

Figure 1: Structures of the mMDH-CS complex and the simulated electrostatic potential on the surface of the complex. (*A*) Native tissue mitochondrial metabolon. (*B*) *In vitro* complex formed by commercial enzymes. (*C*) *In vitro* complex formed by recombinant enzymes. N- and C-termini are represented by red and blue spheres, respectively. FLAG-tag and Polyhistidine-tag are represented by red and blue sticks, respectively. mMDH and CS active sites are denoted by black arrows. (*D*) *In vitro* complex formed by commercial enzymes. (*E*) *In vitro* complex formed by recombinant enzymes. Surface regions of positive potential and negative potential are colored in blue and red, respectively. The electrostatic channeling path for OAA is highlighted by the yellow edge. Orange arrows indicate the active sites. The surface ESP was calculated with water molecules at pH 7.4.

In contrast to the random association of commercial enzymes that yielded a number of complex conformations, the recombinant enzyme interactions were more restricted and resulted in a unique structure bearing seven DSG cross-links (matching four MS peaks, Table S3) between mMDH Lys81, Lys217, Lys304, Lys305 and CS Lys76, Lys325, Lys432. The α-helices of CS near its N- and C-termini again participate in the binding interface with the inter-subunit region of mMDH. Although mMDH was rotated around the axis perpendicular to the interface by approximately 30 degrees as compared to the metabolon *in vivo*, the final structure maintains most of the natural features (Figure 1c). No termini are buried in the interface, possibly due to spatial hindrance from additional amino acids (FLAG-tag and polyhistidine purification tag) appended to the termini, but the relative locations of termini around the interface are not significantly altered. The two N-termini of the mMDH dimer point away from CS and the mMDH and CS active sites are brought within a closer proximity (40 Å) than what was observed in the complexes of commercial mMDH-CS (73 Å). With this shorter pathway, OAA transfer was expected to be faster than that in the wild-type complexes. In addition, the interfacial areas in the recombinant mMDH-CS complexes are about 12,100 $Å^2$, suggesting that they may be more thermodynamically stable than either the native tissue mitochondrial metabolons (10,000 $Å^2$)[27] or the complexes of commercial mMDH-CS (11,300 $Å^2$).

Formation of commercial and recombinant mMDH-CS-Aco complexes *in vitro* was also examined by docking Aco onto solved mMDH-CS complexes (Figure S5). Three DSG cross-links (matching three MS peaks) were identified between CS Lys16, Lys76, Lys80 and Aco Lys4, Lys117 in the tri-enzyme complex formed by commercial enzymes (Table S4). It was found that CS Lys76 and Lys80 were located in the mMDH-CS interface, implying that mMDH and Aco would not be present on the same subunit of CS. Therefore, each CS dimer can only bind one mMDH dimer and one Aco monomer (Figure S5a). In the recombinant mMDH-CS-Aco complexes, there were four DSG cross-links between CS Lys294, Lys300 and Aco Lys709, Lys712, exhibiting no conflict with the identified cross-links between mMDH and CS, although only one MS peak was matched (Table S5). This result is consistent with that obtained from *in vivo* cross-linking of CS and Aco. Residues within C-terminal region of the recombinant Aco were recognized at the CS-Aco interface. A groove formed between mMDH and CS appeared to accommodate the C-terminal of Aco (Figure S5b). Hence, the resulted tri-enzyme association was found to be more compact than that of the metabolon formed by commercial mMDH and

CS. Similarly to the native tissue mitochondrial metabolon, a recombinant octamer comprised of one CS dimer, two mMDH dimers and two Aco monomers could possibly form *in vitro*.[27]

A model of the three-enzyme system was built on the assumption that inclusion of Aco does not alter the complex formation between mMDH and CS. The interaction between Aco and CS (or mMDH) is weaker than that between mMDH and CS according to previous observations *in vivo*, even though there is a lower chance that CS (or mMDH) binds Aco prior to mMDH (or CS) in dilute solution. Therefore, the contribution of Aco to the structural assignment between mMDH and CS was of lesser interest, and the remainder of the experimental efforts were focused on the investigation of the channeling of OAA within the mMDH-CS complex which is consistent with most of the related research in the literature.[17,19]

Simulated electrostatic channeling in wild-type/recombinant complexes. Elcock and McCammon previously demonstrated through Brownian dynamics simulations that electrostatic forces at the surface of a yeast mMDH-CS fusion protein greatly improved the OAA transfer efficiency.[19,37] In their fusion protein, a continuous surface of positive electrostatic potential bridged the active sites implying an important role of surface charge in the directed transport of OAA.[11] In the natural TCA cycle metabolon, theoretical evidence for electrostatic channeling was also found between mMDH and CS active sites using simulation tools.[27] To further investigate electrostatic channeling in the mMDH-CS complex formed *in vitro*, the electrostatic surface potential (ESP) was examined using the Poisson-Boltzmann equation in the presence of water molecules at pH 7.4. As illustrated in Figure 1d, a long and broad band of positive potential covers the majority of the complex surface of the commercial enzymes on one side, connecting the active sites. In the recombinant mMDH-CS complex (Figure 1e), the positive patch connecting active sites was reduced due to their increased proximity and relative orientation. Taken together with previous results from simulation of surface ESP of free enzymes, the formation of substrate channeling in such dynamic complexes is a product of electrostatic protein-protein interactions and rearrangement of surface charges upon association. Charged surface residues, especially positively charged arginines and lysines, likely play an essential role in directed transport of negatively charged OAA.

To explore this, interfacial residues of the recombinant complex were identified by screening surface arginine and lysine residues within a distance of 20 Å from each other. As a result, CS Arg65 and Arg67 were estimated to be important for the formation of the positive channel. Site-directed mutagenesis was performed at these positions and six different CS mutants were explored, where Arg65 and Arg67 were replaced by either alanine or aspartic acid: R65A, R67A, R65A/R67A, R65D, R67D and R65D/R67D. Prior mutational studies of CS have involved the active site residues,[38-41] aiming for the improvement of enzyme catalysis while the two residues mutated in this work (Arg65 and Arg67) are not located near the active site (Figure S6, Table S6).

Specific activities of the CS mutants were determined (Table S7). Arg67 was found to be crucial for the enzymatic activity of the recombinant CS. Any mutation of this side chain decreased or eliminated the enzymatic activity. In addition, CS(R67D) and CS(R65D/R67D) were found to be structurally affected by the mutations as shown in (Figure S7). CS(R67A), CS(R65A/R67A), CS(R65D) exhibited two or three orders of magnitude reductions of specific activities in comparison to the recombinant wild-type CS. CS(R67D) and CS(R65D/R67D) enzymatic activities could not be determined. CS(R65A) had similar enzymatic activity compared to recombinant wild-type CS. However, this mutation resulted in the dissociation of the mMDH-CS complex as implied by the disappearance of the mMDH-CS complex band in native PAGE gels. (Figure S8). Residues 65 and 67 were compared among different species, and Arg67 is highly conserved whereas Arg65 is generally well conserved suggesting the importance of positive charge at these positions (Table S8).

The steady state kinetics of the recombinant mMDH, recombinant CS and mutant CS enzymes were evaluated. Both mMDH and CS follow the ordered bi-bi kinetic mechanism, where mMDH binds to its cofactor and CS binds to OAA first.[28,29] The full steady state kinetic parameters were determined for recombinant mMDH, CS and CS(R65A) (Table 1). Recombinant CS had a $k_{cat}/K_{M,acetyl\text{-}CoA}$ value of 4.3 $\mu M^{-1}s^{-1}$ and $k_{cat}/K_{M,OAA}$ value of and 11 $\mu M^{-1}s^{-1}$ whereas CS(R65A) had a $k_{cat}/K_{M,acetyl\text{-}CoA}$ value of 5.6 $\mu M^{-1}s^{-1}$ and a $k_{cat}/K_{M,OAA}$ value of 39 $\mu M^{-1}s^{-1}$. These values indicate that R65A mutation did not impair the kinetic behavior of the enzyme.

Table 1: Kinetic parameters of recombinant enzymes.[a]

Enzyme	k_{cat} (s^{-1})	$K_{i,A}$ (mM)[b]	$K_{M,A}$ (mM)[b]	$K_{M,B}$ (mM)[c]
mMDH, fwd	31 ± 2	0.42 ± 0.08	0.13 ± 0.03	0.83 ± 0.10
mMDH, rev	870 ± 140	15 ± 2	87 ± 22	33 ± 7.9
CS	88 ± 4	4.6 ± 0.8	7.9 ± 1.2	21 ± 3
CS(R65A)	44 ± 3	1.7 ± 0.1	1.1 ± 0.3	7.8 ± 2.3

[a] Data is given as mean values ± s.d. from at least three independent measurements. [b] Substrate A is NAD^+ for mMDH, fwd, NADH for mMDH, rev and OAA for both CS and CS(R65A). [c] Substrate B is L-malate for mMDH, fwd, OAA for mMDH, rev and Acetyl-CoA for both CS and CS(R65A).

Electrostatic channeling of OAA in the presence of a competing enzyme and in viscous solutions. A common method to probe substrate channeling is to introduce an enzyme competing for the same intermediate.[42] As illustrated in Figure 2a, the mMDH-CS complex catalyzes sequential conversion of L-malate to citrate via OAA as the intermediate, using NAD^+ and acetyl-CoA as cofactors. A competitive pathway was introduced with aspartate aminotransferase (AAT), which catalyzes the conversion of OAA and L-glutamate to aspartate and α-ketoglutarate. In the presence of AAT, the resultant rate of citrate generation measured with crude lysate containing the native tissue mitochondrial mMDH-CS complex showed little change (Figure 2b). Approximately 88% of the recombinant mMDH-CS activity was retained, whereas

72% of the commercial mMDH-CS activity was retained in the presence of 1 U/mL of AAT. As the AAT concentration was increased to 5 U/mL, 89%, 77% and 68% of the coupled activity remained in the native tissue mitochondrial, recombinant commercial enzyme complexes, respectively (Figure 2b). The mutant recombinant complex (mMDH-CS(R65A)) only retained 53% of the coupled activity for 5 U/mL AAT. To minimize potential mMDH-AAT interactions, coupled catalysis was also explored with complexes immobilized in modified chitosan polymers. This ensured that AAT was physically separated from the complex and could not interact with the metabolon. Similar results were obtained compared to the free complexes in solution (Figure S9).

Glycerol was added into the assay solution to simulate the viscous matrix *in vivo* and the efficiency of mass transport in different mMDH-CS complexes were compared. As Figure 2c demonstrates, coupled activity of the native tissue mitochondrial mMDH-CS complex in crude lysate was not affected by the increased viscosity. For the recombinant complex, catalysis was similar in 10% glycerol, but decreased by 16% in 20% glycerol. This indicates that substrate channeling in the artificial complex functions in a “leaky” fashion. When compared to the complex of commercial enzymes and the mutant recombinant complex (mMDH-CS(R65A)), which respectively lost 15% and 20% of coupled activity in 10% glycerol and 30% and 35% of coupled activity in 20% glycerol, the recombinant complex (mMDH-CS) was less affected by increases in viscosity, indicating improved mass transport.

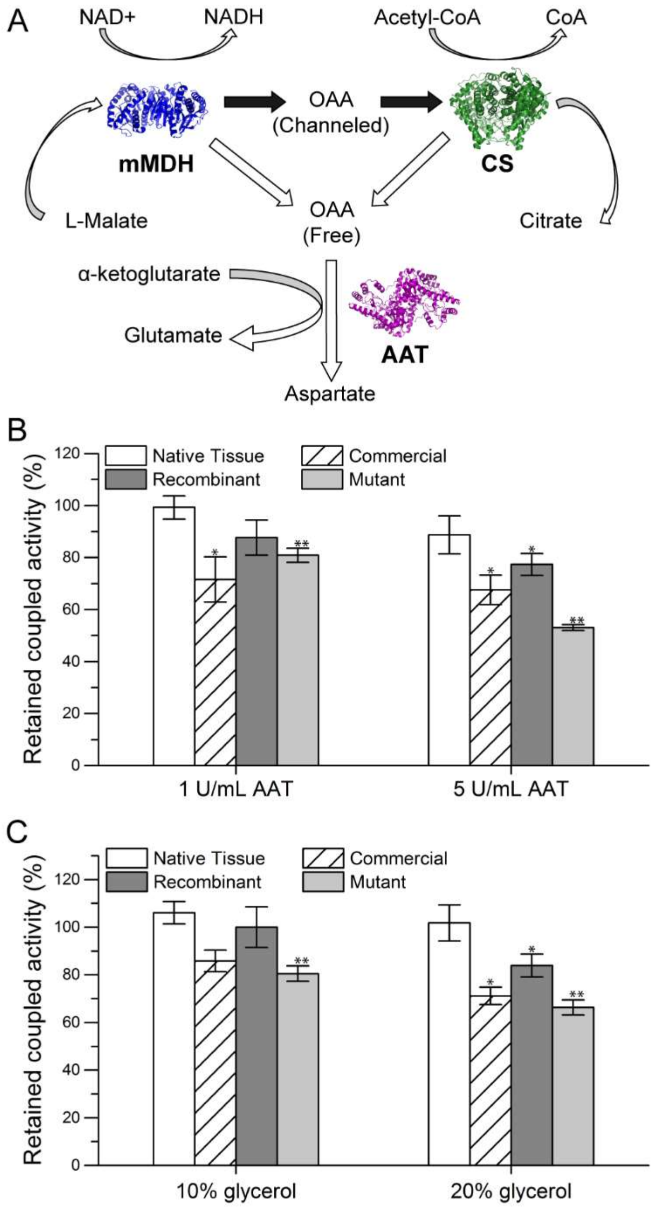

Figure 2: Demonstration of channeling of OAA within the mMDH-CS complex. (*A*) Schematic of the coupled mMDH-CS catalysis in the presence of competing enzyme AAT. White and black arrows represent diffusion and directed channeling, respectively. Crystal structure of AAT is obtained from Protein Data Bank (PDB ID: 1AAT). (*B*) Coupled activity retention calculated as the ratio of reaction rate before and after adding AAT measured with 100 μM mMDH-CS complex or crude mitochondrial lysate (about 5 μM protein in total). (*C*) Coupled activity retention in the presence of glycerol. Error bars represent standard deviation calculated from three independent experiments. Statistical significance (p-value) with respect to samples without AAT was calculated by a two-sample t-test with Welch correction for unequal variances: * = $p < 0.05$, ** = $p < 0.01$.

In a non-channeling system, OAA escaping into the bulk phase would be consumed by AAT, thus reducing the production of citrate. The coupled production of citrate by the recombinant complex was significantly less affected by the presence of a competing enzyme (AAT) or a viscous reagent (glycerol). Taken together with the structural evidence, these results demonstrate that assembly of sequential enzymes is important for efficient substrate channeling. In this work, the ESP of commercial and recombinant mMDH-CS complexes were calculated, and it was shown that an electrostatic channeling path bridging active sites forms at the surface of commercial as well as recombinant enzymes. However, the recombinant complex with its active sites closely facing each other provides a channeling advantage over the complex of commercial enzymes whose active sites are further apart and facing oppositely. Moreover, the R65A mutation prevents association and the formation of the electrostatic channel in the metabolon. Mutated recombinant complexes retained only 50% of citrate production in the presence of 5 U/mL AAT demonstrating that intermediate transport in the mMDH-CS(R65A) is more prone to being interrupted by competing pathways.

Characterization of electrostatic channeling by transient-time analysis. Transient time (τ) is used to describe the lifetime of intermediates in coupled catalysis. In unassembled systems, intermediate species will require more time to diffuse to the next active site, resulting in longer observed transient times before steady state activities are reached. Substrate channeling can reduce this effect.[43] Here, the ordered bi bi enzymatic reactions were treated as pseudo first-order by saturating the cofactors in the system. The overall initial reaction rates were limited by the OAA transport, which is dependent on the diffusion coefficient (D_i) of intermediates and the diffusing length (l) between active sites. Assuming that diffusion coefficients of OAA were not altered, the transient time is related to the diffusion distance length between the mMDH and CS active sites.

The transient times of OAA were measured in the native tissue mitochondrial metabolon and metabolons formed by commercial, recombinant and mutant mMDH and CS (Figure 3, Table 2). The simulated electrostatic channeling pathway (40 Å) for OAA was shorter in the mMDH-CS complex formed by recombinant enzymes, compared to commercial enzymes (73 Å). Consequently, the transient time of OAA in the recombinant complex was measured to be 30 ± 11 ms, which is comparable to the value of 40 ± 5 ms measured with crude lysate containing the native tissue mitochondrial TCA cycle metabolon. In comparison, the transient time of OAA in the complex of commercial enzymes was almost one order of magnitude higher, with a value of 290 ± 40 ms. In the case of the mutant mMDH-CS(R65A) complex, the resultant transient time was increased to 880 ± 60 ms, approaching 1 s. According to these results, the channeling of OAA was fastest in the native tissue mitochondrial complex followed by the recombinant complex, complex of commercial enzymes and the mutant mMDH-CS(R65A) complex.

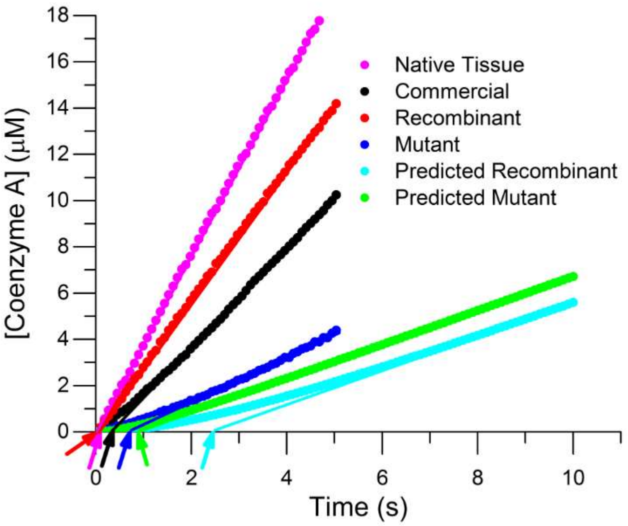

Figure 3: Characterization of OAA channeling via transient-time analysis where citrate production was measured over time. Transient time for each enzyme sample was determined by extrapolating the linear line fitted to the curve to the time axis as indicated by arrows (Table 2).

Agreeing with previous experiments, transient-time analysis also demonstrated that the mMDH-CS complex formed by recombinant enzymes in solution achieved similar channeling characteristics as the native tissue mitochondrial metabolon. The transient time of OAA in the recombinant mMDH-CS complex was reduced by 90% compared to the complex of commercial enzymes, indicating a higher channeling efficiency. The reduction of transient time in the recombinant complex, as compared to complex of commercial enzymes, was larger than the expected value of 70%, according to the equation for one-dimensional random walk, $l^2 = 2D_i$.[44] This is likely a result of the better orientation of the active sites in the recombinant complex. In the complex of commercial enzymes, the active site clefts in mMDH are facing oppositely to CS and are open to the bulk phase, resulting in an increased chance of OAA escape. Although substrate channeling in both systems was found to be "leaky", it is evident that recombinant enzymes exhibit higher catalysis coupling efficiency.

An analytical approach has been developed, which relates the substrate channeling phenomena to the Michaelis-Menten parameters of the enzymes.[37,43,45] A channeling probability parameter has been defined as $p_c\, p_r$, which can be obtained using the transient time, K_M and V_{max} of the second enzyme in the complex. The equation applicable to it mMDH-CS system is defined as the following:[37]

$$\tau = \frac{K_{M,app,OAA}\,(1-p_c p_r)}{V_{max,app}} \qquad [1]$$

By using the ordered bi bi rate equation and the kinetic parameters of the recombinant mMDH, CS and CS(R65A) enzymes, simulated citrate formation by the unassembled enzymes was calculated (Table 2). From this prediction, the transient times of OAA in recombinant mMDH-CS and mMDH-CS(R65A) systems were estimated to be 2.5 s and 0.90 s, respectively. These values represent the transient times with no interaction and no channeling, thus the probability parameter, $p_c\,p_r$, can be taken to be equal to 0. As shown by Eq. 1, $K_{M,app}/V_{max,app}$ is equal to the transient time in the case of no channeling. When this $K_{M,app}/V_{max,app}$ parameter is used together with the observed transient times of the complexes formed by the enzymes (0.03 s and 0.88 s for the recombinant and mutant complex respectively), the combined channeling parameters are calculated to be 0.99 and 0.023 for the recombinant mMDH-CS and mMDH-CS(R65A) respectively.

Table 2: Measured and predicted transient times of OAA.[a]

Sample	τ (ms)
Native Tissue	40 ± 5
Commercial	290 ± 40
Recombinant	30 ± 11
Mutant	880 ± 60
Predicted Recombinant	2500
Predicted Mutant	900

[a] Transient times were determined from linear fits from Figure 3. Mean and standard deviation for experimental values were calculated from three independent experiments.

This analysis further confirms the channel formation is disrupted in the mutant mMDH-CS(R65A) complex. The predicted and measured transient times are very similar for mMDH-CS(R65A) (0.90 s vs 0.88 s), which indicates that the intermediate OAA is channeling poorly after the arginine mutation. On the contrary, the measured time lag for the recombinant complex was 0.03 s, indicating efficient channeling of OAA within the metabolon. The probability parameter, $p_c\,p_r$, should approach 1 as intermediates are efficiently channeled[37] and this value was found to be 0.99 and 0.023 for mMDH-CS and for mMDH-CS(R65A) respectively. A comparison of the $k_{cat}/K_{M,AcCoA}$ values for the recombinant wild type (4.3 $\mu M^{-1}s^{-1}$) and mutant CS (5.6 $\mu M^{-1}s^{-1}$) as well as the $k_{cat}/K_{M,OAA}$ values (11 $\mu M^{-1}s^{-1}$ for wild type and 39 $M^{-1}s^{-1}$ for the mutant CS) indicate that these results arise from changes in the transport efficiency of the complexes and are not due to major changes in kinetic activities.

Metabolic Control Analysis (MCA) provides a framework to understand how metabolic fluxes are regulated by enzymatic activities.[46,47] The TCA cycle is a highly regulated network in central metabolism. To further investigate the potential implications of the R65A mutation, the elasticity coefficients of CS and CS(R65A) with respect to substrate OAA were estimated to be 0.79 and 0.63 (Equation S2), respectively, based on the steady-state substrate concentrations obtained with our model. Thus, the sensitivity of CS to OAA concentrations was decreased by the mutation. Taking the connectivity theorem into account, it can be concluded that this mutation would lead to an increased flux control coefficient indicating a potentially increased role in regulating metabolic control. The potential impact on the flux control may explain why this mutation is rarely observed in nature.

Conclusion

Complex metabolic pathways, such as the TCA cycle, involve multiple enzymatic steps that require efficient mass transfer of intermediates between active sites. The metabolon formation within the TCA cycle and the interactions between malate dehydrogenase and citrate synthase in particular, have been a major research focus. In this work, we presented the first direct evidence for metabolon formation among recombinantly produced mMDH and CS. The structural and kinetic analyses demonstrated that the recombinant versions of these enzymes self-assemble *in vitro*, similar to their native counterparts *in vivo*. Important residues for the enzyme interactions were identified and site-directed mutational analysis was performed for the first time to investigate the substrate channeling among these enzymes. A single mutation in CS, R65A, along the positively charged patch connecting the active sites, disrupted the transport of the negatively-charged intermediate, decreasing the overall channeling probability from 0.99 to 0.023. These results demonstrate the importance of substrate channeling in this critical biological pathway.

Methods

Recombinant porcine mMDH and CS were constructed and expressed in *E. coli*. Highly purified recombinant enzymes and commercially purchased enzymes were chemically crosslinked with disuccinimidyl glutarate, and the trypsin-digested peptides were analyzed with liquid chromatography-tandem mass spectrometry (LC-MS/MS). Peptide crosslinks were identified and complex structures were determined using previously published methods.[27] Mutations in CS were made by site directed mutagenesis. Kinetic parameters for an ordered bi-bi mechanism were determined spectrophotomerically for recombinant mMDH, CS and CS(R65A). mMDH/CS complexes were analyzed for substrate channeling spectrophotomerically with coupled enzymatic assays. Detailed materials and methods are given in the Supporting Information.

References

(1) Schoffelen, S., and van Hest, J. C. M. (2012) Multi-enzyme systems: bringing enzymes together in vitro. *Soft Matter 8*, 1736–1746.

(2) Ovádi, J., and Sreret, P. A. (1999) Macromolecular Compartmentation and Channeling, in

Microcompartmentation and Phase Separation in Cytoplasm, pp 255–280. Elsevier.

(3) Srere, P. A., and Mosbach, K. (1974) Metabolic Compartmentation: Symbiotic, Organellar, Multienzymic, and Microenvironmental. *Annual Review of Microbiology 28*, 61–84.

(4) Srere, P. A. (1985) The metabolon. *Trends in Biochemical Sciences 10*, 109–110.

(5) Ovádi, J. (1991) Physiological significance of metabolic channelling. *J. Theor. Biol. 152*, 1–22.

(6) Spivey, H. O., and Ovádi, J. (1999) Substrate channeling. *Methods 19*, 306–321.

(7) Wheeldon, I., Minteer, S. D., Banta, S., Barton, S. C., Atanassov, P., and Sigman, M. (2016) Substrate channelling as an approach to cascade reactions. *Nat Chem 8*, 299–309.

(8) Morgunov, I., and Srere, P. A. (1998) Interaction between citrate synthase and malate dehydrogenase. Substrate channeling of oxaloacetate. *Journal of Biological Chemistry 273*, 29540–29544.

(9) Huang, X., Holden, H. M., and Raushel, F. M. (2001) Channeling of substrates and intermediates in enzyme-catalyzed reactions. *Annu. Rev. Biochem. 70*, 149–180.

(10) Conrado, R. J., Varner, J. D., and DeLisa, M. P. (2008) Engineering the spatial organization of metabolic enzymes: mimicking nature's synergy. *Current Opinion in Biotechnology 19*, 492–499.

(11) Srere, P. A. (1987) Complexes of sequential metabolic enzymes. *Annu. Rev. Biochem. 56*, 89–124.

(12) Moore, G. E., Gadol, S. M., Robinson, J. B., and Srere, P. A. (1984) Binding of citrate synthase and malate dehydrogenase to mitochondrial inner membranes: tissue distribution and metabolite effects. *Biochemical and Biophysical Research Communications 121*, 612–618.

(13) D'Souza, S. F., and Srere, P. A. (1983) Cross-linking of mitochondrial matrix proteins in situ. *Biochim. Biophys. Acta 724*, 40–51.

(14) Robinson, J. B., and Srere, P. A. (1985) Organization of Krebs tricarboxylic acid cycle enzymes in mitochondria. *Journal of Biological Chemistry 260*, 10800–10805.

(15) Velot, C., Mixon, M. B., Teige, M., and Srere, P. A. (1997) Model of a quinary structure between Krebs TCA cycle enzymes: a model for the metabolon. *Biochemistry 36*, 14271–14276.

(16) Fernie, A. R., Carrari, F., and Sweetlove, L. J. (2004) Respiratory metabolism: glycolysis, the TCA cycle and mitochondrial electron transport. *Curr. Opin. Plant Biol. 7*, 254–261.

(17) Shatalin, K., Lebreton, S., Rault-Leonardon, M., Velot, C., and Srere, P. A. (1999) Electrostatic channeling of oxaloacetate in a fusion protein of porcine citrate synthase and porcine mitochondrial malate dehydrogenase. *Biochemistry 38*, 881–889.

(18) Lyubarev, A. E., and Kurganov, B. I. (1989) Supramolecular organization of tricarboxylic

acid cycle enzymes. *BioSystems 22*, 91–102.

(19) Elcock, A. H., and McCammon, J. A. (1996) Evidence for Electrostatic Channeling in a Fusion Protein of Malate Dehydrogenase and Citrate Synthase. *Biochemistry 35*, 12652–12658.

(20) Robinson, J. B., INMAN, L., Sumegi, B., and Srere, P. A. (1987) Further characterization of the Krebs tricarboxylic acid cycle metabolon. *Journal of Biological Chemistry 262*, 1786–1790.

(21) Lindbladh, C., Rault, M., Hagglund, C., Small, W. C., Mosbach, K., Bulow, L., Evans, C., and Srere, P. A. (1994) Preparation and kinetic characterization of a fusion protein of yeast mitochondrial citrate synthase and malate dehydrogenase. *Biochemistry 33*, 11692–11698.

(22) Srere, P. A., Mattiasson, B., and Mosbach, K. (1973) An immobilized three-enzyme system: a model for microenvironmental compartmentation in mitochondria. *Proceedings of the National Academy of Sciences 70*, 2534–2538.

(23) Beeckmans, S., and Kanarek, L. (1981) Demonstration of physical interactions between consecutive enzymes of the citric acid cycle and of the aspartate-malate shuttle. A study involving fumarase, malate dehydrogenase, citrate synthesis and aspartate aminotransferase. *European Journal of Biochemistry 117*, 527–535.

(24) Hyde, C. C., Ahmed, S. A., Padlan, E. A., Miles, E. W., and Davies, D. R. (1988) Three-dimensional structure of the tryptophan synthase alpha 2 beta 2 multienzyme complex from Salmonella typhimurium. *Journal of Biological Chemistry 263*, 17857–17871.

(25) Miles, E. W., Rhee, S., and Davies, D. R. (1999) The Molecular Basis of Substrate Channeling. *Journal of Biological Chemistry 274*, 12193–12196.

(26) Raushel, F. M., Thoden, J. B., and Holden, H. M. (2003) Enzymes with molecular tunnels. *Acc. Chem. Res. 36*, 539–548.

(27) Wu, F., and Minteer, S. (2015) Krebs cycle metabolon: structural evidence of substrate channeling revealed by cross-linking and mass spectrometry. *Angew. Chem. Int. Ed. 54*, 1851–1854.

(28) Minarik, P., Tomaskova, N., Kollarova, M., and Antalik, M. (2002) Malate dehydrogenases--structure and function. *Gen. Physiol. Biophys. 21*, 257–265.

(29) Wiegand, G., and Remington, S. J. (1986) Citrate synthase: structure, control, and mechanism. *Annu Rev Biophys Biophys Chem 15*, 97–117.

(30) Beinert, H., Kennedy, M. C., and Stout, C. D. (1996) Aconitase as iron-sulfur protein, enzyme, and iron-regulatory protein. *Chem. Rev. 96*, 2335–2374.

(31) Lee, Y. J. (2008) Mass spectrometric analysis of cross-linking sites for the structure of proteins and protein complexes. *Mol. BioSyst. 4*, 816–823.

(32) Rappsilber, J. (2011) The beginning of a beautiful friendship: Cross-linking/mass spectrometry and modelling of proteins and multi-protein complexes. *Journal of Structural Biology 173*, 530–540.

(33) Haggie, P. M., and Verkman, A. S. (2002) Diffusion of tricarboxylic acid cycle enzymes in the mitochondrial matrix in vivo. Evidence for restricted mobility of a multienzyme complex. *Journal of Biological Chemistry 277*, 40782–40788.

(34) Saks, V., Beraud, N., and Wallimann, T. (2008) Metabolic Compartmentation – A System Level Property of Muscle Cells. *International Journal of Molecular Sciences 2008, Vol. 9, Pages 751-767 9*, 751–767.

(35) Senske, M., Törk, L., Born, B., Havenith, M., Herrmann, C., and Ebbinghaus, S. (2014) Protein Stabilization by Macromolecular Crowding through Enthalpy Rather Than Entropy. *J. Am. Chem. Soc. 136*, 9036–9041.

(36) Zhou, H.-X., Rivas, G., and Minton, A. P. (2008) Macromolecular crowding and confinement: biochemical, biophysical, and potential physiological consequences. *Annu. Rev. Biophys. 37*, 375–397.

(37) Adrian H Elcock, Gary A Huber, A., and McCammon, J. A. (1997) Electrostatic Channeling of Substrates between Enzyme Active Sites: Comparison of Simulation and Experiment. *Biochemistry*, pp 16049–16058. American Chemical Society.

(38) Claudia T Evans, Linda C Kurz, S James Remington, A., Paul A Srere. (1996) Active Site Mutants of Pig Citrate Synthase: Effects of Mutations on the Enzyme Catalytic and Structural Properties†. *Biochemistry*, pp 10661–10672. American Chemical Society.

(39) Evans, C. T., Owens, D. D., Slaughter, C. A., and Srere, P. A. (1988) Characterization of Mutant Tmk368k Pig Citrate Synthase Expressed in and Isolated From Escherichia-Coli. *Biochemical and Biophysical Research Communications 157*, 1231–1238.

(40) Linda C Kurz, Tanuj Nakra, Richard Stein, Wanda Plungkhen, Marian Riley, Fong Hsu, A., and Drysdale, G. R. (1998) Effects of Changes in Three Catalytic Residues on the Relative Stabilities of Some of the Intermediates and Transition States in the Citrate Synthase Reaction†. *Biochemistry 37*, 9724–9737.

(41) Alter, G. M., Casazza, J. P., Zhi, W., Nemeth, P., Srere, P. A., and Evans, C. T. (1990) Mutation of essential catalytic residues in pig citrate synthase. *Biochemistry 29*, 7557–7563.

(42) Lin, J.-L., Palomec, L., and Wheeldon, I. (2014) Design and Analysis of Enhanced Catalysis in Scaffolded Multienzyme Cascade Reactions. *ACS Catal. 4*, 505–511.

(43) Ovádi, J., Tompa, P., Vértessy, B., Orosz, F., Keleti, T., and Welch, G. R. (1989) Transient-time analysis of substrate-channelling in interacting enzyme systems. *Biochem. J. 257*, 187–190.

(44) Bard, A. J., and Faulkner, L. R. (2001) Electrochemical methods: fundamentals and applications 2nd ed. Wiley.

(45) Easterby, J. S. (1981) A generalized theory of the transition time for sequential enzyme reactions. *Biochem. J. 199*, 155–161.

(46) Fell, D. A. (1992) Metabolic control analysis: a survey of its theoretical and experimental

development. *Biochem. J. 286 (Pt 2)*, 313–330.

(47) Kell, D. B., and Westerhoff, H. V. (1986) Metabolic control theory: its role in microbiology and biotechnology. *FEMS Microbiology Letters 39*, 305–320.

Expanded Materials and Methods

Genes, chemicals and bacterial strains

Synthetic genes coding for the porcine heart enzymes were synthesized by Genscript. All genes have a Flag-tag at the N-terminus and a 6xHis-tag at theC-terminus, for identification and purification purposes, respectively. Restriction enzymes for DNA cloning were purchased from New England Biolabs. Isopropyl β-D-1-thiogalactopyranoside (IPTG) and ampicillin sodium salt, were purchased from Gold Biotechnology. Amicon centrifugal filters were purchased from Millipore. Disuccinimidyl glutarate (DSG), sodium dodecyl sulfate polyacrylamide electrophoresis gels (SDS-PAGE) and running buffers were purchased from Invitrogen-Life Technologies. *E. coli* BL21 and BL21(DE3) cell lines were purchased from Bioline. Chaperon plasmid pGro7 was purchased from Clontech Laboratories–Takara. Ala-chitosan was prepared as previously described.[4] Fresh bovine heart was purchased from a local slaughterhouse and used immediately. All other reagents and materials were purchased from Sigma-Aldrich unless otherwise stated.

Construction, expression and purification of enzymes

Cloning of the synthetic genes into expression plasmids

The genes coding for CS and Aco were cloned into pET-20b(+) backbone using the NdeI and HindIII restriction sites. Resulting plasmids were transformed into BL21(DE3) cells. mMDH was inserted into pMAL-c4e expression vector via the same restriction sites. The resulting construct and the chaperon plasmid pGro7 were co-transformed into BL21 cells for expression.

Site-directed mutagenesis of recombinant CS

CS Arg65 and Arg67 were mutated to alanine and aspartic acid to create single and double mutants via site-directed mutagenesis: CS(R65A), CS(R67A), CS(R65A/R67A), CS(R65D), CS(R67D), CS(R65D/R67D). CS(R65A) was used as the template to mutate the Arg67 to alanine and CS(R65D) was used as the template to mutate Arg67 to aspartic acid. Corresponding primer sequences used during the PCR reaction are given in Table S9.

Expression and purification of the recombinant enzymes

All constructs were expressed in 1L of sterilized Terrific Broth, inoculated with 10 ml overnight culture. For Aco and CS, the media was supplemented with 100 ug/mL ampicillin. 35ug/mL chloramphenicol was added to mMDH cultures in addition to the ampicillin. The cells were grown to an OD_{600} of 0.6 while shaking at 37°C, and protein expression was induced with 0.5 mM IPTG for mMDH and CS, and with 0.6mM IPTG for Aco. Expression was carried out for

18-20 h at 25°C. Cells were harvested by centrifugation at 5000 × g for 10 min and resuspended in 50 mL HisTrap binding buffer (20 mM Tris, 150 mM NaCl and 20 mM imidazole, pH 7.4) per L of culture. Soluble proteins were collected via centrifugation at 15000 × g for 30 min after the cells were lysed by sonication with an ultrasonication probe in an ice bath for 6 min (5 s on pulse and 2 s off pulse). Enzymes of interest were purified by immobilized metal affinity chromatography using a HisTrap columns (GE Healthcare Life Sciences), where bound enzymes were eluted with the elution buffer (20mM Tris, 150mM NaCl, 500mM imidazole (pH 7.4). mMDH was buffer exchanged into 20mM Tris-HCl (pH 8.7) and purified via anion exchange chromatography where the enzyme was eluted using a linear NaCl gradient from 0 to 1 M NaCl. All enzymes were further purified with size exclusion chromatography after buffer exchanging into 50mM Tris, 150mM NaCl (pH 7.4). Amicon filters (Milipore) with 30kDa (for mMDH and CS) and 50kDa (for Aco) molecular weight cutoff were used in order to concentrate the protein solutions as well as to exchange the buffer in between different purification steps.

Preparation of crude mitochondrial lysate

Extraction of the bovine heart mitochondria was done according to the procedure described by Rogers *et al.* with some modifications.[5] Bovine heart cubes were blended with cold isolation buffer (70 mM sucrose, 210 mM mannitol, 5 mM HEPES, 1 mM EGTA and 0.5% BSA, pH 7.2) in a Waring laboratory blender. Meat suspension was centrifuged at 500 × g for 10 min, and the supernatant was centrifuged at 26000 × g for 20 min. Pellet was homogenized in the isolation buffer and centrifuged twice again at 500 × g for 10 min. Supernatant was filtered through a double-layer cheesecloth and centrifuged at 1000 × g for 20 min. The mitochondria pellet was washed with lysis buffer (50 mM Tris, 150 mM NaCl, 2 mM EDTA and 1 mM PMSF, pH 7.4) at 26000 × g for 10 min. Pellet resuspended in the lysis buffer was sonicated with an ultrasonication probe in ice bath for 4 min (5 s on pulse and 15 s off pulse). The crude lysate was initially cleared at 5000 × g for 30 min. EDTA and PMSF were removed through the pre-packed Sephadex™ G-25M column. Protein concentration in the mitochondrial lysate was determined to be 1 mg/mL by BCA assay.

Structural analysis

In vitro chemical cross-linking of mMDH, CS and Aco

Commercially available enzymes purchased from Sigma-Adrich and recombinant enzymes were cleaned up by a pre-packed Sephadex™ G-25M column (GE Healthcare) to remove ammonium sulfate and other salts containing primary amine. Afterwards, mMDH, CS and Aco were mixed equally to a total protein concentration of 20 μM in 10 mM PBS (pH 7.4). DSG dissolved in 50 μL of DMF was added to the enzyme mixture to a final concentration of 1 mM. The approximate DSG/protein molar ratio was 50:1 to ensure an efficient capture of weak protein-protein interactions in dilute solution without dramatic loss of enzyme activity. As the non-cross-linked control, 50 μL of DMF containing no DSG was used. Cross-linking was carried out at room temperature for 30 min under gentle shaking and quenched by adding 2 M Tris buffer (pH 8.3) to a final concentration of 20 mM.

Separation and in-gel digestion of enzyme complexes

Enzyme mixtures were washed with 50 mM Tris buffer (pH 7.4) in filter-incorporated Amicon tubes with a mass cutoff at 10 kDa (Millipore) at 5000 × g for 15 min to remove phosphates and extra DSG. Afterwards, cross-linked and non-cross-linked samples were directly separated by reducing SDS PAGE, which was performed on a 4-20% gradient gel according to the protocol provided by the manufacturer. Gel bands of interest were excised and de-stained twice in 1 mL of 50% methanol with 50 mM ammonium bicarbonate at room temperature, under gentle vortexing for 1 h. The gel slices were rehydrated in 1 mL of 50 mM ammonium bicarbonate at room temperature for 30 min, and the gel bands/spots of interest were cut into several pieces. These gel pieces were rehydrated in 1 mL of 100% acetonitrile at room temperature under gentle shaking for 30 min. Acetonitrile was carefully removed from the gel pieces with a pipette tip prior to trypsin digestion. The gel pieces were incubated with 10-20 µL of sequence-grade modified trypsin (20 ng/µL, Promega) in 50 mM ammonium bicarbonate overnight at 37 °C. Digestion was quenched by adding 20 µL of 1% formic acid. Then, the solution was allowed to stand, and peptides that dissolved in the 1% formic solution were extracted and collected. Further extraction of peptides from the gel material was performed twice by adding 50% acetonitrile with 1% formic acid and sonicating at 37 °C for 20 min. All these solutions were collected and combined. A final complete dehydration of the gel pieces was accomplished by adding 20 µL of 100% acetonitrile followed by incubation at 37 °C for 20 min. The combined supernatant solutions of extracted peptides were dried in a vacuum centrifuge (Speed-Vac). The peptides were reconstituted in 100 µL of 5% acetonitrile with 0.1% formic acid for mass spectrometric analysis.

Mass spectrometric instrumentation

Peptides were analyzed using a nano-liquid chromatography-tandem mass spectrometry (LC-MS/MS) system comprised of a nano-LC pump (Eksigent) and a LTQ-FT mass spectrometer (ThermoElectron Corporation). The LTQ-FT is a hybrid mass spectrometer with a linear ion trap used typically for MS/MS fragmentation (i.e. peptide sequence) and a Fourier transform ion-cyclotron resonance (FT-ICR) mass spectrometer used for primary accurate mass measurement of peptide ions. The LTQ-FT is equipped with a nanospray ion source (ThermoElectron Corporation). Approximately 5 to 20 fM of tryptic-digested or phosphopeptide-enriched samples were dissolved in 5% acetonitrile with 0.1% formic acid and injected onto a homemade C18 nanobore LC column for nano-LC-MS/MS. A linear gradient LC profile was used to separate and elute peptides, consisting of 5 to 70% solvent B in 78 min with a flow rate of 350 nL/min (solvent A: 5% acetonitrile with 0.1% formic acid; solvent B: 80% acetonitrile with 0.1% formic acid). The LTQ-FT mass spectrometer was operated in the data-dependent acquisition mode controlled by *Xcalibur 1.4* software, in which the “top 10” most intense peaks observed in an FT primary scan (i.e. MS survey spectrum) were determined by the computer on-the-fly and each peak was subsequently trapped for MS/MS analysis and sequenced through peptide fragmentation by collision-induced dissociation. Spectra in the FT-ICR were acquired from m/z 400 to 1700 at 50000 resolving power with about 3 ppm mass accuracy. The LTQ linear ion trap was operated with the following parameters: precursor activation time was 30 ms and activation Q was 0.25; collision energy was set at 35%; dynamic exclusion width was set at low mass of 0.1 Da with one repeat count and duration of 10 s.

Mascot database searches

LTQ-FT MS raw data files were processed to peak lists with *BioworksBrowser 3.2* software (ThermoElectron Corporation). Processing parameters used to generate peak lists were as followed: precursor mass was between 401-5500 Da; grouping was enabled to allow five intermediate MS/MS scans; precursor mass tolerance was set at 5 ppm; minimum ion count in MS/MS was set to 15, and minimum group count was set to 1. Resulting DTA files from each data acquisition were merged and searched against the NCBI or custom databases for identified proteins, using *MASCOT* search engine (Matrix Science Ltd; version 2.2.1; in-house licensed). Searches were done with tryptic specificity, allowing two missed cleavages or "non-specific cleavage" and a mass error tolerance of 5 ppm in MS spectra (i.e. FT-ICR data) and 0.5 Da for MS/MS ions (i.e. LTQ Linear ion trap). Identified peptides were generally accepted only when the *MASCOT* ion score value exceeded 20.

Identification of cross-linked peptides

Mass spectrometric raw files were analyzed via *Thermo Xcalibur* software and peptide peaks of interest were picked manually. A theoretical mass database of potential inter-protein cross-links was built up using a spreadsheet by combining two peptides, which were identified in individual (non-cross-linked) enzymes but missed in the cross-linked enzyme complex by *MASCOT* database search. Additional peptide peaks only found in cross-linked spectra were screened against the mass database. Cross-link candidates were selected by the following rules: trypsin did not cut at the C-terminus of modified lysines or lysines with proline on the C-terminus; up to two missed cleavages were allowed, but non-specific cuttings were not considered; peptide length was 5 ~ 30 amino acids; each cross-linked peptide had at least one lysine for cross-linking as well as a lysine or arginine at C-terminal; peaks showed up in at least duplicate experiments; mass error = 5 ppm. Flexible modifications that might be obtained by oxidation or during SDS-PAGE running were applied to specific residues for identification and the respective mass variations were previously summarized.[6] Identified cross-links were examined by *Mascot* automated target-decoy search against NCBI database to estimate false-discovery rate (FDR) and no protein hits were reported above identity threshold ($p = 0.05$)

Hybrid protein docking

Global docking and local docking were carried out to solve the structure of the mMDH-CS-Aco complex. In global docking, an automated protein docking web server, *Cluspro* (http://cluspro.bu.edu/), was utilized.[7-9] Cross-linked lysines identified by manual search were set as attracting residues. All proteins were treated as rigid bodies with their "open" conformations obtained from crystal structures, giving top 100 ~ 120 structures of highest score based on surface shape complementarity and free energies of desolvation and electrostatic interactions. Prior to local docking, all model candidates were screened by *Xwalk* software suite to filter out false positives by distance constraints.[10] Maximum Euclidean distance limit was set to 25 Å, resulting from a combination of DSG spacer arm length (7.7 Å), lysine side chain length (6 Å × 2) and backbone flexibility. In addition to Euclidean distance limit, solvent accessible surface (SAS) distance was set to 30 Å to mimic molecular flexibility of DSG. Solvent radius was 1.4 Å by default and set to 2 Å for SAS distance calculation. Rotamers were removed and only the distance of Cβ-Cβ between two lysines was calculated. A pair of lysines on two proteins in global candidates were considered as a potential cross-link, if their *Xwalk*-calculated separation is no more than the limits.[11] After distance filtering, global candidates bearing at least two potential cross-links were subject to local docking by another protein docking web server, *Rosetta* (http://rosie.rosettacommons.org/).[12-14] Derived from each starting global structure, 10 local candidates of lowest interface energy were screened again by *Xwalk*. Final complex structures were chosen based on two criteria: local candidates of lowest interface energy were clustered around a single position on the energy landscape and the structure had the highest number of potential cross-linkers in agreement with experimental results. Interfacial residues in final structures were determined when the measured Euclidean distance was less than 20 Å.

Simulation of electrostatic surface potential

Prior to simulation, docked structures were modified by *PDB2PQR* web server (http://nbcr-222.ucsd.edu/pdb2pqr_2.0.0/) to add missing hydrogens and/or heavy atoms and to estimate their titration states.[15,16] Protein complexes were protonated with favorable hydrogen bonds. Charges and radius were assigned from Amber force field. *PROPKA* was used to predict pK_a shifts in complexes at pH 7.4.[17] Calculation of surface ESP by Poisson-Boltzmann equation was done by *APBS* web server (http://www.poissonboltzmann.org/docs/apbs-installation/)[18,19] with the following parameter settings: water molecules were not removed; no additional ions were added at zero ionic strength; biomolecular dielectric constant was set at 2; and solvent dielectric constant was set at 78.54.

Kinetic analysis

Kinetic analysis of the recombinant enzymes

mMDH and CS activity measurements were carried out as in Shatalin *et al*. with some modifications.[20] mMDH was measured for activity with different substrate concentrations for the forward and reverse reactions, in 100 mM potassium phosphate buffer (pH 7.4) in a 96-well plate. L-malate, NAD^+, oxaloacetate (OAA) and NADH concentrations were varied from zero to

3 mM, 4 mM, 0.1 mM and 0.1 mM, respectively. NADH concentration was measured spectrophotomerically at 340 nm after the addition of 1 nM and 0.1 nM mMDH for the forward and reverse reactions, respectively. CS activity was determined in 100 mM potassium phosphate buffer (pH 7.4) as well, via monitoring the coenzyme A (CoA) production at 412 nm in the presence of 0.2 mM DTNB (5,5'-dithiobis(2-nitrobenzoate)) with 1 nM of enzyme in a 96-well plate. OAA and acetyl coenzyme A (acetyl-CoA) concentrations were varied from zero to 0.5 mM and 0.2 mM, respectively. NADH production/consumption was calculated using the extinction coefficients 6220 $M^{-1}cm^{-1}$. Production of citrate can be spectrophotometrically monitored through a subsequent reaction of CoA and DTNB, which yields a di-anion (TNB^{2-}) absorbing at 412 nm. Citrate production rate was determined from the maximum linear slope of the curve of absorbance over time. Extinction coefficient of TNB^{2-} at 412 nm was 14,150 $M^{-1}cm^{-1}$, and the light path length was 0.56 cm. All enzyme concentrations were determined by BCA assay (Thermo Scientific) following the protocol provided by the manufacturer and a SpectraMax M2 (Molecular Devices) was used for absorbance readings. Obtained data was fitted into ordered bi-bi equation in order to calculate the kinetic parameters of the enzymes:

$$v = \frac{V_{max}[A][B]}{K_{iA}K_B + K_B[A] + K_A[B] + [A][B]} \tag{1}$$

Coupled activity assays of the mMDH-CS complex in solution with aspartate aminotransferase (AAT) or glycerol

Equal amounts of mMDH and CS were mixed in 10 mM PBS (pH 7.4) to a final total protein concentration of 20 µM, and incubated under gentle shaking at room temperature for 30 min. The coupled activity of the mMDH-CS complex (100 nM) or the crude lysate (0.5 mg/mL) was assayed in a 96-well plate with 1 mM L-malate, 2 mM NAD^+, 0.1 mM acetyl coenzyme A, 0.2 mM DTNB and10 mM glutamate in 200 µL of 100 mM potassium phosphate buffer (pH 7.4) in the presence of 1 or 5 U/mL AAT. Control experiments were done without adding AAT. Glycerol was added to the enzyme and substrate solutions to 10% and 20% prior to mixing. Then the coupled activity of the mMDH-CS complex (100 nM) or the crude lysate (0.5 mg/mL) was assayed in a 96-well plate with 1 mM L-malate, 2 mM NAD^+, 0.1 mM acetyl-CoA and 0.2 mM DTNB in 200 µL of 100 mM potassium phosphate buffer (pH 7.4). Control experiments were done without adding glycerol. The absorbance increase at 412 nm was monitored by Synergy^{TM} HTX multi-mode microplate reader (BioTek) over 1 min at 1 s intervals. One unit (U) of enzyme activity was defined as 1 µmole of product formed in one minute.

Coupled activity assay of immobilized mMDH-CS complex with AAT

The mMDH-CS complex solutions (4 µM) and ala-chitosan solution (10 mg/mL) were mixed at a volume ratio of 2:1, and incubated on vortex at room temperature for 15 min. Cross-linked samples were prepared by incubating mixtures of mMDH and CS at 20 µM with 0.2 mM DSG under gentle shaking at room temperature for 30 min, followed by quenching with 2 M Tris (pH 8.3). The cross-linking ratio of DSG:protein was lowered to 10:1 to minimize potential deactivation of enzymes by excessive cross-linkers. 25 μL of the enzyme/polymer suspension was pipetted to the bottom of a polystyrene cuvette (1 cm for light path length) and dried in a vacuum at room temperature for 2 h. Coupled activity of immobilized enzyme complex was assayed in 1 mL of 100 mM potassium phosphate buffer (pH 7.4) containing 1 mM L-malate, 2 mM NAD$^+$, 0.1 mM acetyl-CoA, 0.2 mM DTNB, 10 mM glutamate and AAT at 0 or 1 U/mL. The absorbance change at 412 nm was monitored by a UV-Vis spectrophotometer (Evolution 260 Bio, Thermo Scientific).

Transient time measurement by fast kinetic study

Fast kinetic experiment was carried out in a 96-well plate measured by the plate reader equipped with a dual injection module. Before assays, 10 μL of mMDH (20 μM) and 10 μL of CS (20 μM) were mixed in 10 mM PBS (pH 7.4) and incubated under gentle shaking at room temperature for 30 min, followed by dilution to 2 mL in 100 mM potassium phosphate buffer (pH 7.4). The crude lysate was directly used without further dilution. Substrate solution was prepared in 2 mL of potassium phosphate buffer containing 2 mM L-malate, 4 mM NAD$^+$, 0.2 mM acetyl-CoA and 0.4 mM DTNB. To setup the assay condition, enzyme and substrate solutions were respectively injected by two separate syringes at a flow rate of 250 μL/s. Total assay volume was 200 μL/s per well. Absorbance at 412 nm was read every 90 ms over 1 min. Transient time of OAA was determined by extrapolating the linear line fitted to the absorbance curve within the first recorded 5 s.

Predicted transient time calculations

In addition to the experimental fast kinetic study of mMDH-CS complex, transient time analysis was performed using the experimentally obtained kinetic parameters of individual recombinant mMDH, recombinant CS and mutant CS(R65A). In Matlab, a function “xprime” is defined as the change in substrate / product concentrations with respect to time and ode45 function is used to solve the differential equations describing these substrate (OAA and acetyl-CoA) consumptions / product (citrate and CoA) formations. Obtained data is fitted using Excel and transient time of OAA was determined by extrapolating the linear line fitted to the time versus product concentration plot. The Matlab code is given below:

```
function xprime = concentrations(t,x);
```

```
xprime=[(v0-((V1*x(1)*x(2))/((KiA*KB)+(KA*x(2))+(KB*x(1))+(x(1)*x(2)))));(-
1)*(V1*x(1)*x(2))/((KiA*KB)+(KA*x(2))+(KB*x(1))+(x(1)*x(2)));(V1*x(1)*x(2))/((KiA*KB)
+(KA*x(2))+(KB*x(1))+(x(1)*x(2)));(V1*x(1)*x(2))/((KiA*KB)+(KA*x(2))+(KB*x(1))+(x(1)
*x(2)))];
```

where x(1) is OAA and x(2) is acetyl-CoA.

Elasticity coefficient calculations

In order to calculate the elasticity coefficient of CS with respect to OAA, following equation is used (18):

$$\varepsilon_{OAA}^{CS} = \frac{\partial v_{CS}}{\partial [OAA]} \frac{[OAA]}{v_{CS}} \tag{2}$$

where v is the reaction rate of CS and $[OAA]$ is the concentration of substrate OAA. After taking the derivative of the rate equation with respect to OAA, kinetic parameters and steady state OAA concentration belonging to CS and CS(R65A) are fitted to the Eq. 2, in order to obtain the steady state elasticity coefficients.[21]

Methods References

(1) Claudia T Evans, Linda C Kurz, S James Remington, A., Paul A Srere. (1996) Active Site Mutants of Pig Citrate Synthase: Effects of Mutations on the Enzyme Catalytic and Structural Properties†. *Biochemistry*, pp 10661–10672. American Chemical Society.

(2) Alter, G. M., Casazza, J. P., Zhi, W., Nemeth, P., Srere, P. A., and Evans, C. T. (1990) Mutation of essential catalytic residues in pig citrate synthase. *Biochemistry 29*, 7557–7563.

(3) Altschul, S. F., Madden, T. L., Schäffer, A. A., Zhang, J., Zhang, Z., Miller, W., and Lipman, D. J. (1997) Gapped BLAST and PSI-BLAST: a new generation of protein database search programs. *Nucleic Acids Research 25*, 3389–3402.

(4) Martin, G. L., Minteer, S. D., and Cooney, M. J. (2009) Spatial Distribution of Malate Dehydrogenase in Chitosan Scaffolds. *ACS Appl. Mater. Interfaces 1*, 367–372.

(5) Rogers, G. W., Brand, M. D., Petrosyan, S., Ashok, D., Elorza, A. A., Ferrick, D. A., and Murphy, A. N. (2011) High Throughput Microplate Respiratory Measurements Using Minimal Quantities Of Isolated Mitochondria. *PLoS ONE* (Kowaltowski, A. J., Ed.) *6*, e21746.

(6) Wu, F., and Minteer, S. (2015) Krebs cycle metabolon: structural evidence of substrate channeling revealed by cross-linking and mass spectrometry. *Angew. Chem. Int. Ed. 54*, 1851–1854.

(7) Comeau, S. R., Gatchell, D. W., Vajda, S., and Camacho, C. J. (2004) ClusPro: a fully automated algorithm for protein-protein docking. *Nucleic Acids Research 32*, W96–9.

(8) Comeau, S. R., Gatchell, D. W., Vajda, S., and Camacho, C. J. (2004) ClusPro: an automated docking and discrimination method for the prediction of protein complexes. *Bioinformatics 20*, 45–50.

(9) Kozakov, D., Beglov, D., Bohnuud, T., Mottarella, S. E., Xia, B., Hall, D. R., and Vajda, S. (2013) How good is automated protein docking? *Proteins: Structure, Function, and Bioinformatics* (Bonvin, A. M. J. J., Janin, J., and Wodak, S. J., Eds.) *81*, 2159–2166.

(10) Kahraman, A., Malmström, L., and Aebersold, R. (2011) Xwalk: computing and visualizing

distances in cross-linking experiments. *Bioinformatics 27*, 2163–2164.

(11) Herzog, F., Kahraman, A., Boehringer, D., Mak, R., Bracher, A., Walzthoeni, T., Leitner, A., Beck, M., Hartl, F.-U., Ban, N., Malmström, L., and Aebersold, R. (2012) Structural Probing of a Protein Phosphatase 2A Network by Chemical Cross-Linking and Mass Spectrometry. *Science 337*, 1348–1352.

(12) Chaudhury, S., Berrondo, M., Weitzner, B. D., Muthu, P., Bergman, H., and Gray, J. J. (2011) Benchmarking and Analysis of Protein Docking Performance in Rosetta v3.2. *PLoS ONE* (Uversky, V. N., Ed.) *6*, e22477.

(13) Lyskov, S., Chou, F.-C., Conchúir, S. Ó., Der, B. S., Drew, K., Kuroda, D., Xu, J., Weitzner, B. D., Renfrew, P. D., Sripakdeevong, P., Borgo, B., Havranek, J. J., Kuhlman, B., Kortemme, T., Bonneau, R., Gray, J. J., and Das, R. (2013) Serverification of Molecular Modeling Applications: The Rosetta Online Server That Includes Everyone (ROSIE). *PLoS ONE* (Uversky, V. N., Ed.) *8*, e63906.

(14) Lyskov, S., and Gray, J. J. (2008) The RosettaDock server for local protein-protein docking. *Nucleic Acids Research 36*, W233–8.

(15) Dolinsky, T. J., Czodrowski, P., Li, H., Nielsen, J. E., Jensen, J. H., Klebe, G., and Baker, N. A. (2007) PDB2PQR: expanding and upgrading automated preparation of biomolecular structures for molecular simulations. *Nucleic Acids Research 35*, W522–5.

(16) Dolinsky, T. J., Nielsen, J. E., McCammon, J. A., and Baker, N. A. (2004) PDB2PQR: an automated pipeline for the setup of Poisson-Boltzmann electrostatics calculations. *Nucleic Acids Research 32*, W665–7.

(17) Olsson, M. H. M., Søndergaard, C. R., Rostkowski, M., and Jensen, J. H. (2011) PROPKA3: Consistent Treatment of Internal and Surface Residues in Empirical pKa Predictions. *J. Chem. Theory Comput. 7*, 525–537.

(18) Baker, N. A., Sept, D., Joseph, S., and Holst, M. J. (2001) Electrostatics of nanosystems: application to microtubules and the ribosome. Proceedings of the ….

(19) Søndergaard, C. R., Olsson, M. H. M., Rostkowski, M., and Jensen, J. H. (2011) Improved Treatment of Ligands and Coupling Effects in Empirical Calculation and Rationalization of pKa Values. *J. Chem. Theory Comput. 7*, 2284–2295.

(20) Shatalin, K., Lebreton, S., Rault-Leonardon, M., Velot, C., and Srere, P. A. (1999) Electrostatic channeling of oxaloacetate in a fusion protein of porcine citrate synthase and porcine mitochondrial malate dehydrogenase. *Biochemistry 38*, 881–889.

(21) Fell, D. A. (1992) Metabolic control analysis: a survey of its theoretical and experimental development. *Biochem. J. 286 (Pt 2)*, 313–330.

Recombinant TCA Cycle Enzymes Arranged on DNA scaffolds by Fused Zinc Finger Domains

Introduction

Over the past few decades, highly organized multi-enzyme complexes within sequential multienzyme pathways, termed metabolons, have been the focus of intense research in the field of enzymology.[1,2] In a metabolon, intermediates can be channeled directly from one enzyme to the next without diffusing into the bulk phase through mechanisms including physical tunnels and electrostatic channels connecting active sites.[3] Metabolon formation and substrate channeling phenomena have several advantages over free enzymes including high local metabolite concentrations, promoting the progression of reactions as well as minimizing the cross-talk between competitive pathways.[4] Overall, a better mass transport within the pathway can be achieved, resulting in enhanced kinetics of the metabolic process, allowing the cell to operate at high efficiency. In order to improve and better engineer new reaction pathways with multiple enzyme catalysts we can assemble multienzyme complexes using information learned from nature.

Mitochondrial malate dehydrogenase (mMDH) and citrate synthase (CS) from the TCA cycle have been well-studied for metabolon formation and substrate channeling of the negatively charged intermediate oxaloacetate (OAA).[5,6] We previously examined the structure of native and recombinant mMDH/CS metabolons and located a patch of positively charged amino acids connecting the enzyme active sites along which OAA could be channeled by bounded diffusion.[7] Cytosolic malate dehydrogenase has not been shown to channel with CS. It has previously been used as a control previously in order to study substrate channeling between mMDH and CS,[6] and we can use these nonchanneling enzymes (cMDH/CS) to test engineered multienzyme complexes for substrate channeling.

The sequence-specific binding of DNA binding proteins such as zinc finger proteins to DNA makes it an attractive scaffold for multienzyme assembly.[8] Natural and engineered zinc finer proteins have been used to decorate DNA,[9] and by varying the DNA sequence, facors such as enzyme spacing and stoichiometry can be controlled. In this work, we construct zinc finger/enzyme fusion proteins for cMDH and CS using two zinc finger proteins with different DNA binding sequences in order to assemble a multienzyme complex on a DNA scaffold.

Materials and Methods

Genes, chemicals and bacterial strains

Synthetic genes coding for the porcine cytosolic malate dehydrogenase (cMDH) and AZP4[10] were synthesized by Genscript. The gene for cMDH was codon optimized for *E. coli* and included an NdeI restriction site and FLAG-tag at the N-terminus and a 6xHis-tag and HindIII restrictions site at the C-terminus. AZP4 included a linker segment at its N-terminus (GGSGGGGSGGGGYPG), and the gene was flanked by two HindIII restriction sites. Constructs for CS-His and SLAC-3ZF-His[11] were previously cloned. Restriction enzymes for DNA cloning were purchased from New England Biolabs. DNA oligos were purchased from Integrated DNA Technologies. Isopropyl β-D-1-thiogalactopyranoside (IPTG) and ampicillin sodium salt, were purchased from Gold Biotechnology. Amicon centrifugal filters were purchased from Millipore. Sodium dodecyl sulfate polyacrylamide electrophoresis gels (SDS-PAGE), running buffers and electrophoretic mobility-shift assay (EMSA) kits were purchased from Invitrogen-Life Technologies. *E. coli* BL21(DE3) cell lines were purchased from Bioline. All other reagents and materials were purchased from Sigma-Aldrich unless otherwise stated.

Cloning of the synthetic genes into expression plasmids

The gene coding for cMDH was cloned into pET-20b(+) backbone using the NdeI and HindIII restriction sites. In order to insert the zinc finger domains at the C-terminus prior to the 6xHis purification tag, the genes for cMDH and CS were PCR amplified using the primers in Table 1, restriction digested with NdeI and HindIII and ligated into pET-20b(+), generating pcMDH-HindIII-His and pCS-HindIII-His. The genes encoding SLAC-3ZF-His and AZP4 were digested with HindIII, and the zinc fingers were inserted into the HindIII-digested pcMDH-HindIII-His and pCS-HindIII-His, respectively generating pcMDH-3ZF-His and pCS-AZP4-His. The resulting plasmids were transformed into BL21(DE3) cells for cMDH-His, cMDH-3ZF-His and CS-AZP4-His expression.

Table 1: PCR primers

Enzyme	Primer	Sequence
cMDH	Forward	5’ GAGCACCATATGAGCGAACCGATCCGTGTGC 3’
	Reverse	5’ GAGCACAAGCTTCGCGCTGCTCAGGAACTCGAAC
CS	Forward	5’ GAGCACCATATGAGCAGCACGAACCTGAAAGACA
	Reverse	5’ GAGCACAAGCTTTTTGCTATCGACCAGTTTAATCAGACCGTCC 3’

Expression and purification of the recombinant enzymes

All constructs were expressed in 1L of sterilized Terrific Broth, inoculated with 10 ml overnight culture. For Aco and CS, the media was supplemented with 100 ug/mL ampicillin. The cells were grown to an OD_{600} of 0.6 while shaking at 37°C, and protein expression was induced with 0.5 mM IPTG. Expression was carried out for 18-20 h at 25°C. Cells were harvested by centrifugation at 5000 × g for 10 min and resuspended in 50 mL HisTrap binding buffer (20 mM

Tris, 150 mM NaCl and 20 mM imidazole, pH 7.4) per L of culture. Soluble proteins were collected via centrifugation at 15000 × g for 30 min after the cells were lysed by sonication with an ultrasonication probe in an ice bath for 6 min (5 s on pulse and 2 s off pulse). Enzymes of interest were purified by immobilized metal affinity chromatography using a HisTrap columns (GE Healthcare Life Sciences), where bound enzymes were eluted with the elution buffer (20mM Tris, 150mM NaCl, 500mM imidazole (pH 7.4). All enzymes were further purified with size exclusion chromatography after buffer exchanging into 50mM Tris, 150mM NaCl (pH 7.4) (Figure 1). Amicon filters (Milipore) with 30kDa (for mMDH and CS) and 50kDa (for Aco) molecular weight cutoff were used in order to concentrate the protein solutions as well as to exchange the buffer in between different purification steps.

Kinetic analysis of the recombinant enzymes

CS-His and CS-AZP4-His activity was measured in activity assay buffer (100 mM potassium phosphate buffer, pH 7.4) with 0.1 mM oxaloacetate (OAA) and 0.1 mM acetyl coenzyme A (acetyl-CoA) in the presence of 0.2 mM DTNB (5,5'-dithiobis(2-nitrobenzoate)). Coenzyme A production was monitored spectrophotometrically through a subsequent reaction of CoA and DTNB, which yields a di-anion (TNB^{2-}) absorbing at 412 nm with an extinction coefficient of 14,150 $M^{-1}cm^{-1}$. Activities of cMDH-His and cMDH-3ZF-His were also measured in activity assay buffer with 0.1 mM NADH and 0.1 mM OAA. Consumption of NADH measured spectrophotomerically at 340 nm, and an extention coefficient of coefficients 6220 $M^{-1}cm^{-1}$ was used for NADH. All measurements were performed on a SpectraMax M2 (Molecular Devices).

Oligo preparations

Sense, biotinylated sense and antisense oligos were purchased containing the 3ZF, AZP4 and Control binding sites (Table 2). Oligos were suspended in annealing buffer (10 mM Tris-HCl, 50 mM NaCl, 1 mM EDTA, pH 8). Sense and antisense oligos were mixed at equimolar concentrations and annealed by heating samples for 10 minutes at 95°C and slowly cooled to room temperature. The resulting six samples are referred to as 3ZF-DNA, AZP4-DNA, Control-DNA, Biotin-3ZF-DNA, Biotin-AZP4-DNA and Biotin-Control-DNA.

Table 2: Oligos for DNA binding assays

DNA Target Name	Oligo	Sequence
3ZF-DNA	Sense	5’ TATGGATCCTACCATGGAGCGTGGGCGTAAGCTTAT 3’
	Antisense	5’ ATAAGCTTACGCCCACGCTCCATGGTAGGATCCATA 3’
AZP4-DNA	Sense	5’ TATGGATCCTACCATGGATACGTGGCATAAGC 3’
	Antisense	5’ ATAAGCTTATGCCACGTATCCATGGTAGGATCCATA 3’
Control-DNA	Sense	5’ TATGGATCCTACCATGGACCTATGTGCTAAGCTTAT 3’
	Antisense	5’ ATAAGCTTAGCACATAGGTCCATGGTAGGATCCATA 3’
Biotin-3ZF-DNA	Sense	Biotin- 5’ TATGGATCCTACCATGGAGCGTGGGCGTAAGCTTAT 3’
Biotin-AZP4-DNA	Sense	Biotin- 5’ TATGGATCCTACCATGGATACGTGGCATAAGC 3’
Biotin-Control-DNA	Sense	Biotin- 5’ TATGGATCCTACCATGGACCTATGTGCTAAGCTTAT 3’

Electrophoretic mobility shift assay

Purified enzymes were incubated for 2 hours at 4°C with 0.75 µM of 3ZF-DNA, AZP4-DNA and Control-DNA in DNA assay buffer (50 mM Tris-HCl, 0.5 M NaCl, 0.05% IGEPAL, 0.1 mM $ZnSO_4$ and 1 mM dithiotheitol, pH 8.0. Enzyme concentrations ranged from 0.15µM to 18.75 µM. Glycerol was added for a 10% final concentration, and samples were loaded onto a 6% DNA retardation gel and electrophoresed at 100 V for 85 minutes at 4°C. Gels were dyed with SYBR Green I nucleic acid stain.

DNA binding using magnetic bead capture

Protein binding to biotinylated DNA was analyzed as previously described with modifications.[11] Streptavidin coated magnetic beads were washed twice and incubated with blocking buffer (50 mM Tris-HCl, 150 mM NaCl, 0.5% BSA, pH 7.5) for 1 hour at 4°C with rotation. Beads were then incubated with 0.75 µM Biotin-3ZF-DNA, Biotin-AZP4-DNA and Biotin-Control-DNA in DNA assay buffer for 2 hours at 4°C with rotation and washed six times with DNA assay buffer. Purified enzyme (0.2 µM) was incubated with the DNA/bead samples for 4 hours at 4°C with rotation in DNA assay buffer, washed three times with DNA assay buffer and then resuspended in 100 activity assay buffer. The amount of bound enzyme was determined by measuring the enzyme activity as previously described.

Results and Discussion

The recombinant enzymes cMDH-His, CS-His and the enzyme/zinc finger fusion proteins cMDH-3ZF-His and CS-AZP4-His were expressed in *E. coli* and purified. All enzymes were determined to be active (Figure 2), and the activity of the enzyme/zinc finger fusion proteins was similar to the enzymes without the zinc finger proteins.

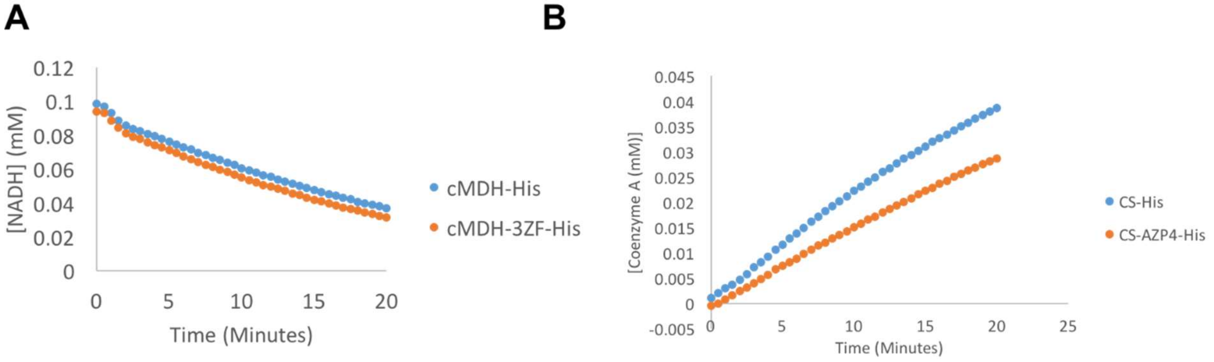

Figure 1: Enzyme activity assays. (A) cMDH-His and cMDH-3ZF-His assayed with 0.1 mM OAA and 0.1 mM NADH with 1 nM enzyme. (B) CS-His and CS-AZP4-His assayed with 0.1 mM Acetyl-CoA, 0.1 mM OAA and 0.2 mM DTNB with 1 nM enzyme.

Both enzyme/zinc finger fusion proteins were found to bind to their target DNA by EMSA (Figure 2). In the EMSA, when CS-AZP4-His was incubated with its DNA target AZP4-DNA, a DNA/protein complex is seen, and the amount of complexed DNA increases with protein concentration (Figure 2a). A decrease in the non-complexed DNA is also observed with increasing protein concentration. When combined with Control-DNA and 3ZF-DNA, there is not a decrease in the concentration or an appearance of a DNA/protein complex for any concentration of CS-AZP4-His. When cMDH-3ZF-His is incubated with its target DNA 3ZF-DNA, a DNA/protein also appears (Figure 2b). There is an increase in the amount of the DNA/protein complex and a decrease in non-complexed DNA with respect to enzyme concentration. The non-complexed DNA nearly disappears for the highest protein concentration, indicating that cMDH-3ZF-His binds to its target DNA better than CS-AZP4-His. When cMDH-3ZF is incubated with the other DNA targets AZP4-DNA and Control-DNA, a DNA/protein complex does appear with increasing protein concentration, but the binding is much weaker than for 3ZF-DNA.

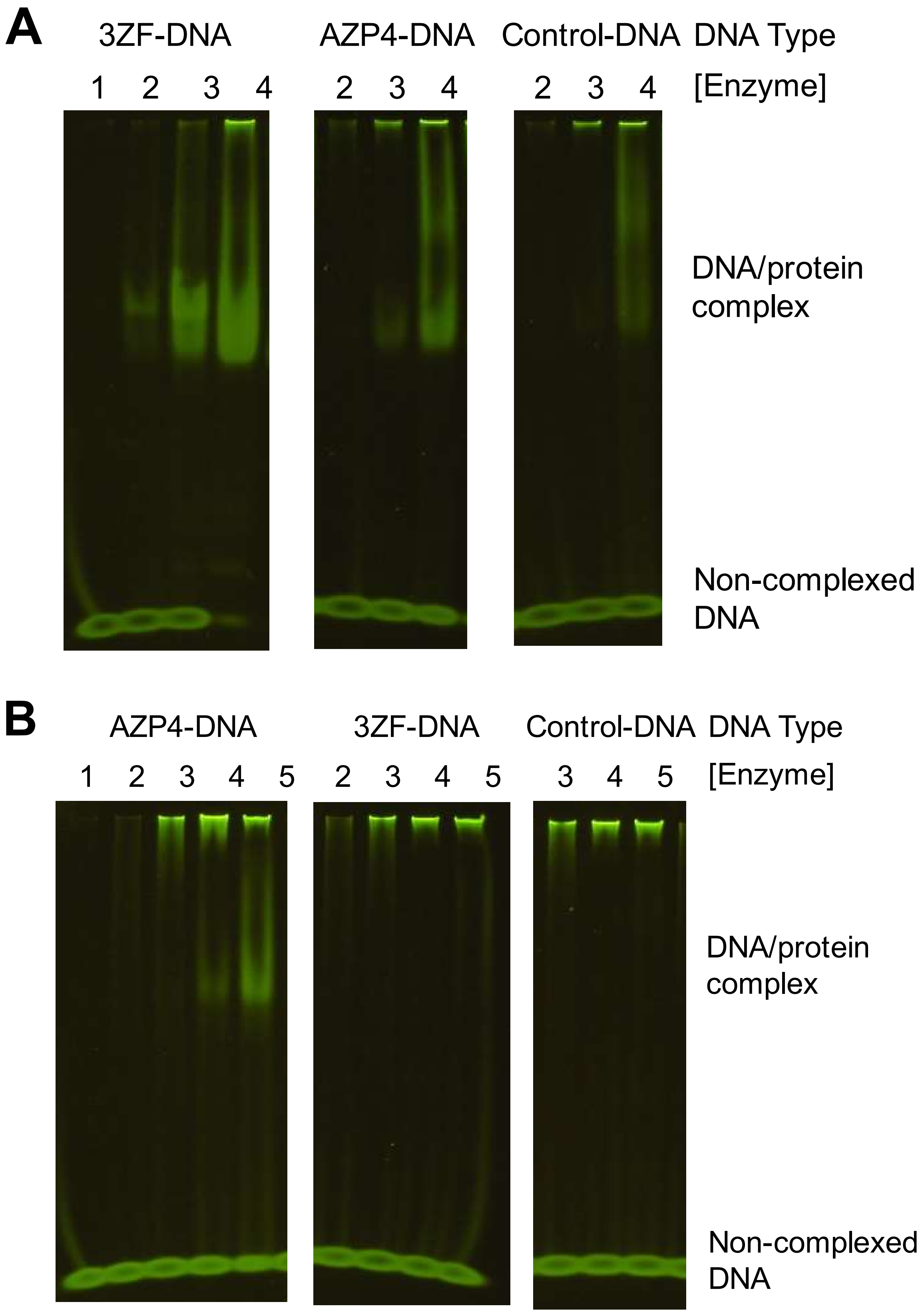
A
3ZF-DNA
AZP4-DNA
Control-DNA
DNA Type
1 2 3 4
2 3 4
2 3 4
[Enzyme]
DNA/protein complex
Non-complexed DNA
B
AZP4-DNA
3ZF-DNA
Control-DNA
DNA Type
1 2 3 4 5
2 3 4 5
3 4 5
[Enzyme]
DNA/protein complex
Non-complexed DNA

Figure 2: EMSA of target oligos and recombinant enzymes for 0.75 µM DNA and (1) 0 µM, (2) 0.15 µM, (3) 0.75 µM, (4) 3.75 µM and (5) 18.75 µM of (A) cMDH-3ZF-His and (B) CS-AZP4-His.

Zinc finger fusion proteins were also found to bind to their target DNA by and magnetic bead capture assays (Figure 3). When cMDH-3ZF is incubated with its target DNA 3ZF-DNA, there is more remaining cMDH-3ZF-His after washing than for the other DNA sequences. There is a 67% and 81% decrease in the remaining enzyme for Control-DNA and AZP4-DNA, respectively. There is a similar behavior for CS-AZP4-His and AZP4-DNA, with a 46% and 50% decrease in the amount of bound CS-AZP4-His for Control-DNA and 3ZF-DNA, respectively. There is a lower amount of bound CS-AZP4-His compared to cMDH-3ZF-His with 0.35 nM of CS-AZP4-His/AZP4-DNA and 5.42 nM for cMDH-3ZF-His/3ZF-DNA. These results agree with the EMSA results showing a higher concentration of DNA/protein complex for cMDH-3ZF-His/3ZF-DNA and CS-AZP4-His/AZP4-DNA.

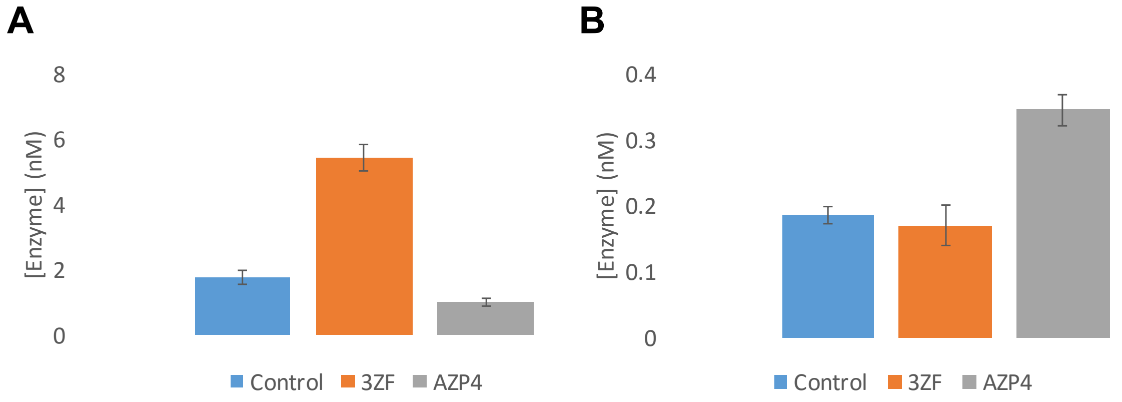

Figure 3: Amount of protein bound to biotinylated DNA targets captured with streptavidin coated magnetic beads. (A) cMDH-3ZF-His and (B) CS-AZP4-His.

Now that zinc finger fusion proteins have been shown to bind to their target sequences, the next step is to assemble multienzyme complexes using the DNA scaffolds. By placing each target site on the same DNA, we can have both cMDH-3ZF-His and CS-AZP4-His in close proximity via the DNA/zinc finger protein interactions. The binding of each individual zinc finger/enzyme fusion to each DNA scaffold will be evaluated by EMSA and bead binding assays. Substrate channeling between the two enzymes will be evaluated via a coupled/competitive enzyme assay. In this assay, NAD+, L-malate and acetyl-CoA are all supplied and the production of coenzyme A is monitored with the addition of DTNB. In this assay, cMDH-3ZF-His will produce OAA, which is then transferred to CS-AZP4-His. A third enzyme, aspartate aminotransferase, is added to the activity assay in increasing amounts in order to consume OAA in the bulk solution. If the intermediate OAA is channeled between the two enzymes, we can expect a lower decrease in the coupled activity than if the enzymes are freely diffusing. Several DNA scaffolds will be evaluated, with various spacing between the two DNA target sites in order to examine proximity effects on channeling. The addition of positively charged peptide/oligonucleotide conjugates can be examined that may be able to shuttle the negatively charged OAA between enzymes. These results will be compared to substrate channeling in the naturally occurring multienzyme complex between mMDH and CS.

References

(1) Srere, P. A.; Mosbach, K. *Annual Review of Microbiology* 1974, *28* (1), 61–84.

(2) Ovádi, J.; Sreret, P. A. In *Microcompartmentation and Phase Separation in Cytoplasm*; International Review of Cytology; Elsevier, 1999; Vol. 192, pp 255–280.

(3) Ovádi, J. *J. Theor. Biol.* 1991, *152* (1), 1–22.

(4) Wheeldon, I.; Minteer, S. D.; Banta, S.; Barton, S. C.; Atanassov, P.; Sigman, M. *Nat Chem* 2016, *8* (4), 299–309.

(5) Velot, C.; Mixon, M. B.; Teige, M.; Srere, P. A. *Biochemistry* 1997, *36* (47), 14271–14276.

(6) Shatalin, K.; Lebreton, S.; Rault-Leonardon, M.; Vélot, C.; Srere, P. A. *Biochemistry* 1999, *38* (3), 881–889.

(7) Wu, F.; Minteer, S. *Angew. Chem. Int. Ed.* 2014, *54* (6), 1851–1854.

(8) Sun, Q.; Madan, B.; Tsai, S.-L.; DeLisa, M. P.; Chen, W. *Chem. Commun.* 2014, *50* (12), 1423–1425.

(9) Nakata, E.; Liew, F. F.; Uwatoko, C.; Kiyonaka, S.; Mori, Y.; Katsuda, Y.; Endo, M.; Sugiyama, H.; Morii, T. *Angew. Chem. Int. Ed.* 2012, *51* (10), 2421–2424.

(10) Sera, T.; Uranga, C. *Biochemistry* 2002, *41* (22), 7074–7081.

(11) Szilvay, G. R.; Brocato, S.; Ivnitski, D.; Li, C.; Iglesia, P. D. L.; Lau, C.; Chi, E.; Werner-Washburne, M.; Banta, S.; Atanassov, P. *Chem. Commun.* 2011, *47* (26), 7464–3.